

AD-A267 510 AGE

Form Approved  
CMB No. 0704-0188Public reporting burden  
estimate for this form  
is 1 hour per response,  
including reviewing  
instructions, searching  
existing data sources,  
gathering and maintaining  
the data needed, reviewing  
and revising the  
information, and completing  
and reviewing the  
collection of information.  
Send comments regarding this  
burden estimate to Washington  
Headquarters, Directorate for  
Information Operations and  
Reports, 1215 Jefferson  
Road, Paperwork Reduction  
Project (0704-0188), Washington, DC 20503.

1. AGENCY USE ONLY (Leave blank)		2. REPORT DATE Aug 1991		3. REPORT TYPE AND DATES COVERED THESIS/DISSERTATION	
4. TITLE AND SUBTITLE A Synoptic Climatology of the Elevated Mixed Layer Inversion Over the Southern Great Plains in Spring				5. FUNDING NUMBERS	
6. AUTHOR(S) John M Lanicci					
7. PERFORMING ORGANIZATION NAME(S) AND ADDRESS(ES) AFIT Student Attending: Penn State University				8. PERFORMING ORGANIZATION REPORT NUMBER AFIT/CI/CIA- 93-016D	
9. SPONSORING/MONITORING AGENCY NAME(S) AND ADDRESS(ES) DEPARTMENT OF THE AIR FORCE AFIT/CI 2950 P STREET WRIGHT-PATTERSON AFB OH 45433-7765				10. SPONSORING/MONITORING AGENCY REPORT NUMBER	
11. SUPPLEMENTARY NOTES					
12a. DISTRIBUTION AVAILABILITY STATEMENT Approved for Public Release IAW 190-1 Distribution Unlimited MICHAEL M. BRICKER, SMSgt, USAF Chief Administration				12b. DISTRIBUTION CODE	
13. ABSTRACT (Maximum 200 words)					
14. SUBJECT TERMS					
				15. NUMBER OF PAGES 291	
				16. PRICE CODE	
17. SECURITY CLASSIFICATION OF REPORT		18. SECURITY CLASSIFICATION OF THIS PAGE		19. SECURITY CLASSIFICATION OF ABSTRACT	
				20. LIMITATION OF ABSTRACT	

93 8 05 1 2

93-18099



1

The Pennsylvania State University  
The Graduate School  
College of Earth and Mineral Sciences  
  
A SYNOPTIC CLIMATOLOGY  
OF THE ELEVATED MIXED LAYER INVERSION  
OVER THE SOUTHERN GREAT PLAINS IN SPRING

A Thesis in  
Meteorology

by

John M. Lanicci

Submitted in Partial Fulfillment  
of the Requirements  
for the Degree of

**DTIC QUALITY INSPECTED 3**

Doctor of Philosophy

August 1991

Accession For	
NTIS CRA&I	<input checked="checked" type="checkbox"/>
DTIC TAB	<input type="checkbox"/>
Unannounced	<input type="checkbox"/>
Justification	
By	
Distribution /	
Availability Codes	
Dist	Avail and/or Special
A-1	

## ABSTRACT

A synoptic climatology is presented of the atmospheric conditions associated with the creation of the elevated mixed layer inversion, or lid, over the southern Great Plains of the U.S. (defined as Kansas, Oklahoma, and Texas, and portions of the surrounding states) during four spring (April, May, June) seasons from 1983 through 1986. The lid sounding, also known as a Type 1 tornado sounding, is created through the superposition of a potentially warm, nearly dry-adiabatic elevated mixed layer (EML) over a potentially unstable moist layer. This study examines the synoptic patterns associated with the creation of the EML and the moist layer, and the subsequent evolution of these component airmasses into a lid sounding. The study utilizes EML and lid-occurrence statistics, analyses of the EML and moist layer, and a subjective synoptic typing system based on the geostrophic wind relationship at the surface and 500 mb. The temporal and spatial variability of lid occurrence and the associated synoptic types are used to determine the periodicity of lid occurrence over the southern Plains, including the seasonal tendencies and relationships between different stages of lid development and specific synoptic flow types. This study also investigates the relationships between lid occurrence and the occurrence of severe storm outbreaks over the Kansas-Oklahoma-Texas region.

This study shows that the lid coverage over the southern Great Plains undergoes a seasonal evolution in which the lid area responds to changes in the location of the EML source region and the orientation of

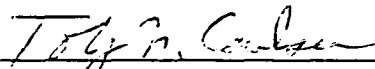
We approve the thesis of John M. Lanicci.

Date of Signature



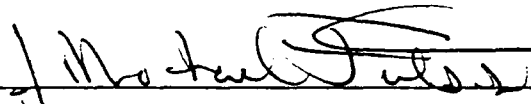
Thomas T. Warner  
Associate Professor of Meteorology  
Thesis Adviser  
Chair of Committee

30 May 1991



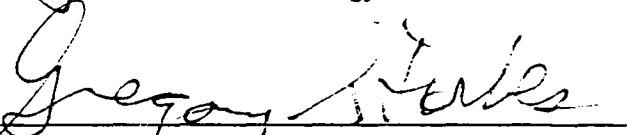
Toby M. Carlson  
Professor of Meteorology

22 May 1991



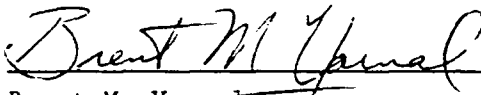
J. Michael Fritsch  
Professor of Meteorology

24 May 1991



Gregory S. Forbes  
Associate Professor of Meteorology

30 April 1991



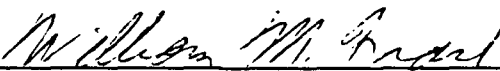
Brent M. Yarnal  
Associate Professor of Geography

30 April 1991



Charles A. Doswell III  
Research Meteorologist  
National Severe Storms Laboratory  
Special Member

4/30/91



William M. Frank  
Professor of Meteorology  
Head of the Department of Meteorology

22 May 1991



the mean low level moist tongue. The relative airstream configuration associated with the classic models of lid formation and severe weather over this region occurs most frequently in April and May, and is typically associated with the largest lid-coverage areas in all three months. By the late spring, the lid is observed with a variety of additional flow types, such as northwesterly and anticyclonic midlevel flows. These two flow types are mainly associated with large scale subsidence, leading to an airstream configuration in which the lid base sinks downstream from the source region, in stark contrast to the classic southwest flow type in which the lid base rises and the lid weakens in an environment of large scale ascent.

Time-series analyses of lid occurrence and synoptic types reveals a cyclic tendency with a mean period of about one week. Two types of lid cycles are identified: one that is associated with polar-air outbreaks and baroclinic waves in the westerlies, and one that is associated with weak southerly low level flow, subtropical circulations, and weak short wave features that are characteristic of the late spring. A relationship between the size of a severe storm outbreak and the antecedent lid coverage is best defined in early spring, and rapidly deteriorates from May to June.

An example of an early-spring lid cycle is analyzed using both conventional data and a 120-h simulation with the Penn State/NCAR mesoscale model. The case study examines the creation and evolution of the EML and moist layer, and reveals information about some of the important physical processes involved. The results of the case study clarify important aspects of the synoptic climatology that the composite datasets alone are unable to reveal.

## TABLE OF CONTENTS

	<u>Page</u>
LIST OF TABLES . . . . .	ix
LIST OF FIGURES . . . . .	x
PREFACE . . . . .	xxii
Chapter 1. INTRODUCTION . . . . .	1
1.1. Literature Review of Severe-Storms Climatology . . . . .	2
1.2. The Creation and Evolution of the Components of the Lid Sounding . . . . .	3
1.3. Purpose of Thesis . . . . .	12
Chapter 2. THE SYNOPTIC CLIMATOLOGY: STRUCTURE DYNAMICS, AND SEASONAL EVOLUTION . . . . .	14
2.1. Chapter Introduction . . . . .	14
2.2. Lid Characteristics Over the Southern Plains: April-June 1983-1986 . . . . .	18
2.2.1. The Sounding Analysis Procedure . . . . .	20
2.2.2. Monthly Lid Frequency . . . . .	27
2.2.3. Monthly Geographic Distribution of Lid Frequency . . . . .	29
2.2.4. Elevated Mixed Layer Source-Region Climatology . . . . .	31
2.3. Synoptic Typing of Surface and 500-mb Flows Over the Southern Plains . . . . .	34
2.3.1. Methodology and Physical Assumptions . . . . .	35
2.3.2. Lid Frequencies Associated with the Various Flow Types . . . . .	40

	<u>Page</u>
2.3.3. Mean Monthly EML and Lid Characteristics as Related to Synoptic Flow Patterns . . . . .	45
2.3.4. Seasonal Changes in the Characteristics of the EML and Lid . . . . .	50
2.4. Discussion . . . . .	54
Chapter 3. THE SYNOPTIC CLIMATOLOGY: THE LIFE OF THE LID . . . . .	57
3.1. Chapter Introduction . . . . .	57
3.2. Time Series Analysis of Lid Occurrence . . . . .	60
3.3. A Schematic Life Cycle of the Lid . . . . .	64
3.3.1. Types of Lid Cycles . . . . .	64
3.3.2. Characteristics of the Lid Cycle Stages. . . . .	67
3.4. Synoptic Flow Patterns During the Lid Cycle . . . . .	76
3.4.1. Prevailing Synoptic Types During the Lid Cycle . . . . .	76
3.4.2. Flow Structure During the Lid Cycle . . . . .	81
3.4.2.1. The Early-Season H Lid Cycle . . . . .	84
3.4.2.2. The Late-Spring H Lid Cycle . . . . .	90
3.4.2.3. The R Lid Cycle . . . . .	93
3.5. Discussion and Summary . . . . .	97
Chapter 4. THE SYNOPTIC CLIMATOLOGY: RELATIONSHIP TO SEVERE-STORMS CLIMATOLOGY . . . . .	103
4.1. Chapter Introduction . . . . .	103
4.2. Severe-Storm Statistics for the Southern Plains: April-June 1983-1986 . . . . .	107
4.3. Relationship of the Outbreak Size to the Lid . . . . .	114
4.4. Relationships Between the Lid, Severe Weather, and Representative Synoptic Flow Types . . . . .	122
4.4.1. Severe Weather Associated with the Lid Cycle . . . . .	122

4.4.2. Lid and Severe Weather Occurrence for Representative Synoptic Types . . . . .	126
4.5. Conclusions . . . . .	138
Chapter 5. AN EXAMPLE OF AN EARLY SPRING LID CYCLE . . . . .	142
5.1. Overview of the 4-9 April 1984 H Lid Cycle . . . . .	142
5.2. Examination of the Lid Cycle by Stages . . . . .	152
5.2.1. The High-Pressure Stage (1200 UTC 4 April- 0000 UTC 6 April) . . . . .	152
5.2.2. The Return-Flow Stage (0000 UTC 6 April- 0000 UTC 7 April). . . . .	169
5.2.3. Lid Genesis (0000 UTC-1200 UTC 7 April). . . . .	173
5.2.4. The Lid-Maximum Stage and Severe-Weather Outbreak (1200 UTC 7 April-1200 UTC 8 April) . . . .	180
5.2.5. The Post Lid-Maximum Stage and The Second Severe- Weather Outbreak (1200 UTC 8 April-0000 UTC 9 April) . . . . .	189
5.2.6. The End Stage of the Cycle (0000 UTC-1200 UTC 9 April) . . . . .	192
Chapter 6. NUMERICAL SIMULATION OF THE 4-9 APRIL 1984 LID CYCLE WITH THE PENN STATE/NCAR MESOSCALE MODEL . . . . .	200
6.1. MM4 Characteristics . . . . .	201
6.1.1. General Description . . . . .	201
6.1.2. Specific Characteristics of the Version of MM4 Used in This Study . . . . .	203
6.2. Model Verification of Large Scale Flow Features During the Lid Cycle . . . . .	215
6.3. Examination of Physical Processes Involved in the Formation and Evolution of the EML and Moist Layer . . . . .	217

	<u>Page</u>
6.3.1. Formation of the Western U.S. and Mexican EMLs . . . . .	219
6.3.2. Formation of the Moist Layer Over the Gulf of Mexico . . . . .	243
6.4. Formation of the Lid Over the Southern Great Plains . . . . .	255
Chapter 7. CONCLUSIONS AND DISCUSSION . . . . .	271
7.1. Summary of Results . . . . .	271
7.2. Suggestions for Future Research . . . . .	279
REFERENCES . . . . .	281

## LIST OF TABLES

	<u>Page</u>
Table 1.1 Event-Based Severe-Storm Climatologies . . . . .	4
Table 2.1 Uncapped Soundings for Four Gulf Coast Stations (Based on 1200 UTC data) . . . . .	52
Table 3.1 The Stages of the Lid Cycle . . . . .	68
Table 3.2 Spring Lid Cycles: 1983-1986 . . . . .	70
Table 3.3 Occurrence Frequency of Synoptic Types at Each Stage of the Lid Cycle . . . . .	77
Table 4.1 Linear Correlation Coefficients Between Severe- Weather Event Areas and Antecedent Lid-Coverage Areas Exceeding Certain LS and BUO Threshold Values . . . . .	120
Table 6.1 Full and Half Sigma Levels and Standard Pressures (assumed $P_{sfc} = 1000$ mb) For MM4 . . . . .	207
Table 6.2 Description of MM4 Land-Use Categories and Surface Parameters in This Modeling Study . . . . .	213

## LIST OF FIGURES

	<u>Page</u>
Figure 2.1. The study region, showing the locations and three-letter identifiers of the rawinsonde stations which are frequently referred to in the text . . . . .	19
Figure 2.2. Cumulative occurrence frequencies (in %) of a seasonal sample of EML soundings observed over the study region during the study period. The sample consists of 195 soundings whose EML obeyed the RH criterion, and 118 soundings that did not. The cumulative occurrence frequencies are computed based on the separate sample sizes, and are categorized by static stability intervals, as shown on the abscissa . . . . .	22
Figure 2.3. Skew-T Log P diagrams representing various types of soundings characterized by the automated sounding-analysis program. In each panel, the temperature sounding is indicated by the thick solid line and the dewpoint sounding is shown by the thin solid line. Winds are plotted along the right axis of each sounding using conventional notation (speed is in kt). Types of soundings shown are a) non-EML, b) EML, c) subsidence-type, d) lid with no relative humidity increase with height in the EML, and e) lid with relative humidity increasing with height in the EML . . . . .	26
Figure 2.4. Histograms showing the total number of lid stations observed over the region at both 0000 and 1200 UTC, and their occurrence frequencies for a) April, b) May, and c) June. The mean number of lid stations (excluding the no-lid days) for each month is shown in the upper right, along with the median number of lid stations (including all days) . . . . .	28
Figure 2.5. Mean number of lid days over the region (see text for the definition of a "lid day"). An asterisk (*) next to the station means that the 1200 UTC lid frequency is greater than or equal to twice the 0000 UTC frequency. Charts are shown for a) April, b) May, and c) June. The change in lid days from April to June is shown by the difference field in (d) . . . . .	30
Figure 2.6. Climatological mean maximum surface potential temperature analysis (in °C) over northern Mexico and the western U.S. for a) April, b) May, and c) June. Values greater than or equal to 44°C are alternately highlighted in 4°C intervals as shown in the lower left corner of chart (a). . . . .	33

- Figure 2.7. Idealized patterns of sea level isobars for surface synoptic flow types. Types shown are: a) high pressure with north-south oriented ridge axis, b) high pressure with northwest-southeast ridge axis, c) weak return flow with surface ridge over southeastern portion of region (Gulf not "open"), d) weak return flow after high pressure exits the region (Gulf "open"), e) strong return flow, and f) frontal passage . . . . . 37
- Figure 2.8. Idealized patterns of 500-mb geopotential heights for upper-air flow types. Shown here are: a) north-westerly flow, b) westerly flow, c) southwesterly flow, d) anticyclonic flow, and e) cyclonic flow . . . . . 39
- Figure 2.9. Lid frequency by synoptic type for a) April, b) May, and c) June. The ordinate denotes the number of lid stations, and the abscissa denotes the five surface synoptic types (each separated by the vertical line), subdivided by 500-mb type. The numbers along the abscissa refer to the following surface types: 1 = N-S pressure ridge, 2 = NW-SE pressure ridge, 3 = weak return flow, 4 = strong return flow, and 5 = frontal passage. The 500-mb flow types are abbreviated as follows: NW = northwest, W = west, A = anticyclonic, SW = southwest, and C = cyclonic. The number of occurrences of each synoptic type and corresponding number of lid stations are shown. The horizontal dashed line separates "small" and "large" lid-coverage areas . . . . . 43
- Figure 2.10. Mean analyses of EML and lid parameters for the most frequently occurring EML/lid-producing synoptic patterns. Charts are shown for a) April, b) May, and c) June. The solid lines denote mean "best" wet-bulb potential temperature in °C and are analyzed at 2°C intervals. The dashed lines are the mean potential temperature (°C) in the EML (when observed), and are drawn every degree. The light shading highlights regions having a mean EML base above 750 mb, with the dark shading indicating a mean EML base below 800 mb. The scalloped border outlines the 25% occurrence frequency of the EML/lid . . . . . 47



- Figure 3.1. Time series of lid occurrence for the period April-June 1985. The ordinate denotes the lid-coverage area in terms of the number of "lid stations" over the study region; the dates on the abscissa correspond to the 1200 UTC analysis time only. The horizontal dashed line marks the boundary between the "small" and "large" lid-coverage areas (see Figs. 2.4 and 2.9 for details). For the purpose of the analysis, any missing 1200 UTC data were compensated for by using data from the adjacent 0000 UTC data times and the synoptic type for that date. . . . . 62
- Figure 3.2. Occurrence frequency of lid cycle length (days) for the study period . . . . . 65
- Figure 3.3. Mean lid-coverage area for each phase of the lid cycle (see Table 3.1 for definitions of lid cycle phases). Cycles shown are a) early-season H, b) late-season H, and c) late-season R . . . . . 72
- Figure 3.4. Lid cycle phase length (in whole days) and frequencies for the three types of lid cycles shown in Fig. 3.3 (legend is shown in panel 'a'). Phases shown are a) high pressure, b) return flow, c) pre-lid-maximum, d) lid maximum, e) post-lid-maximum, and f) end . . . . . 74
- Figure 3.5. Composite mean charts for synoptic types representing different stages of the early-spring H lid cycle. The "peel back" in the lower left in (a) shows the grid mesh used to produce the composite fields. Mean sea level isobars are depicted by thick solid lines labelled in mb (interval of 4 mb); mean 500-mb heights are shown by thick dotted lines labelled in decameters (interval of 6 dm); representative mean surface isodrosotherms (55°F and 65°F) are shown as dot-dashed lines; representative mean 700-mb isotherms (6°C and 10°C) are shown by thin dashed lines. The areas of occurrence frequency equal to or greater than 50% are shown for the following parameters: unstable buoyancy (vertical shading), EML (horizontal shading), and the areas of overlap (indicative of high lid occurrence frequency, "checkerboard" shading). Surface highs, lows, fronts, and troughs are shown using conventional symbols. Highs and lows at 500 mb are displayed using "open" lettering. Charts are displayed for the following lid cycle stages with the synoptic types (see notation in Table 3.3) in parentheses: a) high pressure ("1-NW"), b) return flow ("3-A"), c) pre-lid-maximum ("4-SW"), d) lid maximum ("4-SW"), and e) post-lid-maximum ("5-C"). . . 83

Page

- Figure 3.6. Same as Fig. 3.5, except for late-spring H cycle. Charts are shown for the following lid cycle phases and synoptic types: a) high pressure ("1-NW") and b) combined pre-lid-maximum, lid-maximum, and post-lid-maximum stages ("4-SW") . . . . . 91
- Figure 3.7. Same as Fig. 3.5, except for late-season R cycle. Charts are shown for the following lid cycle phases and synoptic types: a) return flow ("3-A"; Bermuda anticyclone dominant), and b) combined pre-lid-maximum, lid-maximum, and post-lid-maximum stages ("3-A"; Pacific anticyclone dominant). Note that the isopleth interval for the mean 500-mb heights is 3 dm in this figure . . . . . 94
- Figure 4.1. Percentile graph displaying the cumulative occurrence frequency of severe storm events as a function of the total area of each event (given as the number of 40-km squares). . . . . 109
- Figure 4.2. Geographic frequency of severe storm events over the study region in terms of number of events per 40-km square. Light shading denotes 3-5 events per square, medium shading denotes 6-8 events per square, and dark shading denotes greater than 8 events per square. Charts are shown for April, May, and June. . . . . 112
- Figure 4.3. Histograms displaying the occurrence frequencies of 1200 and 0000 UTC lid coverage areas, given as the number of upper air stations with a lid sounding ("lid stations") for non-event days and event days (legend is shown in panel 'a'). Charts are shown for April, May, and June . . . . . 115
- Figure 4.4. Scatter plot showing the antecedent lid coverage (in terms of number of lid stations at either 1200 or 0000 UTC) versus the size of the subsequent severe storm event (given as the number of 40-km squares). Non-event days are given an event size of zero. The numbers on the plot refer to the occurrence frequency. The linear regression line and error bars for one standard deviation are also displayed. Charts are shown for April, May, and June . . . . . 117

- Figure 4.5. Scatter plot showing the 1200 UTC lid coverage (in terms of the number of lid stations) versus the subsequent severe-storm event(s) area for the following 24-h period (given as the number of 40-km squares in log base 2 coordinates on the abscissa) for each stage of the early-season H lid cycle. The numbers on the plots refer to the occurrence frequency. Non-event days are given an event size of zero. An "m" denotes the mean lid/severe-weather event coverage for each phase of the lid cycle. Total number of event squares for each stage is shown by an inset on each panel . . . 123
- Figure 4.6. Same as Fig. 4.5, except for the late-season H lid cycle. . . . . 125
- Figure 4.7. Same as Fig. 4.5, except for the late-season R lid cycle. . . . . 127
- Figure 4.8. Composite mean analyses of key meteorological features at 1200 UTC and subsequent 12-h severe-weather event areas for representative synoptic types during the lid cycle. A legend is shown in panel (a). Charts are shown for the following synoptic types representing various stages of the early-season H lid cycle: b) N-S pressure ridge with northwest flow aloft, representing the high-pressure stage; c) weak return flow with anticyclonic flow aloft, representing the return-flow stage; strong return flow with southwest flow aloft, representing both d) the pre-lid-maximum stage, and e) the lid-maximum stage; and f) frontal passage with cyclonic flow aloft, representing the post-lid-maximum stage. . . . . 130
- Figure 4.9. Same as Fig. 4.8, except for the late-season R lid cycle. Charts are shown for the following synoptic types and cycle phases: a) weak return flow/anticyclonic flow aloft (Bermuda high dominant), representing the return-flow stage; b) the same as panel (a) except that the geographic frequency composite includes uncapped, EML, and subsidence-layer soundings; and c) weak return flow/anticyclonic flow aloft (Pacific high dominant), representing the large lid-coverage stages. . . . . 135

Page

- Figure 5.1. Analysis of surface and 500-mb features at 1200 UTC on each day of the 4-9 April 1984 lid cycle. The 1016 and 1008-mb sea level isobars are shown by the thin lines, and the thick lines with arrows denote the subjectively analyzed 500-mb jets. Surface fronts, troughs, highs and lows are shown using conventional notation. Locations of 500-mb highs and lows are shown using "open" lettering. The locations of the stations used in the time series of Fig. 5.3 are shown in panel (a). On panel (d), the position of the surface dryline is shown using a solid, scalloped line. Analyses are shown for a) 4 April, b) 5 April, c) 6 April, d) 7 April, e) 8 April, and f) 9 April. . . . . 144
- Figure 5.2. Locations of severe weather and heavy rainfall ( $\geq 1$  inch in 24 h) rainfall reported over Texas and Oklahoma from 1200 UTC 7 April to 1200 UTC 8 April (panel 'a'), and over Arkansas, Louisiana, and Mississippi from 1200 UTC 8 April to 1200 UTC 9 April (panel 'b'). Symbols are explained in upper left portion of panel (a). Reports are compiled from the U.S. Department of Commerce publication Storm Data. . . . . 150
- Figure 5.3. Time series of surface observations over the Gulf coastal region from south Texas to the Yucatan Peninsula of Mexico, from 1200 UTC 4 April to 1200 UTC 6 April. Stations are listed so they form a counterclockwise arc beginning in south Texas. Stations shown are BRO (Brownsville, Texas), SOM (Soto La Marina, Mexico), TUX Tuxpan, Mexico), VER (Veracruz, Mexico), MTT (Coatzacoalcos, Mexico), and MID (Merida, Mexico). . . . . 155
- Figure 5.4. Series of 850-mb temperature analyses for the following times: a) 1200 UTC 4 April, b) 0000 UTC 5 April, c) 1200 UTC 5 April, d) 0000 UTC 6 April, and e) 1200 UTC 6 April. Isotherms are analyzed every  $2^{\circ}\text{C}$ , and the intersection of the 850-mb level with the ground is shown by the dashed line. . . . . 157
- Figure 5.5. Series of GOES visible satellite images for the following times: a) 1430 UTC 4 April, b) 2030 UTC 4 April, c) 1431 UTC 5 April, d) 2031 UTC 5 April, and e) 1431 UTC 6 April. . . . . 161

- Figure 5.6. Analysis of 700-500 mb temperature lapse rate in  $^{\circ}\text{C km}^{-1}$ , isoplethed every  $0.5^{\circ}\text{C km}^{-1}$ . The thicker lines denote the  $7.5$  and  $4.5^{\circ}\text{C km}^{-1}$  isopleths, which are representative of low and high static stability areas, respectively. In panel (b), the shaded region denotes 850-700 mb lapse rates  $\geq 7.5^{\circ}\text{C km}^{-1}$ . Analyses shown for a) 1200 UTC 4 April, b) 0000 UTC 5 April, and c) 1200 UTC 5 April. . . . . 165
- Figure 5.7. Positions of subjectively analyzed 200-mb jet and its ridge axis over the region of the subtropical jet. The location of the jet's ridge axis is shown by the jagged line, and is labelled for each time. Jet positions are displayed for 1200 UTC 4 April (solid line), 0000 UTC 5 April (long dashed line), and 1200 UTC 5 April (short dashed lines). . . . . 168
- Figure 5.8. Low level features at 1200 UTC 6 April. Surface fronts, troughs, highs, and lows are shown using conventional symbols. The solid line denotes the  $50^{\circ}\text{F}$  isodrosotherm, and the solid lines with arrows denote the LLJ as determined from the winds aloft observations for the second standard level above the surface. The thin line with the open arrowhead over south Texas is a streamline indicating the flow direction over this area . . . . . 171
- Figure 5.9. As in Fig. 5.6, except for a) 0000 UTC and b) 1200 UTC 6 April . . . . . 172
- Figure 5.10. Temporal continuity of  $50^{\circ}\text{F}$  isodrosotherm and surface highs and lows for the period 1200-2100 UTC 6 April. Isodrosotherm locations are coded as follows: 1200 UTC = solid line, 1500 UTC = long dashed line, 1800 UTC = dotted line, and 2100 UTC = short dashed line. The locations of pressure troughs (heavy long dashed lines) are for 2100 UTC only . . . . . 174
- Figure 5.11. As in Fig. 5.8, except for 0000 UTC 7 April. Surface dryline is shown using a solid, scalloped line. . . . . 175
- Figure 5.12. As in Fig. 5.6, except for a) 0000 UTC and b) 1200 UTC 7 April. The location of the cross section shown in Fig. 5.20 is displayed in panel (b). . . . . 177

Figure 5.13.	Lid strength (LS) and buoyancy (BUO) term analyses for a) 0000 UTC and b) 1200 UTC 7 April. Lid strengths are only analyzed where an EML is present, within the scalloped borders. Isopleths of lid strength are shown by solid lines, contoured every 2°C, and buoyancy term isopleths are displayed as dashed lines, and are also contoured every 2°C. The location of the lid-coverage area is shown by the shaded region. . . . .	179
Figure 5.14.	Composite surface/upper-air analysis for 1200 UTC 7 April (panel 'b'). Symbols are shown in the legend panel (a). . . . .	182
Figure 5.15.	Surface analysis and manually digitized radar summary overlay. Surface fronts, troughs, highs, and lows are shown using conventional symbols. The locations of surface moist tongues are shown using the same symbol as in Fig. 5.14a. The locations of radar echoes with DVIP level of 3 or greater are shown as dark shaded regions. A circle with a dot inside denotes the first observation of a particular echo. Thin solid lines connecting the shaded regions denote a squall line. Analysis/radar summary times are a) 1500/1535 UTC, b) 1800/1835 UTC, and c) 2100/2035 UTC 7 April . . . . .	185
Figure 5.16.	As in Fig. 5.14, except for 0000 UTC 8 April. See Fig. 5.14a for symbols. . . . .	188
Figure 5.17.	As in Fig. 5.6, except for a) 0000 UTC and b) 1200 UTC 8 April . . . . .	190
Figure 5.18.	As in Fig. 5.14, except for 1200 UTC 8 April. See Fig. 5.14a for symbols. . . . .	191
Figure 5.19.	As in Fig. 5.6, except for a) 0000 UTC and b) 1200 UTC 9 April. . . . .	193

- Figure 5.20. Isentropic cross sections from southern California to the Louisiana coast (see Fig. 5.12b for exact location) for the following times: a) 1200 UTC 7 April, b) 0000 UTC 8 April, and c) 1200 UTC 8 April. Isentropes (in K) are analyzed at 3 K intervals, and are labelled every 12 K. The vertical coordinate is log pressure, and is labelled in 100 mb intervals along right side of figure . . . . . 196
- Figure 6.1. Map of the model domain showing the location (shaded areas) of the persistent snow cover used for the simulation . . . . . 206
- Figure 6.2. Sea surface temperatures (in °C, isoplethed every degree) used in the model over the Gulf of Mexico and adjacent waters. The position of the Loop Current (LC) is marked by the dashed line . . . . . 211
- Figure 6.3. Map of the model land-use categories used in this study. A legend is shown to the left of the map . . . . . 214
- Figure 6.4. Model-derived analysis of surface and 500-mb features at 1200 UTC 7 April 1984. The symbols used are identical to those in Fig. 5.1, except the dryline at  $\sigma = 0.96$  is shown using an open scalloped line . . . . . 216
- Figure 6.5. EML source-region and elevated-region analysis for a) 0000 UTC 5 April. Location of model-generated EML source region is outlined by scalloped lines. Mean potential temperature in the source/elevated region (°C) is shown by dashed lines, and is isoplethed at 4°C intervals; the pressure at the top of the layer is shown by the solid lines, is labelled in mb, and is isoplethed every 50 mb . . . . . 221
- Figure 6.6. Model temperature/dewpoint soundings (skew T log P) for 0000 UTC (solid lines) and 1200 UTC (dot-dashed lines). Locations of soundings are a) Torreon, Mexico (TRC); b) Albuquerque, New Mexico (ABQ); and c) Lander, Wyoming (LND). Wind profiles for both times are displayed at the right; wind speeds are in kt. The locations for the trajectories discussed in the text are shown by large solid dots with numbers . . . . . 223

- Figure 6.7. Horizontal parcel trajectories for the three sounding locations in Fig. 6.6. Trajectories are displayed as thin, solid lines and are labelled with numbers. Simulated surface and 500-mb features are shown for the temporal midpoint of the trajectories (0000 UTC 5 April) and are shown using the notation of Fig. 6.4 . . . . . 226
- Figure 6.8. Parcel histories for the trajectories originating at the three sounding locations in Fig. 6.6. Potential temperature history is shown in panels (a), (c), and (e). The ordinate displays the potential temperature (in K), and the abscissa shows the hour of the simulation (note that time is read from right to left). A key below the abscissa indicates the symbols used to denote each parcel. Vertical displacement history is shown in panels (b), (d), and (f). The ordinate displays the sigma level above the local surface (see Eq. 6.1 for a definition of the sigma vertical coordinate; the ordinate value from 1.0). The abscissa and the legend are the same as in the potential temperature histories . . . . . 229
- Figure 6.9. Same as Fig. 6.5, except for a) 0000 UTC 6 April, and b) 1200 UTC 6 April. Maximum potential temperature values within the EML source/elevated regions are indicated by a 'W', with the value shown below (in °C) . . . . . 236
- Figure 6.10. Same as Fig. 6.7, except for the horizontal trajectories originating at locations near Chihuahua, Mexico (CUU) and Amarillo, Texas (AMA). Meteorological features are shown for the temporal midpoint of the parcel trajectories (0000 UTC 6 April). . . . . 238
- Figure 6.11. Same as Fig. 6.8, except for the locations shown in Fig. 6.10. Potential temperature histories are displayed in panels (a) and (c), and vertical displacement histories are displayed in panels (b) and (d) . . . . . 240



- Figure 6.12. Model simulation of 850-mb temperature (panel 'a'), analyzed in °C and isoplethed every 2°C, for 0000 UTC 5 April. The intersection of the 850-mb surface with the ground is depicted by the dashed line. Panel (b) shows a time-height cross section of potential temperature (°C, isoplethed every 4°C), mixing ratio ( $\text{g kg}^{-1}$ , isoplethed every 2  $\text{g kg}^{-1}$ ), and wind direction and speed (in kt) for Veracruz, Mexico from 1200 UTC 4 April to 0000 UTC 6 April. Note that time is read from right to left . . . . . 245
- Figure 6.13. Horizontal trajectory for parcel originating in offshore PBL flow along Texas coast at initial time (1200 UTC 4 April). Tick marks along the trajectory are used to denote the simulation hour; the table inset displays parcel values of potential temperature, mixing ratio, relative humidity, and sigma level above the ground at these times . . . . . 248
- Figure 6.14. Horizontal trajectories for six sets of parcels originating in the offshore PBL flow along the Gulf coast at the initial time (panel 'a'). Circled numbers denote the origin of each parcel set; parcel trajectories are indicated by solid lines with arrows. The position of the Loop Current in the eastern Gulf is shown using the same symbol as in Fig. 6.2. Panel (b) shows simulated surface anticyclone position (conventional notation) and pressure ridge position (solid lines) during the high-pressure and return-flow stages of the lid cycle. Labels are used to indicate the simulation time: A = 12 h, B = 24 h, C = 36 h, D = 48 h, and E = 60 h . . . . . 252
- Figure 6.15. Same as Fig. 6.14a, except for six sets of parcels originating within the moist layer over coastal Mexico at the 36-h point, and ending at the 72-h point . . . . . 254
- Figure 6.16. Same as Fig. 6.5, except for 0000 UTC 7 April. The area with a lid stratification is shown by the shading . . . . . 256

- Figure 6.17. Major surface and upper-air features in model simulation at the 66-h point (0600 UTC 7 April; panel 'a'). Symbols are shown in the legend panel (d). Panel (b) displays the model precipitation amounts greater than 0.3 cm for the periods 0600-0900 UTC (solid) and 0900-1200 UTC (dashed) 7 April. Panel (c) is identical to panel (b) except for 1500-1800 UTC 7 April (solid) and 2100 UTC 7 April-0000 UTC 8 April (dashed). . . . . 258
- Figure 6.18. Same as Fig. 6.6, except for single sounding time (0600 UTC 7 April), at Abilene, Texas . . . . . 262
- Figure 6.19. Same as Fig. 6.7, except for moist-layer parcels (1-3), and EML parcels (6-16), originating at the 0600 UTC Abilene sounding . . . . . 263
- Figure 6.20. Same as Fig. 6.8, except for parcels originating in the moist layer and EML of the 0600 UTC Abilene sounding. Panel (a) displays a mixing ratio history for parcels 1-3, with the ordinate denoting the parcel mixing ratio in  $\text{g kg}^{-1}$ , and the abscissa denoting simulation time (note that the time is read from right to left). A legend below the abscissa shows the symbols used for each parcel. Panel (b) shows the vertical displacement history for parcels 1-3. Panel (c) illustrates the potential temperature history for EML parcels (6-16), and panel (d) denotes the vertical displacement history for the EML parcels . . . . . 265

## PREFACE

Chapters 2 through 4 represent a three-part journal paper appearing in the June 1991 issue of *Weather and Forecasting*, entitled "A Synoptic Climatology of the Elevated Mixed Layer Inversion over the Southern Great Plains in Spring," by John M. Lanicci and Thomas T. Warner. Chapter 2 corresponds to "Part 1: Structure, Dynamics, and Seasonal Evolution"; Chapter 3 corresponds to "Part 2: The Life Cycle of the Lid"; and Chapter 4 corresponds to "Part 3: Relationship to Severe-Storms Climatology." Since the papers were written to stand alone, there is some redundancy between the material in Chapter 1 (Introduction) and the introductory sections of Chapters 2-4, and between the conclusion sections of Chapters 2-4.

I wish to express my deepest thanks to my thesis advisor, Prof. Thomas T. Warner. My doctoral research underwent many changes during my three years at Penn State, and Prof. Warner was always ready with prudent guidance and insight from his years of experience. The guidance of my doctoral committee was also valuable during my time here. I express my gratitude to Prof. Toby N. Carlson for his guidance and pioneering work in my area of study; to Prof. Gregory S. Forbes for the many discussions we had during the course of my research; to Prof. J. Michael Fritsch for his helpful suggestions; to Prof. Brent Yarnal, whose experience as a synoptic climatologist was invaluable to me, and to Dr. Charles A. Doswell III of the National Severe Storms Laboratory, who helped me grow professionally during my research.

There are many others who lent me their support during my research. In the Meteorology department, I had many fruitful discussions with Prof. Nelson L. Seaman, Prof. George S. Young, and Prof. John J. Cahir. From the NWP staff, Ms. Annette Lario, Dr. David Stauffer, and Dr. James Doyle helped me through the many steps of preparing and running the Penn State/NCAR mesoscale model and its supporting software. Tasks such as data gathering, tabulation, plotting and reproduction were professionally done by Ms. Laura Matason, Mr. Michael Hopkins, and Mrs. Amy Erlick. Superb graphics were provided by Ms. Mary Carpenter of the Deasy Geographics Lab at Penn State, and Tek-Art, Inc. of State College. Computer resources were provided by the Department of Meteorology, the National Center for Atmospheric Research (supported by the National Science Foundation), and Cray Research's facilities at Mendota Heights, MN. I was sponsored by the Air Force Institute of Technology, Wright-Patterson AFB, OH, and the research was funded by the Air Force Office of Scientific Research under Grant No. AFOSR-88-0050. This manuscript was very professionally prepared by Mrs. Joann Singer.

This work is the culmination of a goal I have had for many years. I would like to thank my wife, Kathy, and my sons, Michael and Mark, for the many sacrifices they made as a family to see this dream come to fruition. My parents, Richard and Susanna Lanicci, taught me the work ethic necessary to persevere through this demanding program. I thank God for making it possible for me to achieve the difficult goals I set for myself every day. This thesis is dedicated to the memory of my maternal grandmother, Anna D'Antonio, who taught me about the value of an education and the joy of learning.

## Chapter 1

### INTRODUCTION

The Great Plains region of the United States has the highest frequency of severe convective weather events in the world. To the forecaster and researcher alike, the myriad mesoscale features associated with the large scale environment of this area, i.e., the dryline, the low level jet, transitory upper level jet streaks, the elevated mixed layer, and the inversion that the elevated mixed layer produces when it overlies moist, unstable air (hereafter referred to as a "lid"), are fairly well known. However, predicting whether the complex interaction of these features will result in a severe thunderstorm outbreak remains one of the most daunting challenges to operational meteorology, despite nearly 50 years of continuous research. The primary focus of this research is on the generation of a representative synoptic climatology of the lid and its various component structures, and the relationship of this climatology to the occurrence or nonoccurrence of severe local storms. In this introduction, the historical foundation for the existing literature on severe-storms climatology is presented, along with a brief review of those studies addressing the creation and evolution of the important components of the lid sounding. Following these sections, an outline of the objectives of this research are presented.

### 1.1 Literature Review of Severe-Storms Climatology

The development of severe-storm analysis and prediction techniques has an historical background that is largely rooted in climatological studies. Before the mid 1920s, most of the literature on severe storms consisted primarily of storm-damage documentation, although two notable exceptions were the studies of Ferrel (1885) and Finley (1890), who described some common atmospheric features found in severe-storm situations. A review paper by Galway (1977) describes the history of storm-event documentation, including a good summary of the problems involved with the early periods of record keeping. As methods of probing the atmosphere were developed (e.g., kites and balloons with instrumentation), attempts were made by Varney (1926), Humphreys (1926), and others to describe the thermodynamic and wind environments of the tornadic thunderstorm. The advent of routine radiosonde ascents and the adoption of the airmass/frontal theories of the Bergen School influenced subsequent research. The works of Lloyd (1942) and Showalter and Fulks (1943) are illustrative of this period of "new" technology and theory. As the upper-air networks improved and the database grew, a natural extension of the earlier investigations was the generation of severe-storm climatologies. These climatological studies used the available surface and upper-air data archive to obtain a set of common atmospheric features associated with severe-storm events. Hereafter, these are referred to as *event-based climatology* studies.

A survey of the numerous event-based climatologies produced over the U.S. since 1950 is summarized in Table 1.1. The analysis techniques used in these studies generally fall into three main categories: 1)

statistical analysis of the characteristics of the tornado-damage and storm-damage events; 2) creation and evaluation of mean proximity soundings taken from the near-storm/tornado environments; and 3) categorization of synoptic patterns associated with the severe-storm and tornadic environments. These studies give us much insight into the synoptic characteristics of both the pre-storm as well as the near-storm environments. However, some problems exist with these studies, which are related to the fact that they use storm events as the basis for generating the climatology. These problems include incomplete documentation of every severe-storm event, artificial constraints put on the event data in order to generate specialized climatologies (e.g., for "large" or "progressive" outbreaks), and the exclusion of the meteorological conditions associated with non-severe-storm event days. A more complete discussion of the limitations of event-based studies, and a description of other types of climatological studies (such as satellite-derived composites) appear in Section 4.1.

### 1.2 The Creation and Evolution of the Components of the Lid Sounding

One of the first outcomes of the event-based studies documented in Table 1.1 was the generation of a mean proximity sounding for the tornadic environment. Fawbush and Miller (1952, 1954) are generally credited with the first composite sounding of the tornadic environment, although their result is similar to that of an earlier investigation by Showalter and Fulks (1943). The tornado proximity sounding, also known as a Type 1 or "loaded gun sounding," is characterized by a moist layer near the surface with high values of  $\theta_w$ , above which a relative-humidity

Table 1.1 Event-Based Severe-Storm Climatologies

<u>Study (year)</u>	<u>Area of Interest</u>	<u>Analysis Technique</u>
Fawbush et al. (1951)	Continental U.S.	Statistical (tornado events are categorized by location, month, mean terrain elevation, etc. A set of subjectively determined synoptic conditions are presented based on multi-year database of tornadic events).
Fawbush and Miller (1952)	Continental U.S.	Proximity soundings (mean sounding generated from multi-year sample of tornado situations)
Fawbush and Miller (1954)	Continental U.S.	Proximity soundings (same technique as above)
Beebe (1956)	East of Rockies	Mean meteorological charts (based on multi-year sample of tornado situations)
Fawbush et al. (1957)	Continental U.S.	Categorization of 500-mb flow patterns associated with severe local storms over a 10-year period
Beebe (1958)	Central U.S.	Proximity and precedence soundings (the latter are characteristic of tornadic storm airmass but removed in time and space from vicinity of tornado occurrence)
Miller (1959)	East of Rockies	Composite meteorological charts (analogs based on multi-year sample of tornado situations)
Darkow (1969)	Central Plains, Northern Plains, Gulf Coast	Proximity and check soundings (latter are taken at tornado event time at closest upper-air station in an upstream direction with respect to mean low-level flow). All rain-affected soundings are removed from data sample.



Table 1.1 (continued)

<u>Study (year)</u>	<u>Area of Interest</u>	<u>Analysis Technique</u>
Willis (1969)	East of Rockies	Tornado proximity soundings; examined them by region and two special categories (tropical storm and warm airmass). Vertical shear and parcel buoyancy statistics were used to develop Tornado Likelihood Index.
Darkow and Fowler (1971)	Central Plains, Northern Plains, Gulf Coast	Proximity, upstream check, and right check soundings. Right check soundings were taken at event time at the closest upper air station normal and to the right of the low-level flow.
Notis and Stanford (1973)	Iowa	Statistical (categorized tornadoes by direction of movement; computed means, standard deviations, correlations with meteorological variables)
Maddox (1976)	East of Rockies	Proximity soundings (includes separate tornado and severe thunderstorm categories; also computes stability index, mean sounding winds)
Williams (1976)	From Rockies eastward	Statistical (mean regional surface conditions based on multi-year sample of tornado situations)
David (1976)	Continental U.S.	Mean meteorological conditions based on multi-station objective analysis of rawinsonde data near location of tornado; multi-year database
Galway (1977)	East Rockies	Statistical (restricted to outbreaks of 10 or more tornadoes; categorized tornadoes by month, region, total deaths, etc.)

Table 1.1 (continued)

<u>Study (year)</u>	<u>Area of Interest</u>	<u>Analysis Technique</u>
Kelly et al. (1978)	From Rockies eastward	Statistical (categorized tornadoes by "normalized solar time", pairs of months, geographic location, path length, region, total deaths, etc.)
Moller (1979)	Kansas, Oklahoma, Texas	Statistical (tornado outbreak types based on shape criteria are categorized by month, time of day, location) and analog (typical synoptic patterns are presented for different outbreak types)
Schaefer (1983)	Continental U.S.	Synoptic pattern typing for different types of tornadic outbreaks using empirical orthogonal function (EOF) expansion; multi-year database
Schaefer and Doswell (1984)	West of Appalachians	Synoptic pattern typing for "progressive" tornado outbreaks using EOF analysis; multi-year database
Kelly et al. (1985)	Continental U.S.	Statistical (restricted to non-tornadic severe thunderstorm events; categorized by month, geographic location, type of severe weather (hail versus wind gusts, region, etc.))
Livingston and Wilson (1986)	Non-geographic; analysis area is centered on location of event	Mean surface meteorological conditions based on objective analysis of observations 0-6 h prior to touchdown of violent (F4, F5) tornado; multi-event database
Schaefer and Livingston (1988)	West of Appalachians	Proximity soundings for tornado events are categorized statistically using EOF

Table 1.1 (continued)

<u>Study year)</u>	<u>Area of Interest</u>	<u>Analysis Technique</u>
Johns and Sammler (1989)	Continental U.S.	Statistical and proximity soundings (compiled "violent tornado outbreaks" statistics, and computed "seasonal" 850, 700, and 500-mb temperature change statistics to determine mean destabilization, and 850-mb dew point change and 700-mb wind maxima information to characterize moisture changes and wind characteristics of violent outbreaks)
Davies (1989)	East of Rockies	Proximity soundings used to determine wind hodograph characteristics for 54 tornado cases of F2 or greater from 1980-1989. Divided statistics by season (cool/warm) and layers (0-1 km, 0-4 km). Examined "positive shear" characteristics for two cases.

Note: In addition to the above climatological studies, the following seasonal studies were also conducted:

- 1) McNulty (1978) related upper-tropospheric wind maxima and the associated divergence fields to severe-weather occurrence. He used a combination of representative cases and statistical analysis of tornado situations using one month and one season of data.
- 2) Graziano and Carlson (1987) produced a statistical analysis of lid strength and buoyancy versus deep convection and severe weather (defined using a combination of intense radar echoes and severe-storm reports). Their database covered a six-month period (March through August) over the U.S. east of the Rockies and west of the Appalachians. They categorized the radar data by intensity and echo top, and correlated these observations with the lid strength and buoyancy using a proximity sounding technique. The data were further categorized by month and region (simultaneously), and then related to actual severe-storm events to generate probabilities of severe weather based on the values of the lid strength and buoyancy terms.

Table 1.1 (continued)

- 3) Sanders (1988) produced a seasonal composite of intense convective systems using manually digitized radar summaries for the period January to May 1987. His analysis categorized the occurrence frequency of intense (VIP-5) echoes by date (in a time series), time of day, and geographic location of system starts (subdivided by time of day). A sample day was also discussed.

break and thermal inversion layer appears. Above the inversion layer (around 800 mb), there is layer resembling a well-mixed boundary layer, which has a nearly dry-adiabatic lapse rate and nearly constant or increasing mixing ratio. This layer extends to near or above 500 mb. For many years, it was thought that the origin of the inversion layer in the Type 1 sounding was due to large scale subsidence. However, this process would be incapable of producing the low static stability observed in the layer above the inversion, and the synoptic scale environment in which the tornado sounding exists could not support large scale subsidence (the opposite situation was often observed). Carlson and Ludlam (1968) first proposed that the tornado sounding, which they referred to as a lid (after Means 1952), was produced as a result of the superposition of two vastly different airstreams. The moist layer was a result of low level flow from the Gulf of Mexico, while the well-mixed layer above originated over the arid, elevated regions of northern Mexico and the U.S. desert southwest. The latter was, in fact, a boundary layer which was transported northward where it overran the moist layer from the Gulf. The capping inversion was essentially the boundary between these two different airstreams.

Subsequent studies during the last 23 years have validated and confirmed the Carlson-Ludlam model of lid formation. Several of these studies have attempted to examine individually the two components of the lid sounding, namely, the low level moist layer and the elevated mixed layer, or EML. An observational study by Doswell et al. (1985) utilized analyses of 700-500 mb lapse rate over a 36-h period to track the EML from source regions over the Rockies and northern Mexico into the

southern and central Great Plains. Their work suggests that a combination of surface heating over the source region along with rising motion in the synoptic scale environment produces the high lapse rates associated with the EML.

A two-dimensional modeling study by Benjamin (1986) examined the creation of the EML over an idealized plateau resembling northern Mexico, and its subsequent downwind transport over regions of lower terrain. His work shows that the development of the EML over the plateau is largely the result of intense surface heating over the arid elevated source region, and that the EML begins to form a capping inversion over the potentially cooler air downstream between 12 and 18 h after its movement off the plateau. Additionally, the differential surface heating between the arid plateau and relatively moister lowlands enhances the development of the lee-side trough, which in turn increases the low level inflow towards the region of potential convection, reaching a maximum intensity in the late afternoon and early evening. A similar two-dimensional modeling study was conducted by Arritt and Young (1990), using an idealized mountain range resembling the Rockies, to examine EML formation and subsequent downwind transport over the western high Plains. Their results, in terms of the formation of the EML and downwind lid inversion, are remarkably similar to Benjamin's results, despite the fact that the spatial scale of their study is nearly an order of magnitude less than Benjamin's!

Unfortunately, there has not been as much study of the characteristics and evolution of the moist layer as there has been of the EML. Some early studies of return flow over the Gulf (Johnson 1976;

Henry and Thompson 1976; Karnavas 1978) attempted to combine surface trajectories and satellite-image continuity to document the characteristics of the modified airmass returning into southern Texas following a polar-air outbreak. The effect of the Loop Current in the eastern Gulf on surface level trajectories was explored in a climatological study by Molinari (1987). A recent field experiment over the Gulf of Mexico (GUFMEX; Lewis et al. 1989) collected data which will be used to investigate the characteristics of the low level air from the time the continental polar airmass first moves into the Gulf until the time that it returns northward into Texas as a moist layer.

The studies mentioned above raise some interesting questions regarding the creation and subsequent evolution of the moist layer and the EML, and the formation of the lid sounding. The first question involves the time and space scales for the creation of the EML and moist layer, and whether or not they are similar. A related question concerns the variability in EML and moist layer creation and evolution as a result of different sequences of synoptic flow patterns. A third question involves the various physical processes at work in the creation and evolution of the EML and moist layer. This last question is particularly intriguing because the processes that affect the dry static stability (through the EML) can feed back into the large scale vertical motion field (subsequently affecting the synoptic scale system), as well as influence the likelihood of localized deep convection in the vicinity of upper level jet streaks, for example. The processes that affect the creation and evolution of the moist layer can also have important

influences on the large scale and local environments through feedbacks resulting from latent heat release in cloud and precipitation areas.

### 1.3 Purpose of Thesis

This study will provide an improved understanding of the climatology of severe local storms over the southern Great Plains during the convectively active months of April, May, and June. In order to address the concerns raised in Section 1.1 about the representativeness of event-based studies, the climatology developed in this research will be based on the EML, moist layer, and the lid. By employing an approach that concentrates on physical features known to exist in the severe-storm environment, the occurrence of severe weather is addressed within the context of these three features (EML, moist layer, and lid) in contrast to the opposite approach. The resulting climatology includes days with a variety of severe weather events, from the largest outbreaks to the isolated events, and even the days with no severe weather, hereafter referred to as "non-event" days.

The questions raised in Section 1.2 about the creation and evolution of the EML, moist layer, and lid are addressed in the following ways by this study. In Chapter 2, monthly analyses of various parameters associated with the EML, moist layer, and lid are produced to examine the seasonal evolution. The applicability of the lid climatology in different parts of the spring season is examined through the construction of a subjective synoptic typing scheme that is based on the thermal wind. The synoptic flow types are then analyzed with regard to their seasonal frequency and their association with the



occurrence/nonoccurrence of the lid. In Chapter 3, a conceptual model of the life cycle of lid development and dissipation is presented, and its seasonal sensitivity is examined. This portion of the study addresses the characteristic time and space scales for the creation and evolution of the EML, moist layer, and lid through a synoptic climatological approach. The synoptic types defined in Chapter 2 are used in this portion of the study to explore the variability in EML, moist layer, and lid evolution resulting from different sequences of synoptic flow types. The seasonal aspects of this variability are also addressed here. The compilation of severe-weather statistics for the period of study and their relationship to various synoptic patterns occurring during the life cycle of the lid is addressed in Chapter 4. Chapter 5 illustrates how the lid climatology can be applied to a real-data case by examining a five-day lid cycle that occurred in April 1984. The physical processes involved in EML and moist layer creation and evolution during this lid cycle are investigated in Chapter 6 through analysis of the results of a five-day simulation using the Penn State/NCAR mesoscale prediction model, hereafter referred to as MM4 (Anthes and Warner 1978; Anthes et al. 1987).

## Chapter 2

### THE SYNOPTIC CLIMATOLOGY: STRUCTURE, DYNAMICS, AND SEASONAL EVOLUTION

#### 2.1 Chapter Introduction

It has been generally accepted by the meteorological community that the elevated mixed layer inversion, or lid, is a crucial feature of the springtime severe storm environment of the southern and central Great Plains of the United States. The typical lid sounding, also known as a Type 1 tornado sounding (Fawbush and Miller 1954), is characterized by a moist, potentially unstable layer about 100 mb thick, capped by a potentially warm, nearly dry-adiabatic elevated mixed layer (EML), which typically extends upward from the base of a strong inversion located near 800 mb. The presence of this EML results in a large region of buoyant instability aloft (Carlson and Ludlam 1968; Doswell et al. 1985). Also, the EML often overlies areas with marginally unstable or stable stratification, and presents forecasters with the difficult task of predicting whether the stratification below the EML will destabilize during the forecast period.

In the classic model of lid formation, an approaching upper level trough in the westerlies induces a southwesterly flow over a hot, arid, elevated source region such as northern Mexico, and transports a deep, neutrally stratified mixed layer northeastward, where it overruns a cooler, moister airstream whose source is over the Gulf of Mexico. A third airstream descends around the rear of the upper trough and forms a confluence zone at midlevels (near 700 mb) with the western edge of the dry Mexican airstream. This area of confluence creates a baroclinic

zone along the edge of the lid. The baroclinic zone and its importance in focusing convection along the lid edge have been described in analyses of lid cases (e.g. Carlson et al. 1980, 1983; Farrell and Carlson 1989), as well as in modeling studies (Keyser and Carlson 1984; Benjamin and Carlson 1986; Lakhtakia and Warner 1987; Lanicci et al. 1987).

According to the classic model, the lid is formed in an area of large scale vertical ascent ahead of the upper level trough, and thus the lid base rises to the north and east with increasing distance from the EML source region. The western edge of the lid often is coincident with the position of the dryline, a related feature which frequently appears in the severe storm environment over this region. It has been demonstrated that deep, moist convection and severe weather associated with the lid environment occur through one or both of the following mechanisms: 1) low level ageostrophic flow from beneath the lid edge develops in response to an isallobaric minimum (known as underrunning); and 2) lid removal occurs through concentrated, strong upward motion caused by the vertical circulations from a dynamic feature such as an upper level jet streak. Carlson et al. (1983) state, "The most intense convection occurs in the region near the intersection of the axis of the moist tongue and the lid edge."

Although there have been studies of lid occurrences in other parts of the world (see Carlson et al. 1983 for a brief review), the great majority of case studies over the U.S. have been confined to severe storm outbreaks in April and May over the Great Plains. An exception is the Farrell and Carlson (1989) study of the 31 May 1985 tornado outbreak

in the Northeast. All of the aforementioned studies involved southwest flow aloft, and the EML source regions were Mexico and the southwestern U.S. deserts. A common theme in these studies is that the lid is created in a synoptic flow situation that is "anomalous" compared to the climatological mean of zonal flow. In these cases, there is a net northward transport of warm, moist air at low levels and warm, dry air at midlevels, in an environment of veering wind shear. It is implied that differential thermal advection is very important for creating the three dimensional lid stratification. Also, it has been shown that, as the spring season progresses, surface heating and evapotranspiration contribute more to the development of low level potential instability (Benjamin and Carlson 1986; Lanicci et al. 1987). Additionally, during the spring, the western plateau of the U.S. undergoes a transition from an elevated cold source to a heat source (Tang and Reiter 1984), and the advection of potentially warm, dry air aloft can occur with several mid-tropospheric wind directions. Thus, by late spring and early summer, the "anomalous" southerly/southwesterly flow regime is not the only flow type that can create the three dimensional stratification associated with the lid.

We hypothesize that the classic model of lid formation over the central U.S. is only applicable to a limited set of synoptic flow regimes (southwesterly) for the early spring season. Our objective is to learn whether there are other flow configurations that produce the EML and lid, and if the mechanism for the creation of this stratification undergoes significant changes during the spring. Thus,

we pose the following questions concerning EML and lid formation and structure in the springtime over the southern Great Plains:

- 1) *Over which areas does the lid appear most often? Does the location of this lid formation region change during the spring?*
- 2) *How do the structures of the EML and lid change during the spring?*
- 3) *Which synoptic regimes in addition to southwest flow aloft can create a lid?*

One aspect of the present study is the production of a synoptic climatology for the southern Great Plains (defined here as Kansas, Oklahoma, Texas, and the immediate surrounding area) for April, May, and June. The climatology makes use of conventional surface and standard-level data, as well as derived parameters that define the lid and EML structure based on the automated procedure described in Farrell and Carlson (1989) (hereafter referred to as FC89). Section 2.2 describes the analysis of the lid- and EML-occurrence statistics for each month, and relates them to the EML source-region climatology. Section 2.3 discusses the physically based synoptic-typing scheme, presents the predominant flow types for each month, and relates these physically based flow types to lid and EML occurrences, as well as mean monthly analyses of EML and lid parameters during the spring season. Two companion papers (Lanicci and Warner 1991b; Lanicci and Warner 1991c) take the lid/EML climatology presented in this study and relate it to a seasonally dependent conceptual model of lid formation, and to

severe weather occurrence statistics for the same period as the present study.

## 2.2 Lid Characteristics Over the Southern Plains: April-June 1983-1986

The study area for this climatology extends from 88 to 107°W longitude, and from 25 to 42°N latitude. There are 22 U.S. and two Mexican rawinsonde stations in this area (Fig. 2.1). Lid statistics were generated for the U.S. stations using an automated procedure developed at Penn State (Carlson et al. 1980, 1983; Graziano and Carlson 1987; FC89). The climatological data base for this study (1983-1986) is the same as that of FC89 (i.e., the Penn State Meteorology department's tape archive). From examination of some 16,000 soundings, statistics concerning lid frequency, geographic distribution of the lid, and characteristics of the lid soundings were produced for the study region. We tabulated data availability statistics for each station during the period of record to determine if some stations had more missing observation times than others. The statistics include those days in which no data were available from the Penn State archive. A plot of the data availability for each station (not shown) reveals a normal distribution with only two stations (BVE, ELP) below 80% data availability. Due to ELP's low lid frequency (to be shown later), only BVE's data availability was of concern. After careful examination of the statistics for BVE, we concluded that the missing days were not biased towards any portion of the lid-size distribution to be discussed in section 2.2.2.

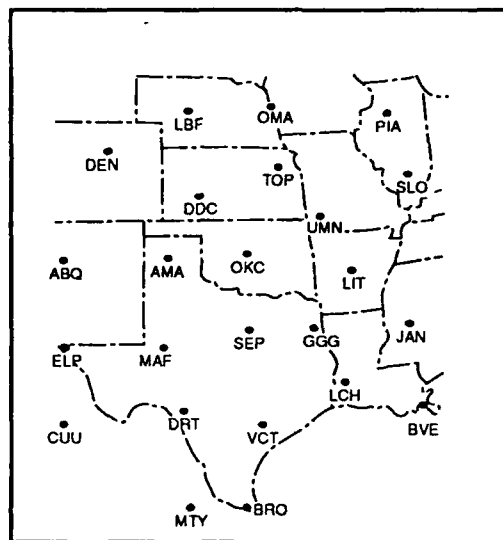


Figure 2.1. The study region, showing the locations and three-letter identifiers of the rawinsonde stations which are frequently referred to in the text.

### 2.2.1 The Sounding Analysis Procedure

The algorithm used in this study is discussed in detail by Farrell (1988) and FC89. Their program examines the temperature and relative humidity profiles of each sounding to determine the presence of a lid based on the following criteria:

- 1) A relative humidity discontinuity must exist below 500 mb, with a critical gradient of at least 0.87% per mb. Surface-based inversions are identified and do not count as relative humidity breaks in this procedure.
- 2) A layer in which the lapse rate of the saturation wet-bulb potential temperature,  $\theta_{sw}$ , is greater than or equal to zero must exist within 100 mb of the relative humidity break defined in (1). The  $\theta_{sw}$  value at the "nose" of the inversion is defined as  $\theta_{swmax}$ .
- 3) The static stability,  $\sigma$  defined as  $\sigma = -T\theta^{-1} (\partial\theta/\partial p)$ , in the layer above the inversion must be less than 4.5°C per 100 mb.
- 4) The relative humidity in the layer above the inversion must show an increase with height.
- 5) The lid strength, LS, defined as  $LS = \theta_{swmax} - \theta_{wb}$ , is equal to or greater than 1.0°C, where  $\theta_{wb}$  is the "best" (most unstable) wet-bulb potential temperature found in a 50-mb thick layer below the relative humidity break.
- 6) The buoyancy term, BUO, defined as  $BUO = \theta_{sw500} - \theta_{wb}$ , is less than 0.5°C, where  $\theta_{sw500}$  is the saturation wet-bulb potential temperature at 500 mb. This definition of the buoyancy results in values that are approximately one-half the



magnitude of the lifted index (Galway 1956) that is currently in use by the National Weather Service. The  $0.5^{\circ}\text{C}$  threshold accounts for marginal stability situations.

In our study, the existence of an EML is determined on the basis of criteria 1 - 3 only. The critical value of the static stability used in criterion 3 was determined by Farrell (1988) to be an optimum value based on previous studies involving soundings with EMLs, such as those of Fawbush and Miller (1954) and Karyampudi (1986), and on sensitivity tests with the present dataset. However, in order to determine what fraction of the sample has static stabilities that may be associated with subsidence layers, we analyzed a sample of 313 soundings diagnosed as containing an EML using criteria 1 - 3, from the months of April, May, and June during the study period. Figure 2.2 shows a cumulative frequency diagram that describes the distribution of  $\sigma$  for the sample. Figure 2.2 shows that the vast majority (about 85%) of EML soundings have  $\sigma$  values below  $3.5^{\circ}\text{C } 100 \text{ mb}^{-1}$ , which is close to the mean static stability ( $3.6^{\circ}\text{C } 100 \text{ mb}^{-1}$ ) of the type 1 tornado sounding (as computed from the layer above the inversion in Fig. 1 of Fawbush and Miller 1954). Less than 10% of the sample soundings have  $\sigma$  values in the range  $4.0 - 4.5^{\circ}\text{C } 100 \text{ mb}^{-1}$ , which may arguably be associated with subsidence layers.

The results of Fig. 2.2 also show that a substantial number of EML soundings are excluded from the database if the RH criterion is retained. We screened the sample on the basis of whether the RH criterion (4) was met. Interestingly, Fig. 2.2 shows that a substantial number (118) of EML soundings do not meet the RH criterion employed by

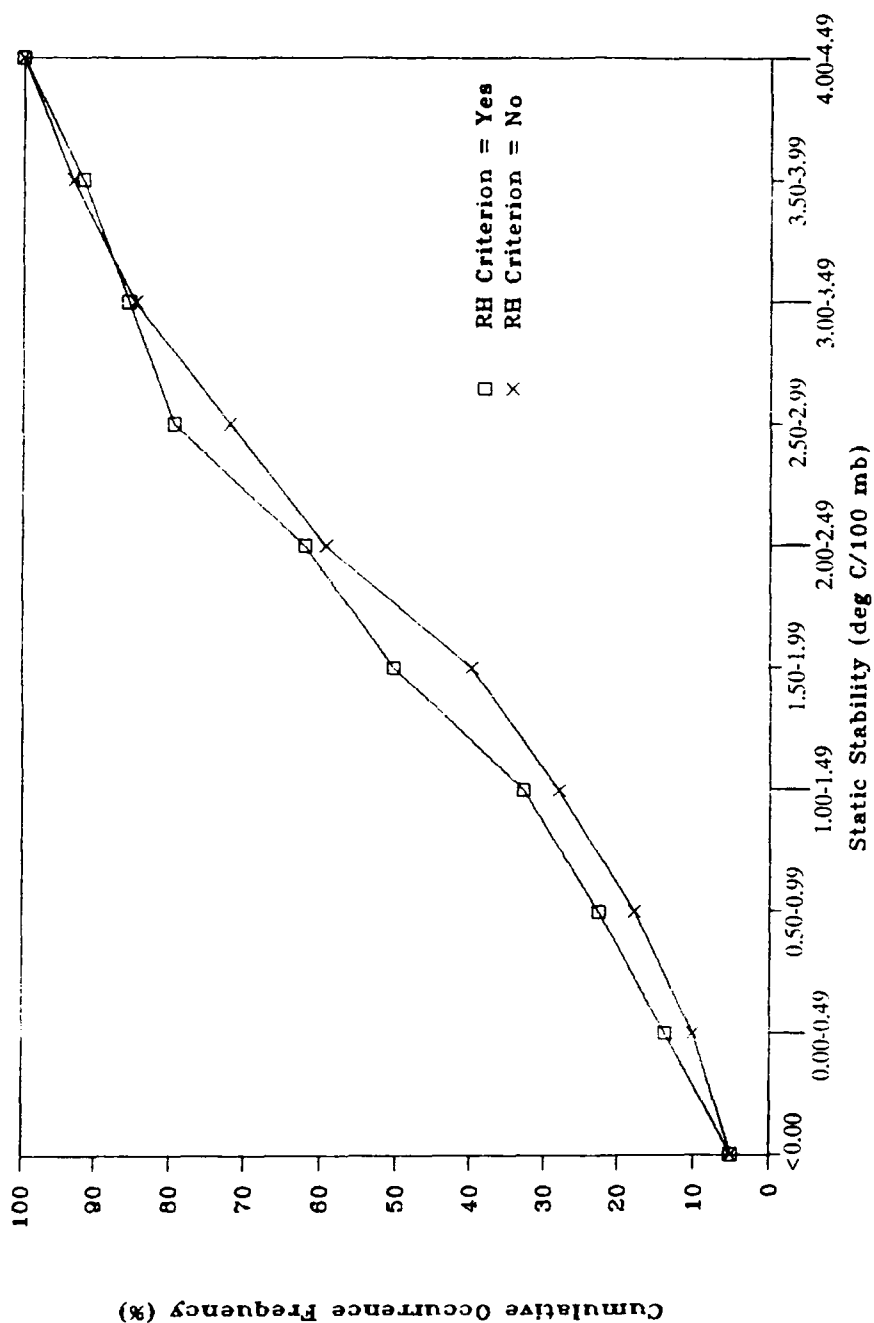


Figure 2.2. Cumulative occurrence frequencies (in %) of a seasonal sample of EML soundings observed over the study region during the study period. The sample consists of 195 soundings whose EML obeyed the RH criterion, and 118 soundings that did not. The cumulative occurrence frequencies are computed based on the separate sample sizes, and are categorized by static stability intervals, as shown on the abscissa.

FC89, and a considerable fraction (100) of these soundings have  $\sigma$  values below  $3.5^{\circ}\text{C } 100 \text{ mb}^{-1}$ . In addition to the evidence shown by Fig. 2.2, Farrell (1988) also points out that the RH criterion has other problems, most notably with the radiosonde humidity sensor's failure to recover from dewpoint depressions greater than  $30^{\circ}\text{C}$ , and with the current convention of reporting dewpoint depressions greater than  $30^{\circ}\text{C}$  as being equal to  $30^{\circ}\text{C}$ . Additionally, studies of the mixed layer (e.g., Mahrt 1976) have shown that, while the typical well-mixed PBL has a nearly dry-adiabatic lapse rate in temperature, the lapse rate of mixing ratio often is not well-mixed, for reasons such as differential moisture advection and growth of the PBL into an extremely dry layer. The fact that Mahrt's study was conducted over the western Great Plains makes his results particularly relevant to the present study. Based on these findings, it was decided to exclude RH criterion (4) from the EML screening procedure.

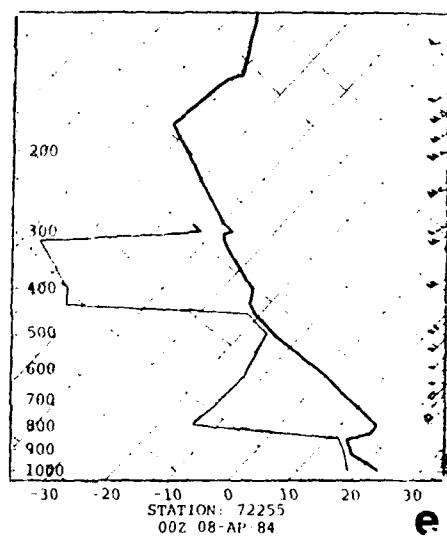
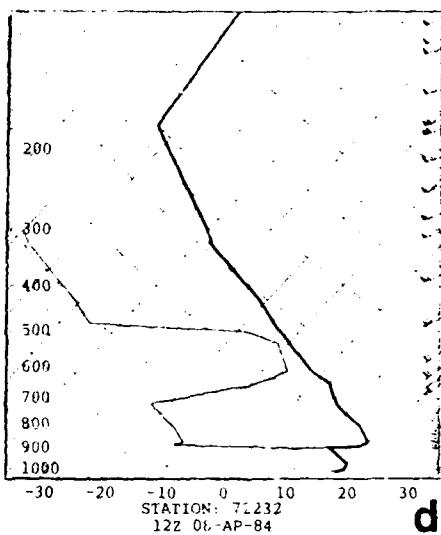
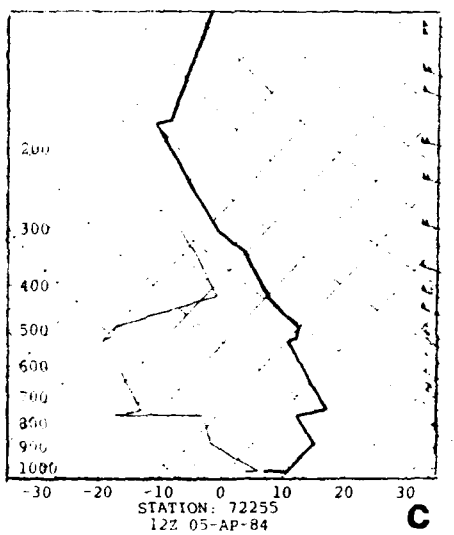
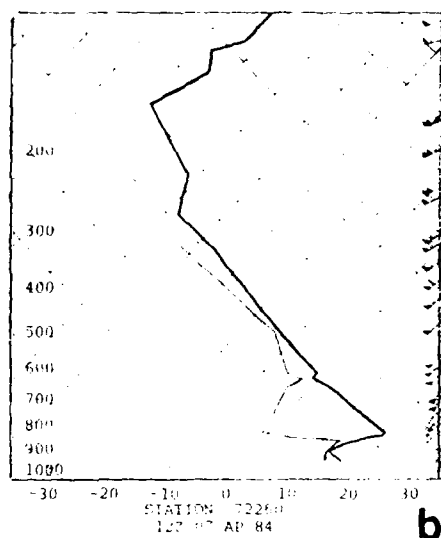
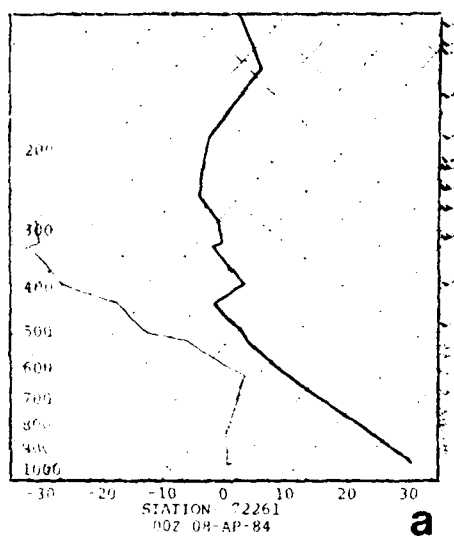
Regarding criterion (5), we distinguish between soundings with positive and non-positive lid strengths by defining a "capped" sounding as one with  $LS > 0.0^{\circ}\text{C}$ . This modification of FC89's criterion allows us to distinguish between the characteristics of both capped as well as "uncapped" ( $LS \leq 0.0^{\circ}\text{C}$ ) soundings. We further screen the capped soundings manually to determine if the EML base coincides with the warmest point on the sounding. Requiring that the EML base coincide with the level of  $\theta_{swmax}$  screens out soundings whose EML lies below the level of  $\theta_{swmax}$ . In our study, we define a "lid" sounding as one containing an EML (criteria 1-3) which effectively caps a PBL (modified criterion 5) that is buoyantly unstable (i.e.,  $BUO < 0.5^{\circ}\text{C}$ ) with respect

to the 500-mb level (criterion 6). A capped "EML" sounding (hereafter referred to as simply an EML sounding), by contrast, meets criteria (1) - (3), effectively caps the PBL (modified criterion 5), but is buoyantly stable ( $\text{BUO} \geq 0.5^{\circ}\text{C}$ ). Separate identification of both EML and lid soundings is important because the EML is a more ubiquitous and spatially and temporally continuous feature than the lid. This gives the forecaster a temporal continuity that is extremely important when distinguishing between favorable and marginal areas for deep convection.

Figure 2.3 presents examples of soundings classified according to the criteria presented in this section. The DRT sounding shown in Fig. 2.3a meets none of the criteria for an EML, and indeed looks more representative of a sounding from west of the surface dryline (Schaefer 1974). The SEP sounding in Fig. 2.3b is classified as an EML sounding due to its stable BUO value of  $0.6^{\circ}\text{C}$ . The VCT sounding in Fig. 2.3c contains a capping inversion and a relative humidity break at 768 mb. However, the layer above the inversion is marked by a lapse rate close to moist adiabatic, so it fails to meet criterion (3) and is classified as a subsidence-inversion sounding. The BVE sounding in Fig. 2.3d contains the inversion and EML (from 804 to 719 mb), and is buoyantly unstable, but the EML does not meet the RH criterion. This sounding is *still* classified as having a lid in our study. Finally, the VCT sounding in Fig. 2.3e meets all six criteria discussed in this section, and closely resembles the classic lid sounding presented in the severe storms literature. This sounding has a BUO of  $-2.8^{\circ}\text{C}$  and an LS of  $4.8^{\circ}\text{C}$ .



Figure 2.3. Skew-T Log P diagrams representing various types of soundings characterized by the automated sounding-analysis program. In each panel, the temperature sounding is indicated by the thick solid line and the dewpoint sounding is shown by the thin solid line. Winds are plotted along the right axis of each sounding using conventional notation (speed is in kt). Types of soundings shown are a) non-EML, b) EML, c) subsidence-type, d) lid with no relative humidity increase with height in the EML, and e) lid with relative humidity increasing with height in the EML.



### 2.2.2 Monthly Lid Frequency

A lid-frequency histogram for each month of the study period is shown in Fig. 2.4. We use the term "lid station" to denote a rawinsonde station that has a lid sounding at either the 0000 UTC or 1200 UTC observation time. Note from Fig. 2.4 that the largest number of lid stations observed over the 22 station region is 13; this occurred only eight times during the four three-month periods. If we assume that each station represents a similar surface area, 13 stations represent about a 60% areal coverage. Therefore, the majority of the time that a lid is observed over the region, it covers less than half the area. The histograms also show that the mean number of lid stations for each of the months is relatively uniform and is between 4.3 and 4.6 (about 20% areal coverage) if we neglect the no-lid days, so the typical lid covers an area nearly  $8 \times 10^5 \text{ km}^2$ , or about 4.3 times the area of the state of Oklahoma. If we use the definition of Orlanski (1975), this length scale (close to 900 km, assuming a square coverage area) falls into the meso-alpha range. Another observation from the lid histograms concerns the shape of the lid frequency distribution and how it changes each month. The April distribution has a bimodal character, with maxima at zero and five lid stations. However, the May and June histograms show that this bimodal distribution gradually disappears through the spring season, with the distribution becoming rather flat by June. This seasonal change is perhaps best illustrated by noting the increase in the three-station category from 13 occurrences in April to 30 in June, and the decrease in the no-lid category from 63 occurrences in April to 12 in June.



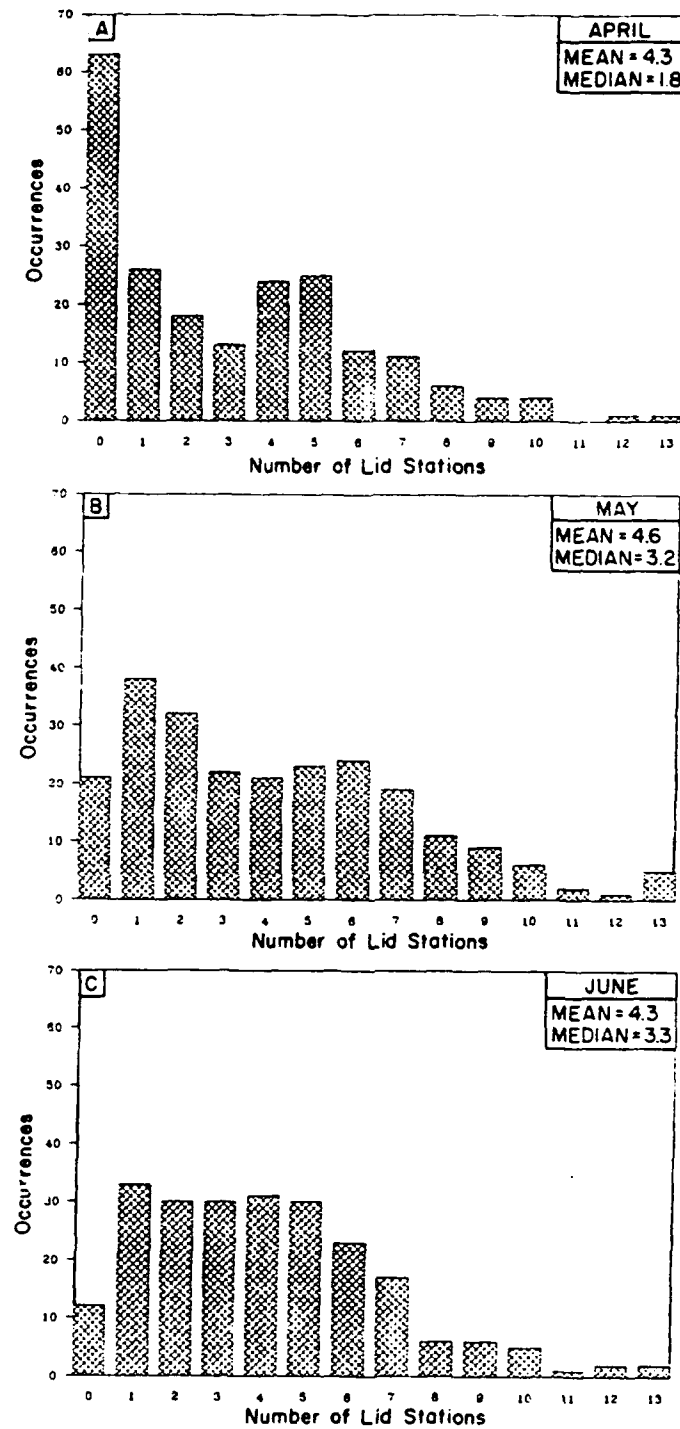


Figure 2.4. Histograms showing the total number of lid stations observed over the region at both 0000 and 1200 UTC, and their occurrence frequencies for a) April, b) May, and c) June. The mean number of lid stations (excluding the no-lid days) for each month is shown in the upper right, along with the median number of lid stations (including all days).

### 2.2.3 Monthly Geographic Distribution of Lid Frequency

The geographic distribution of the lid during the spring is illustrated in the series of charts shown in Fig. 2.5. The seasonal progression of lid frequency shown here is expressed in terms of the number of "lid days," where a lid day is defined as the total number of 1200 and 0000 UTC lid soundings at a station for a particular month during the four year period of record, divided by the total number of scheduled data times multiplied by the number of days in the particular month. The primary reason for the quantitative discrepancies between these lid frequency charts and those of FC89 (their Fig. 17) is due to the fact that FC89 employed the RH criterion in the EML definition, as discussed in the previous section. However, comparison of our geographic lid frequency charts with those of FC89 shows that they are qualitatively similar. Figure 2.5 shows a maximum in lid frequency over southern Texas in both April and May, which shifts northwestward in June towards DRT (see Fig. 2.1 for location). A second, smaller frequency maximum appears over LBF in June. The well defined lid-frequency maxima over DRT and LBF in June do not appear in FC89's charts. There were diurnal differences observed in the number of lid soundings over the study area. We highlight the stations (asterisks) in which the 1200 UTC frequency is equal to or greater than twice the 0000 UTC frequency, and note that the largest of these differences appear over west Texas in April and May. This result suggests that the diurnal movement of the dryline (Schaefer 1974) has an influence on the lid; i.e., the daytime eastward dryline movement erodes the lid over this area (leading to a 0000 UTC minimum), while the westward retreat at night reestablishes the

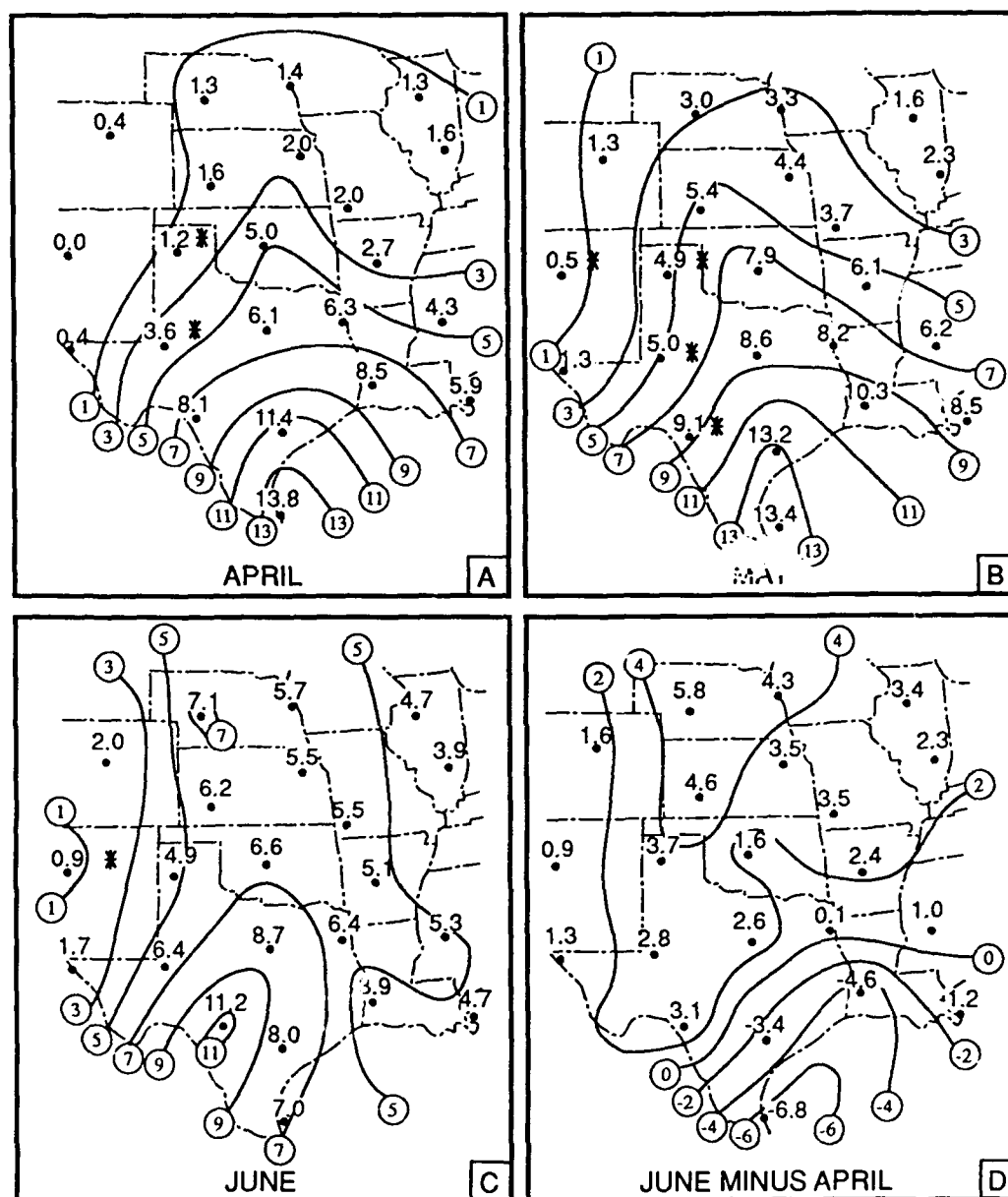


Figure 2.5. Mean number of lid days over the region (see text for the definition of a "lid day"). An asterisk (\*) next to the station means that the 1200 UTC lid frequency is greater than or equal to twice the 0000 UTC frequency. Charts are shown for a) April, b) May, and c) June. The change in lid days from April to June is shown by the difference field in (d).

low level moist layer (leading to a 1200 UTC lid maximum). The seasonal trend in lid frequency is shown by the June-April difference field of Fig. 2.5d, in which the westward and northward frequency progression is well illustrated. Most of the change in geographic lid frequency occurs between May and June over much of the study area. This shift in lid frequency is caused by a combination of several different processes that evolve during the spring season. In this study we will explore this evolution in detail.

#### 2.2.4 Elevated Mixed Layer Source-Region Climatology

The formation of the EML and lid in spring is largely controlled by topographic influences. Previous studies (Carlson and Ludlam 1968; Tang and Reiter 1984) have shown that the spring season is a transitional one over the North American plateau, with the EML source region beginning in northern Mexico in April and progressing northward with the season. In order to complement the analyses of these previous investigations, we use climatological values of mean maximum surface temperature to derive surface potential temperatures ( $\theta$ ) over northern Mexico and the western U.S., utilizing the terrain elevation and the U.S. Standard Atmosphere (1976) to derive surface pressure. Our analysis uses 161 Mexican climatological stations, most having longer than a 15-year record, and 239 U.S. stations above 1000 m elevation, each having a 30-year record. These surface  $\theta$  values are indicative of the mean  $\theta$  in the mixed layer over the source region. Our calculations complement those of Carlson and Ludlam by extending the analyses farther north and through the entire spring. Our approach differs from that of Tang and Reiter in

that we use more surface climatological stations, and calculate surface  $\theta$  instead of 850-mb geopotential heights and temperatures.

The results of the analyses for April through June are shown in Fig. 2.6. The warmer source regions in April (Fig. 2.6a) are the central and northwestern portions of the Mexican plateau, with  $\theta$  between 44 and 52°C. These results are in good agreement with Carlson and Ludlam's Fig. 2. In our analysis, however, surface values between 36 and 40°C extend as far north as southern Colorado (Carlson and Ludlam's figure ends in northern New Mexico), which implies that a westerly or southwesterly flow over this region could transport this mixed layer to the east, forming a "cool" lid over the Great Plains. From April to May, there is a large increase in the area of the source region, with surface  $\theta$  values of 36-40°C extending into Wyoming, Utah, Nevada, and eastern California (Fig. 2.6b). The 44-52°C values primarily exist in northern Mexico, but pockets of very warm air are also observed over portions of New Mexico and Colorado. The chart for June (Fig. 2.6c) shows the 36°C isentrope extending into southern Montana, Idaho, southeastern Oregon, and a large portion of California. The 44-52°C region has expanded into Colorado, southern Wyoming, Utah, Nevada, Arizona, New Mexico, and southwest Texas. The May to June transition in mean maximum surface  $\theta$  values over the Rockies and the Great Basin is greater than that for April to May. This is consistent with the lid-frequency charts in Fig. 2.5, which show the emergence of a secondary lid frequency maximum over western Nebraska in June. A rough comparison of our June surface  $\theta$  analysis with Tang and Reiter's July 850-mb chart (their Fig. 1) shows that the 850-mb warm air has the same broad west-

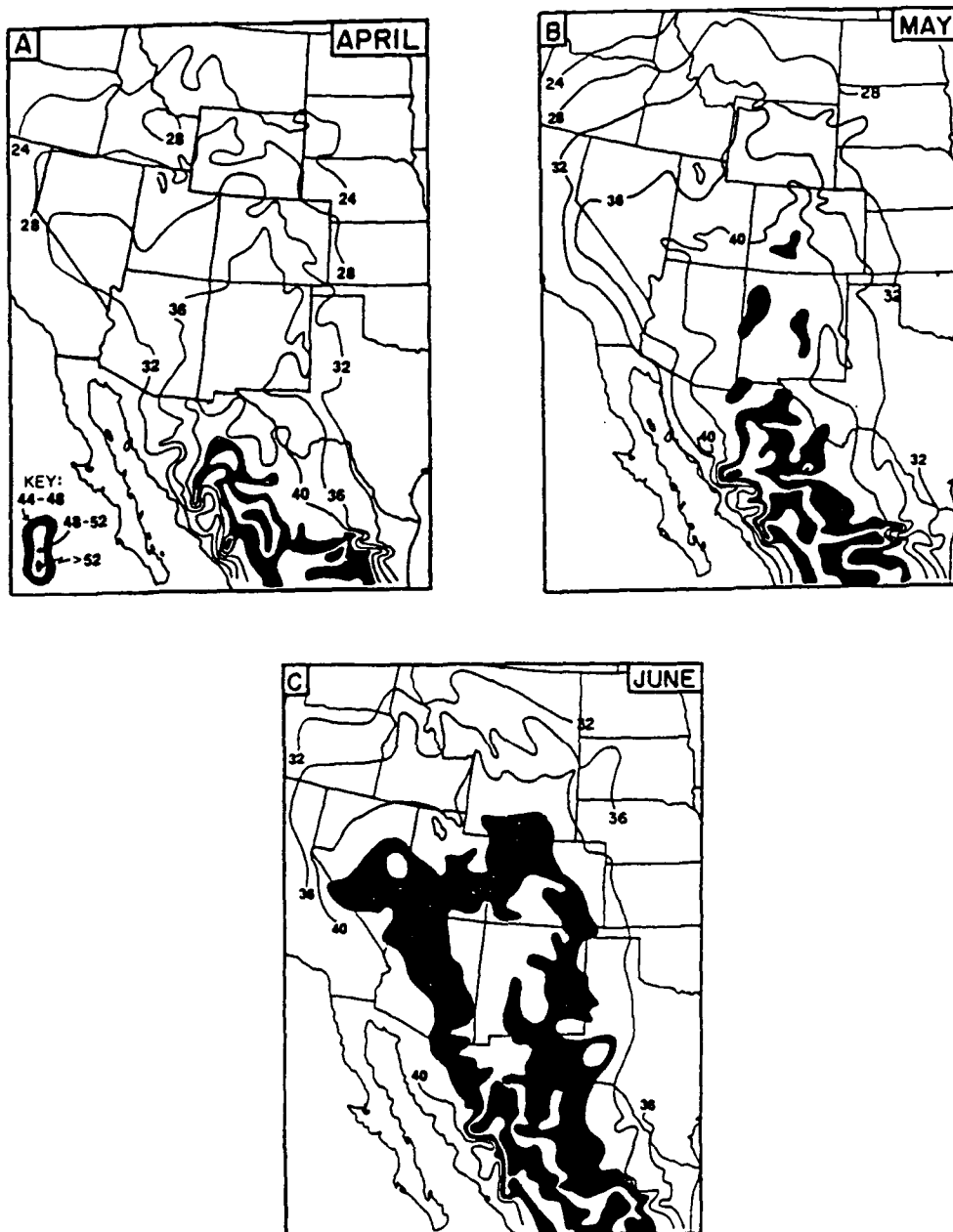


Figure 2.6. Climatological mean maximum surface potential temperature analysis (in °C) over northern Mexico and the western U.S. for a) April, b) May, and c) June. Values greater than or equal to 44°C are alternately highlighted in 4°C intervals as shown in the lower left corner of chart (a).

east expanse and large latitudinal extent as do our high  $\theta$  values. Their temperature maxima are equivalent to a  $\theta$  value of around  $41^{\circ}\text{C}$ , which is not unreasonable considering that they used monthly mean temperatures as opposed to mean maximum temperatures. Indeed, their analysis shows the persistence of the large EML source region into July.

Comparison of the lid frequency charts in Fig. 2.5 with the surface  $\theta$  analyses in Fig. 2.6 suggests that the westward and northward shift in lid frequency from April to June is partially tied to the northward expansion of the potentially warm EML source region into the Rocky Mountains and Great Basin during the spring. Figure 2.6 also reveals that the May to June change in surface  $\theta$  over northern Mexico is relatively small compared to the change in regions farther north, and is probably tied to the onset of the Mexican monsoon (see Fig. 14e in Tang and Reiter 1984, and Fig. 5.26 in Lanicci 1984).

### 2.3 Synoptic Typing of Surface and 500-mb Flows Over the Southern Plains

The motivation for producing synoptic flow types for the Great Plains during the springtime is to determine the relationships between the monthly changes in lid frequency and characteristics, and the occurrence of specific flow regimes. This allows us to go beyond the statistical analyses and determine what physical processes are associated with these patterns that make them favorable or unfavorable for lid formation.

### 2.3.1 Methodology and Physical Assumptions

There are a number of typing techniques available for producing synoptic climatologies. In most applications, the typing technique is a formal procedure for classifying the dominant flow patterns. Due to data storage limitations, the techniques are usually applied at only one level in the atmosphere at a time. Although Schaefer and Doswell (1984) used an empirical orthogonal function analysis to examine predominant flow patterns at both 850 and 500 mb for progressive tornado outbreaks, the data reductions were not done simultaneously.

In our study, we utilize a subjective typing technique that is based on the physical processes important in lid formation and evolution. In order to accomplish this effectively, the typing is performed at two levels simultaneously. We chose the surface and the 500-mb level because the surface flow pattern controls the low level moisture component of the lid sounding, while the 500-mb flow (near the top of the EML in the majority of soundings) is a good indicator of the advecting flow for the EML. Consideration of these two levels allows us to define flow types on the basis of mean thermal advection in the intervening layers through use of the thermal wind relationship. For example, in the classic lid model, the flow veers with height and there is warm-air advection in the lower half of the troposphere (see Fig. 1 in Carlson et al. 1983). The same thermal wind relation can be used to argue that a flow regime in which the winds are backing with height is unfavorable for lid formation because there is cold-air advection in the layer.



Given this physical basis (mean thermal advection in the lower troposphere) for the typing technique, the sea level pressure and 500-mb wind direction analyses at 1200 UTC for each day of the study period were examined. Based on these charts, five surface and five upper air categories are defined. A schematic diagram of each surface type is shown in Fig. 2.7. The surface types are:

- High pressure ridging in a north-south axis over the region (originating as a continental high from Canada) (Fig 2.7a);
- High pressure ridging in a northwest-southeast axis over the region (usually the extension of a maritime high centered over the Great Basin) (Fig. 2.7b);
- Weak return flow from the Gulf of Mexico (defined as a situation where either the high pressure ridge has remained anchored over the southeastern portion of the region--i.e., the Gulf is not completely "open", or the ridge has moved out of the region and weak southerly flow with geostrophic windspeeds less than  $10 \text{ m s}^{-1}$  have developed) (Figs. 2.7c,d);
- Strong return flow from the Gulf of Mexico (defined as a regime where the high pressure ridge has moved out of the region and strong southerly flow with geostrophic wind speeds on the order of  $10 \text{ m s}^{-1}$  or greater have developed) (Fig. 2.7e); and
- A frontal system traverses at least half the area by analysis time (Fig. 2.7f).

The need for the last type arises because the incursion of a frontal system across the entire region cuts off the source of the EML. The

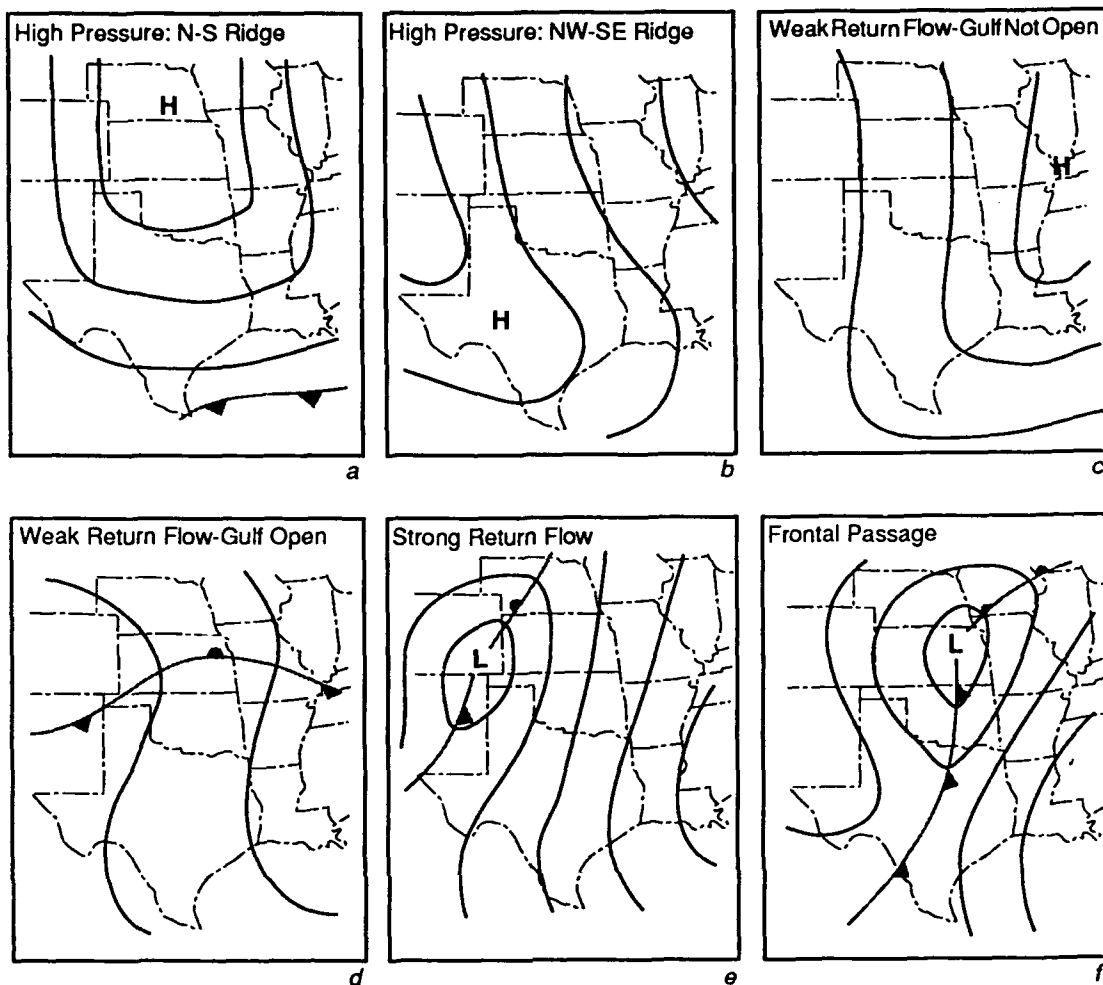


Figure 2.7. Idealized patterns of sea level isobars for surface synoptic flow types. Types shown are: a) high pressure with north-south oriented ridge axis, b) high pressure with northwest-southeast ridge axis, c) weak return flow with surface ridge over south-eastern portion of region (Gulf not "open"), d) weak return flow after high pressure exits the region (Gulf "open"), e) strong return flow, and f) frontal passage.

surface types have a natural temporal continuity, with the high pressure types usually followed by a strengthening flow, with a transition taking place as the surface front moves through the area. This temporal continuity was frequently observed in our data, but other transitions occurred as well. The timing of the moist "return" flow from the Gulf of Mexico, after the eastward retreat of the surface high, is very important in setting up the pre-convective environment. For example, the moist return flow was shown to be important in the initial formation of the surface dryline (Schaefer 1974). We also note that our surface high-pressure and weak return-flow synoptic types are nearly identical to the synoptic patterns presented by Lewis and Crisp (1989) and Weiss (1989), in their wintertime studies of return-flow situations in the southern Plains (compare the descriptions of our high pressure types with the discussion in sections 2.1 and 2.2 of Lewis and Crisp 1989; also compare our Figs. 2.7c,a,d with Figs. 2-4, respectively, in Weiss, 1989). Further discussion of the temporal continuity in synoptic types as related to lid formation appears in Part 2 of this study (Lanicci and Warner 1991b). The 500-mb flow types were based on the flow patterns which appeared over the study area during the study period, and are depicted in Fig. 2.8.

The flow categories are:

- Northwesterly (Fig. 2.8a);
- Westerly (Fig. 2.8b);
- Southwesterly (Fig. 2.8c);
- Anticyclonically curved (Fig. 2.8d); and
- Cyclonically curved (Fig. 2.8e).

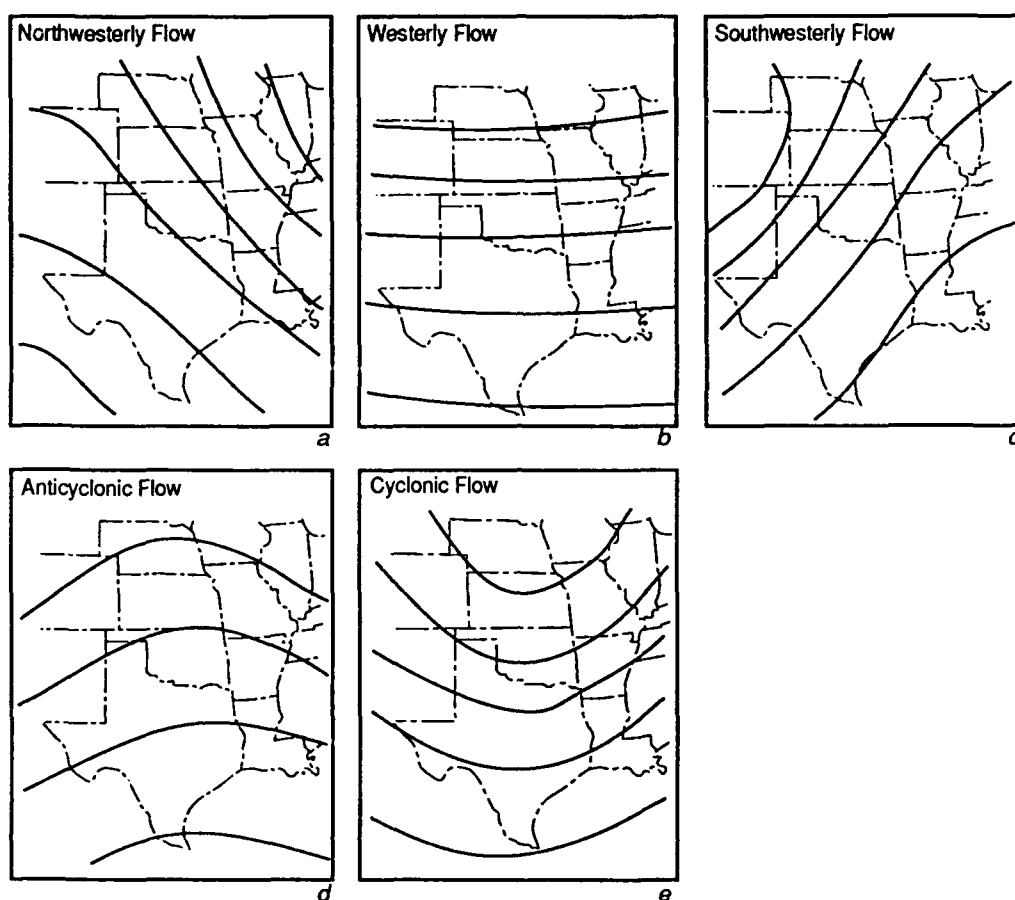


Figure 2.8. Idealized patterns of 500-mb geopotential heights for upper-air flow types. Shown here are: a) northwesterly flow, b) westerly flow, c) southwesterly flow, d) anticyclonic flow, and e) cyclonic flow.

There were several other 500-mb flow directions observed over the region, such as northerly, southerly, southeasterly, and easterly, but these directions were not observed in April, and only accounted for 2.4% of the May patterns and 7.5% of the June patterns.

Combining these surface and 500-mb flow patterns produces categories for which we can qualitatively infer the thermal advection in the intervening layer. For example, north-south surface ridging with northwesterly flow aloft (Figs. 2.7a, 2.8a) represents an unfavorable situation for EML and lid formation because the winds are backing with height everywhere except in the extreme western portion of the study area, and the surface high restricts the high  $\theta_w$  air to the Gulf of Mexico and extreme southern Texas. Conversely, a strong return flow from the Gulf with southwesterly flow aloft (Figs 2.7e, 2.8c) has winds veering with height, allowing the EML to enter the Plains from the Mexican plateau and overrun the moist, southerly low level flow. This is the flow configuration most closely associated with the classic lid model discussed earlier. Some flow configurations are unambiguously associated with either the unfavorable or favorable conditions for lid creation. However, we will see shortly that some flow types can actually be associated with both favorable and unfavorable lid-formation situations, depending upon the critical superposition of specific features at different levels.

### 2.3.2 Lid Frequencies Associated with the Various Flow Types

After determining the dominant synoptic flow type for each day of the study period, we compiled the monthly lid-occurrence frequencies of

each type. Figure 2.9 shows, for each flow type, the number of days on which different numbers of lid soundings were observed during the period. The dashed line for each month separates "large" (L) and "small" (S) lid-coverage areas, and is based on the median lid frequency for the month (see Fig. 2.4).

For April (Fig. 2.9a), the high pressure surface types are primarily unfavorable for lid formation, while the strong return-flow and frontal-passage surface types are primarily favorable for lid formation. In general, the midtropospheric southwest-flow types, collectively, have the highest mean number of lid stations, which confirms that the southwest flow regime has the greatest contribution to the April EML/lid occurrence frequency. Of the seven types with occurrences in both the L and S coverage ranges, three are associated with 500-mb troughs, while four are associated with weak return flow.

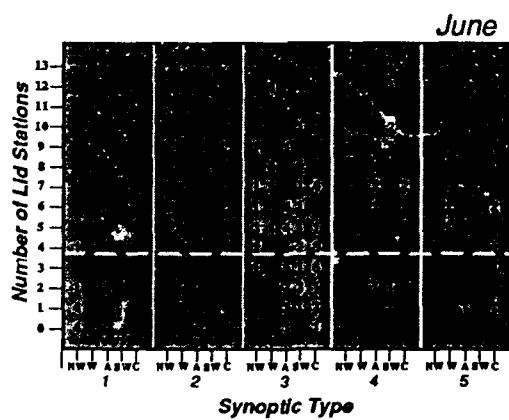
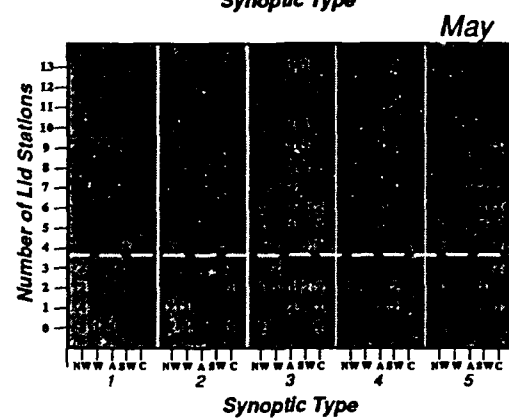
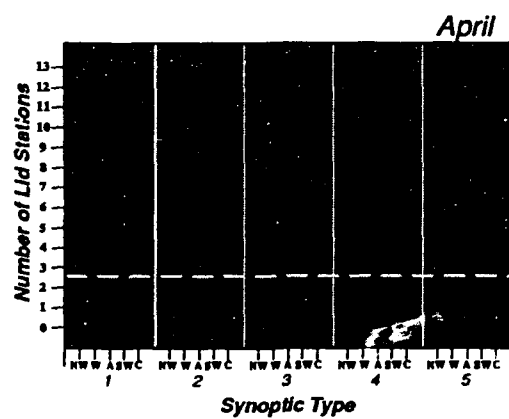
For May (Fig. 2.9b), there is a greater range in the number of lid stations for some flow types. For example, the flow type with the highest mean number of lid stations (strong return flow with southwest flow aloft) has four occurrences in the S range. The high pressure types still remain largely unfavorable for lid formation.

By June, the Great Plains abuts elevated heat sources to the south and to the west (Fig. 2.6c). At low levels, weak return flow has a combined occurrence frequency of 71.7%, and provides for a nearly continuous presence of high  $\theta_w$  air over most of the Plains region. Now, in June (Fig. 2.9c), there is only one high pressure type and it is associated primarily with small lid-area coverages. The northwest-southeast ridge surface type no longer appears in June. This



Figure 2.9. Lid frequency by synoptic type for a) April, b) May, and c) June. The ordinate denotes the number of lid stations, and the abscissa denotes the five surface synoptic types (each separated by the vertical line), subdivided by 500-mb type. The numbers along the abscissa refer to the following surface types: 1 = N-S pressure ridge, 2 = NW-SE pressure ridge, 3 = weak return flow, 4 = strong return flow, and 5 = frontal passage. The 500-mb flow types are abbreviated as follows: NW = northwest, W = west, A = anticyclonic, SW = southwest, and C = cyclonic. The number of occurrences of each synoptic type and corresponding number of lid stations are shown. The horizontal dashed line separates "small" and "large" lid-coverage areas.





disappearance is consistent with the transition of the Great Basin from an elevated cold source to a heat source. For example, the transient-surface-anticyclone frequencies for January and July presented by Bryson and Hare (1974) for North America (their Figs. 26 and 27) show that there is a January maximum over the Great Basin and a primary track towards the southern Plains, which disappears by July. The dominance of weak return flow in June is consistent with the westward expansion of the Bermuda anticyclone, which changes the mean low level flow direction from southwesterly in April to southerly by June, and strengthens the gradient-level flow over the western Plains (see Figs. 2d-f in Tang and Reiter 1984).

The 500-mb southwest flow, which accounts for 32.5 and 25.8% of all flows in April and May, respectively, only accounts for 17.5% in June. However, the strong return flow/southwest flow aloft pattern still has the highest mean number of lid stations (8.3), and this is higher than either the April or May values. Despite the decrease in occurrence frequency of this flow type, it remains the best producer of widespread lids. While 500-mb southwest flow has decreased in occurrence frequency during the season, anticyclonic flow has increased from 15.8% in April to 30.8% by June. This increase in 500-mb anticyclonic flow frequency during the spring is consistent with the 500-mb closed-anticyclone climatology of Parker et al. (1989) (see their Figs. 4d-f). Another interesting observation from Fig. 2.9 is the transition of the weak return flow/northwest flow aloft pattern from a largely unfavorable synoptic type in April to a more favorable one in June as a result of the northward movement of the EML source region.

Finally note that, in general during the spring season, surface types associated with strong return flow and frontal incursions are predominantly associated with favorable lid situations, while weak return flow has many occurrences in both ranges. It appears from Figs. 2.7c,d that weak return flow appears to be a transitory type. In early spring, this transition is between the high-pressure regime and the strong return-flow regime. In the weak return-flow type, the exact location of the surface pressure ridge, as depicted in the schematic charts of Figs. 2.7c,d, appears to play a crucial role in determining the evolution of the low level moist flow that defines the lower layer of the lid sounding. This phenomenon will be examined in more detail in Lanicci and Warner (1991b). In late spring, when there is abundant low level moisture and return flow dominates, the upper level flow direction becomes more important in determining whether a hot, dry EML source region is tapped, or whether the flow instead comes from a source of abundant midlevel moisture, such as the subtropics or an active monsoonal region.

### 2.3.3 Mean Monthly EML and Lid Characteristics as Related to Synoptic Flow Patterns

Various mean characteristics of the EML and lid over the study region were determined for each month. The following parameters were analyzed:

- 1) "best" wet-bulb potential temperature ( $\theta_{wb}$ ) in the boundary layer,
- 2) mean  $\theta$  in the EML, and
- 3) base of the EML.

The charts of mean EML characteristics were constructed using *both* EML and lid soundings for each rawinsonde station at 1200 UTC. Recall from section 2.2.1 that EML soundings contain the capping inversion with the EML above, and a PBL that is buoyantly stable, whereas the lid soundings have a PBL that is buoyantly unstable. In order to eliminate situations with only isolated EML/lid coverage, the data tabulation includes only those days for which a minimum of four lid stations (three in April) was observed over the region (above the dashed line in Fig. 2.9). Furthermore, only the most frequent lid-producing synoptic patterns were included in the compilation, accounting for roughly 80% of all the days with greater than the median number of lid stations during the study period.

The monthly mean analyses are shown in Fig. 2.10. For April (Fig. 2.10a), the mean EML  $\theta$  pattern (dashed lines) shows a slight ridge extending from south-central Texas into Mississippi, and a second ridge extending from northeast Texas into western Missouri. The orientations of the potential-isotherm ridges suggest that the primary EML source region is northern Mexico during this month. The highest EML  $\theta$  values (greater than 39°C) are confined to southern and southwestern Texas, and the  $\theta$  gradient has a general north-south orientation over nearly the entire region. However, EML  $\theta$  values as low as 32-34°C appear in the northern sections of the study region, suggesting that the cooler source regions of the southern Rockies may be playing a role in producing the EML over this area, as suggested by Fig. 2.5a. Indeed, this result indicates that a much cooler EML can form a lid in the early spring, and that the Carlson et al. (1983) estimate of 38-48°C for a typical EML  $\theta$

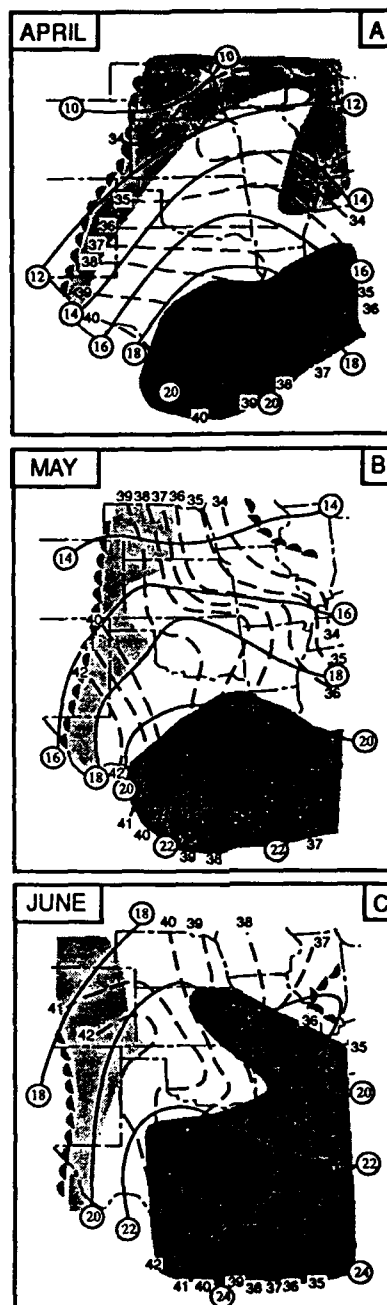


Figure 2.10. Mean analyses of EML and lid parameters for the most frequently occurring EML/lid-producing synoptic patterns. Charts are shown for a) April, b) May, and c) June. The solid lines denote mean "best" wet-bulb potential temperature in  $^{\circ}\text{C}$  and are analyzed at  $2^{\circ}\text{C}$  intervals. The dashed lines are the mean potential temperature ( $^{\circ}\text{C}$ ) in the EML (when observed), and are drawn every degree. The light shading highlights regions having a mean EML base above 750 mb, with the dark shading indicating a mean EML base below 800 mb. The scalloped border outlines the 25% occurrence frequency of the EML/lid.

is most valid over Texas. The mean EML base (shading) rises toward the north over the region, reflecting the dominance of the southwesterly flow regime (Fig. 2.9a). The  $\theta_{wb}$  pattern for this month (solid lines) also supports the dominance of the strong southerly low level flow, with a ridge of  $\theta_{wb}$  oriented along a nearly north-south axis from the Gulf coast of Texas to the Kansas-Missouri region. The inclusion in Fig. 2.10 of only the patterns that produce greater than the median number of lid stations reveals a much more structured  $\theta_{wb}$  field than was shown in FC89 (their Fig. 18) which represented an average for *all* April days in the study period. Thus, our results for April (Figs. 2.9a, 2.10a) complement those of FC89 (their Figs. 18, 19) by illustrating the synoptic patterns that contribute to both the creation of the EML and the existence of high  $\theta_w$  air beneath the inversion.

The overall EML/lid character changes as we move into May (Fig. 2.10b). The EML potential temperature pattern has changed dramatically, with the emergence of a gradient aligned roughly west to east, and a ridge axis oriented from western Oklahoma into southern Illinois. The 39°C potential temperature isopleth now extends from western Nebraska southward into southern Texas, and values as high as 42°C appear over southwest Texas. The northward expansion of the warm EML is consistent with the source region analysis in Fig. 2.6b, and the appearance of the warmest EML in southwest Texas is consistent with the observation that the warmest surface  $\theta$  values remain over northern Mexico in May. Although the height of the mean EML base still generally increases toward the north, from Texas to Nebraska and Iowa, there is more of a west-east component to the gradient than in April, reflecting the

increasing contribution to lid formation from midtropospheric anticyclonic and northwest flows (Fig. 2.9b). The EML is lower than in April over Nebraska, Kansas, Missouri, Illinois and Arkansas, and has changed little elsewhere, except over the Texas panhandle where it has risen. The changes in the structures of the EML  $\theta$  and base confirm that there are multiple flow patterns contributing to EML and lid creation. The  $\theta_{wb}$  pattern has also changed from April, showing a broad ridge axis with two branches, one over southwest Texas, and a second from central Oklahoma to western Kansas. The westward shift in the location of the  $\theta_{wb}$  ridge axis in May is in the same direction as the shift in the location of the maximum lid-frequency axis (Fig. 2.5b).

The composite analysis for June (Fig. 2.10c) shows still further changes in the structure of the EML and lid. The  $\theta_{wb}$  ridge, which was broad in May with two small branches, has consolidated into a single axis with a distinct anticyclonic curvature from south Texas into west-central Oklahoma and central Kansas. Also notice that there is abundant moisture present in the June  $\theta_{wb}$  field, reflecting the warming and moistening of the boundary layer that takes place as a result of increasing surface fluxes. The EML thermal pattern is similar to that of May, but the ridge axis now has a distinct northwest to southeast orientation, extending from southwest Kansas into southern Arkansas and northern Louisiana. A trough exists over the Gulf of Mexico and extends into the Texas coastal region, which is the same area that showed the decrease in lid frequency from May to June (Fig. 2.5d). The orientation of the EML thermal ridge axis reflects the observation from Fig. 2.9c that southwest flow is no longer the dominant EML-producing pattern in

June. Perhaps the most important observation from Fig. 2.10c is that the EML base near the thermal ridge axis actually lowers from northwest to southeast, suggesting that the flow is subsiding away from the source region. This is in stark contrast to the classic model for southwest flow that describes large scale vertical ascent along the trajectory of the EML. In general, the mean EML base is lower in June over the majority of the study region, indicating an increasing influence on the EML base from large scale flow patterns associated with subsidence as the late spring approaches. This is in contrast to our intuitive expectation that the boundary layer depths and inversion heights should be higher at this time of year than in the early spring. Northwest and anticyclonic 500-mb flows are associated with large scale subsidence over the majority of the study region due to the location of the ridge axis (recall Figs. 2.8a,d). A monthly examination of EML static stabilities in our sample from Fig. 2.2 shows that there is a slight increase in mean  $\sigma$  from  $1.98^{\circ}\text{C } 100 \text{ mb}^{-1}$  in April to  $2.21^{\circ}\text{C } 100 \text{ mb}^{-1}$  in June. Thus, while subsidence is not a contributing process to most early-spring lid situations, it appears to be important in many late-spring lid situations.

#### 2.3.4 Seasonal Changes in the Characteristics of the EML and Lid

The westward shift in the  $\theta_{wb}$  ridge axis from April through June corresponds closely to the shift in lid frequency shown in Fig. 2.5d. While the northward expansion of the high lid frequencies during the season is likely tied to the northward expansion of the EML source region and the increase in low level moisture, the westward shift in the



axis of maximum lid frequency is primarily related to the westward shift of the  $\theta_{wb}$  ridge axis and the increase in EML  $\theta$  over the western Plains. A difference chart between June and April (not shown) reveals that the values along the maximum-change axes of  $\theta_{wb}$  and EML  $\theta$  are nearly coincident over this area.

There is an additional factor which accounts for the decrease in lid frequency over the Gulf coastal area during the spring. We observed a large number of uncapped soundings in the late spring over the Gulf coast and adjacent areas to the north. These soundings, defined in section 2.2.1, are often associated with an unusually moist layer below the inversion, with resulting high  $\theta_w$  values that prevent the EML from effectively capping the PBL. An examination of 1200 UTC sounding data over the study region reveals that these uncapped soundings appear most frequently over the Gulf coastal area in June, as shown by the occurrence statistics in Table 2.1. In order to isolate the situations in which the uncapped sounding is caused by the appearance of an unusually moist PBL, we consider only those soundings in which the EML is at least 80 mb deep (roughly 1 km) and the base is at or below 700 mb. The 80-mb EML depth criterion is used to eliminate those situations in which the EML is shallow, which itself can be a reason for the lid strength being non-positive. The additional criterion of an EML base at or below 700 mb is based on an estimate from Carlson et al. (1983), who stated that a typical lid base would have to be below 650-750 mb in order to form an effective cap on a layer with  $\theta_w \approx 22-24^\circ\text{C}$ . The application of these EML depth and base criteria allows us to isolate

Table 2.1 Uncapped<sup>1</sup> Soundings for Four Gulf Coast Stations  
(Based on 1200 UTC data)

Station	Occurrences		
	April	May	June
Brownsville, Texas	1	4	11
Victoria, Texas	1	2	6
Lake Charles, Louisiana	0	5	9
Boothville, Louisiana	<u>3</u>	<u>2</u>	<u>6</u>
Total for 4 Gulf Coast stations	5	13	32
Total for all 22 stations	12	20	66
Total capped soundings for 4 Gulf Coast stations	190	203	102

Mean EML/Lid Parameters (all four Gulf Coast stations)

Parameter	April		May		June	
	uncapped <sup>1</sup>	capped	uncapped <sup>1</sup>	capped	uncapped <sup>1</sup>	capped
$\theta_{wb}$ (°C)	20.9	18.8	22.6	20.9	24.1	22.9
Level of						
RH break (mb)	828	897	796	904	827	909
$P_{base}$ (mb)	798	821	727	829	788	842
$P_{top}$ (mb)	603	548	510	614	614	644
$\theta_{eml}$ (°C)	36.0	37.6	40.7	37.0	38.8	37.5
$\theta_{swmax}$ (°C)	20.7	23.9	21.3	24.7	23.1	25.4

<sup>1</sup>See text for lid-base and lid-depth criteria

those soundings in which a deep EML cannot effectively cap the moist PBL below.

The EML/lid comparison statistics in the lower portion of Table 2.1 reveal that the PBL  $\theta_{wb}$  of the mean uncapped sounding is 1.2 - 2.1°C higher than that of the mean capped sounding. Additionally, the level of the RH break of the mean uncapped sounding is consistently above 830 mb in all three months, while that of the mean capped sounding is near or below 900 mb each month. Since the level of the RH break is an indicator of the moist-layer depth, this result suggests that the uncapped soundings generally have a much deeper moist layer than the capped soundings. Although a higher-based EML over a deeper moist layer results in the absence of a negative energy area in the uncapped sounding, the sounding still contains considerable potential instability due to the presence of the dry EML above the deep moist layer. An examination of the lid coverage on the days when uncapped soundings were observed reveals that about 40% of the Gulf Coast uncapped soundings occur on small lid-coverage days. The synoptic type most frequently observed with these uncapped soundings is a weak surface return flow, with either cyclonic or anticyclonic flow aloft. We conclude that the Gulf Coast uncapped sounding is primarily associated with those late-spring synoptic patterns in which the trade-wind flow regime dominates the Gulf and its adjacent coastal region. In such a regime, deep moist layers are possible due to the height of the trade-wind inversion over the moist-layer source region, which is typically around 2600 m over the western Caribbean in early summer (Gutnick 1958). In such synoptic flow patterns, the Gulf coast is not likely to

have a capping lid owing to the difficulty of transporting an EML to this area that is potentially warm enough to cap such a deep moist layer. Thus, the presence of uncapped soundings over the Gulf coastal region is consistent with the westward "shift" in the axis of maximum lid frequency from April to June (Fig. 2.5d). If the Gulf Coast uncapped soundings are added to the mean EML/lid composite charts in Fig. 2.10, they would only slightly affect the April and May  $\theta_{wb}$  and EML  $\theta$  patterns, but would significantly raise the mean June EML base, and alter the mean  $\theta_{wb}$  and EML  $\theta$  patterns over this area.

#### 2.4 Discussion

A complete description of the EML and lid climatology in the spring has been presented. It has been shown that the lid typically covers about 20 to 25% of the southern Great Plains, and that lid-coverage areas greater than 50% are rare (less than 2% of the days). Although the mean lid-coverage area stays roughly the same during the season, lid soundings are observed more often as the season progresses. The study shows that the northward expansion of the lid-coverage area during Spring is primarily controlled by the northward expansion of both the EML source region and the low-level moisture. The westward shift of the maximum lid-frequency axis is associated with a seasonal displacement of the low-level moisture axis caused by the westward expansion of the Bermuda anticyclone, as well as the appearance of uncapped EML soundings over the humid Gulf coastal region in late spring. The flow patterns most closely associated with the classic lid model have their highest occurrence frequencies in the early and midspring and have the highest

mean number of lid stations in all three months. As the EML source region expands, more flow types can produce a lid over the region, as evidenced by the evolution of the weak-return-flow/northwest-flow aloft type from a largely unfavorable lid-producing pattern in April to a favorable one in June. The decrease in midtropospheric southwest flow types and the concurrent increase in anticyclonic flow types help explain the gradual lowering of the mean lid base during the spring season. More importantly, the dominant lid-producing patterns in the late spring are associated with large scale subsidence, in stark contrast to the southwest flow regime that dominates the early spring and is associated with rising motion to the east of the upper level trough. Perhaps even more important is the coincidence of the emerging lid-producing anticyclonic and northwest flows with the beginning of the severe storms season in the central and northern Great Plains; a season which is characterized by the presence of anticyclonically curved and northwest flow patterns in the middle troposphere over this area (Johns 1982; 1984).

The implications of this EML/lid climatology on severe weather analysis and prediction over the southern Plains are very important, and are summarized below:

- 1) The southwest flow regime associated with classic models of lid formation and severe weather only accounts for 25 to 30% of all early spring days, and only about 18% of all June days. These flows are, however, the most efficient producers of lids during the entire season.

- 2) By midspring, the lid can occur with several different flow types because the Rocky Mountains and Great Basin have become elevated heat sources. The additional flow patterns are likely to produce different configurations of the low level moisture tongue, lid-edge front, and other important severe storm features.
- 3) The flow regimes with favorable wind shear (i.e., veering with height in the lower half of the troposphere) may not always produce an appreciable lid area; the forecaster must perform careful analyses of the important low level moisture and midlevel thermal features, especially in weak return-flow situations.
- 4) Since the lid forms more often in flow patterns associated with large scale subsidence during the late spring and early summer, diabatic processes such as surface heating may become more important in locally removing the lid in the absence of dynamical forcing.

## Chapter 3

### THE SYNOPTIC CLIMATOLOGY: THE LIFE CYCLE OF THE LID

#### 3.1 Chapter Introduction

The elevated mixed layer inversion, or lid, is an important feature of the severe-storm environment over the central U.S. in spring and summer. The lid sounding, as defined here, is essentially the same as the type 1 tornado sounding (Miller 1972) that is familiar to severe storm forecasters. The two components of the lid sounding, namely the warm, nearly adiabatic elevated mixed layer (EML) and the moist boundary layer below the inversion, have vastly different geographic origins. From early to midspring, the primary source region for the EML is the Mexican plateau and the adjacent desert southwest of the U.S. The moist layer below the EML originates through advection from the Gulf of Mexico. In late spring and summer, there are multiple EML source regions: the Mexican plateau, and the Great Basin and Rocky Mountain sections of the western U.S. At this time, a persistent moist return flow from the Gulf combines with substantial evapotranspiration from surface vegetation to allow a large area of buoyantly unstable<sup>1</sup> air to exist over most of the southern and central Great Plains of the U.S. from early June through the summer season.

---

<sup>1</sup> Buoyant instability, as defined in this paper, refers to the stability of a saturated surface/low-level parcel with respect to the mid-tropospheric environment, as used in the Lifted Index of the National Weather Service and the buoyancy term of the Lid Strength Index.

A previous study (Lanucci and Warner 1991a, hereafter referred to as LW1) identified certain synoptic flow patterns which are favorable and unfavorable for lid formation during the spring (April, May, and June) season. Surface high pressure systems over the southern Plains (Kansas, Oklahoma, and Texas) were found to be associated with conditions unfavorable for lid formation because they advect cold, dry air southward and push the moist layer into the Gulf of Mexico. Additionally, the geostrophic wind in these situations has a backing wind profile and cold-air advection exists in the lower half of the troposphere. In such situations, the midtropospheric warm layer is confined to areas west of the Plains. These high pressure incursions decrease in frequency from April to June, but appear as late as the end of June during the period of study (1983-1986). Return flow from the Gulf, combined with a midlevel flow from the EML source regions, produces the necessary lid stratification when the EML thermal ridge overruns the low level moist tongue in the southern and central Plains. It was shown that midtropospheric southwesterly flow regimes produce the largest areal lid coverages throughout the season. This is the configuration most closely associated with the idealized conceptual model of the lid for the central U.S. first proposed by Carlson and Ludlam (1968). However, in late spring, synoptic patterns associated with large scale subsidence downstream from the EML source, such as midlevel anticyclonic and northwest flows, become associated with lids over the central and northern Plains. These occur more frequently in late spring than do southwesterly flow patterns. The lid-producing patterns of the late spring are characterized by a more northern EML



source region (the Great Basin and Rocky Mountains), and a low-level  $\theta_w$  tongue that is located over the western Plains.

Although LW1 demonstrate that the patterns of EML and lid occurrence undergo a significant seasonal evolution, the entire life cycle of EML and lid formation and dissipation has not been documented. Portions of the life cycle of the lid have been investigated in observational studies (e.g., Carlson et al. 1983, Doswell et al. 1985, and Rockwood and Maddox 1988), three dimensional modeling studies (e.g., Anthes et al. 1982, Benjamin and Carlson 1986, and Lanicci et al. 1987), and two-dimensional modeling studies (e.g., Benjamin 1986). The modeling studies examined the sensitivity of EML formation over northern Mexico and lid formation over the southern Plains to the horizontally varying surface fluxes and soil moisture. The three dimensional simulations were initialized during time periods when the lid was already established over the Plains states, while the two-dimensional study examined formation of the EML over an idealized plateau during a single diurnal heating cycle. The present study examines the entire cycle of lid formation and dissipation, utilizing the same database as LW1 and Farrell and Carlson (1989). We examine time-series analyses of lid occurrence for each of the spring seasons in our four-year period of record to determine the cyclic characteristics of lid occurrence, and any seasonal trends in that periodicity. We then define two types of lid cycles, and discuss the various stages in each type, including the initial formation of the EML over the source region. The combined surface/500-mb synoptic types defined in LW1 are employed in this study to characterize the flow evolution at each stage of the lid cycle, and

build on the results of LW1 by putting the various flow types into a temporal context. Finally, we produce composite mean analyses of representative synoptic types to examine the three-dimensional structure and dynamics at different stages of the lid cycle.

### 3.2 Time Series Analysis of Lid Occurrence

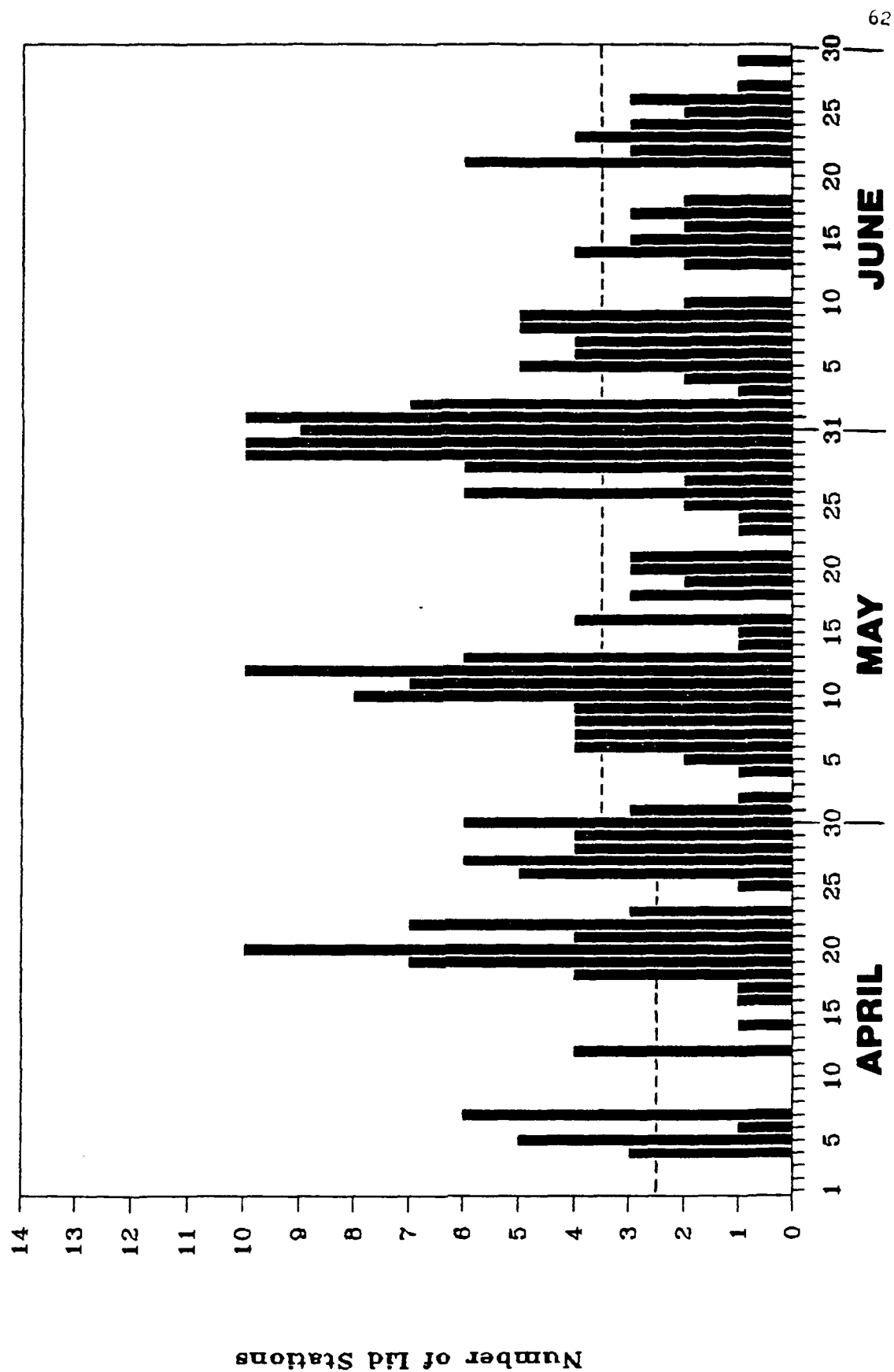
A time series of lid occurrence over the study area was produced for each of the four years in the study. The study region encompasses the southern Great Plains and surrounding states (see Fig. 2.1). Only 1200 UTC analyses are used in order to minimize biases in the horizontal extent of the lid area owing to daytime heating and moist convection. Possible biases in lid frequency due to nocturnal inversions are eliminated by the lid analysis program, which screens them out. The number of U.S. rawinsonde stations in the study region is 22; the maximum number of lid soundings observed at any one time during the study period was 13. Figure 3.1 shows the number of lid soundings in the study region for each of the 91 days in the 1985 record, which had the fewest missing data of the study period. This time series, which is representative of the four year record, shows a definite periodicity in the lid's occurrence, including three cycles associated with a large lid-coverage area (10 stations) which occurred about three weeks apart.

We examined each of the four time series in order to identify the number of separate lid cycles that occurred during the period in each year. The following criteria were used to define the beginning and end of each cycle:



Figure 3.1.

Time series of lid occurrence for the period April-June 1985. The ordinate denotes the lid-coverage area in terms of the number of "lid stations" over the study region; the dates on the abscissa correspond to the 1200 UTC analysis time only. The horizontal dashed line marks the boundary between the "small" and "large" lid-coverage areas (see Figs. 2.4 and 2.9 for details). For the purpose of the analysis, any missing 1200 UTC data were compensated for by using data from the adjacent 0000 UTC data times and the synoptic type for that date.



- 1) The beginning of the lid cycle is defined as the day when a minimum lid coverage is first observed; the number must be below three stations in April, and below four in May and June. The three- and four-station criteria denote the separation between what we define as "large" and "small" lid-coverage areas.<sup>2</sup>
- 2) A cycle extends from the lid-coverage minimum defined above, through a maximum that is at least three stations in April and four in May and June, and then to the next lid-coverage minimum.
- 3) When a surface synoptic type associated with high pressure is observed over the region near the time of lid-coverage minimum, that day is designated as the beginning of a new lid cycle, even if it is not the day with the actual minimum lid coverage. This is done because the high pressure incursion is responsible for generating the lid-coverage minimum.

The cycles, so defined, do not include all the days in the study period because some days showed no lid coverage in the large-area range. See, for example, the 17-22 May 1985 period in Fig. 3.1. Also, the cycles which began prior to 1 April or ended after 30 June could not be included because portions of these cycles fell outside the period of the study, resulting in the exclusion of some early April and late June

---

<sup>2</sup>Plots of the occurrence frequency of different numbers of lid soundings (Fig. 2.4) are bimodal in April and May. A point of local frequency minimum between the two lid-area modes is chosen as a boundary between the small lid-area and the large lid-area portions of the distribution. The median of the distribution is used as a basis for dividing the June distribution.

days. Altogether, 44 lid cycles were identified using the above criteria, accounting for 81% of all the days in the study. A frequency histogram of lid-cycle lengths for the three-month periods is shown in Fig. 3.2. The mean period for the lid cycle during the spring season is 6.7 days, with a standard deviation of 2.6 days. The modal value is five days, and the median is six days. The lid cycles range in length from two to 15 days.

### 3.3 A Schematic Life Cycle of the Lid

#### 3.3.1 Types of Lid Cycles

A chronology of the synoptic types that occurred during each of the four springs in the study period was developed. The synoptic type is defined in terms of a surface flow component, based on the sea level isobaric pattern, and a 500-mb flow component based on the predominant wind direction at this level over the study region. The synoptic typing scheme is defined in LW1, to which the reader is referred for details. Examination of the synoptic types occurring during each of the 44 lid cycles reveals that certain types are well correlated with specific stages of the lid cycle, whereas others can be associated with several stages of the cycle. Certain flow types, such as a north-south surface ridge with northwesterly flow aloft, are nearly always correlated with a low number of lid stations because the surface component is associated with cold, dry low level flow from the north, and the wind profile is backing with height from the surface to 500 mb. Other types, such as strong surface return flow with southwest flow aloft are usually

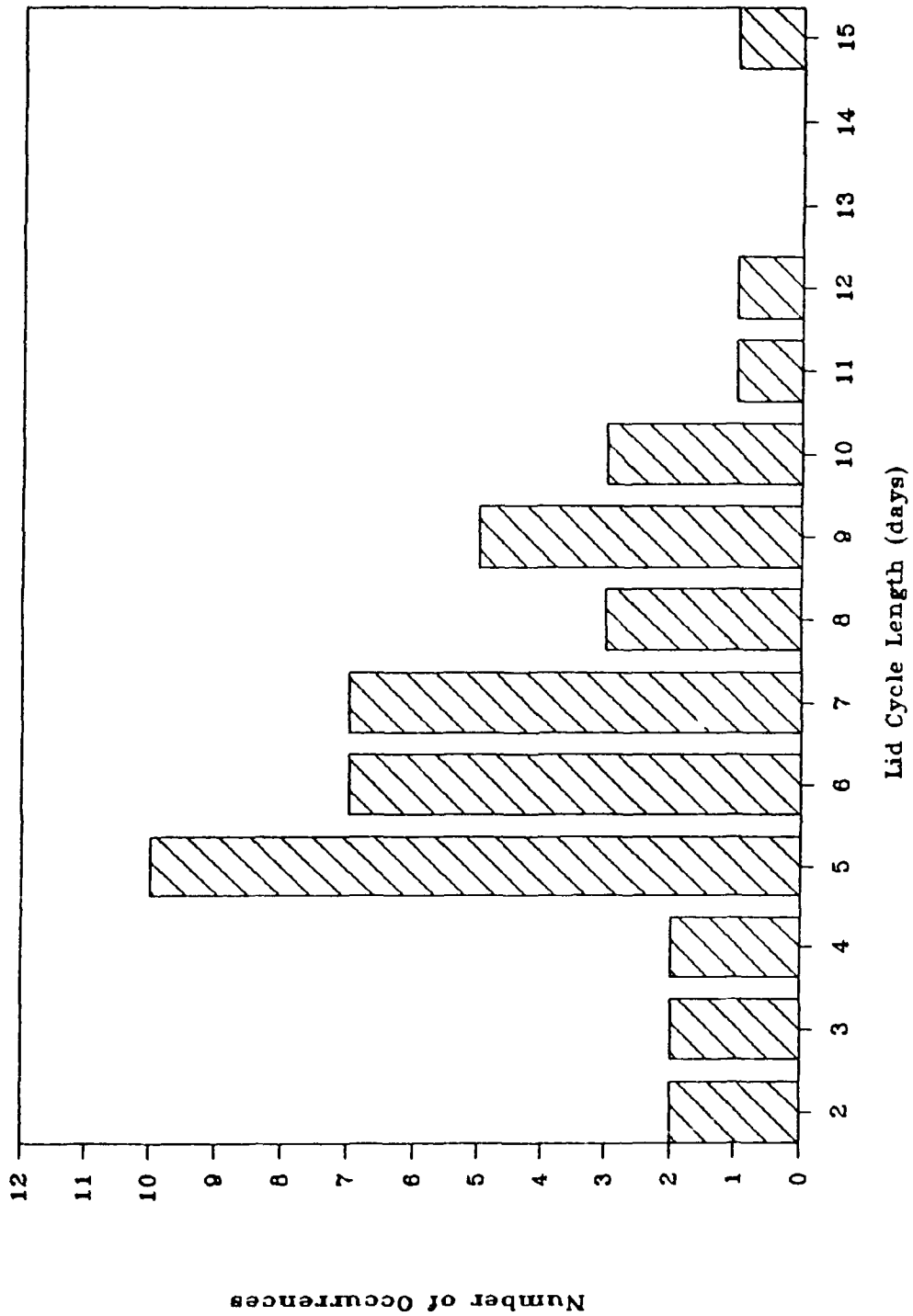


Figure 3.2. Occurrence frequency of lid cycle length (days) for the study period.



favorable for lid formation due to the combination of moist low level flow being overrun by the warm, dry EML originating over the desert southwest and northern Mexico.

Examination of the lid-occurrence and synoptic-flow time series reveals that there are two primary types of lid cycles. These cycles are defined as follows in terms of the surface flow type that prevails at the *beginning* of the cycle: 1) those that begin with a surface high-pressure incursion into the region (designated as H cycles); and 2) those that begin with a weak return flow over the area (designated as R cycles). Both types of cycles begin with no EML aloft, and must develop a superposition of the two components of the lid sounding (i.e., the EML and moist boundary layer) in order to attain a large lid area. The high pressure incursions that begin the H cycle are associated with polar-air outbreaks originating from the north or northwest. In this phase, the low level flow is offshore, and the midtroposphere is dominated by cold, stable air. After the high pressure phase, the atmosphere begins to establish a low level moist layer over the Great Plains by passing through a return-flow stage, during which the EML is forming over the western states through surface heating over elevated terrain. A large lid-coverage area is attained when the EML emerges from the west or southwest and overruns the low level moist layer. In the R cycle, there is no high pressure system present at the start of the cycle, and a low level moist layer is *already established* at the outset. In the latter case, a large lid-coverage area is reached earlier and the cycle has a shorter mean period (5.5 days vs. 7.1 days). The R cycle is characterized by the presence of weak low level flow, subtropical

circulations, and short wave features in the midtroposphere. Both cycles can end with a frontal passage and a subsequent high pressure incursion into the area, or with the removal of the EML while the moist layer remains intact over the region. The H cycle is observed more often than the R cycle (30 vs. 14 occurrences in the study period). Table 3.1 formally defines the different phases of each lid cycle.

The decreasing frequency of high pressure incursions into the region during the spring (LW1 and others) affects the seasonal trend in the occurrence of H and R lid cycles. Table 3.2 shows the four year frequency of lid cycle types at five-day intervals through the season. It reveals that the H cycle is dominant from early April to mid May. By mid May the H and R lid cycles become equally frequent, with the H cycle diminishing near the end of June. To further illustrate this May transition, Table 3.2 shows a division of the spring season into "early" and "late" segments. This division is consistent with the EML/lid composite analyses of LW1, which showed that May represents a transition between the early-spring lid regime, dominated by midtropospheric southwest flows from northern Mexico, and the late spring, in which lid production is mostly associated with midtropospheric northwesterly and anticyclonically curved flows originating over the Great Basin and Rocky Mountains.

### 3.3.2 Characteristics of the Lid Cycle Stages

Table 3.2 shows that the majority of lid-cycle days involve early-spring H cycles (19), late-spring H cycles (11), and late-spring R cycles (11). Each of these 41 lid cycles is analyzed in terms of the

Table 3.1 The Stages of the Lid Cycle

## H Cycle

Phase	Description
High-pressure (offshore flow) stage	High-pressure system observed over the region, low-level offshore flow, minimum lid coverage observed as EML and moist layer are absent.
Return-flow stage	Return (onshore) flow begins as the high exits the Great Plains and the moist layer begins to return inland. Isolated lid coverage may exist as EML starts to emerge into western Plains.
Pre-lid- coverage- maximum stage	Return flow continues over the region and moist layer is now established. Large lid-coverage area (three or more lid stations in April; four or more in May and June) is first observed over the region as EML overlies moist layer. Lid-coverage maximum has not yet been reached.
Lid-coverage- maximum stage	Moist layer and EML reach their greatest areal extent by this stage, leading to maximum lid coverage observed in the cycle.
Post-lid- coverage- maximum stage	Large lid-coverage area still observed over the region, but EML source region starting to be cut off.
End stage	A return to minimum lid coverage occurs as EML is removed and/or frontal passage occurs, usually followed by new high pressure system into region.

Table 3.1 The Stages of the Lid Cycle (continued)

## R Cycle

Phase	Description
	No high-pressure system is observed over the region at start of this cycle. Cycle begins with next phase.
Return-flow stage	Return flow is observed over the region, moist layer is established, minimum lid coverage observed as EML is largely absent.
Pre-lid-coverage-maximum stage	Large lid-coverage area is first observed over the region as EML emerges to overrun already established moist layer. Lid-coverage maximum has not yet been reached.
Lid-coverage-maximum stage	EML reaches its greatest areal extent by this time, leading to maximum overlap with the moist layer, and maximum lid-coverage area.
Post-lid-coverage-maximum stage	Large lid-coverage area still observed over the region, but EML source region starting to be cut off.
End stage	A return to minimum lid coverage occurs as EML is transported out of the region. In most situations, moist layer remains intact over the area.

Table 3.2 Spring Lid-Cycles: 1983-1986

Period Ending	April										May										June										
	5	10	15	20	25	30	5	10	15	20	25	31	5	10	15	20	25	30													
Type	<u>Number of Days</u>										<u>Number of Days</u>										<u>Number of Days</u>										
H	11	14	15	15	15	15	16	15	15	7	10	11	12	10	11	12	9	3													
R	0	2	0	0	0	0	2	5	5	9	9	13	8	10	9	8	9	15													
Other*	9 <sup>1</sup>	4 <sup>1,2</sup>	52,3	5 <sup>3</sup>	5 <sup>3</sup>	5 <sup>3</sup>	2 <sup>3</sup>	0	0	4 <sup>2</sup>	1 <sup>2</sup>	0	0	0	0	0	2 <sup>2</sup>	2 <sup>2</sup>													
Totals:	1 Apr-30 June										1 Apr-15 May										16 May-30 Jun										
H cycle days	216										131										85										
R cycle days	104										14										90										
"Other" days	44										35										9										

\* The "other" category includes the following:

- 1 - Cycle began in March (12 days)
- 2 - No lid cycle identifiable (14 days)
- 3 - Missing data; unable to identify type of cycle (18 days)

number of lid stations observed during each day of the cycle and the synoptic type observed on each day of the cycle. Cycles are counted as early or late spring on the basis of the beginning and ending dates. For example, two cycles that ended on 16 May are counted in the early season, and another cycle beginning on 15 May is counted in the late season. All cycles are assumed to begin and end at 1200 UTC. Figure 3.3 shows the mean number of lid stations in each phase for each of the three types of cycles. The late-spring H lid cycle (Fig. 3.3b) has the highest overall mean lid-coverage area, likely owing to the expanded EML and moisture sources in the late season. A common feature in both H cycles is the rapid increase in lid coverage as the moist layer is established over the Great Plains. There is also a rapid decrease in lid coverage occurring over the region as the frontal system moves through, followed by a new high pressure system at the end of the H cycle. By contrast, the R cycle (Fig. 3.3c) has smoother transitions between phases because the low level moist layer remains well-established throughout the entire cycle. It also has smaller mean lid coverages than the H cycle.

Figure 3.4 displays the lengths of each phase of the early- and late-season H, and the late-season R lid cycles. An interesting observation from Fig. 3.4 concerns the mean lengths of the high pressure and return flow stages. The high pressure stage is basically a period of low level offshore flow, after which time the period of onshore flow begins. For the early- and late-spring H cycles the mean period of offshore flow (Fig. 3.4a) is about 1.4 - 1.6 days (about 36 h), which compares favorably with the mean transition period between offshore and

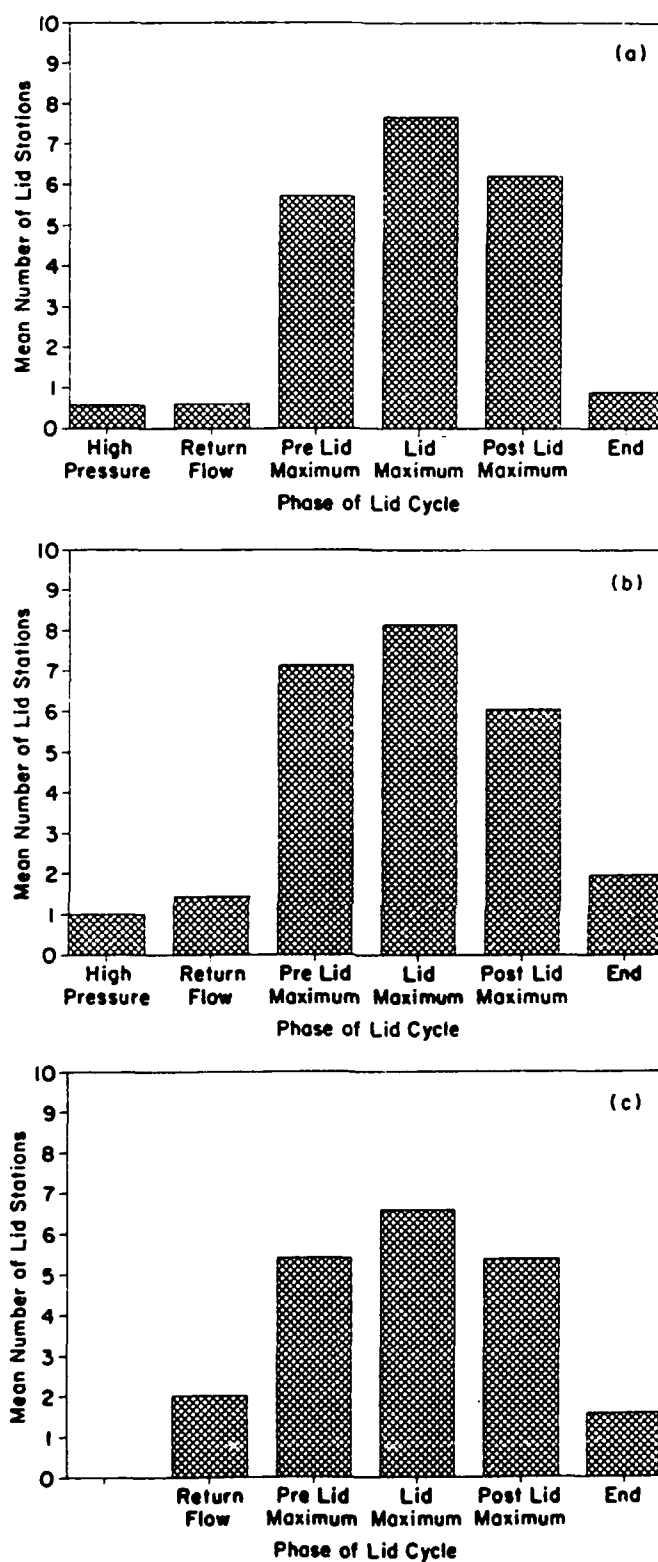
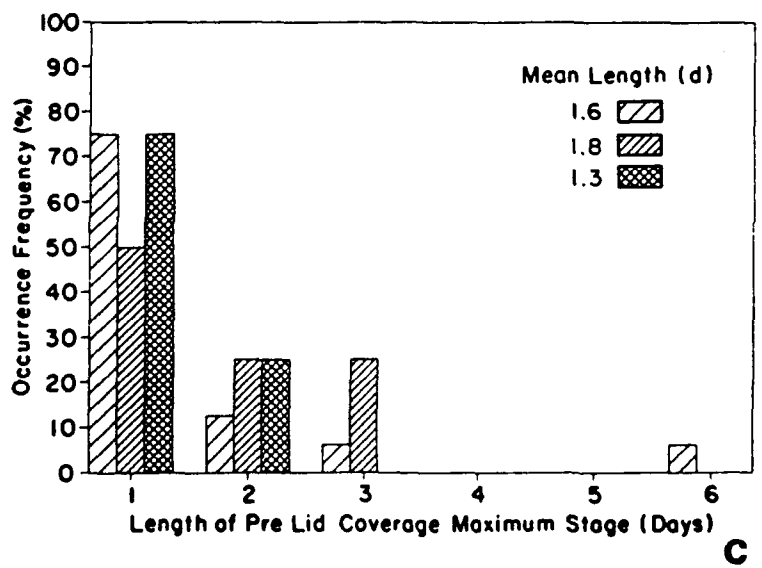
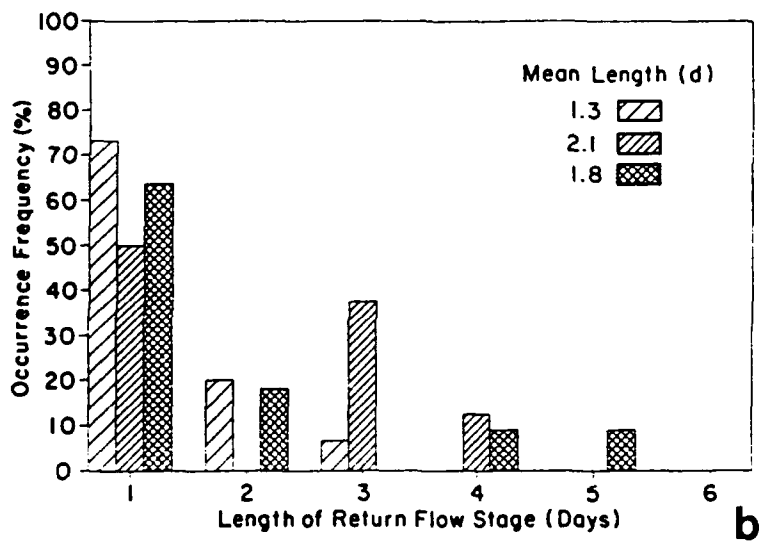
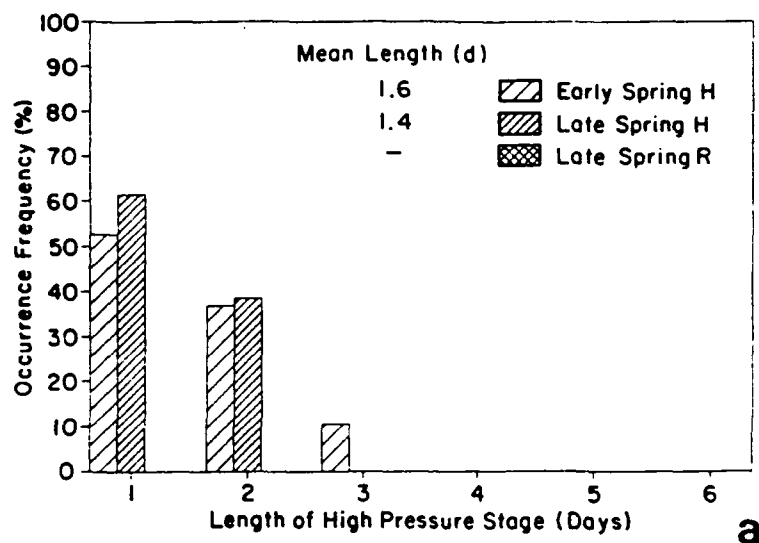


Figure 3.3. Mean lid-coverage area for each phase of the lid cycle (see Table 3.1 for definitions of lid cycle phases). Cycles shown are a) early season H, b) late-season H, and c) late-season R.





Figure 3.4. Lid cycle phase length (in whole days) and frequencies for the three types of lid cycles shown in Fig. 3 (legend is shown in panel 'a'). Phases shown are a) high pressure, b) return flow, c) pre-lid-maximum, d) lid maximum, e) post-lid-maximum, and f) end.



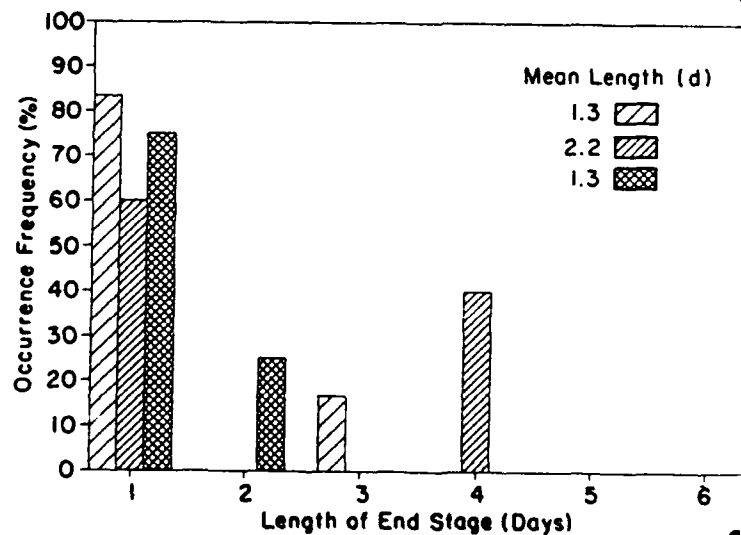
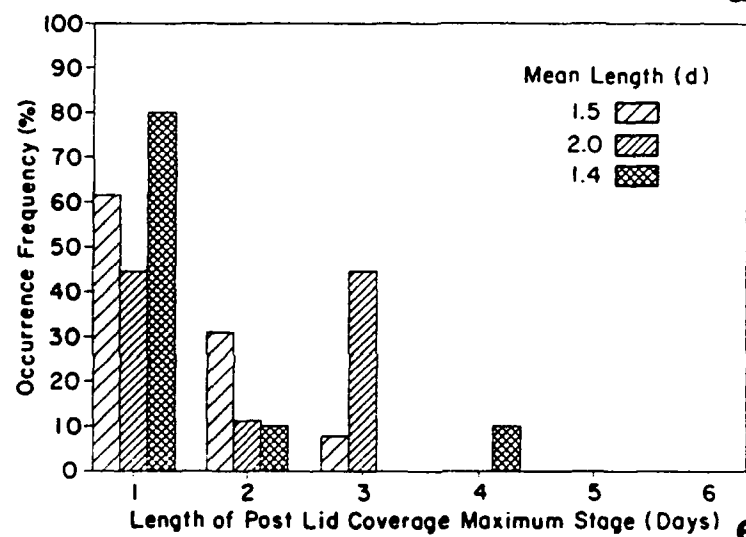
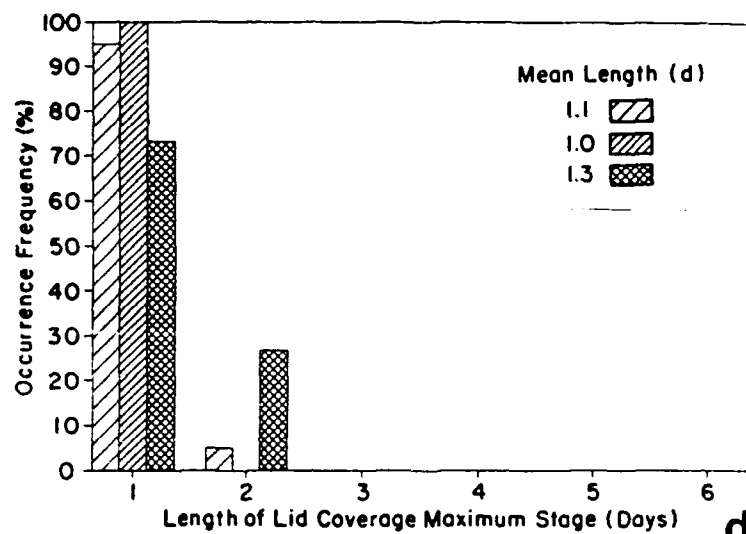


Figure 3.4. (Continued)

onshore flows (38.5 h) observed by Lewis and Crisp (1989) in their 10-year return-flow climatology for February and March. The length of the return-flow stage for the H cycle (Fig. 3.4b) shows that there is a significant time lag between the onset of return flow and the appearance of a large lid-coverage area; this time lag averages roughly 30 h in early spring and 50 h in late spring. With the moist layer already established at the beginning of the R cycle, its transition to maximum lid coverage only depends on the transport of the EML into the Great Plains. Thus, the R cycle (on average) has the fastest transition to lid-coverage maximum (75 h) of all three cycles, whereas the early- and late-spring H cycles both require 36 h longer to reach lid-coverage maximum.

### 3.4 Synoptic Flow Patterns During the Lid Cycle

In this section the prevailing synoptic flow types that were observed during each stage of the lid cycle are discussed. Differences among the three types of lid cycles (early-season H, late-season H and R) are also examined in terms of prevailing flow types.

#### 3.4.1 Prevailing Synoptic Types During the Lid Cycle

Table 3.3 shows the occurrence frequency of synoptic types that were observed during different stages of the lid cycle. For the early-season H cycle, Table 3.3 shows that the high pressure stage is dominated by northwest and cyclonic flows at 500 mb. The next phase (return flow) is primarily associated with anticyclonic and northwest flows at 500 mb. The control of the H cycle by the long wave pattern is

Table 3.3 Occurrence Frequency of Synoptic Types at Each Stage of the Lid Cycle

Stage	Surface Type	Early-season H cycle					Late-season H cycle					Late-season R cycle				
		500-mb type					500-mb type					500-mb type				
High pressure	1	NW	W	A	SW	C	NW	W	A	SW	C	NW	W	A	SW	C
	2	7	2	3	1	1	11	1	0	0	0	12	0	0	0	0
	3	6	0	2	0	8	0	2	0	0	1	3	0	0	0	0
	Total	13	2	5	1	9	11	3	0	0	1	15	0	0	0	0
Return flow	3	NW	W	A	SW	C	NW	W	A	SW	C	NW	W	A	SW	C
	4	5	1	5	0	2	2	0	1	4	3	10	0	1	6	3
	5	0	2	2	3	0	1	0	0	2	0	3	0	0	1	0
	Total	5	3	7	3	2	3	0	1	7	3	14	0	1	6	5
Pre-lid maximum	3	NW	W	A	SW	C	NW	W	A	SW	C	NW	W	A	SW	C
	4	0	2	3	8	2	1	0	0	1	0	3	0	1	1	0
	5	2	1	0	2	0	0	0	0	0	0	4	0	1	0	0
	Total	2	3	5	12	3	1	1	0	3	2	7	0	0	3	1
Lid maximum	3	NW	W	A	SW	C	NW	W	A	SW	C	NW	W	A	SW	C
	4	0	1	1	4	0	2	1	1	1	2	7	3	1	5	2
	5	0	0	0	6	2	0	0	2	3	0	5	0	1	0	0
	Total	0	1	1	14	5	2	1	3	4	3	13	3	1	6	5

Table 3.3 (continued)

Stage	Surface Type	Early-season H cycle					Late-season H cycle					Late-season R cycle				
		500-mb type					500-mb type					500-mb type				
		NW	W	A	SW	C	NW	W	A	SW	C	NW	W	A	SW	C
Post-lid	3	0	0	2	1	0	0	1	3	1	4	2	0	2	2	3
maximum	4	0	0	0	7	1	0	0	2	2	1	0	0	0	1	0
	5	0	0	0	4	5	0	2	0	0	2	1	0	1	0	2
Total		0	0	2	12	6	0	3	5	3	5	3	0	3	3	5
		Total					Total					Total				
End	1	5	2	1	3	0	5	0	0	0	0	3	0	0	0	0
	2	1	1	1	0	5	0	0	0	0	1	0	0	0	0	0
	3	0	2	1	0	1	1	1	6	0	5	0	0	2	2	5
	4	0	0	0	0	0	0	0	1	0	0	0	0	0	0	0
	5	0	0	0	1	1	0	0	0	0	2	1	0	1	0	1
Total		6	5	3	4	7	6	1	7	0	8	4	0	3	2	6
		Total					Total					Total				
		11					5					3				
		8					13					9				
		4					1					0				
		2					2					1				
		25					22					15				

Surface types are coded as:

- 1 - high pressure (N-S ridge)
- 2 - high pressure (NW-SE ridge)
- 3 - weak return flow
- 4 - strong return flow
- 5 - frontal passage

500-mb types are coded as:

- NW - northwest
- W - west
- A - anticyclonic
- SW - southwest
- C - cyclonic

evident here, in that the change in 500-mb types between the high-pressure and return-flow stages suggests a transition from long wave trough to ridge over the southern Plains. At the surface, the high moves through the Great Plains region and exits eastward, being replaced by the weak return flow regime (surface "type 3" in Table 3.3). In the pre-lid-maximum stage of the lid cycle, the low level flow strengthens (notice the prevalence of surface "type 4" patterns in Table 3.3), and the 500-mb flow becomes southwesterly. The next 500-mb trough, now located over the western U.S., is often accompanied by lee-side cyclogenesis. Subsequently, in the lid-maximum and post-lid-maximum stages, a surface frontal system begins to move into the region, as shown by the increasing frequency of surface "type 5" flows during these two stages (see Table 3.3). Finally, the cycle ends with the return of another high pressure incursion accompanied by 500-mb types "NW" and "C".

The late-season H cycle is different from its early-season counterpart in all stages (see Table 3.3). In the late-season cycle, the N-S oriented surface ridge ("type 1") is dominant in the high-pressure stage. The transitions between long wave troughs and ridges that characterize the early-season H cycle are not as frequent by late May and June because the polar-jet activity shifts to Canada and the northern tier of the U.S. The return-flow stage in the late-spring H cycle is characterized by 500-mb southwest flow. The appearance of southwest flow in this early stage of lid development seems counterintuitive, since southwest flow is associated primarily with the large lid-coverage stages in the early-spring H cycle. In late spring,

however, southwest flow can draw in moist air from active monsoonal or tropical regions. The resulting vertical moisture profile lacks the midlevel dryness that is characteristic of the lid sounding. Additionally, the appearance of uncapped EML soundings (discussed by LW1) in late-spring situations results from the existence of high  $\theta_w$  air in the PBL, which the EML cannot effectively cap. For these two reasons, the return flow stage is actually *longer* in the late-spring H cycle (see Fig. 3.4b), even though the low level moist layer may actually appear *sooner*. During the large lid-coverage stages, there are no clearly dominant 500-mb flow types, as there were in early spring. Southwest flow, which was dominant in the early spring (63% occurrence), is no longer the most frequent pattern, as anticyclonic, southwest, and cyclonic patterns now cumulatively account for nearly 80% of the large lid-coverage days. At the surface, weak return flow ("type 3" in Table 3.3) is slightly more frequent than is strong return flow ("type 4" in Table 3.3). The decline in frontal activity over the region in late spring is illustrated by the low frequencies of the frontal-passage surface type in both the lid-maximum and post-lid-maximum stages (8 and 25% occurrences, respectively, as opposed to 33 and 45% in early spring). The downward seasonal trend in frontal systems crossing the southern Great Plains is consistent with the climatological studies of frontal incursions into the Gulf of Mexico by DiMego et al. (1976) and Henry (1979). This seasonal tendency is also illustrated by the increase in the occurrences of weak return flow in the end stage, from four in early spring to 13 in late spring. The dominance of weak return flows in the late-spring end stage implies that the moist layer remains



nearly intact over the region, and signals a decrease in the H cycles and an increase in the R cycles.

The R cycle begins with a weak return flow 94% of the time, usually under southwest, anticyclonic, or cyclonic flows at 500 mb (see Table 3.3). The low level flow in the R cycle remains relatively weak, even in the large lid-coverage stages (notice the low combined occurrence frequency of strong-return-flow and frontal-passage surface types in Table 3.3). At 500-mb, types "A" and "C" account for 63% of the large lid-coverage days. These 500-mb types are not associated with progressive ridges and troughs in the polar westerlies, but are instead associated with subtropical circulations and weak short wave features south of the polar jet.

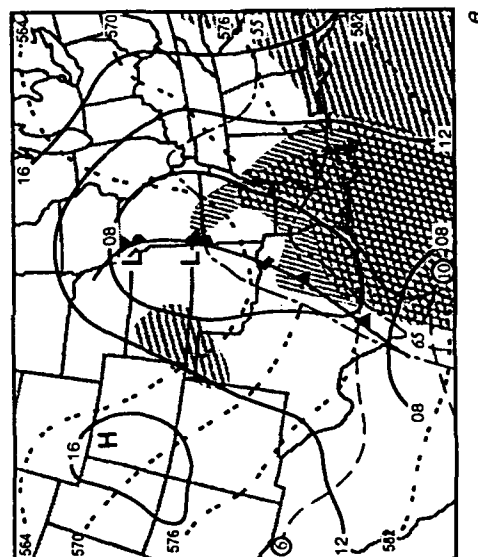
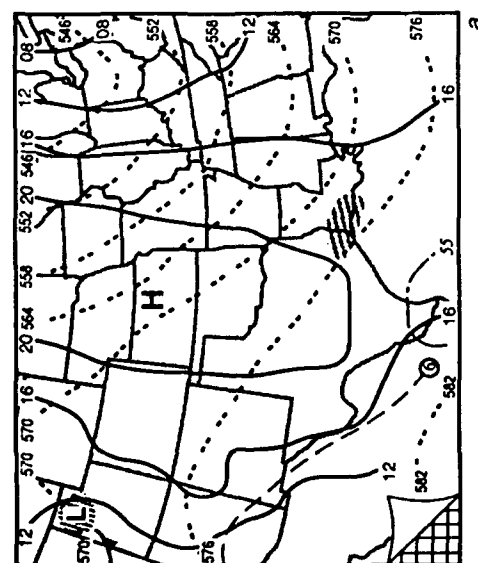
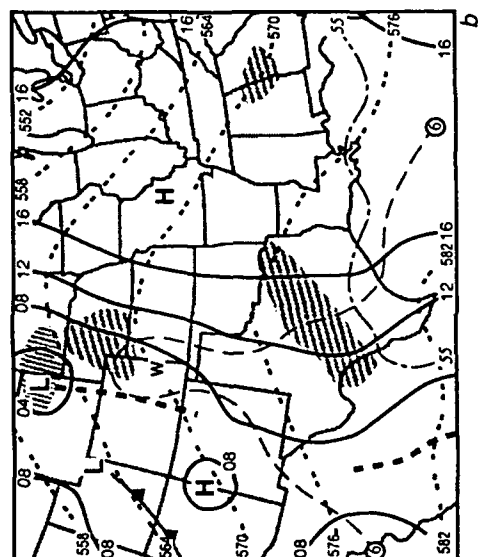
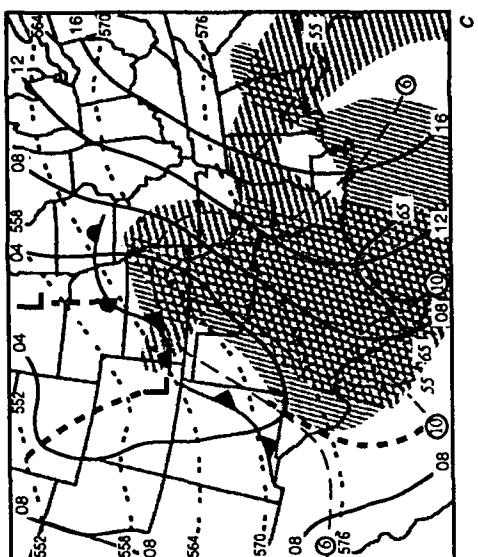
#### 3.4.2 Flow Structure During the Lid Cycle

Frequently appearing synoptic types during different stages of the three lid cycles were composited to examine the representative thermal, moisture, and wind field structures present during the evolution of the lid cycle. Mean fields of sea level pressure (SLP), surface dewpoint, 700-mb temperature, and 500-mb height are constructed for each representative flow type, using surface and mandatory-level data. The 1200 UTC observations for each type-day were analyzed to a 40 by 30 point grid with an 80-km spacing (shown in Fig. 3.5a) using a Cressman (1959) objective analysis. Three successive corrections (using influence radii of 9, 6, and 3 grid spaces) were applied to the upper-air first-guess fields, and two were applied (using influence radii of 3 and 2 grid spaces) to the surface first guess fields. Two



Figure 3.5.

Composite mean charts for synoptic types representing different stages of the early-spring H lid cycle. The "peel back" in the lower left in (a) shows the grid mesh used to produce the composite fields. Mean sea level isobars are depicted by thick solid lines labelled in mb (interval of 4 mb); mean 500-mb heights are shown by thick dotted lines labelled in decameters (interval of 6 dm); representative mean surface isotherms ( $55^{\circ}\text{F}$  and  $65^{\circ}\text{F}$ ) are shown as dot-dashed lines; representative mean 700-mb isotherms ( $6^{\circ}\text{C}$  and  $10^{\circ}\text{C}$ ) are shown by thin dashed lines. The areas of occurrence frequency equal to or greater than 50% are shown for the following parameters: unstable buoyancy (vertical shading), EML (horizontal shading), and the areas of overlap (indicative of high lid occurrence frequency, "checkerboard" shading). Surface highs, lows, fronts, and troughs are shown using conventional symbols. Highs and lows at 500 mb are displayed using "open" lettering. Charts are displayed for the following lid cycle stages with the synoptic types (see notation in Table 3.3) in parentheses: a) high pressure ("1-NW"), b) return flow ("3-A"), c) pre-lid-maximum ("4-SW"), d) lid maximum ("4-SW"), and e) post-lid-maximum ("5-C").



passes of a 1-4-1 smoother were then applied to the gridded analyses. For each synoptic type, the individual gridded fields for each variable were added together, and the mean gridded field was computed simply by dividing the grid point values by the number of days in the sample for each synoptic type. Additionally, we constructed geographic frequencies of EML and buoyantly unstable areas (composited at the upper air stations), in order to examine the evolution of static stability over the region during the lid cycle. See section 2.2.1 for specific criteria used to identify EML and buoyantly unstable soundings. The SLP and 500-mb height fields are meant to illustrate the low level and upper level flows, and the sign of the geostrophic thermal advection in the intervening layer. The surface dewpoints allow us to examine the development of the moist layer beneath the lid, and the 700-mb temperature is used to locate the warm layer that encompasses not only the EML, but its source region (the 700-mb isotherms we used ( $6^{\circ}\text{C}$ ,  $10^{\circ}\text{C}$ ) correspond to  $\theta$  values of  $36^{\circ}\text{C}$  and  $40^{\circ}\text{C}$ ).

#### 3.4.2.1 The Early-Season H Lid Cycle

The high-pressure stage of the early-spring H lid cycle is represented by a north-south pressure ridge/northwest flow aloft pattern (type "1-NW" from Table 3.3), whose composite mean analysis is shown in Fig. 3.5a. Note the secondary pressure ridge extending into the western Gulf of Mexico, roughly coincident with the  $93^{\circ}\text{W}$  longitude meridian. East of the surface ridge, there is strong cold-air advection, while weak warm-air advection is occurring over the western Plains and the Rockies. Genesis of the EML is taking place over the U.S. desert

southwest and northwestern Mexico, as indicated by the  $6^{\circ}\text{C}$  isotherm at 700 mb. The mean 500-mb ridge position is over the Continental Divide. The EML/unstable-buoyancy frequency composite analysis reveals only isolated areas of EML and buoyant instability occurrence at this stage.

The return-flow stage is represented by a weak return flow/anticyclonic flow aloft pattern (type "3-A" from Table 3.3), shown in Fig. 3.5b. Although types "3-A" and "3-NW" have equal occurrence frequencies at this stage (see Table 3.3), we chose this type in order to illustrate better the 500-mb wave progression in the lid cycle. The sea level pressure field shows the ridge axis now extending into the central Gulf, approximately coincident with the  $89^{\circ}\text{W}$  longitude meridian. Examination of the individual days comprising this composite reveals that the surface high either translates eastward into the Mississippi River valley or migrates southward into the Gulf and cuts off during this phase. The specific track of the surface high determines the timing and the location of the return of the moist layer into the southern Plains. The  $55^{\circ}\text{F}$  surface isodrosotherm shows that the moisture is beginning to return in three areas: the Rio Grande valley, southeast Texas, and the Mississippi River delta region. Examination of individual days shows that the latter two locations are "shut off" from returning moisture if the surface ridge penetrates into the Texas coastal region, or the cut-off surface high remains west of about  $90^{\circ}\text{W}$  longitude. In these cases, the moisture returns first into the Rio Grande valley, and only moves into the Gulf coastal regions of Texas and Louisiana after the high moves farther east or starts to weaken. The

appearance of strong southerly flow from Oklahoma northward, beneath the mean 500-mb ridge, implies strong warm-air advection over this area.

Evidence of an emerging EML from the west is shown by both the 700-mb thermal ridge over the western Plains and the pockets of high EML frequency located over portions of Nebraska and Texas. The appearance of an EML in the western half of Nebraska is significant, because it suggests that the relatively cooler mountainous regions of the western U.S. can still produce EMLs in the early spring, as suggested by Fig. 2.10. Because of the position of the surface pressure ridge, the returning moist layer is not in phase with the emerging EML and only isolated lid occurrences are possible at this stage of the lid cycle. As the next 500-mb trough begins to enter the western U.S., surface pressures are falling over the Rockies, which is the precursor to the development of the lee-side trough and low-level jet (LLJ). There is a remarkable resemblance between Fig. 3.5b and stage B of LLJ development (Fig. 4 in Djuric and Ladwig 1983). Although there are differences in the location of strongest surface flow between our composite mean analysis and Djuric and Ladwig's figure, the SLP patterns are very similar, as are the locations of key features such as the surface high, pressure ridge, and lee-side trough.

The "classic" lid producing pattern of strong return flow with southwest flow aloft (type "4-SW" from Table 3.3) represents the pre-lid-maximum stage (Fig. 3.5c). In this phase, the lee-side surface trough is well developed from Wyoming into Mexico. Once the lee-side trough forms and the surface ridge retreats into the eastern Gulf, the return of the moist layer occurs rapidly. This rapid return of the

moist layer into the central portion of the study region is hastened by development of the LLJ over this area. This stage of lid development resembles stage D in the LLJ conceptual model of Djuric and Ladwig. The three dimensional phasing of the moist tongue and the EML thermal ridge allows a lid stratification to develop rapidly, as illustrated by the overlapping EML and unstable areas in Fig. 3.5c. In this phase, there is a large region of lid occurrence covering most of Texas, Oklahoma, and Kansas, and a second, smaller area over Alabama and western Georgia. Notice that the western edge of the lid over Texas and Oklahoma closely parallels the mean position of the 55°F surface isodrosotherm. This suggests that the mean lid edge and dryline are nearly parallel, as observed in many individual case studies (Carlson and Ludlam 1968; Schaefer 1973, Carlson et al. 1983, and others). The mean 500-mb jet, inferred from the geopotential height gradient, extends from southern Arizona and New Mexico into northwest Kansas and central Nebraska, then turns anticyclonically towards the Great Lakes region.

There are several areas in the southern Plains where the unstable-buoyancy frequency exceeds the EML frequency. One area is parallel to the western edge of the lid, to the east of which the low level moist layer is consistently deep enough to support a lid stratification. The proximity of the buoyantly unstable area in western Texas and Oklahoma to the mean 500-mb jet and the dryline suggests that it can be a prime location for the initiation of deep convective storms in this flow type, especially since the low static stability would enhance vertical motion in the vicinity of upper level jet maxima approaching from the southwest (Uccellini and Johnson 1979). A second potential area for deep



convection exists where the low level moist axis reaches the northern lid edge zone over Kansas. This region is close to the mean 500-mb jet, LLJ, and surface front. These two areas of convective potential are likely to expand if the resulting moist convection erodes the lid and taps the highly unstable air located in the interior of the lid-coverage area, where the lid strength is typically greater (Graziano and Carlson 1987). An examination of the actual severe weather associated with these representative synoptic types is presented in a companion paper (Lanicci and Warner 1991c).

A multi-day persistence of 500-mb southwest flow often occurs during the large lid-coverage stages of the early-season H lid cycle (see Table 3.3). In the lid-maximum phase, the strong return flow/southwest flow aloft (type "4-SW" from Table 3.3) is dominant, so it is again chosen to represent this stage of the cycle (see Fig. 3.5d). This stage is characterized by stronger low and upper level flows throughout the eastern half of the study region, associated with falling SLP over the entire southern Plains region and a deepening 500-mb trough over the western U.S. This stage bears some similarity to Djuric and Ladwig's LLJ stage D'. The EML area has a more northerly extent at this stage, and the unstable area extends farther east. The lid-edge zone over Texas is located farther west than in the previous stage, and is very close to the strong 500-mb jet and surface frontal system; for this reason, it is a favorable area for initiation of deep convection, and will expand if the moisture laden air farther east is tapped. A possible second area of convective potential is located over northern Oklahoma and southern Kansas, but convection in this region may be

delayed until the main jet translates eastward, or a jet streak propagates into this area from the southwest. There are similarities between the temporal continuity in our synoptic types representing these two large lid-coverage stages, and that of the type A and B synoptic patterns of Miller (1972). In our composite mean analysis shown in Fig. 3.5d and in Miller's type B pattern, the surface front is beginning to enter the Great Plains, and the jet locations are similar. It is interesting to review Miller's comments regarding the temporal continuity between his synoptic types:

The type A and B patterns are quite similar in configuration and general development. The major difference between the two is the noticeable presence of a major upper trough and frontal system to the west of the threat area in the Type B pattern. This association with the trough and frontal systems designates the Type B pattern as the *last* (emphasis added) of a series of severe weather producing systems. On the other hand, the Type A often repeats from day-to-day until the major trough moves away. (p. 3-5)

Thus, the eastward migration of the 500-mb trough into the Great Plains marks the beginning of the post-lid-maximum stage of the early-season H cycle.

The synoptic type chosen to represent the post-lid-maximum stage of the lid cycle (Fig. 3.5e) illustrates the dynamic and thermodynamic structures that result when the EML source region is cut off by the advancing surface front and upper level trough. This is synoptic type "5-C" from Table 3.3. The mean frontal position in this stage is over eastern Oklahoma and Texas, and the Mississippi valley moist axis has a

more northerly extent by this time in the cycle. The 700-mb temperature field is fairly flat across the extreme southern portion of the study region, and the lid area extends only a little farther north than this warm air, into Mississippi, Louisiana, and southeastern Arkansas. The lid edge and frontal zones are nearly coincident over southern Texas, and diverge to the north of this area. The main 500-mb jet extends from New Mexico into northern Texas and southern Arkansas. The combination of the strong cold front moving eastward, the strong southerly flow ahead of the front with a strong cyclonic upper jet crossing over (generating a strong veering wind shear), and the lid edge and buoyant instability in this vicinity suggests that northeastern Texas, northern Louisiana, southern Arkansas, and (later) western Mississippi are vulnerable to severe weather. A secondary convective area over the south Texas coast can activate if the front removes the lid there.

#### 3.4.2.2 The Late-Spring H Lid Cycle

Table 3.3 shows that the late-spring lid cycles are not associated with the systematic passage of major upper level troughs and ridges, as in the early spring. In order to compare representative flow types between the early and late spring H cycles, we chose types "1-NW" and "4-SW" as representative of the high-pressure and large lid-coverage stages, respectively. Table 3.3 shows that these two synoptic types occurred frequently enough in the late-spring H cycle to allow comparisons with their early-season counterparts.

The composite chart for type "1-NW" is shown in Fig. 3.6a. There are several notable differences between this late-season version and its

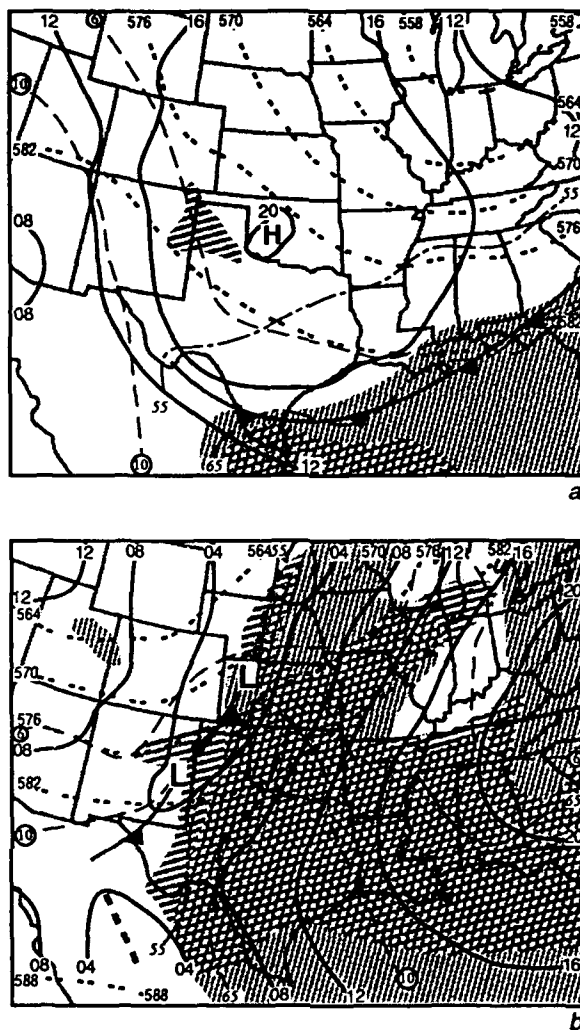


Figure 3.6. Same as Fig. 3.5, except for late-spring H cycle. Charts are shown for the following lid cycle phases and synoptic types: a) high pressure ("1-NW") and b) combined pre-lid-maximum, lid-maximum, and post-lid-maximum stages ("4-SW").

early-season counterpart (Fig. 3.5a). The high pressure system is weaker, and the secondary surface ridge over the Gulf does not appear. Instead, there is an eastward "bulge" of the surface ridge. There is more low level moisture present in this flow type over Texas and the Gulf coastal states than there was early in the season, and a moist axis already exists along the Rio Grande valley at this stage. The large expanse of the EML source region is well illustrated by the 700-mb temperature field, which shows a thermal ridge from northwestern Mexico into Arizona, southern Utah, and eastern Nevada. At 500 mb, the mean trough is over the Mississippi River valley, somewhat to the west of its early spring position, and not as deep. Increased low level moisture over the southern states at this time allows buoyantly unstable air to exist over the Gulf coastal region in this flow type, and as a result there is some lid occurrence in the vicinity of Brownsville, Texas.

The late spring composite chart for type "4-SW" is shown in Fig. 3.6b and can be compared with those for the early season (Figs. 3.5c,d) to examine the seasonal trend in this classic lid-producing synoptic type. Since this late spring composite applies for the duration of the large lid-coverage stages, direct comparisons cannot be made with the early-spring versions shown for the pre-lid-maximum and lid-maximum stages. However, some seasonal differences can be inferred from examining the mean gradients of SLP, 700-mb temperature, and 500-mb height. The SLP pattern over the western Plains, for example, shows a weaker, narrower lee-side trough than in the early season, consistent with a weaker 500-mb trough. There is considerably more low level moisture present than in the early spring patterns, but the eastern

Plains moist axis has a very similar orientation to that for the early season: The 700-mb thermal field indicates warmer conditions than in the early spring with temperatures in excess of  $12^{\circ}\text{C}$  (equivalent to  $\theta$  near  $43^{\circ}\text{C}$ ) over a large portion of Texas. The mean 500-mb jet is more zonal and is located farther north than in the early spring. The buoyantly unstable area is more extensive than the EML because of the large amount of moisture present. The somewhat larger lid-coverage areas observed in the late-season H cycle (compare Figs. 3.3a and 3.3b) are a result of greater overlapping areas of the EML and moist layer. The portion of the western lid edge from the northern Texas panhandle to southwest Kansas is close to the mean 500-mb jet, dryline, and surface front. This area can be considered as a potential genesis zone for deep convection. A second area of convective potential extends from northern Kansas into northern Illinois and is associated with the mean northern lid edge, 500-mb jet, and low level moist axis.

#### 3.4.2.3 The R Lid Cycle

The return flow stage of this cycle is represented by weak return flow with anticyclonic flow aloft (type "3-A" from Table 3.3). This flow type, whose mean composite analysis is shown in Fig. 3.7a, typically is associated with a westward expansion of the Bermuda anticyclone, causing the winds below 700 mb to become southerly or southeasterly over the southern portion of the study region. There is considerable low level moisture associated with this flow, as evidenced by the surface dewpoint analysis. The warmest air at 700 mb ( $> 10^{\circ}\text{C}$ ) is concentrated in a north-south-oriented zone from southern Colorado to central Mexico. When

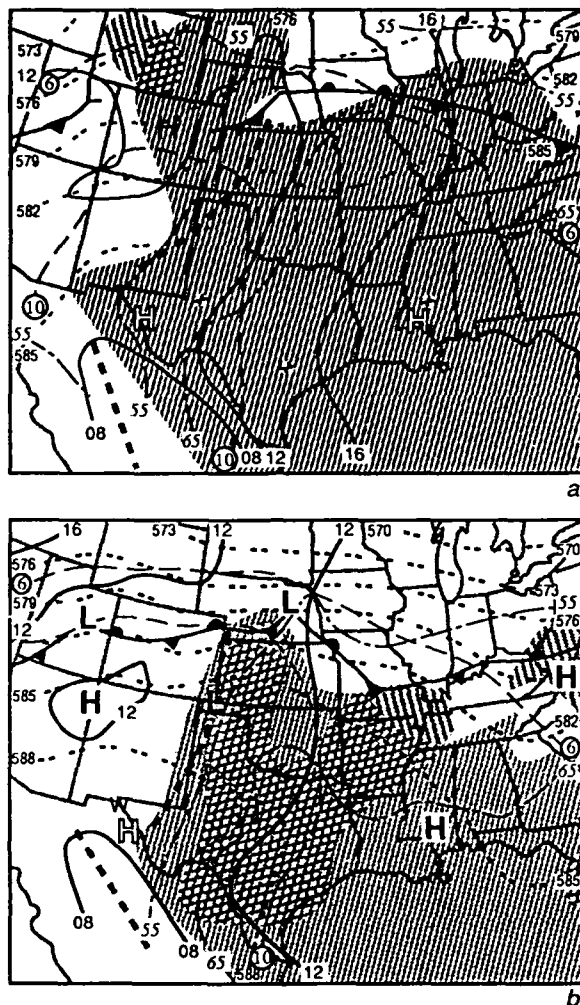


Figure 3.7. Same as Fig. 3.5, except for late-season R cycle. Charts are shown for the following lid cycle phases and synoptic types: a) return flow ("3-A"; Bermuda anticyclone dominant), and b) combined pre-lid-maximum, lid-maximum, and post-lid-maximum stages ("3-A"; Pacific anticyclone dominant). Note that the isopleth interval for the mean 500-mb heights is 3 dm in this figure.

the Bermuda anticyclone expands into the southern Plains, this warm air is restricted to areas west of the Great Plains. The 500-mb analysis shows two high centers over southwest Texas and southern Mississippi. In this flow type, the westward extension of the Bermuda cell dominates the lower half of the troposphere over the south-central U.S. There have been numerous climatological studies of the summertime circulation over the central and western U.S., ranging from the early studies of Reed (1933, 1937), Wexler and Namias (1938), and Riehl (1945), to the specific studies of the southwest U.S. monsoon (Bryson and Lowry 1955; Carleton 1985, 1986, 1987). The studies of the southwest monsoon all show that the orientation and location of the subtropical anticyclonic cell largely controls the precipitation regimes of the desert southwest and northern Mexico. The frequency composites for type "3-A" show a large area of buoyant instability to the east of the Rockies. There are several isolated areas of lid occurrence in this flow type and a slightly larger area over Wyoming. The Wyoming lid area is likely associated with midlevel southwest flow over the Rockies and Great Basin, which taps the warm-air reservoir to the south.

The large lid-coverage stages of the R lid cycle are also represented by a type "3-A", which has weak return flow with anticyclonic flow aloft, but in which the orientation of the anticyclonic flow is different from that in the previous stage. The composite mean analysis for this type is displayed in Fig. 3.7b. The transition to this flow type occurs when the Bermuda cell shrinks and the Pacific ridge builds eastward, raising the 500-mb heights over the southwest U.S. When this occurs, the midlevel warm air over the western



U.S. is transported over the southern Plains states by westerly winds. This situation often is accompanied by a strengthening of the jet to the north of the study region, caused by a strengthening height gradient north of the building anticyclone, as shown by the 500-mb height and 700-mb temperature gradients in Fig. 3.7b. In terms of EML frequency over the Great Plains, the primary distinction between this flow type and the preceding one is that the midtropospheric anticyclonic flow over the southern Plains in this phase is the hot, dry eastern branch of the Pacific anticyclone, as opposed to the cooler, moister western branch of the Bermuda anticyclone. The strengthening of the jet in the northern U.S. introduces a baroclinic zone over this region, which likely contributes to the decreased penetration of the moist layer into this area in this phase of the cycle. The moist axis in this flow type is better defined, and extends from the Texas Gulf coast northward through central Oklahoma and into the northeastern corner of Nebraska. Downwind of the EML source region, large scale subsidence reinforces the lid, as illustrated by the north-south-oriented lid frequency axis from south Texas into western Kansas and southern Nebraska. Given the large area of potential instability present in the lid area over the western Plains and the proximity of the northern portions of this lid area to the mean polar jet, we can define a convective genesis zone from western Oklahoma into Kansas and southern Nebraska. The 500-mb height pattern for this synoptic type in this phase is similar to the basic 500-mb flow pattern for northwest-flow severe weather outbreaks presented by Johns (1984) (his Fig. 7). Our sea level pressure pattern does not match any of his

surface patterns exactly, but most closely resembles his type G category, representing a meridionally oriented pressure trough.

Although not shown by a composite mean analysis, the end stage of the R cycle occurs when a short wave trough moves through the zonal jet and into the Great Plains to the east of the Pacific ridge. Subsequently, the EML is transported eastward ahead of the trough and eventually moves away from the Great Plains, leaving the moist layer intact, but returning the Plains to a lid-coverage minimum, usually under 500-mb type "C" (see Table 3.3).

### 3.5 Discussion and Summary

Our study of the life cycle of the lid over the southern Great Plains reveals that a typical lid cycle has a mean period of about one week. There are two basic types of lid cycles:

- 1) The H cycle that begins with a surface anticyclonic incursion into the region, is associated with the passage of baroclinic features in the westerlies, and has a mean period of about seven days.
- 2) The R cycle that begins with an already established moist layer within a persistent low level return flow from the Gulf of Mexico, is associated with subtropical circulations and weak short wave features after the polar jet has retreated northward, and has a mean period of between five and six days.

The H cycle is dominant in the early half of the spring, when polar-air outbreaks and a progression of long wave troughs and ridges are frequent

over the southern Plains. The R cycle is common in the late spring, when the region is dominated by low level southerly winds and the flow aloft is weak.

We defined various stages of lid evolution for the two types of cycles, based on observations of the lid coverage and prevailing synoptic patterns. The early-spring H cycle begins with a surface high pressure incursion, which changes to a return flow by about 36 h. The beginning of return flow over the southern Plains is characterized by only isolated lid coverage because the surface anticyclone is often anchored to the east of the Great Plains or in the western or central Gulf of Mexico, preventing the returning moist layer from entering the study region for an additional 24 h. A warm mixed layer forms over the high terrain of the western U.S. and emerges into the western Great Plains as an EML within 36 h of the start of the lid cycle. Large area lid coverage occurs when the low level flow strengthens in response to development of the lee-side trough and LLJ over Texas and Mexico, and the rapidly returning moist layer phases together with the EML created over the western states and northern Mexico. Maximum lid coverage typically occurs with the movement of a large scale trough into the western states, creating an overrunning flow of warm, dry EML air from the Mexican plateau above the well established moist layer in the south-central U.S. This cycle usually ends with a frontal passage through the region, followed by another surface high pressure incursion.

The late-spring H cycle is somewhat similar to that of the early season in the high pressure stage, but the midlevel flow is typically weaker throughout the cycle. Since the late spring EML source region

includes the Rocky Mountains and Great Basin, zonal and northwest flow types (in addition to southwest flow) can produce a large lid-coverage area in the late-season H cycle. Owing to the decreasing frequencies of frontal and high pressure incursions into the region as the summer approaches, this cycle often ends with the transport of the EML out of the region while the low level moist layer remains, marking the beginning of the late-season R cycle. The R cycle is characterized by weak low level return flow throughout the cycle, and changes in the midlevel flow pattern that are primarily influenced by the expansion and contraction of large scale, subtropical circulations such as the Bermuda and Pacific anticyclones.

Our analyses identified three primary surface moisture axes: 1) an axis along the Rio Grande valley; 2) a north-south axis through the eastern Great Plains; and 3) a north-south axis through the Mississippi River valley. The three axes develop during the early stages of the H cycle, and also appear in various stages of the R cycle. In the H cycle, the development of the moisture axis is influenced in the early stages by the location and strength of the surface pressure ridge. Our results show that the Rio Grande axis is favored over the others when the ridge extends into the Texas Gulf coast, or a cut-off surface high appears in the Gulf (west of about 89-90°W longitude). The observations suggest that the presence of moisture axes in these three locations is influenced by certain topographic features which tend to divert the moist flow around them. In the case of the Rio Grande axis, these topographic features are the Mexican plateau to the south and the Edwards Plateau to the north, while the Ozark Plateau influences the

eastern Plains axis, and to a lesser extent, the Mississippi River valley axis. These topographic influences are reduced in the late spring, but are still identifiable in our flow-type composites.

Our flow composites for different stages of the lid cycle illustrate the temporal continuity of wind field, moisture, and thermal features throughout the cycle, especially during the early spring. In particular, favorable genesis areas for moist convection are identifiable in the large lid-coverage stages of each lid cycle. In the early spring, these favored areas have a meridional orientation that is consistent with the nature of the midtropospheric flow type (i.e., southwesterly) and the presence of features such as the dryline, LLJ, and upper level jet over the southern Plains. In the late spring, these genesis regions are located to the north and west of the early spring locations. Our results generally suggest that the western lid edge is a *prime climatological location* for initiation of deep convection due to its proximity to approaching features such as surface fronts, drylines, and jet streaks. A second favored area appears along the northern lid edge, and is usually associated with features such as the moist tongue, LLJ, and strong veering wind shear in the lower half of the troposphere. In both locations, the convective region will expand and severe weather will become more widespread if the very moist, potentially unstable air under the interior of the lid area is tapped.

The results of this study complement other climatological investigations over the southern Great Plains. The three surface dewpoint axes identified in our composite analyses are very similar to the return-flow tracks proposed by Lewis and Crisp (1989) in their

10-year climatology of February and March. The persistence of the surface pressure ridge to the east of the Great Plains in the return-flow phase of the early season H cycle has been noted by area forecasters for many years, and the ability of operational numerical models to predict the movement of the surface ridge and the timing of the return flow was addressed in a study by Weiss (1989). The return flow that follows the exit of the surface anticyclone is also an important phase in the life cycle of the surface dryline (Schaefer 1973). In Schaefer's conceptual model, dryline genesis occurs when the moist layer reestablishes itself over the western Plains following the onset of return flow after the retreat of the continental airmass; this corresponds to the broadening of the Rio Grande moisture axis over the western Plains during the transition from the return-flow to the pre-lid-maximum stage in the early-season H lid cycle. Our composite charts for the early-season H cycle also complement the LLJ conceptual model for wintertime presented by Djuric and Ladwig (1983), which shows the initial development of the LLJ in conjunction with the appearance of the lee-side trough, the subsequent translation of the LLJ eastward with the surface cyclone and upper level trough, and the role of the LLJ in transporting the moist layer rapidly northward.

The importance of the results presented in this study is that the analysis and prediction of important severe storm features on any given day can be placed into the context of a climatologically based conceptual model of the lid cycle. The fact that our conceptual model of the early season H lid cycle resembles those of the dryline and LLJ is not surprising. The synoptic scale patterns appearing over the

central U.S. in early spring create a favorable environment for deep convection that includes features such as the dryline, LLJ, and EML. We have shown how the creation of the favorable static stability pattern (i.e., the lid sounding) occurs in concert with the creation of these other features. However, we have also shown that the lid-development cycle has a significant seasonal dependency. Knowledge of this seasonal aspect of lid development is important, because, as shown by this study and LW1, there is a marked change in the tropospheric circulation over the southern Plains from early to late spring. The early spring circulation is marked by a progression of baroclinic waves and frontal systems, whereas the late spring circulation is influenced at different times by relatively weak baroclinic waves, and subtropical circulations such as the Bermuda and Pacific anticyclones, with the latter features becoming more frequent by the end of June.

## Chapter 4

THE SYNOPTIC CLIMATOLOGY: RELATIONSHIP  
TO SEVERE-STORMS CLIMATOLOGY4.1 Chapter Introduction

One of the most challenging problems in operational meteorology is the prediction of severe-thunderstorm outbreaks. Development of severe storm analysis and prediction techniques has an historical background which is strongly rooted in event-based climatological studies. The first scientific attempts at describing atmospheric conditions associated with tornado occurrence were made by Ferrel (1885) and Finley (1890), and the first significant investigation of the thermodynamic and wind structures in the tornadic environment was made by Varney (1926). Further work continued with the studies of Humphreys (1926), Lloyd (1942), and Showalter and Fulks (1943), as routine radiosonde data became available to describe the mid- and upper-tropospheric structures associated with these events. As the upper air networks improved and the database became larger, a natural extension of this early work was the generation of severe-storm climatologies. A survey of the numerous event-based severe-storm climatologies produced over the U.S. since 1950 shows that the analysis techniques can generally be divided into three main categories: 1) statistical analysis of the characteristics of tornado events and storm-damage events; 2) evaluation of mean proximity soundings and horizontal meteorological analyses of the near-storm/tornado environment; and 3) categorization of the synoptic patterns associated with the severe storm and tornadic environments.



The second and third techniques result in the production of analog or mean meteorological fields for the tornadic environment.

There are several points which should be made about the use of reported severe storm or tornadic events as *the primary basis for generation of the resulting climatological database*. First, there are well known limitations in the use of severe storm reports that result from population biases (Schaefer and Galway 1982), difficulties in quantitative measurement of storm-related winds, and difficulties in observing events at night (Kelly et al. 1985). A second point is that the imposition of arbitrary limitations upon the data can strongly influence the resulting climatology. For example, restricting the data sample to tornadic outbreaks of a specified size (e.g., greater than 10 events), results in a climatology that is biased towards the most severe events, and the associated mean or analog meteorological analyses are usually highly baroclinic with strong buoyant instability<sup>1</sup> in the area of the events. Unfortunately, attempts are often made to apply these synoptic analogs to situations where the dynamical and thermal structures are not as well defined. In these "weakly forced" situations, the analyst is presented with a set of atmospheric conditions from which it is very difficult to produce a meaningful diagnosis and prediction (Maddox and Doswell 1982a,b; Doswell 1987). The third (and perhaps the most important) point concerning event-based studies is the exclusion of the "null" case in which severe storms are

---

<sup>1</sup>Buoyant instability, as defined in this paper, refers to the stability of a saturated surface/low-level parcel with respect to the midtropospheric environment, as used in the Lifted Index of the National Weather Service and the buoyancy term of the Lid Strength Index.

predicted but none occur (the "false alarm"). Statistics concerning false-alarm rates for severe storm prediction are routinely kept by the National Severe Storms Forecaster Center (NSSFC) in Kansas City, Missouri. However, few (if any!) of these false alarm/null cases are reanalyzed and presented in the meteorological literature. A reasonable question to ask is whether a severe storm climatology can be generated which eliminates any of these biases.

Another approach to building a severe storm climatology is to base it on a *physical phenomenon* that is known to be associated with the occurrence of severe thunderstorms and tornadoes. Attempts at such a climatology include the dryline study of Rhea (1966), the northwest flow outbreak climatology of Johns (1982, 1984), and the regional severe storm climatology of Giordano (1987). An offshoot of these physically based studies is the use of infrared satellite data to identify and compile climatologies of mesoscale convective systems or complexes. For example, several studies composite meteorological features that are common to mesoscale convective systems that meet certain size, cloud-top-temperature, and duration criteria (e.g., Maddox 1983; Bartels et al. 1984; Velasco and Fritsch 1987; Augustine et al. 1989). In addition to these satellite compositing studies, those of Cuning (1986) and Tollerud and Bartels (1988) also document severe weather events associated with these systems.

Our physically based climatology examines synoptic flow patterns that are favorable and unfavorable for generation of the elevated mixed-layer inversion, or lid, over the southern Great Plains of the U.S. (defined as Kansas, Oklahoma, Texas, and the immediate surrounding

area). This approach simply applies the proximity sounding technique in reverse; where the event-based studies produce a mean sounding of the near-storm environment that clearly has a lid, we instead produce a climatology of the lid itself, and relate this climatology back to severe storm occurrence or nonoccurrence. The period of study encompasses four spring seasons (April, May, and June) from 1983-1986. All of the severe weather events occurring during these periods are documented, resulting in a spectrum of event sizes from widespread outbreaks to isolated events. The non-event days are also documented. The definition of "severe storm" used in this study includes the standard NSSFC severe-thunderstorm criteria (i.e., thunderstorm wind gust equal to or greater than 50 kt; and/or hail with diameter equal to or greater than 3/4 inch; and/or thunderstorm wind damage), as well as observations of tornadoes and funnel clouds. The database for the lid climatology is a twice-daily compilation of lid parameters for the four-year period over U.S. rawinsonde stations from the Rockies eastward, previously described by Farrell and Carlson (1989) and Lanicci and Warner (1991a) (hereafter referred to as LW1). The database for the severe weather events is obtained from Storm Data, published by the U.S. Department of Commerce. Severe storm statistics are examined as a function of geographic location and month for the period of record, and the areal extent of the outbreak is related to the antecedent lid coverage area (lid coverages on non-event days are also examined). By employing such an approach, the lid-related climatology can reveal new, detailed information about the dynamic, moisture, and thermodynamic structures associated with a wide variety of atmospheric states during

the spring season. This study also builds on the results of an investigation that documented the life cycle of springtime lid formation and dissipation (Lanicci and Warner 1991b, hereafter referred to as LW2) by relating severe weather events to different stages of lid development. This is done by means of geographic frequency analyses of the occurrences of the elevated mixed layer (EML), buoyant instability, and severe storms for several synoptic types representing various stages of lid development in the early and late spring.

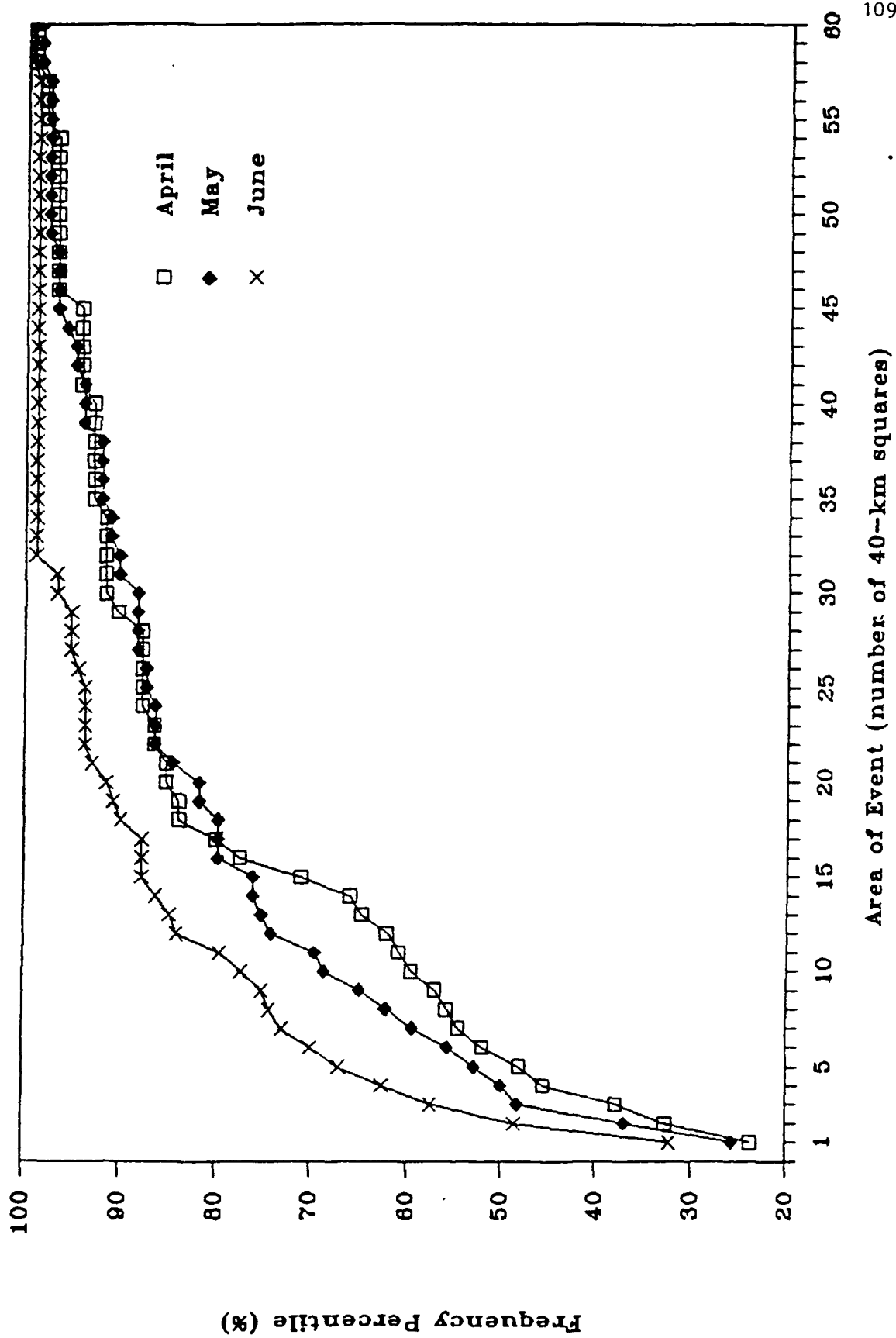
#### 4.2 Severe-Storm Statistics for the Southern Plains: April-June 1983-1986

Our compilation of statistics from Storm Data uses an approach that is similar to those of Galway (1977), Moller (1979), and Johns (1982). An "event" is defined as a severe-weather report or series of reports occurring within the three-state region of Kansas, Oklahoma, and Texas, with the time interval between reports not to exceed 3 h. The reports encompassing each event are then entered onto a 40-km grid covering the region. We are not interested in the number of individual reports occurring in each 40-km square: one report or 10 reports suffice to include the square as part of the event, and the square is only counted once. This was deemed an acceptable procedure since the focus of the data compilation is on the areal extent of an event in relation to the size of the lid-coverage area. The areal extent of each event is determined by simply summing the number of squares included during the lifetime of the event.

A percentile graph depicting the different event sizes in each month is shown in Fig. 4.1. Examination of the curves reveals several



Figure 4.1. Percentile graph displaying the cumulative occurrence frequency of severe storm events as a function of the total area of each event (given as the number of 40-km squares).



characteristics. First, each monthly distribution has its largest contribution from the one-square, or "isolated event," category. In April, a significant secondary contribution comes from the 15-18 square category (corresponding to an area between 24,000 and 29,000 km<sup>2</sup>), and in June, a similar contribution comes from the 9-12 square category (corresponding to an area between 14,500 and 19,000 km<sup>2</sup>). Although, the total number of events increases from 78 in April to 135 in June, the median event size decreases from five squares to two during the same period. The number of non-event days (defined as a 24-h period from 1200 UTC to 1200 UTC with no severe weather events reported) shows a steady decrease from 66 in April to 22 in June. The probability of a day having at least an isolated event increases through the season.

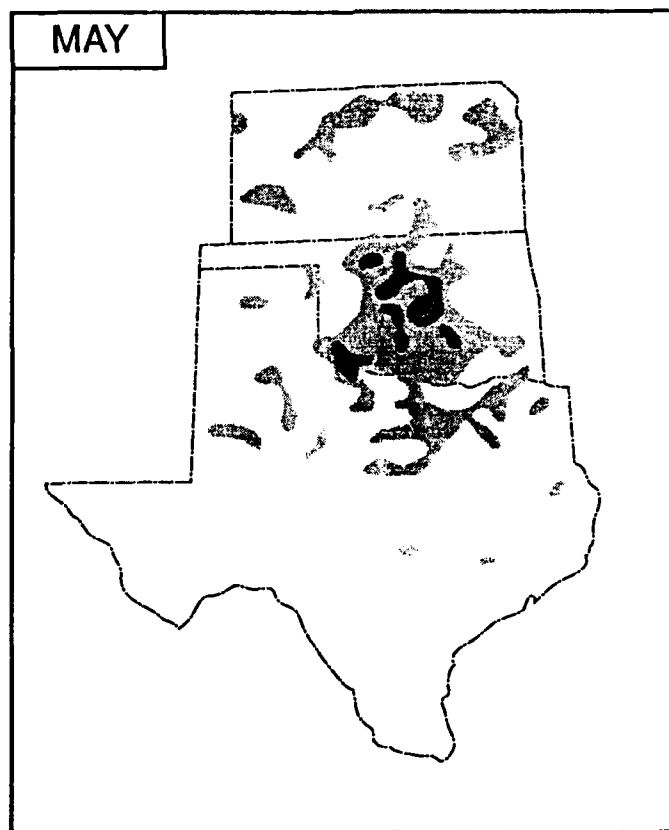
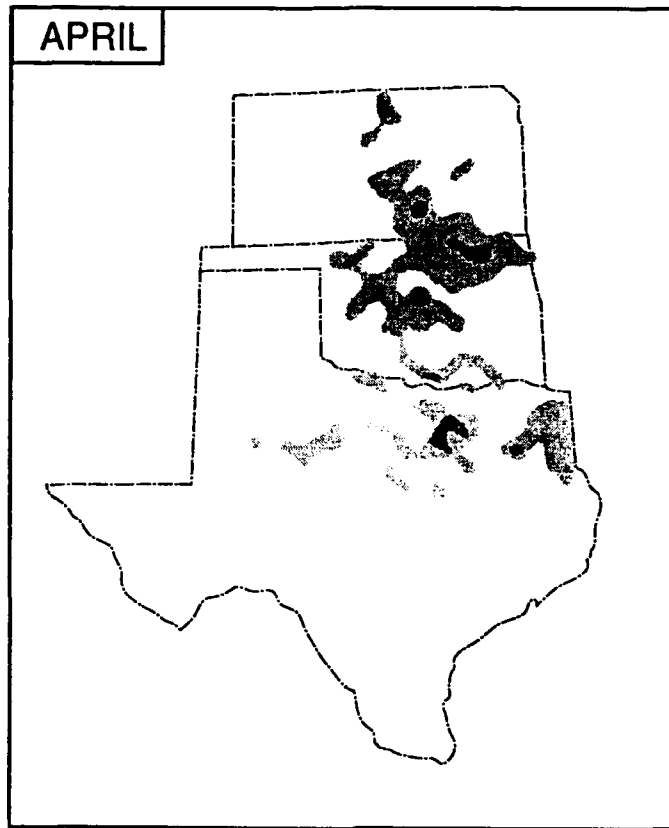
The geographic distributions of the severe weather events for each month are displayed in Fig. 4.2. The April and May distributions each have areas of activity over Oklahoma, Kansas, and the northern tier of Texas. The June distribution shows the near disappearance of activity over northern Texas, and has new centers of activity over the Oklahoma-Kansas border and northern Kansas. If one compares the geographic frequency charts for April and June, it can be seen that there is a general shift of activity to the north and west during the season. Such a seasonal migration of activity to the north and west is consistent with other severe-storm climatologies (e.g. Kelly et al. 1985), the MCC climatology of Velasco and Fritsch (1987), the lid-day climatologies of Farrell and Carlson (1989) and LW1, and the composite mean lid/EML analyses of LW1 (see Fig. 2.10).





111

Figure 4.2. Geographic frequency of severe storm events over the study region in terms of number of events per 40-km square. Light shading denotes 3-5 events per square, medium shading denotes 6-8 events per square, and dark shading denotes greater than 8 events per square. Charts are shown for April, May, and June.



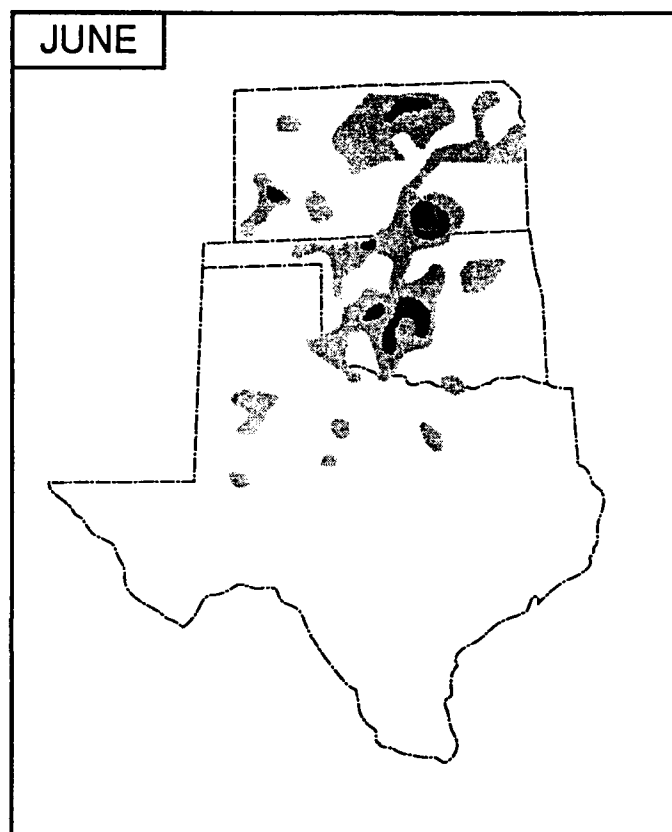


Figure 4.2. (Continued)

#### 4.3 Relationship of the Outbreak Size to the Lid

The relationship between lid occurrence and severe weather is first addressed by examining the monthly frequency of different lid-coverage areas for both event and non-event days. The resulting lid-coverage frequency distribution for each month appears in Fig. 4.3. For April, the non-event days are strongly associated with isolated or zero lid-coverage areas, while the event days have a near-normal distribution with a peak at five lid stations. This peak is very close to the mean lid-coverage area of 4.3 stations for this month (LW1). Geographic frequency analyses of lid occurrence by number of stations (not shown) for April reveal that lid coverage is spatially contiguous in this range. In May, the non-event day distribution peaks at one lid station, with most occurrences in the 0-2 station range, while the event day distribution has two peaks, at two and six stations. There is more of an overlap of the two distributions in May than there is in April. By June, there are very few non-event days (22), while the event-day distribution again has two peaks, at one station, and at four stations.

A second way to address the relationship between lid occurrence and severe weather is to analyze the severe-weather event size in relation to the lid-coverage area. For each event documented in the study period, the size of the antecedent lid over the study region is calculated in terms of the number of rawinsonde stations with a lid sounding. We are primarily interested in the antecedent conditions because the lid size during or after the conclusion of the event is more likely to be influenced by the convection itself. Additionally, a relationship between antecedent lid size and subsequent severe-weather

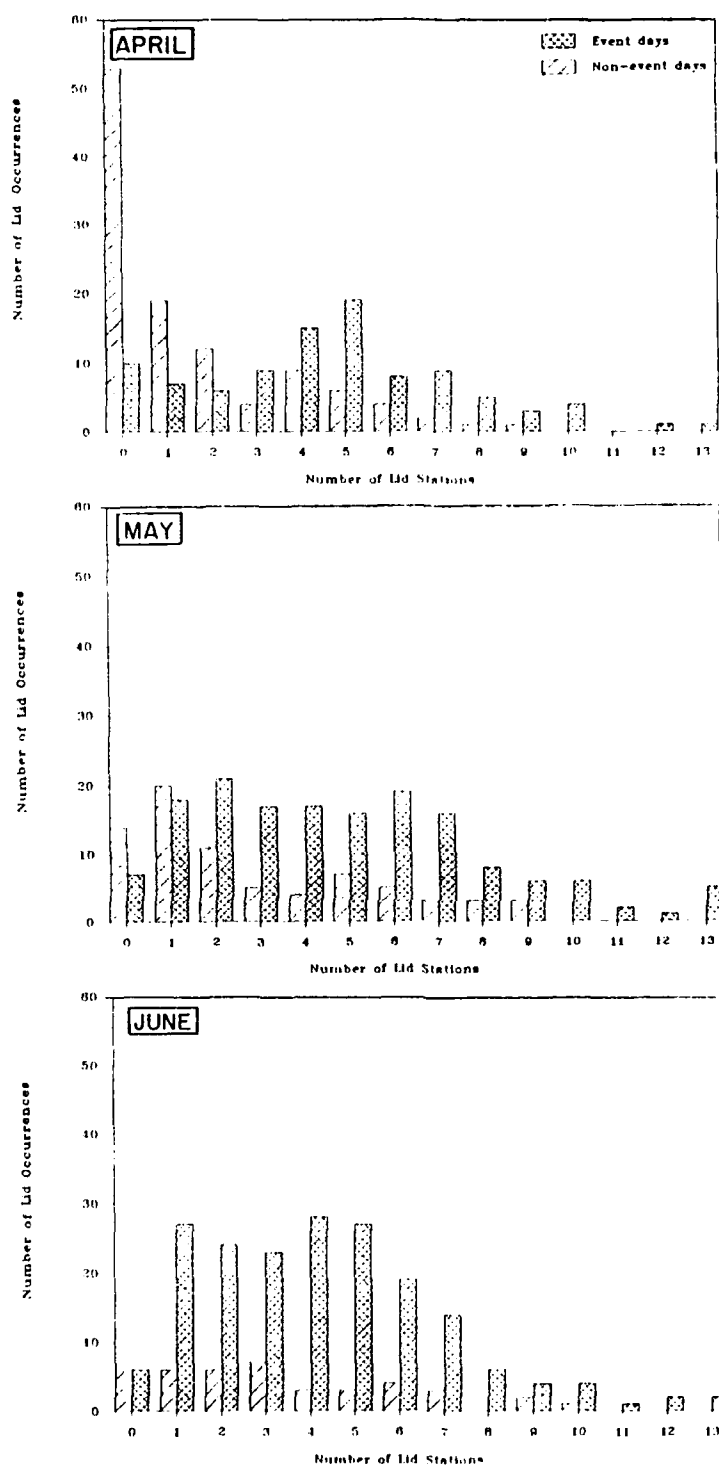


Figure 4.3. Histograms displaying the occurrence frequencies of 1200 and 0000 UTC lid coverage areas, given as the number of upper air stations with a lid sounding ("lid stations") for non-event days and event days (legend is shown in panel a). Charts are shown for April, May, and June.

event size can be potentially useful as a predictive tool. The antecedent conditions were defined at the synoptic time (1200 or 0000 UTC) prior to the start of the event. However, if an event began within two hours of a synoptic time, the lid coverage at that time was used (since radiosonde launch normally occurs about one hour and 15 minutes prior to the synoptic time). Thus, the antecedent lid coverage times range from 0 to 10 h before the start of the event. Non-event days are included in the compilation by taking the 1200 and 0000 UTC lid areas on the non-event days and assigning them an event size of zero. A scatter plot of antecedent lid size versus severe-weather event size for each month is shown in Fig. 4.4, along with a line that is fit to the data using linear regression. There is a great deal of scatter in the April data; the line has a correlation coefficient,  $r$ , of .52 and reduces the scatter by about 15%. The plot for May shows more scatter than the one for April;  $r$  decreases to .46, and the regression line reduces the scatter by about 11%. The increased scatter in May is consistent with the overlap of the event and non-event day distributions for May (Fig. 4.3). In other words, the relationship between the antecedent lid and the severe weather is strongest in early spring. This point is further dramatized by the scatter plot for June, where  $r$  is only .27, and the regression line reduces the scatter by only 4%. The sudden change in  $r$  between May and June is consistent with the changes in the severe-weather event size distribution (Fig. 4.1) and the changes in the lid-area distributions of the event and non-event days between May and June (Figs. 4.3). The significance of the  $r$  values for April, May, and June was tested using Fisher's Z-transformation (Brownlee 1965). The results

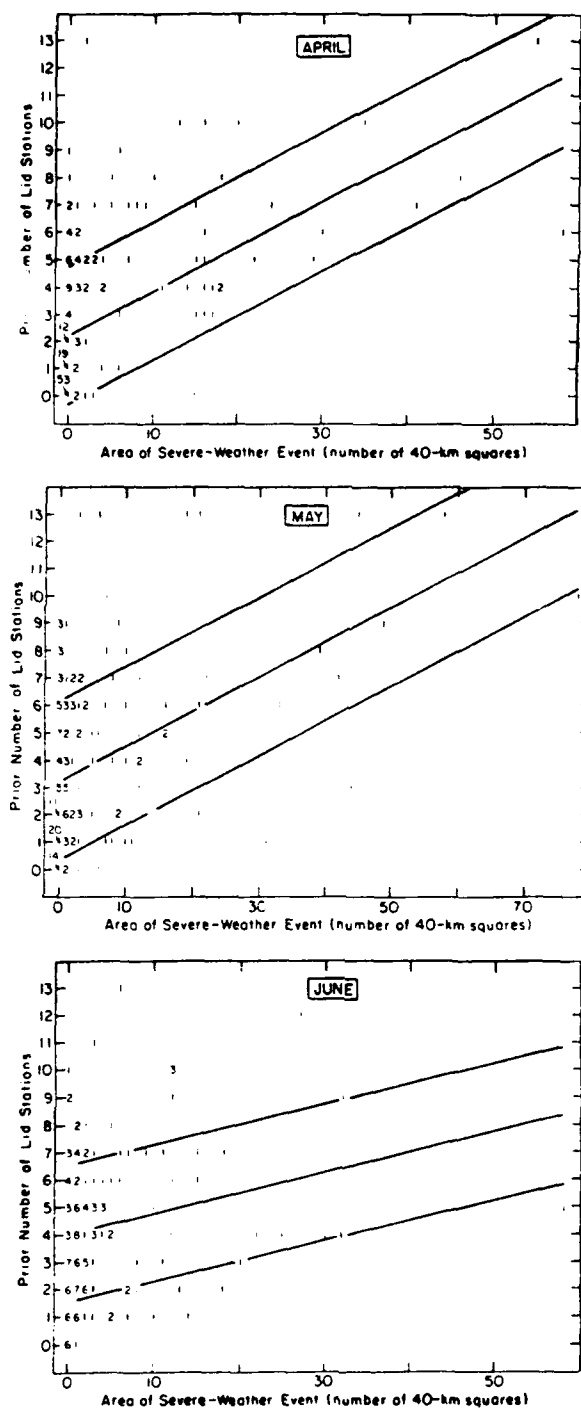


Figure 4.4. Scatter plot showing the antecedent lid coverage (in terms of number of lid stations at either 1200 or 0000 UTC) versus the size of the subsequent severe storm event (given as the number of 40-km squares). Non-event days are given an event size of zero. The numbers on the plot refer to the occurrence frequency. The linear regression line and error bars for one standard deviation are also displayed. Charts are shown for April, May, and June.



indicate that even for the month with the lowest correlation coefficient (June), the  $r$  value is significant at a level in excess of the 99% confidence limit.

A further analysis of the antecedent lid and severe-weather event data was performed in order to examine the relationships between areas exceeding certain threshold values of the lid strength (LS) and buoyancy (BUO) terms of the Lid Strength Index (see section 2.2.1 for definitions of LS and BUO), and the sizes of the ensuing severe weather events. Graziano and Carlson (1987) examined the relationship of deep convective events to the values of LS and BUO, and found a cutoff value for LS, above which the probability of deep convection decreases rapidly. Their critical LS value was uniformly close to  $2^{\circ}\text{C}$  during the months of the analysis (March through August). An analogous critical BUO value equal to  $1^{\circ}\text{C}$  was also found in their study. Since their analysis technique used proximity soundings (see Table 1.1 and the accompanying discussion), no information was available regarding either *antecedent* LS and BUO values or the *areal extent* of each critical values.

We examined the areal extent of severe weather events to the size of antecedent lid areas with  $\text{LS} \geq 4^{\circ}\text{C}$  and  $\text{BUO} \leq -2^{\circ}\text{C}$ . The event sizes were also compared with antecedent lid areas of either  $\text{LS} \geq 4^{\circ}\text{C}$  or  $\text{BUO} \leq -2^{\circ}\text{C}$ , in order to evaluate these parameters separately. The LS and BUO values were chosen to represent both a strong lid and high buoyant instability, respectively. In particular, the BUO value of  $-2^{\circ}\text{C}$  is approximately equal to an LI of  $-4^{\circ}\text{C}$ , which is within the threshold interval for severe thunderstorms (Miller 1972). Consideration of the area with combined LS and BUO values of  $\geq 4^{\circ}\text{C}$  and  $\leq -2^{\circ}\text{C}$  allows

examination of regions with "explosive" convective potential, in which rapid release of the buoyant instability occurs with removal of the strong lid. The results of this analysis are presented in Table 4.1 using the linear correlation coefficients for each category of LS and BUO term threshold area. The results duplicate the downward trend in  $r$  during the spring that was observed for lid size vs. severe-weather event area (also see Fig. 4.4). However, Table 4.1 also shows that the combined LS/BUO threshold is somewhat less useful as a predictive variable than the size of the antecedent lid. This occurs because the size of the area exceeding the LS/BUO threshold was rarely above 3 or 4 lid stations. Not surprisingly, the lowest correlation coefficients are observed for the  $LS \geq 4^{\circ}C$  only threshold, consistent with the idea that a large area of high lid strength is more likely to suppress deep convection (Carlson et al. 1983; Graziano and Carlson 1987). The best indicator (in terms of  $r$  value) of severe-weather event size is the size of the area with  $BUO \leq -2^{\circ}C$ . This result, while not altogether surprising, is significant because our examination was *limited to areas that had a lid*, and suggests that forecasters should look for areas of  $BUO \leq -2^{\circ}C$  *within* the lid-coverage area when evaluating the potential for deep convection. Table 4.1 shows that the buoyancy term threshold area works better than the other predictors even in June, although the  $r$  value has dropped considerably from that of May.

There are two points related to the previous analyses that should be mentioned. First, while the results show that there is far from a one-to-one relationship between the area of favorable static stability (lid) and the area of the resulting deep convection, there is an

Table 4.1 Linear Correlation Coefficients Between Severe-Weather Event Areas<sup>1</sup> and Antecedent Lid-Coverage Areas Exceeding Certain LS and BUO Threshold Values

	<u>April r-value</u>	<u>May r-value</u>	<u>June r-value</u>
Lid area size	.52	.46	.27
LS $\geq 4.0$ and BUO $\leq -2.0$	.48	.41	.27
LS $\geq 4.0$ only	.43	.32	.24
BUO $\leq -2.0$ only	.54	.53	.32

<sup>1</sup> Areal extents of LS and BUO threshold values were also computed for non-event days using the same method as in Fig. 4.4.

important implication in the large-lid-area/small-severe-weather-area portion of the scatter plots of Fig. 4.4. That is, large areas of potential instability generated by the lid are not always consumed by large outbreaks of deep convection. This is important because the EML and moist layer can thus migrate to other regions such as the Ohio River valley and Great Lakes, where they may create the necessary stratification for a lid sounding (Doswell et al. 1985). This situation apparently existed during the period preceding the 31 May 1985 tornado outbreak over the northeast U.S. and southern Ontario (Farrell and Carlson 1989). The second point involves the existence of multiple-event days during the period of study. Sometimes, separate events of different sizes occurred during the same day, and according to our analysis scheme each event could be associated with the same antecedent lid size. When the multiple events with the same antecedent lid-coverage area were combined, the changes in the values of the correlation coefficients in Table 4.1 ranged from  $-.01$  to  $+.08$ . In the following sections, the examination of the relationships between the occurrence of the lid and severe weather is explored using the conceptual model of the lid life cycle defined in LW2. In this approach, the severe-weather events are compiled over 24-h periods, largely eliminating the problem of multi-event days by combining them.

#### 4.4 Relationships Between the Lid, Severe Weather, and Representative Synoptic Flow Types

##### 4.4.1 Severe Weather Associated With the Lid cycle

The study of LW2 shows that there are two types of lid cycles, defined on the basis of the surface type that begins the cycle. The first cycle, designated H, begins with a surface high-pressure incursion into the southern Plains with no low level moist layer or EML present aloft, and is mostly associated with baroclinic waves in the westerlies. The second cycle, designated R, begins with an already established moist layer in a persistent return flow from the Gulf of Mexico, but with no EML aloft, and is associated with subtropical anticyclones and the passage of weak midtropospheric short wave features. In LW2, the spring season was divided into an early and late portion, with a dividing date of 15 May. The early spring is dominated by the H cycle, while the late spring contains both H and R cycles. For the purposes of this study, we keep this seasonal division and consider the relationship between the lid coverage and subsequent severe weather for three types of lid cycles: the early-season H, the late-season H, and the late-season R cycles. Since the cycles are defined on the basis of the 1200 UTC data, the lid-area coverage at this time is used and severe-weather event coverage during the subsequent 24-h period is documented.

The scatter plot of the lid-coverage area versus the subsequent severe-weather event coverage for each phase of the early-season H cycle is shown in Fig. 4.5. See Table 3.1 for formal definitions of the phases of the lid cycle. Also, note the nonlinear scale used for the severe-weather area. As expected, the high-pressure stage is mainly

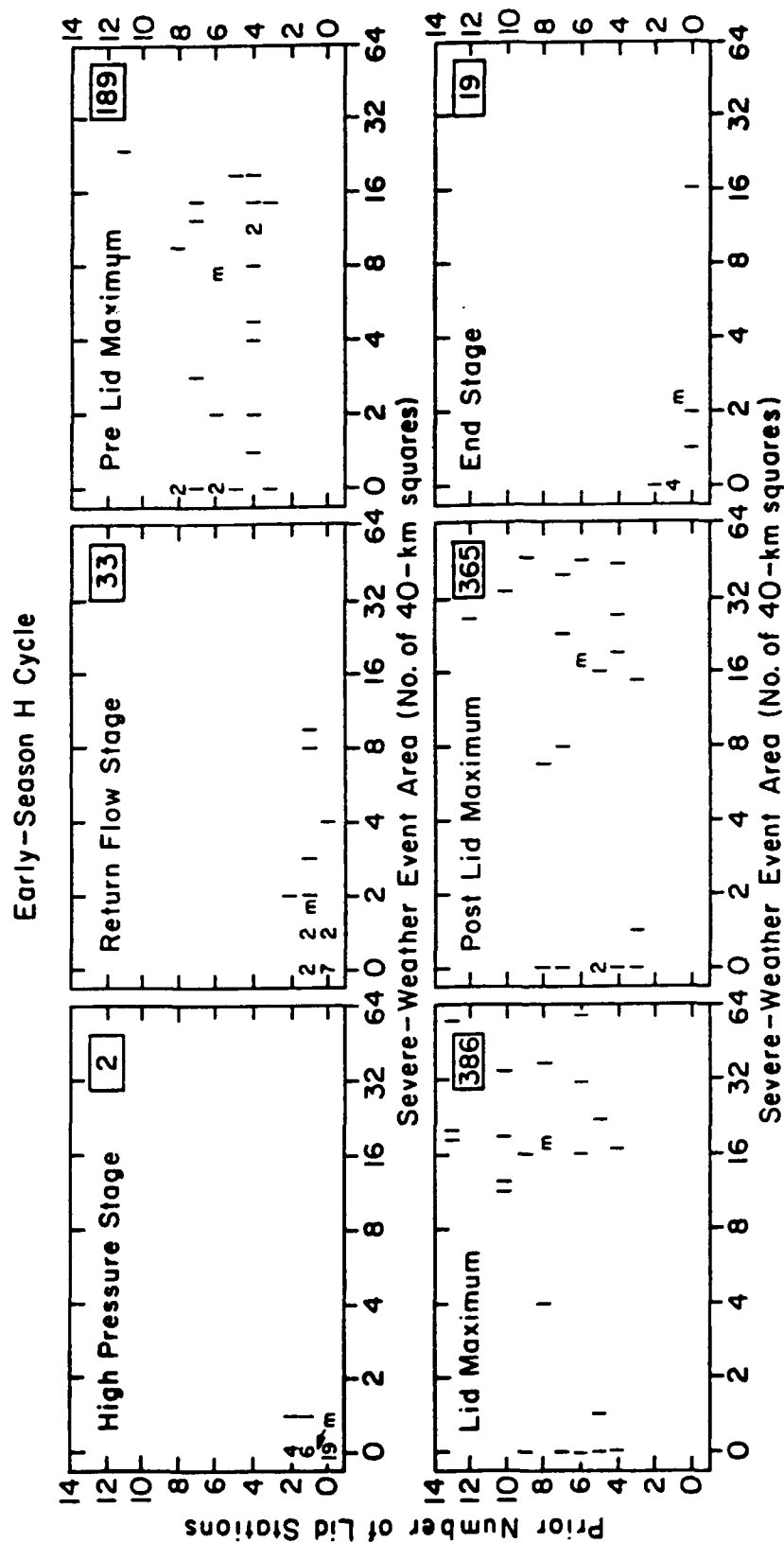


Figure 4.5. Scatter plot showing the 1200 UTC lid coverage (in terms of the number of lid stations) versus the subsequent severe-storm event(s) area for the following 24-h period (given as the number of 40-km squares in log base 2 coordinates on the abscissa) for each stage of the early-season H lid cycle. The numbers on the plots refer to the occurrence frequency. Non-event days are given an event size of zero. An "m" denotes the mean lid/severe-weather event coverage for each phase of the lid cycle. Total number of event squares for each stage is shown by an inset on each panel.

associated with small-lid/small-severe-weather-event areas. When the return-flow stage is reached, there are a few occurrences of larger severe-weather events, which are linked to the subsequent transition between small and large lid-coverage areas. In the pre-lid-maximum stage, there is an increase in both lid and severe-weather coverage areas, but there are still quite a few occurrences of a large lid area with a small or no severe-weather event area. The occurrences of large lid areas with small severe-weather event areas in this phase account for some of the scatter in the upper left portion of the monthly lid/severe-weather plots of April and May (Fig. 4.4). It is not until the lid-maximum and post-lid-maximum stages are reached that the relationship between large lid-coverage area and large severe-weather, event area becomes better defined, as noted by the way the data clusters in the large-lid-area/large-severe-weather-event range in Fig. 4.5. Observe from Fig. 4.5 that the severe weather activity peaks during these two stages of this lid cycle.

The next scatter plot is for the late-season H cycle, and is shown in Fig. 4.6. There is more severe weather occurring during the high-pressure stage than there was earlier in the season. Keep in mind that there is more low level moisture available over the southern Plains in late spring, as shown by LW2's late-spring composite mean analysis for the high-pressure synoptic type (Fig. 3.6a). This seasonal increase becomes more noticeable in the return-flow stage where there are frequent occurrences of severe weather with small-lid coverage areas, which again accounts for a great deal of the scatter in the monthly lid/severe weather plots for May and June (Fig. 4.4). Observe in Fig.

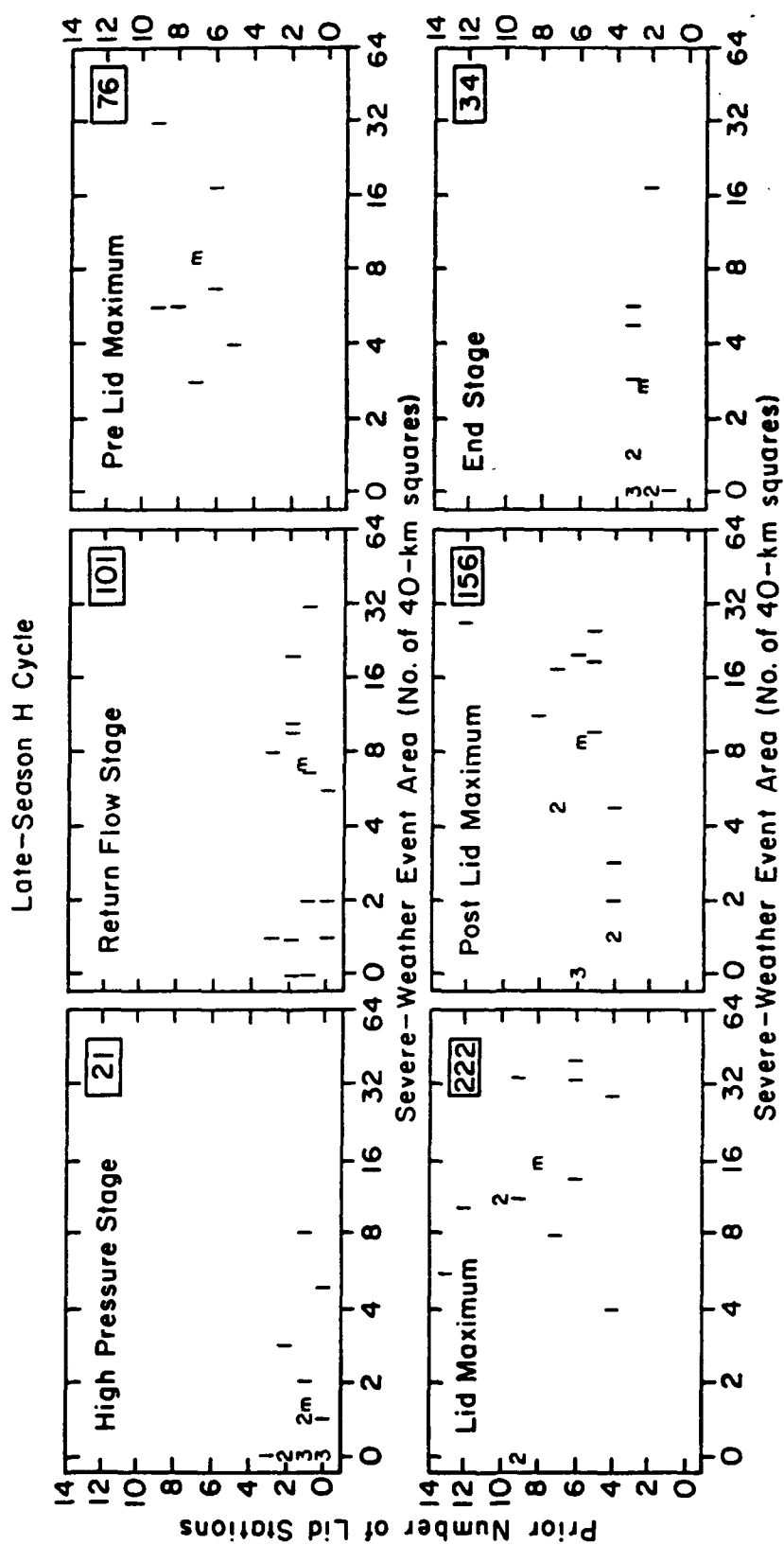


Figure 4.6. Same as Fig. 4.5, except for the late-season H lid cycle.



4.6 that there are relatively few occurrences (7) of the pre-lid-maximum stage in the late-season H cycle, suggesting that transition to lid-coverage maximum sometimes occurs directly from either the high-pressure or return-flow stages. This rapid transition occurred in only four of 19 early-spring H cycles, but was observed in eight of 11 late-season H cycles. Two possible reasons for the transition from the high-pressure/return-flow stages directly to the lid-coverage-maximum stage in the late-season H cycle are the presence of abundant low level moisture early in the cycle and the existence of multiple EML source regions.

Figure 4.7 shows the lid and severe weather relationship during the R cycle. The severe weather events in this cycle are observed with a large range of lid-coverage areas, and are typically associated with between one and three lid stations in the return-flow and end stages, and between four and seven stations in the large lid-coverage stages. Again, there are relatively few (5) occurrences of a pre-lid-maximum stage, and examination of the observations shows that a rapid transition from the return-flow stage to lid-coverage maximum occurred in eight of 11 late-season R cycles. Since both the late-season H cycle and the R cycle are characterized by the presence of multiple EML source regions and large areas of low level moisture, it seems plausible that these factors allow for the rapid transitions in lid coverage to occur.

#### 4.4.2 Lid and Severe Weather Occurrence for Representative Synoptic Types

LW2 showed that definable lid cycles encompassed over 80% of all days in the study period. We use frequently occurring synoptic types to

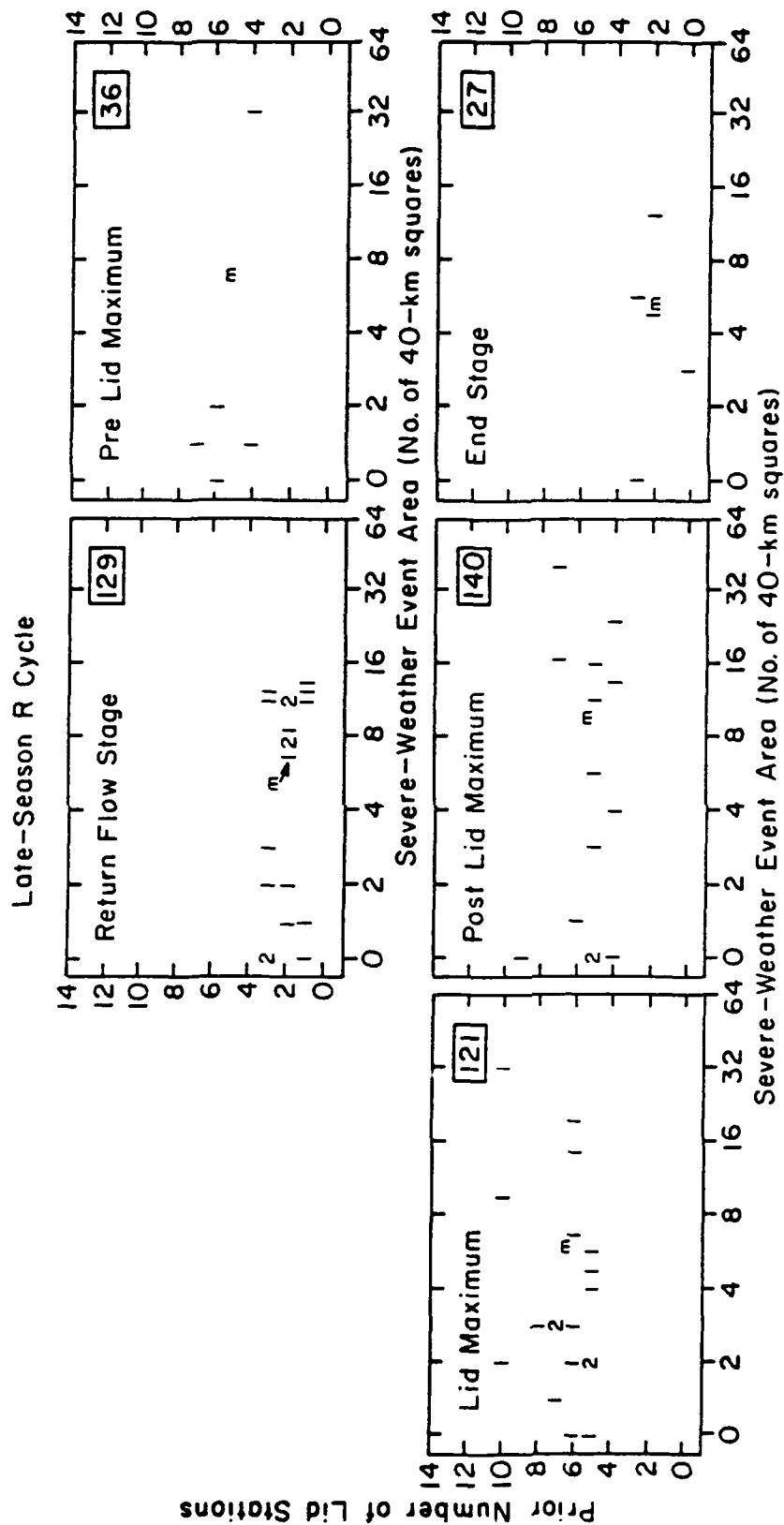


Figure 4.7. Same as Fig. 4.5, except for the late-season R lid cycle.

represent specific phases of the lid cycle. These subjectively determined synoptic types were defined in LW1. To summarize, a synoptic type consists of a surface component based on the sea level isobaric pattern, and a 500-mb component based on the predominant wind direction over the study region. LW2 presented composite mean analyses of relevant atmospheric variables for these synoptic types and related them to geographic frequencies of the EML and buoyant instability. The criterion for buoyant instability used in this analysis is a value of the buoyancy term of the Lid Strength Index of less than  $0.5^{\circ}\text{C}$ , while the procedure for determining the presence of an EML is related to the temperature and dewpoint profiles, and is described in section 2.2.1. Summary charts of specific meteorological features from LW2's composite mean analyses are produced, and include the geographic frequencies of the EML and buoyant instability. Tabulated severe-weather events during the 12-h period following the observed synoptic type are then added to the summary charts in order to relate the geographic distribution of severe weather to the various dynamic and stability features. Areas where the geographic frequencies for the EML and buoyant instability are both greater than 50% can be regarded as lid occurrence areas, since the lid sounding, by definition, must have both buoyant instability and an EML. The reason for distinguishing between the two components (EML and buoyant instability) is to examine the independent evolution of the EML and moist layer, understand how a lid area is created (and destroyed) during a lid cycle, and understand how this evolution impacts the occurrence of severe weather. Use of geographic frequencies for EML and buoyant instability occurrence is preferable to calculation of mean

values for parameters such as lid strength. The lid strength term (defined in section 2.2.1) is only useful in this study when a sounding has an inversion and EML aloft. Since a 100% lid-coverage area does not exist for each day of a synoptic type sample, rawinsonde stations would have different sample sizes going into the calculations of the mean, which would lead to spatial incoherence in a small sample such as a synoptic type composite. To illustrate the large seasonal contrasts in synoptic scale circulation patterns and in the lid coverage vs. severe weather areas, analyses are presented for the early-season H and late-season R cycles.

The first set of summary charts for the early-season H cycle is shown in Fig. 4.8. Figure 4.8a contains the legend for these charts and those in Fig. 4.9. Figure 4.8b shows the frequencies of severe weather, EML, and buoyant instability, as well as relevant meteorological features, for the synoptic type representing a north-south surface ridge with northwest flow aloft. This unfavorable lid-producing pattern represents the high-pressure stage of the cycle, and there are only isolated areas with greater than 50% frequency of either an EML or buoyant instability, and only one severe weather event, over southwest Texas. This particular event occurred on 8 May 1983 and was associated with a strong intrusion of low level moisture through the Rio Grande valley, lid soundings over Del Rio and Brownsville, Texas, and a short wave trough moving through the subtropical jet across northern Mexico.

The return-flow stage is represented by weak return flow with anticyclonic flow aloft (Fig. 4.8c). In this composite analysis, there is evidence of two separately emerging EML areas over Nebraska and

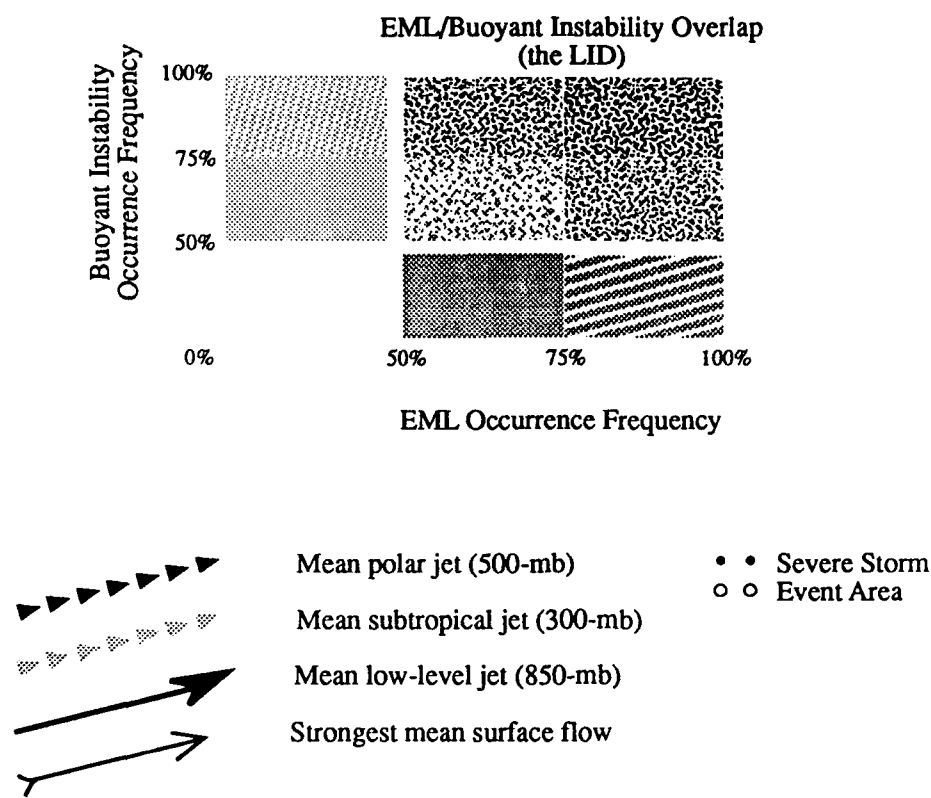
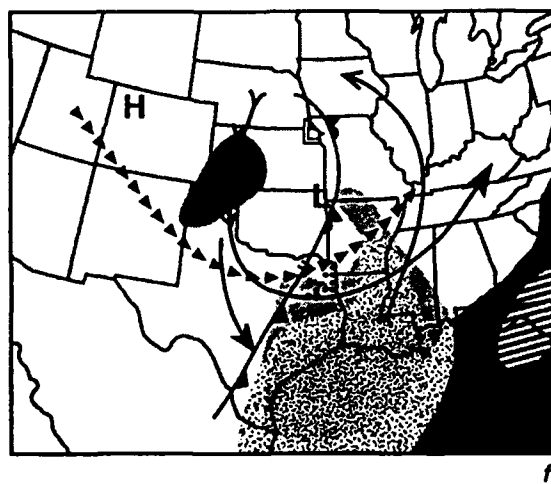
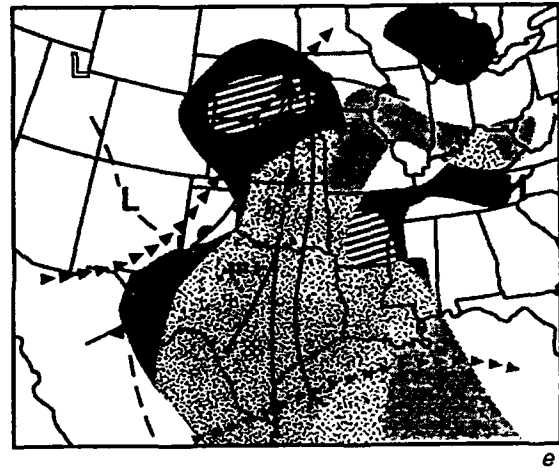
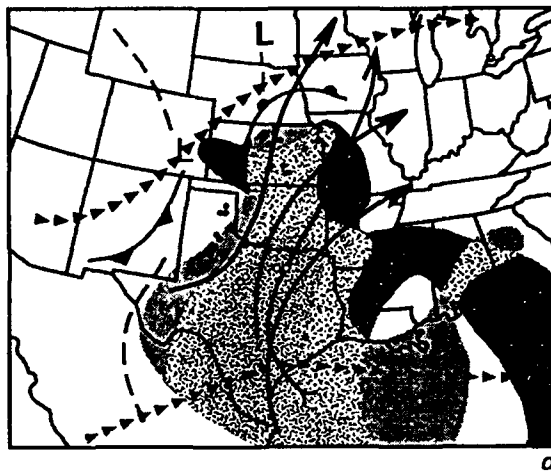
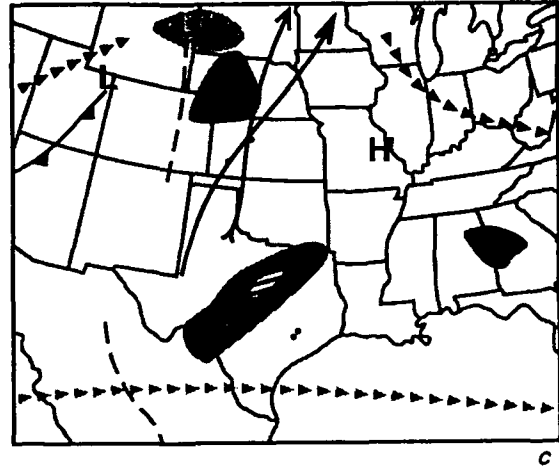
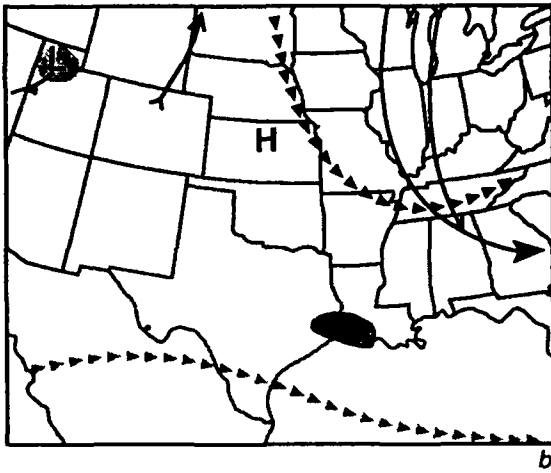


Figure 4.8

Composite mean analyses of key meteorological features at 1200 UTC and subsequent 12-h severe-weather event areas for representative synoptic types during the lid cycle. A legend is shown in panel (a). Charts are shown for the following synoptic types representing various stages of the early-season H lid cycle: b) N-S pressure ridge with northwest flow aloft, representing the high-pressure stage; c) weak return flow with anticyclonic flow aloft, representing the return-flow stage; strong return flow with southwest flow aloft, representing both d) the-pre-lid-maximum stage, and e) the lid-maximum stage; and f) frontal passage with cyclonic flow aloft, representing the post-lid-maximum stage.



Texas. These areas may have separate origins over the central Rockies and desert southwest, respectively. Isolated severe weather is observed with the two EML areas over portions of Kansas and southeast Texas. In these first two stages of the early-spring H lid cycle, there is little relationship between the geographic frequencies of the EML, buoyant instability, and severe weather, due to the isolated nature of each feature early in the cycle.

In the pre-lid-maximum stage, represented by strong return flow with southwest flow aloft (Fig. 4.8d), there now is a considerable overlap in the high frequency areas of the EML and buoyant instability over the study region, meaning that the lid frequency is also high. The interpretation of the lid areas in these composite mean analyses must be made with great care. Although the charts are stratified by synoptic type, some "within-type" variability is present, so the mean locations of features such as jets, fronts, highs, and lows should be considered to be *representative* of the general pattern. Note that the overlap in the 50% frequency of the EML and buoyant instability regions can be interpreted as the lid edge in a mean statistical sense. Also, the locations of severe weather areas in relation to the statistical lid edge at 1200 UTC can be considered as generally representative of the initial areas of deep convection, since the lid area can obviously change location during the 12-h period. It is more helpful to compare these features in adjacent stages in order to search for a consistent temporal evolution of the mean synoptic pattern through the lid cycle. The severe-weather events in this stage generally appear either to the west of, or along the lid-edge zone over Oklahoma and Texas, and to the

north of, or along the northern lid-edge zone in Kansas. The deep convection that is observed near the western lid-edge zone is probably associated with the dryline, while convection along the northern lid edge occurs in proximity to the mean LLJ and its associated moist axis. Notice the beginning of a weak area of upper level diffluence between the mean polar and subtropical jets. This feature was also observed in a satellite composite study of severe storm outbreaks by Whitney (1977). His study noted that the region between the two jets is favorable for deep convection due to the combination of upper divergence to the north of the subtropical jet and low static stability in the same area.

As the cycle moves into the lid-maximum stage, there are several notable changes, even though the same synoptic type (strong return flow with southwest flow aloft) is used to construct the composite (Fig. 4.8e). First, over Texas and southwest Oklahoma, the mean lid edge is located farther west than in the previous stage. This shift is consistent with the stronger moisture and thermal gradients appearing in this pattern as the low and upper level flows strengthen. Despite a westward "shift" in the mean lid edge over Texas and Oklahoma, a great deal of severe weather occurs farther east than in the previous stage, much of it within the lid's interior (especially over Texas). At this stage, the surface frontal system and upper level trough have started to move into the study region, and a stronger veering wind shear is present over the southern Plains, favoring the development of severe thunderstorms. There is stronger diffluence between the mean polar and subtropical jets over Texas, which may contribute to the increase in severe weather observed over west central and southern Texas in this



stage of the cycle. The resulting strong vertical motion helps lid-edge convection to develop and weakens the lid interior, allowing convection to develop near the low level moist tongue.

The post-lid-maximum stage is represented by the frontal-passage/cyclonic-flow aloft synoptic type, and is shown in Fig. 4.8f. This composite illustrates the situation after the EML source region has been cut off, and the main EML and buoyant instability areas are to the east of the southern Plains. The lid edge over eastern Texas is parallel to the frontal zone, and the majority of the severe weather activity is located away from the lid edge over northeast Texas in a region of unstable air and strong frontal lifting. Judging by the location of the intersection of the maximum lid frequency axis, the LLJ, and the upper level jet, the severe-weather events are likely to migrate into the lower Mississippi valley during the following 24 h.

The EML, buoyant instability, and severe weather frequency areas for the late-season R cycle, shown in Fig. 4.9, are vastly different from those in the early-season H cycle. The return-flow stage is represented by weak return flow with anticyclonic flow aloft, shown in Fig. 4.9a. Note that there is considerable buoyant instability over the study region, mostly due to the presence of abundant low level moisture (see the composite mean analysis in Fig. 3.7a). Recall that a well established moist layer throughout the cycle is one of the most important distinctions between the H and R lid cycles. The locations of the mean LLJ and 500-mb jet suggest that they represent the western branch of the Bermuda anticyclone. The 500-mb jet also reflects the confluence of the subtropical airstream with the zonal polar jet to the

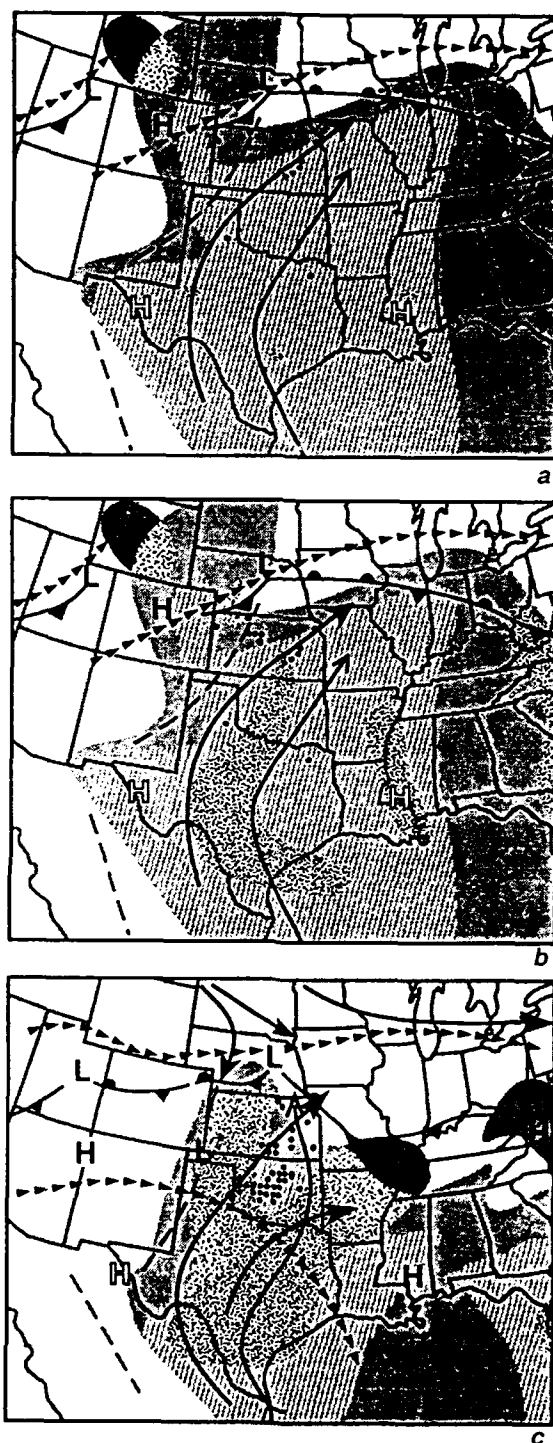


Figure 4.9. Same as Fig. 4.8, except for the late-season R lid cycle. Charts are shown for the following synoptic types and cycle phases: a) weak return flow/anticyclonic flow aloft (Bermuda high dominant), representing the return-flow stage; b) the same as panel (a) except that the geographic frequency composite includes uncapped, EML, and subsidence-layer soundings; and c) weak return flow/anticyclonic flow aloft (Pacific high dominant), representing the large lid-coverage stages.

north. There is much more severe weather activity in this stage of the R cycle than there was in the early stages of the early-season H cycle (Fig. 4.8c). The severe weather activity observed at this stage is not associated with high frequencies of EML/lid occurrence at the analysis time. This result is consistent with our previous observations regarding the deterioration of the relationship between the antecedent lid coverage and severe weather in the late spring. We examined the possibility that other types of soundings may be playing a role in this synoptic pattern. Analysis of the individual days making up this synoptic type sample shows that severe weather occurred in an environment that contains other types of soundings besides the lid type. These included uncapped (zero lid strength) soundings and subsidence-type soundings that were buoyantly unstable. The importance of the uncapped soundings lies in their contribution to both midlevel potential instability and low level buoyant instability due to high lapse rate air in the EML. The subsidence-layer soundings contribute to the low level instability by capping the moist layer. Figure 4.9b shows the same composite analysis as Fig. 4.9a, except that the geographic frequency composite now includes EML, uncapped, and subsidence soundings. The orientation of the maximum frequency axis of EML, uncapped, and subsidence soundings with the western branch of the Bermuda cell suggests that this dry midlevel air probably originates in the easterly flow over the Gulf of Mexico, and is then transported northward into the Great Plains. Studies by Caracena and Fritsch (1983) and Hagemeyer and Darkow (1988) for cases which resemble this synoptic type, demonstrate the importance of such a dry-air intrusion for generating potential

instability, and, subsequently, severe storms when the low level moist air is lifted. From Fig. 4.9b, several features capable of providing such a lifting mechanism can be identified, such as the mean LLJ, the frontal boundary over Nebraska, and the surface trough over the western Plains. It is possible that the area between the mean surface trough and LLJ may experience upward motion from a combination of the cyclonic horizontal shear to the west of the LLJ and the cyclonically curved surface flow to the east of the trough. This general area also has a strong gradient of buoyant instability frequency. Thus, at this stage of the R cycle, in this synoptic type, the presence of several different types of soundings can be important in locally generating potential instability in a region of low-level convergence and abundant moisture.

The large lid-coverage stages are also represented by weak return flow with anticyclonic flow aloft (Fig. 4.9c). However, this synoptic pattern is associated with the Pacific anticyclone, as discussed by LW2 (see Fig. 3.7b). The severe weather in this pattern is clustered to the east of a lid-edge zone over the western Plains, between two mean LLJ axes in a region of strong directional shear between the low levels and 500 mb. Of particular note is the strong directional shear between the surface and 850 mb. This type of strong directional shear in an area of high buoyant instability is characteristic of late spring and summertime severe storm environments (Johns and Sammler 1989, Davies 1989). In this synoptic pattern, a short wave trough often travels along the zonal polar jet into the western Plains, then turns southward along the eastern branch of the Pacific ridge, with a frontal system following it into Oklahoma and northern Texas. The subsequent movement of the short

wave trough out of the study region causes the EML to be transported eastward, and returns the Great Plains to minimum lid coverage, ending the R cycle.

#### 4.5. Conclusions

This study examined the relationships between the occurrence of severe storms over the southern Great Plains, the occurrence-frequency patterns of the EML and buoyant instability, and the occurrence of various representative synoptic flow types. The analysis emphasized the temporal dimension by investigating these relationships during the life cycle of lid development and dissipation. One unique aspect of this study is the inclusion of the non-event days in the analyses, which allows examination of the relationships for these situations as well.

The analysis of the severe-storm events for the four-year period over the southern Plains found that the size distribution of severe-storm events has a large peak in the 1600 km<sup>2</sup>, or "isolated event," category for each month. In April, there is a secondary peak for event sizes on the order of 20,000-25,000 km<sup>2</sup>, and in June a secondary peak is between 14,500 and 19,000 km<sup>2</sup>. In general, the size distribution of severe-weather events remains essentially the same during the season, except for a sharp increase in isolated-event occurrences from May to June. The occurrence frequency of non-event days shows a steady decrease during the spring from 66 days in April to 22 in June. The geographic distribution of severe weather events shows a gradual shift to the west and north during the spring season, consistent with the

seasonal evolution of lid frequency reported in Farrell and Carlson (1989) and LW1, and the composite mean lid/EML analyses of LW1.

The relationship between the occurrence/size of the lid and the subsequent occurrence/size of severe-weather events is best defined in April, and deteriorates rapidly from May to June. This deterioration is due to the existence of different stability and synoptic patterns in the early spring versus the late spring. Early-spring synoptic patterns are mainly associated with the progression of frontal systems and baroclinic waves in the westerlies. At this time, low level moisture is area-limited and mostly determined through advection. Accordingly, buoyantly unstable areas are also limited (McNulty 1980), while the EML usually has an equal or greater areal extent. The progression of strong baroclinic systems, which controls the evolution of both the limited moisture and EML areas, allows a more certain diagnosis of potential severe-storm activity based on the 1200 UTC analysis and continuity. Late-spring synoptic patterns are dominated by weak persistent return flow at low levels, subtropical anticyclones, and weak short wave troughs which drift through the region. There is widespread low level moisture and buoyant instability throughout the region, both of which have a much larger areal extent than does the EML. The evolution of the EML is mostly determined by the position and intensity of subtropical anticyclones such as the Bermuda and Pacific ridges. When the Bermuda cell is dominant over the eastern half of the U.S., dry midlevel air embedded in the easterly flow over the Gulf of Mexico can be drawn northward in the western branch of the cell, producing isolated dry intrusions which may locally produce areas of potential instability and,

subsequently, severe weather. When the Pacific cell dominates the western half of the U.S., a capping lid is produced over the Great Plains in the westerly flow from EML source regions to the west.

In the early-season H lid cycle, the small lid-coverage phases are associated with small severe weather event areas, while the maximum lid/severe-weather activity occurs in the lid-maximum and post-lid-maximum stages. In late spring, both the H and R cycles are capable of supporting severe weather at all stages, but in the H cycle the maximum activity occurs in the lid-maximum stage. In the R cycle, there is no clear relationship between antecedent lid occurrence/size and severe-weather event occurrence/size. In both late-season cycles, a rapid transition from either the high-pressure or return-flow stages to lid, maximum is observed nearly 75% of the time. In the strong baroclinic systems characteristic of the early-season H cycle, there is a clear geographic relationship between severe weather occurrence and EML/buoyant instability areas. In the pre-lid-maximum stage, the events are observed in the vicinity of and along the western and northern lid-edge areas. During the lid-maximum stage, severe-weather events are observed both along the mean lid edge as well as within the high lid-frequency area. In this synoptic environment, both lid-edge convection and convection associated with a weakened lid interior are observed. An example of such a region is southern Texas, where the upper diffluence to the north of the mean subtropical jet may serve to enhance vertical motion and hasten lid removal.

In late spring, severe-weather events are associated with high frequency areas of buoyant instability, but not necessarily with high

frequency areas of the EML. Examination of the composite mean analyses representing the late-season R cycle shows that when the Bermuda cell dominates, the majority of severe weather occurs between the mean LLJ and surface trough, in a region of low level cyclonic vorticity and weak vertical shear. A buoyant instability gradient and localized areas of potential instability characterize this environment, influenced by the presence of the EML and subsidence layers from the western branch of the Bermuda cell. The analyses representing the period when the Pacific ridge dominates show that the majority of severe weather occurs to the east of the lid edge, in a region of buoyant instability and strong directional wind shear, especially between the surface and 850 mb. In these situations, a short wave trough often moves through the zonal polar jet and travels around the eastern branch of the Pacific anticyclone, moving into the Great Plains and pushing a surface front southward through the region. The eastward movement of the short wave trough across the Plains states subsequently transports the EML out of the region, returning the area to minimum lid coverage and marking the beginning of a new lid cycle.



## Chapter 5

## AN EXAMPLE OF AN EARLY SPRING LID CYCLE

The period of 4-9 April 1984 was chosen as an example of an early-season H lid cycle over the southern Great Plains. This lid cycle contained four of the synoptic types documented in the synoptic climatology of Chapters 2-4; extensive lid areas on 7 and 8 April; and severe-weather outbreaks over Texas and Oklahoma on 7 April, and over Arkansas, Louisiana, and Mississippi on 8 April. These features make this a good case with which to examine certain aspects of the synoptic climatology and the early-season H cycle conceptual model discussed in Chapters 2-4.

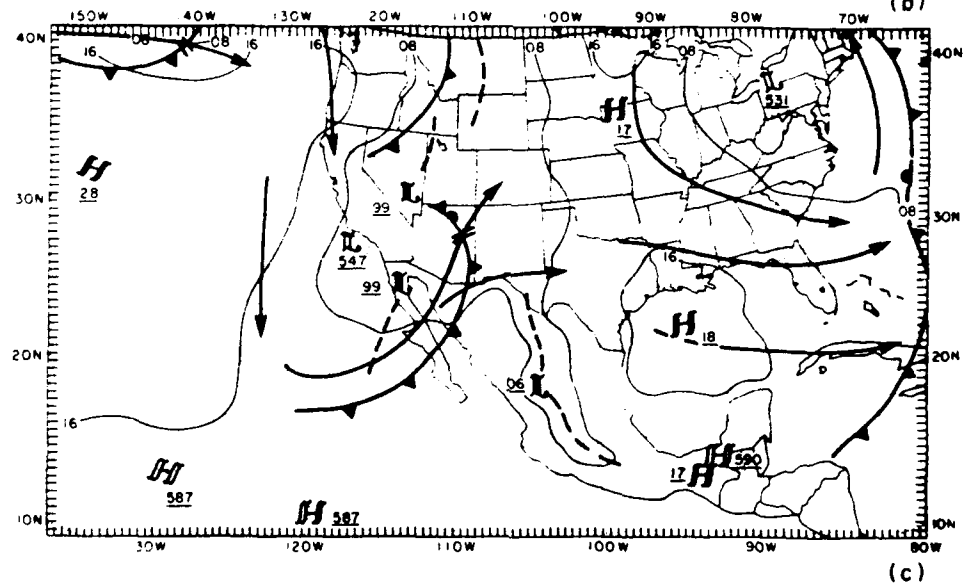
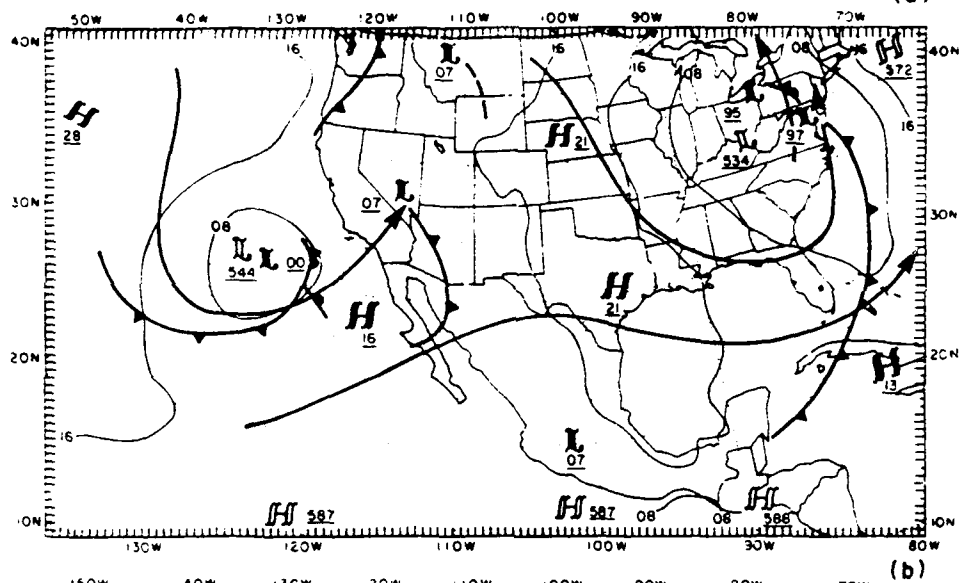
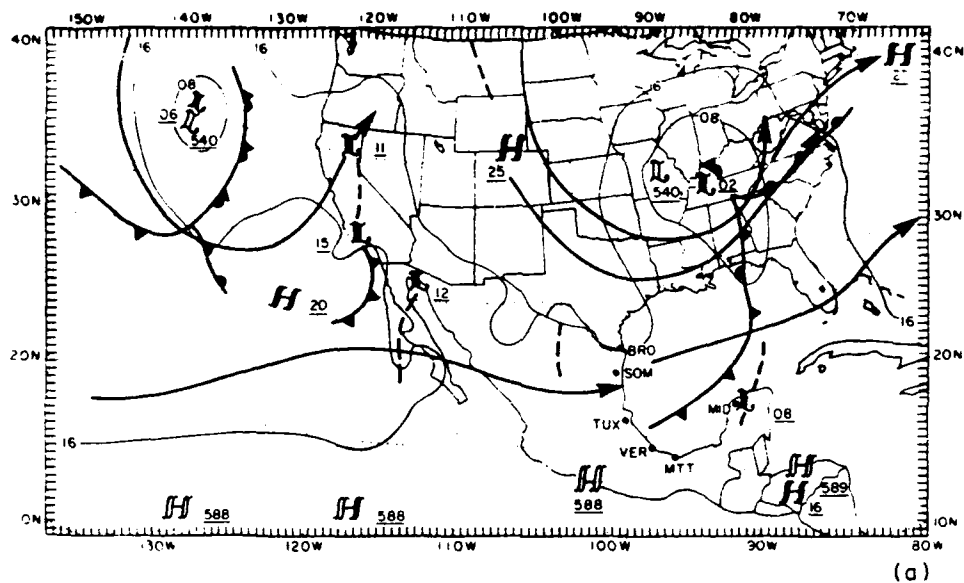
5.1 Overview of the 4-9 April 1984 H Lid Cycle

A summary of the major atmospheric features at 1200 UTC on each day of this five-day period is shown by the series of analyses in Fig. 5.1. The discussion of these atmospheric features is followed by a summary of the severe weather and heavy rainfall associated with the large lid-coverage stages of the cycle over the southern Great Plains and Mississippi River valley on 7 and 8 April.

At 1200 UTC 4 April (Fig. 5.1a), the initial time of the lid cycle, an extratropical cyclone with a central pressure of 1002 mb was located over western Kentucky. The associated frontal system was moving through the central Gulf of Mexico. Behind the system, a surface pressure ridge was expanding southward into the Great Plains. The high was centered



Figure 5.1. Analysis of surface and 500-mb features at 1200 UTC on each day of the 4-9 April 1984 lid cycle. The 1016 and 1008-mb sea level isobars are shown by the thin lines, and the thick lines with arrows denote the subjectively analyzed 500-mb jets. Surface fronts, troughs, highs and lows are shown using conventional notation. Locations of 500-mb highs and lows are shown using "open" lettering. The locations of the stations used in the time series of Fig. 5.3 are shown in panel (a). On panel (d), the position of the surface dryline is shown using a solid, scalloped line. Analyses are shown for a) 4 April, b) 5 April, c) 6 April, d) 7 April, e) 8 April, and f) 9 April.



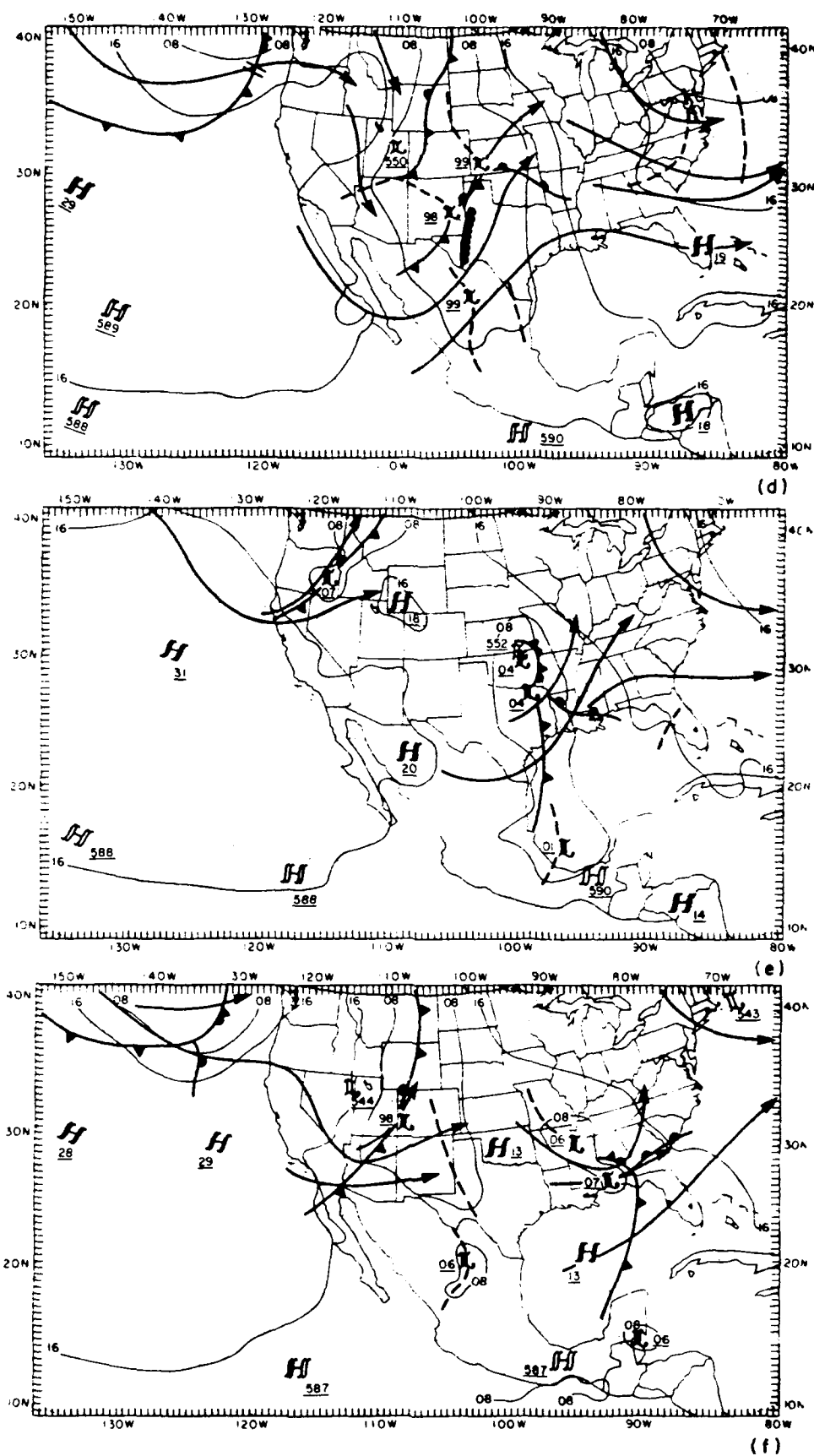


Figure 5.1. (Continued)

over northern Colorado, with a central pressure of 1025 mb. In the midtroposphere, a cut-off 500-mb low was located over Missouri. A cyclonically curved jet was analyzed from the Great Plains to the middle Atlantic states and the Appalachian Mountains. Evidence of a subtropical jet (which will be discussed in more detail later in this chapter) at this level was found from near 20°N latitude, 135°W longitude, through the southern Baja Peninsula, and into central Mexico. A continuation of the subtropical jet was analyzed from the southern Gulf to east of the south Florida coast. A 500-mb ridge was located to the west of the Continental Divide, and a deepening trough was centered near 130°W longitude.

By 5 April (Fig. 5.1b), the surface cyclone had moved into the Appalachian Mountains and middle Atlantic states, while the continental high spread into the southern Plains and western Gulf. The 500-mb ridge was located over the Continental Divide, and the next trough and frontal system were entering the southwestern states. There were actually two fronts associated with this upper trough. The first front was moving through Arizona and Sonora, Mexico, while a second, occluded system was approaching southern California and Baja. To the north of these two systems was another front moving through the Pacific Northwest. This system was associated with an upper level trough which had split with the primary polar jet stream near 135°W longitude.

As the cycle moved into its third day (6 April; Fig. 5.1c), several changes took place. The surface anticyclone which dominated the Great Plains and Gulf of Mexico weakened considerably, with only a small

1018-mb high remaining over the western Gulf, near 27°N latitude, 92°W longitude. Sea-level pressures were falling over the Rockies and northern Mexico during this time, and a surface trough appeared over northern and central Mexico. The two frontal systems that entered the southwestern states on the 5th "merged" to become a single system, and now moved through Arizona and northwestern Mexico. A deep 500-mb trough entered the Desert Southwest during this time, and southwesterly flow was observed over most of this region at 1200 UTC. The northern frontal system continued to move eastward through Montana, Idaho, and Nevada on the 6th.

Further changes occurred as the lid cycle moved into the large lid-coverage stage on the 7th (Fig. 5.1d). The frontal system located over the Desert Southwest on the 6th moved through the Rockies and was emerging into the western Plains on the morning of the 7th. Return flow of moist air from the Gulf began during the day on the 6th and was responsible for the genesis of a surface dryline over west Texas late on the 6th. Strong midtropospheric southwesterly flow was evident over much of the central U.S., with the 500-mb trough position just to the west of the Continental Divide. East of this trough, the 500-mb ridge had strengthened during the previous 24 h, and a strong surface pressure ridge was analyzed from the eastern Gulf into the western Great Lakes. The northern frontal system weakened, and emerged into the Rocky Mountain foothills of Montana, North Dakota, and Wyoming.

The southern Plains frontal system moved through the region on the 7th and began to exit on the morning of the 8th (Fig. 5.1e). The primary surface low was occluded by this time and had weakened to 1004

mb (from 999 mb on the 7th). A second low was located at the point of occlusion (over northeastern Texas), and it also had a central pressure of 1004 mb. The surface cold front had begun to enter the Gulf, and a well-defined warm front extended from the Texas-Louisiana-Arkansas border, through Louisiana, and into the Gulf coastal sections of Mississippi and Alabama. The midtropospheric flow was cyclonic over the southern Plains, as a cut-off 500-mb low moved into southeastern Kansas from Colorado and Utah. Behind the front, surface pressure ridging from the Pacific high was evident over the Desert Southwest and portions of Wyoming, Colorado, and Utah. A new frontal system and upper trough entered the Pacific Northwest during the previous 24 h and were moving steadily across the northwestern U.S.

The last day of this cycle (9 April; Fig. 5.1f) was characterized by anticyclonic flow at the midlevels over the Great Plains, but no strong surface features existed. Weak high pressure centers were located over Oklahoma and the west-central Gulf; both had central values of only 1013 mb. The frontal system and 500-mb trough that had moved through the Plains on the 7th and 8th were now located over the Gulf coastal states and moving toward the southeastern states. The frontal system and trough from the northwestern U.S. were continuing eastward. The surface low was located over western Colorado with a central pressure of 998 mb, and the front extended from eastern Montana into Arizona and northern Baja. A strong jet and deep 500-mb low (544 dm) were associated with the upper trough, and a lee-side surface pressure trough was observed from eastern Colorado into northern and central Mexico. Although there was no dominant anticyclone to transport cold,



dry air into the Gulf in this case, the cold front did have drier air behind it, so lid soundings were not possible over the southern Great Plains at this time. This returned the region to a minimum lid coverage and signalled the end of this lid cycle.

Figure 5.2a depicts the type and extent of severe weather and heavy rainfall during the 24-h period from 1200 UTC 7 April to 1200 UTC 8 April. For a description of the criteria used to define "severe weather" in this study, see section 4.1. During this period, most of the heavy rainfall occurred in western Oklahoma and southeastern Kansas, while the majority of the severe weather was reported in west-central and south-central Texas. The heaviest rainfall totals were in western Oklahoma, with Taloga, Oklahoma reporting 3.08 inches during the 24-h period. The severe-weather outbreak began around 0900 CST (1500 UTC) with isolated wind and hail reports in northwestern and southern Oklahoma. The first severe weather in Texas began shortly after 1000 CST, with reports of tornadoes west of Abilene. This outbreak lasted for about 4½ h and moved into the vicinity of Mineral Wells by mid-afternoon. A second area of severe weather, over south-central Texas, began around 1130 CST with radar reports of line echo wave pattern activity northwest of Del Rio. This outbreak moved eastward over the next 5 h and reached San Antonio. After 1630 CST, only two more severe-weather reports were recorded in Texas; one was in the area of Waco (winds in excess of 50 kt, at 1650 CST) and the other (an F0 tornado, as defined using Fujita's F-scale) occurred early on 8 April (0145 CST) on the outskirts of Jasper (near the Louisiana border).

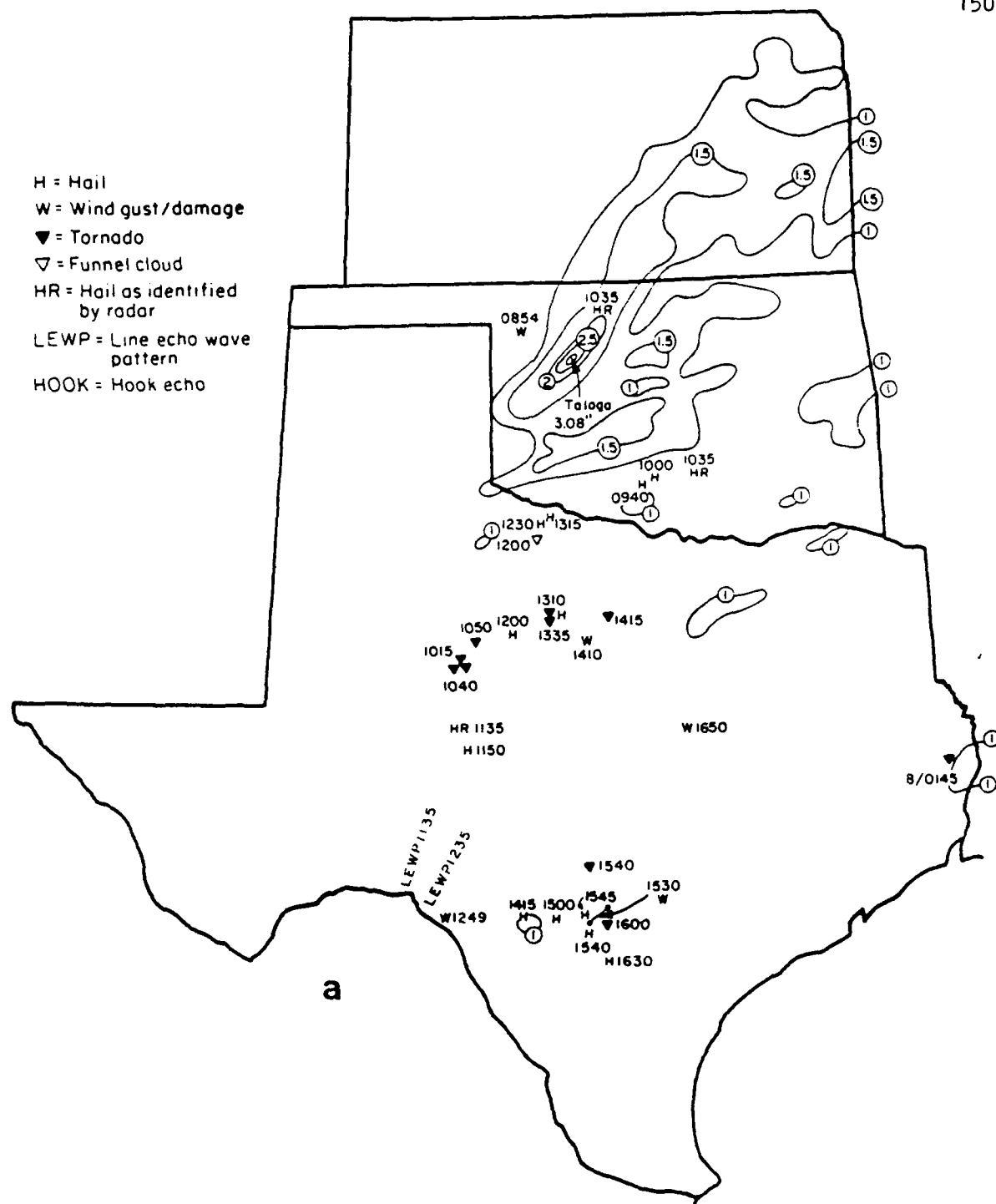


Figure 5.2. Locations of severe weather and heavy rainfall ( $\geq 1$  inch in 24 h) rainfall reported over Texas and Oklahoma from 1200 UTC 7 April to 1200 UTC 8 April (panel 'a'), and over Arkansas, Louisiana, and Mississippi from 1200 UTC 8 April to 1200 UTC 9 April (panel 'b'). Symbols are explained in upper left portion of panel (a). Reports are compiled from the U.S. Department of Commerce publication Storm Data.

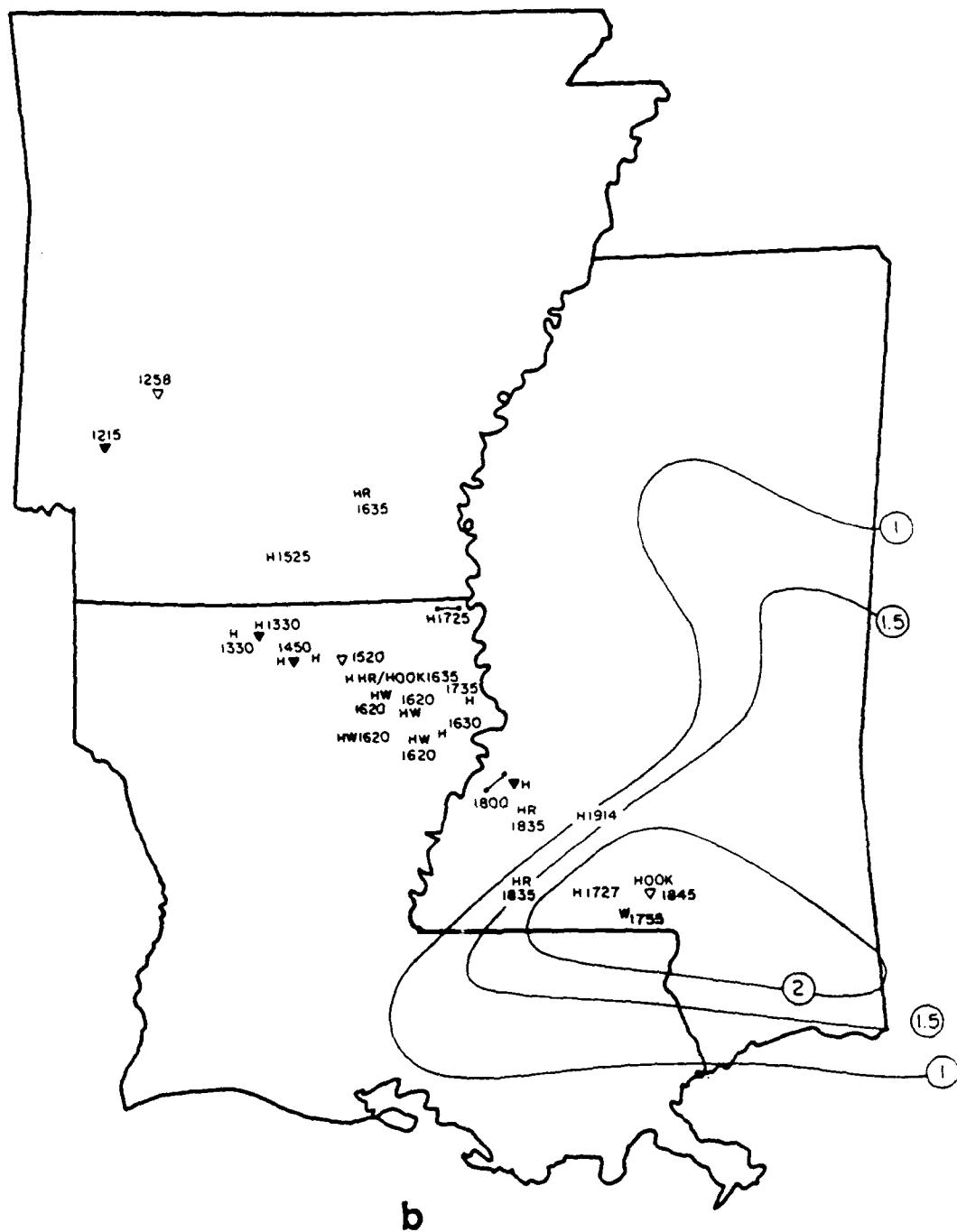


Figure 5.2 (Continued)

The severe weather and heavy rainfall that occurred from 1200 UTC 8 April until 1200 UTC 9 April over Arkansas, Louisiana, and Mississippi, are summarized in Fig. 5.2b. Both severe weather and heavy rainfall were observed over Mississippi during this time, with the heaviest amounts over the southern part of the state, from McComb to north of Biloxi. Severe weather began after 1200 CST over southwestern Arkansas with a report of an F1 tornado in the area of Nashville. Reports associated with this outbreak were isolated over southern Arkansas, but became more widespread as new cells that developed over the southwest corner of Arkansas in the late morning moved into northern Louisiana during the early afternoon. During the next 4 h, there were reports of wind damage, large hail, funnel clouds, and several tornadoes moving in a southeasterly direction through northern Louisiana. New cells developing along the southern Louisiana-Mississippi border during the late afternoon were responsible for the severe weather reported over portions of southern Mississippi from about 1730 CST to 1915 CST. After 1915 CST on 8 April, only heavy rainfall occurred with these thunderstorms as they moved eastward into southern Alabama and the Florida panhandle.

## 5.2 Examination of the Lid Cycle by Stages

### 5.2.1 The High-Pressure Stage (1200 UTC 4 April-0000 UTC 6 April)

This first stage of the 4-9 April lid cycle was characterized by a large surface anticyclone over the Great Plains and western Gulf of Mexico. During the high-pressure stage (see Table 3.1 for definitions

of the cycle stages), cold, dry air moved southward into the southern Plains and Gulf. During the first 24 h of the cycle, a strong north-south pressure ridge developed over the western Plains, and moved into the central Plains while spreading southward into the Gulf. This surface anticyclone originated over southern Canada on 2 April and strengthened under the confluent northwesterly flow behind a midtropospheric trough over the western Plains on 3 and 4 April. Figures 5.1a,b show that the surface ridge strengthened further over the Great Plains during the first 24 h of the lid cycle as the midtropospheric flow became increasingly confluent over the southern Plains and Gulf coast. Cold-air advection was present to the east of the surface ridge axis during this time, which also contributed to the anticyclone's intensification during the first 24 h of the cycle. Cold-air advection is also present in the climatological composite for the high-pressure stage of the early-spring H cycle (Fig. 3.5a); a comparison of Figs. 3.5a and 5.1b shows that the synoptic pattern on the second day of the cycle is similar to the climatological composite, including the extension of the mean surface pressure ridge into the Gulf.

The surface ridge eventually developed as far south as the Bay of Campeche (around 18°N latitude; well south of the subtropical jet) by 1200 UTC on 5 April. The southern extension of the surface pressure ridge seemed to develop independently of the midtropospheric "steering" flow, and resembles the latter stages of a Front Range wintertime cold surge documented by Tilley (1990). The Front Range cold surge is closely controlled by the terrain gradient, and is attributed to

topographically trapped edge waves according to Tilley's study.

Tilley's Front Range case occurred in December 1983, and featured a southward developing pressure ridge along the eastern slopes of the Rockies, accompanied by a narrow surge of cold air. This cold surge and pressure ridging continued to move south along the eastern slopes of the Sierra Madre Oriental range in Mexico. Despite the fact that our case occurred in April, there are similarities between it and this December 1983 case. For example, in the December 1983 cold surge, strong northerly winds were observed with the surge as it moved into Mexico. A time series of Gulf coastal surface station reports from 1200 UTC 4 April to 1200 UTC 6 April, displayed in Fig. 5.3, shows strong northerly winds and blowing dust at Veracruz, Mexico at 0000 UTC 5 April.

Although there is no evidence of a surface cold surge at any of the stations in Fig. 5.3, low level temperature analyses reveal that this cold surge was apparent over the adjacent coastal waters from just above the surface to about 750 mb. A series of 850-mb temperature analyses from 1200 UTC 4 April through 1200 UTC 6 April is shown in Fig. 5.4. The most rapid southward advance of this shallow layer occurs during the first 12 h of the lid cycle, after which time the cold surge continues to move slowly southward, becoming totally detached from the primary cold airmass over the southern Plains. The Gulf cold surge and its accompanying surface pressure ridge reached maximum intensity by 1200 UTC 5 April, and began to slowly dissipate afterward.

The developing surface pressure ridge and low level cold surge are responsible for splitting the moist layer over the western Gulf. As the surface front moved eastward through the Gulf and the surface ridge

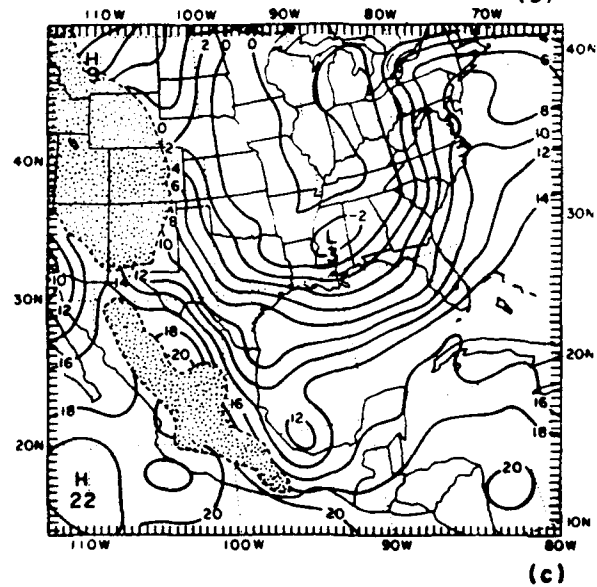
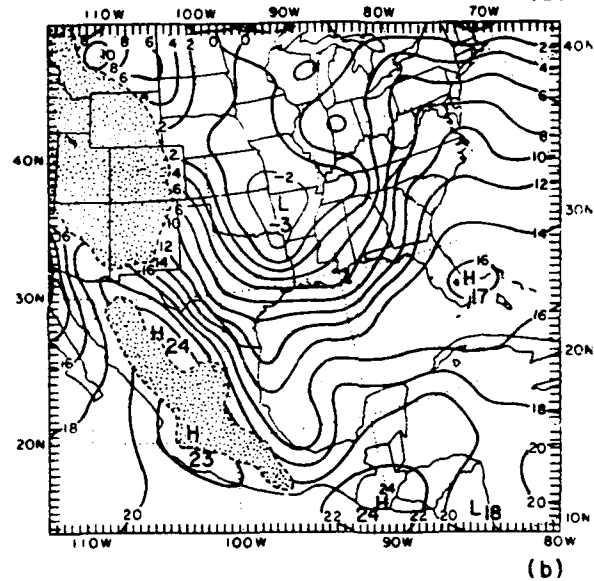
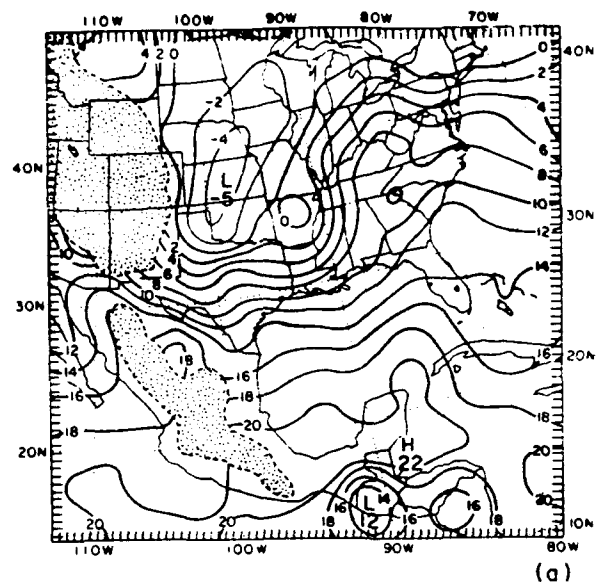
BRO 72250	61 153 76 188 70 166 56 52 5/ 48 7 10/ 53 57 188 53 189 74 203 69 172 63 162 62 144 15 10/ 50 10/ 54 7 53 58 10 59 5
SOM 76499	62 146 82 183 75 176 60 16/ 60 1/ 57 4/ 63 188 82 195 76 163 65 167 66 144 56 8 54 20 60 7 63 7
TUX 76639	68 130 75 159 68 180 80 196 76 160 72 171 67 0 70 4 66 2 75 0 70 10 67 3/ MSG MSG
VER 76692	74 1088 79 124 75 120 74 156 73 150 80 167 77 138 148 72 123 69 10 70 19/ 72 12 69 14 64 4 66 0 66 6 65 2 67 0 72 11 72 7 72 1/ 75 153 81 188 78 167 71 66 5 66 5/ MSG MSG
MID 76670	72 080 78 093 73 134 67 138 77 150 61 153 64 150 70 3 65 17 56 8/ 55 59 4 56 12/ MSG MSG
DATE/TIME (UTC)	4/12 4/18 5/00 5/06 5/12 5/18 6/00 6/06 6/12

Figure 5.3. Time series of surface observations over the Gulf coastal region from south Texas to the Yucatan Peninsula of Mexico, from 1200 UTC 4 April to 1200 UTC 6 April. Stations are listed so they form a counterclockwise arc beginning in south Texas. Stations shown are BRO (Brownsville, Texas), SOM (Soto La Marina, Mexico), TUX (Tuxpan, Mexico), VER (Veracruz, Mexico), MTT (Coatzacoalcas, Mexico), and MID (Merida, Mexico).





Figure 5.4. Series of 850-mb temperature analyses for the following times: a) 1200 UTC 4 April, b) 0000 UTC 5 April, c) 1200 UTC 5 April, d) 0000 UTC 6 April, and e) 1200 UTC 6 April. Isotherms are analyzed every 2°C, and the intersection of the 850-mb level with the ground is shown by the dashed line.



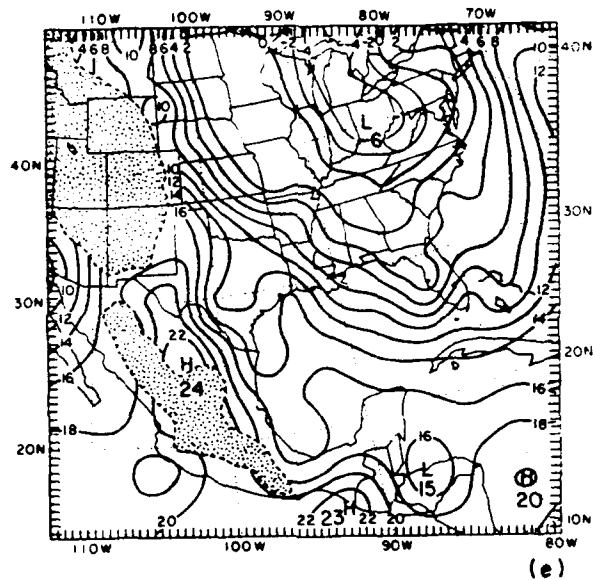
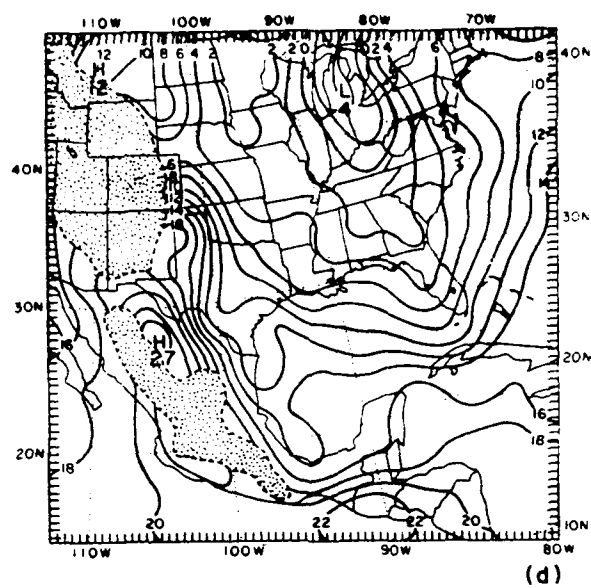


Figure 5.4. (Continued)

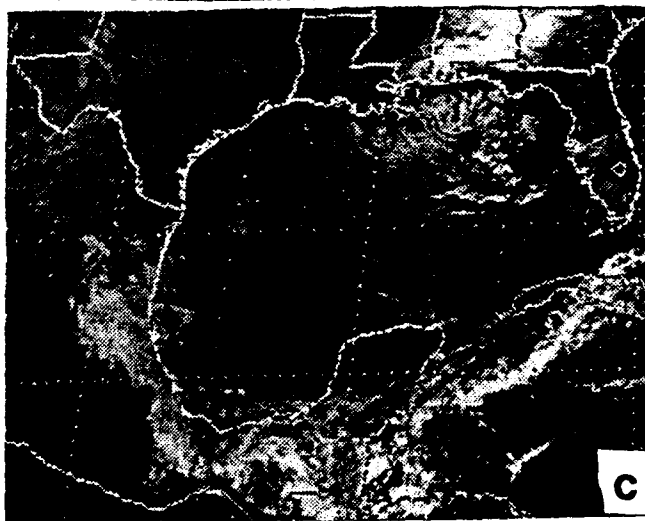
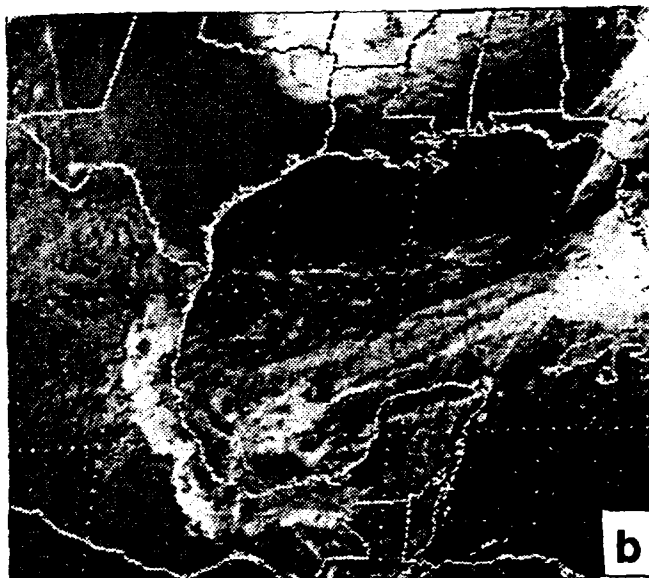
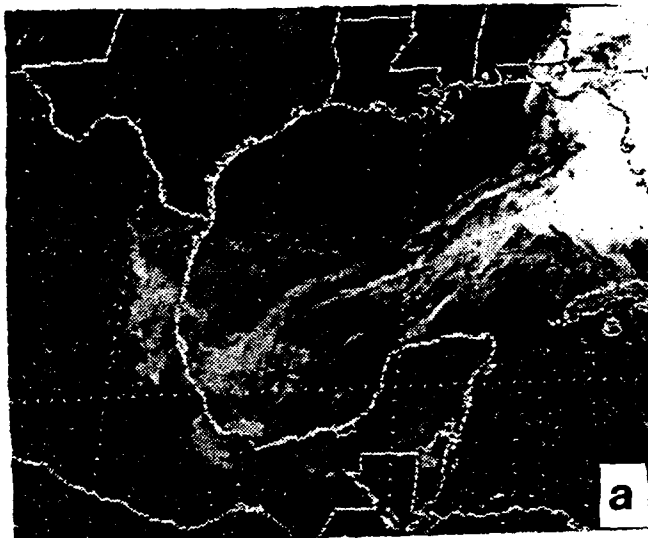
developed southward, the western portion of the moist layer was "trapped" along the eastern Mexican coast and the Bay of Campeche, while the eastern portion of the moist layer was transported by the surface front into the Caribbean. The temporal evolution of the moist layer over the western Gulf is also illustrated in the time series of Fig.

5.3. The time series shows that some low level drying was observed over Brownsville (BRO) and Soto La Marina (SOM) during the day on 4 and 5 April, but south of these two stations, the moist layer remained intact as surface dewpoints consistently stayed in the middle 60's (°F) and lower 70's. Over Merida, the cold frontal passage during the afternoon of 4 April resulted in a dewpoint decrease of nearly 15°F in 12 h. The dewpoints over Merida remained in the mid 50's under a weak northerly flow until after 0600 UTC 7 April. Further evidence of the moist layer remaining over the western Gulf is shown by a series of visible satellite images (Fig. 5.5) for the same period as Fig. 5.3. Notice the persistent area of low clouds along the eastern slopes of the Sierra Madre Oriental. The cloud area appears to follow the topography and actually moves inland slightly on 5 April. The appearance of low clouds along the western Gulf prior to the beginning of return flow has been documented in a study by Karnavas (1978). His study reported that the generation of stratus clouds in this region is a result of long-wave cooling in the modified polar air. Our satellite continuity suggests that upslope flow along the Mexican coast may have generated the cloud area, which grew in size during the daylight hours of 4 April.

According to the conceptual model described in Chapter 3, the high-pressure stage of the lid cycle is also the period of EML genesis. In



Figure 5.5. Series of GOES visible satellite images for the following times: a) 1430 UTC 4 April, b) 2030 UTC 4 April, c) 1431 UTC 5 April, d) 2031 UTC 5 April, and e) 1431 UTC 6 April.



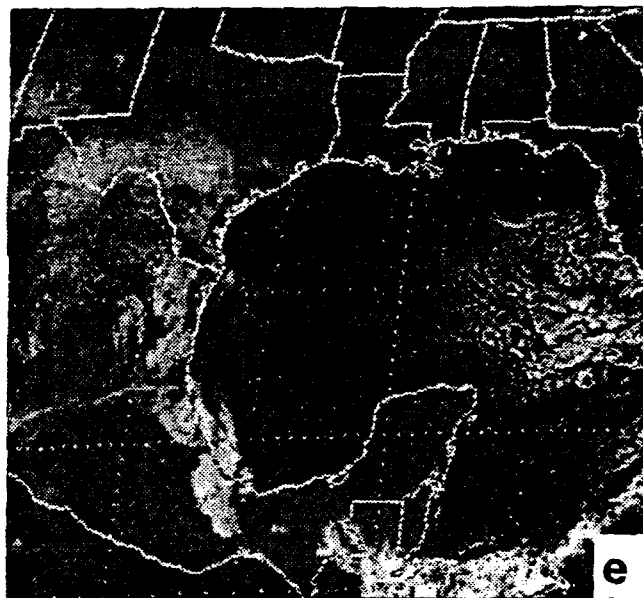
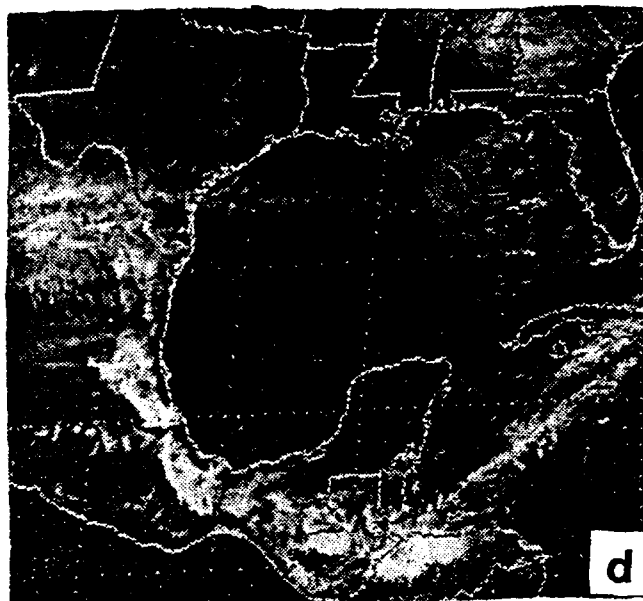


Figure 5.5. (Continued)



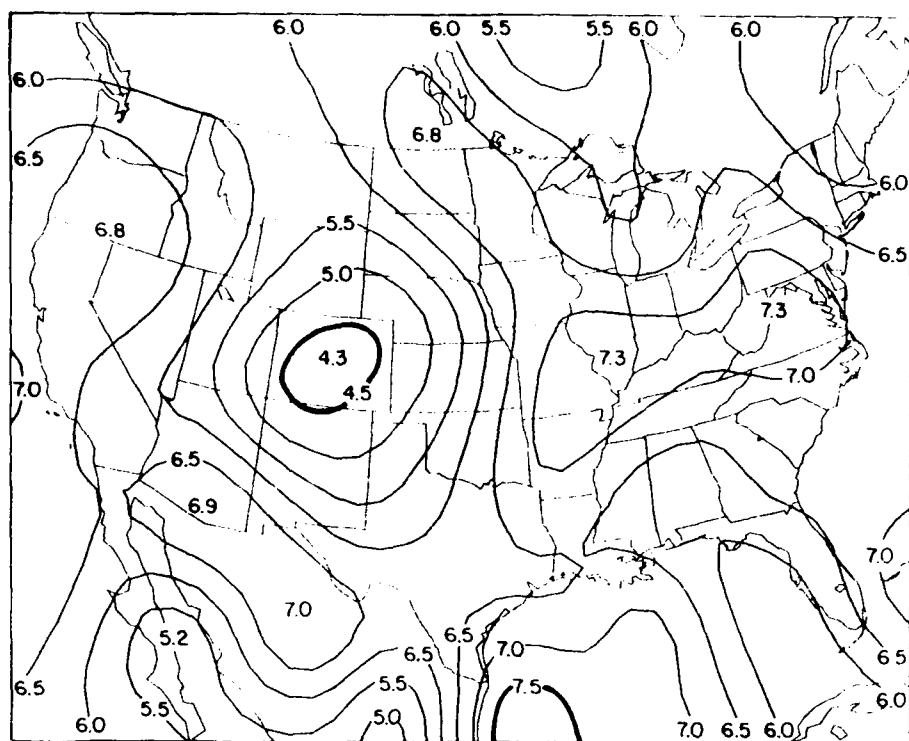
this case study, analyses of temperature lapse rates are used to examine the EML from the source region to its downstream elevated location. The temperature lapse rate between two pressure levels is a good indicator of the dry static stability (Doswell et al. 1985). In particular, the 700-500 mb layer is important because the EML usually resides within it (see Fig. 2.10), and this layer often contains the maximum vertical velocity. Some disadvantages of this parameter include the neglect of any intervening stable or unstable layers, and any knowledge of the moisture profile through the layer. To compensate for these disadvantages, information from the automated sounding analysis described in section 2.2.1 is included to help delineate the EML from other layers of low static stability. Such distinctions are sometimes difficult to make, since the EML is really a subset of the more general category of low static stability layers in the atmosphere. This topic will be discussed further in the appendix.

The 700-500 mb lapse rate analysis for 1200 UTC 4 April is shown in Fig. 5.6a. One EML area is identified off the east coast of Mexico, while other areas of relatively high lapse rates exist over the lower Ohio River valley and Appalachian regions. Stable layers are observed over the western U.S. and southern Baja. An examination of the sounding analysis for this time confirms the presence of a midtropospheric EML area over the Ohio River valley, north of the surface cyclone.

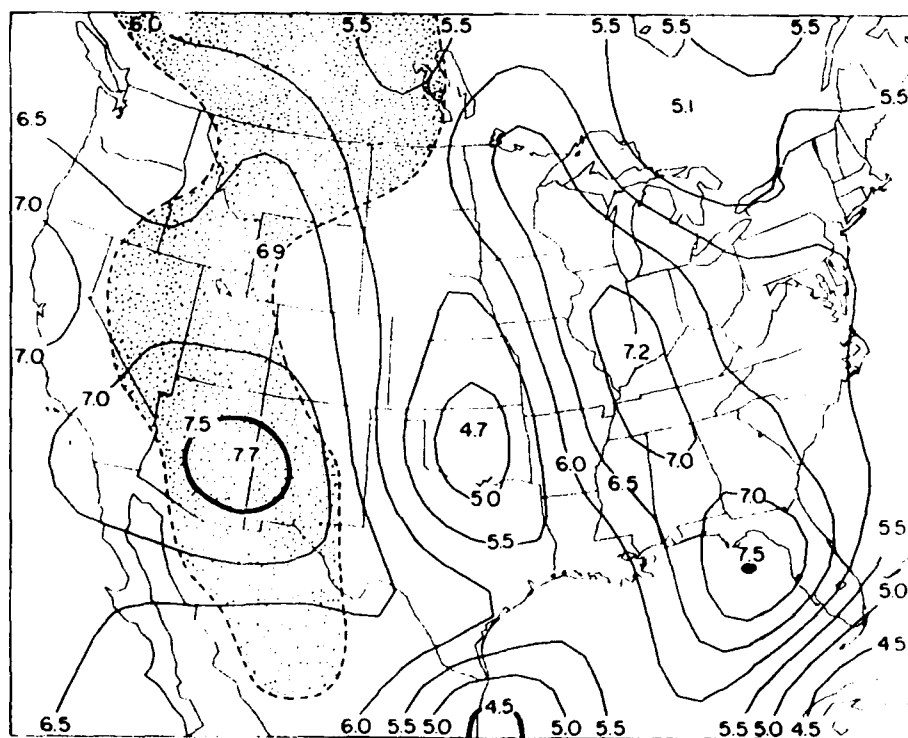
By 0000 UTC 5 April (Fig. 5.6b), an area of high lapse rate is observed over Arizona and western New Mexico. This area is primarily a result of daytime PBL growth, as indicated by the overlay of 850-700 mb lapse rates  $\geq 7.5^{\circ}\text{C km}^{-1}$ . The stable layer over the western U.S. at



Figure 5.6. Analysis of 700-500 mb temperature lapse rate in  $^{\circ}\text{C km}^{-1}$ , isoplethed every  $0.5^{\circ}\text{C km}^{-1}$ . The thicker lines denote the  $7.5$  and  $4.5^{\circ}\text{C km}^{-1}$  isopleths, which are representative of low and high static stability areas, respectively. In panel (b), the shaded region denotes 850-700 mb lapse rates  $\geq 7.5^{\circ}\text{C km}^{-1}$ . Analyses shown for a) 1200 UTC 4 April, b) 0000 UTC 5 April, and c) 1200 UTC 5 April.

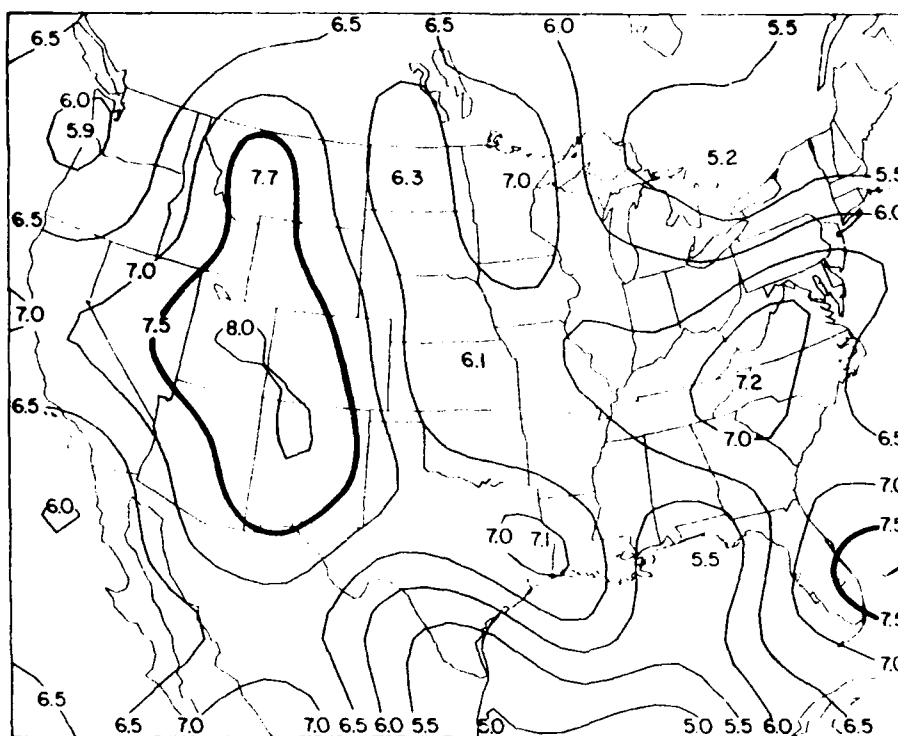


700 TL7  
WED 12Z 04-AP-84

**a**

700 TL7  
THU 00Z 05-AP-84

**b**



700 TI.7  
THU 12Z 05-AP-84

C

Figure 5.6. (Continued)

1200 UTC has migrated to Oklahoma. The low static stability area over the western Gulf has moved towards the Florida panhandle by 0000 UTC.

The area of high lapse rate over the Desert Southwest expanded dramatically during the next 12 h, covering large portions of the Rocky Mountain states by 1200 UTC 5 April (Fig. 5.6c). This expansion of the EML source region during a time of diurnal cooling is curious, and suggests that other processes are at work in destabilizing this layer. Notice the area of relatively low static stability over northern and eastern Texas and western Louisiana. Sounding analysis reveals that this low static stability generally resides in the 700-500 mb layer. This region is situated just south of the polar jet and north of the subtropical jet, in an area of midtropospheric confluence (Fig. 5.1b). It is interesting that, from 0000-1200 UTC 5 April, the 700-500 mb layer destabilizes over much of the western U.S., but remains relatively unchanged over northwestern Mexico. One possible explanation may involve the influence that the subtropical jet has over northern Mexico and southern Texas during this period. The study of Whitney (1977) discussed the considerable horizontal gradient of static stability observed across the subtropical jet, especially in the upper troposphere, with low static stability north of the jet, and high static stability to the south. A series of 200-mb jet positions for the first 24 h of the cycle (Fig. 5.7) indicates the position of the subtropical jet and its ridge axis. The jet, originally located over northern Mexico, migrates into central Texas while the ridge axis moves into New Mexico by 0000 UTC 5 April. Relative-vorticity analyses for this level (not shown) reveal that northern Mexico and southern Texas remained

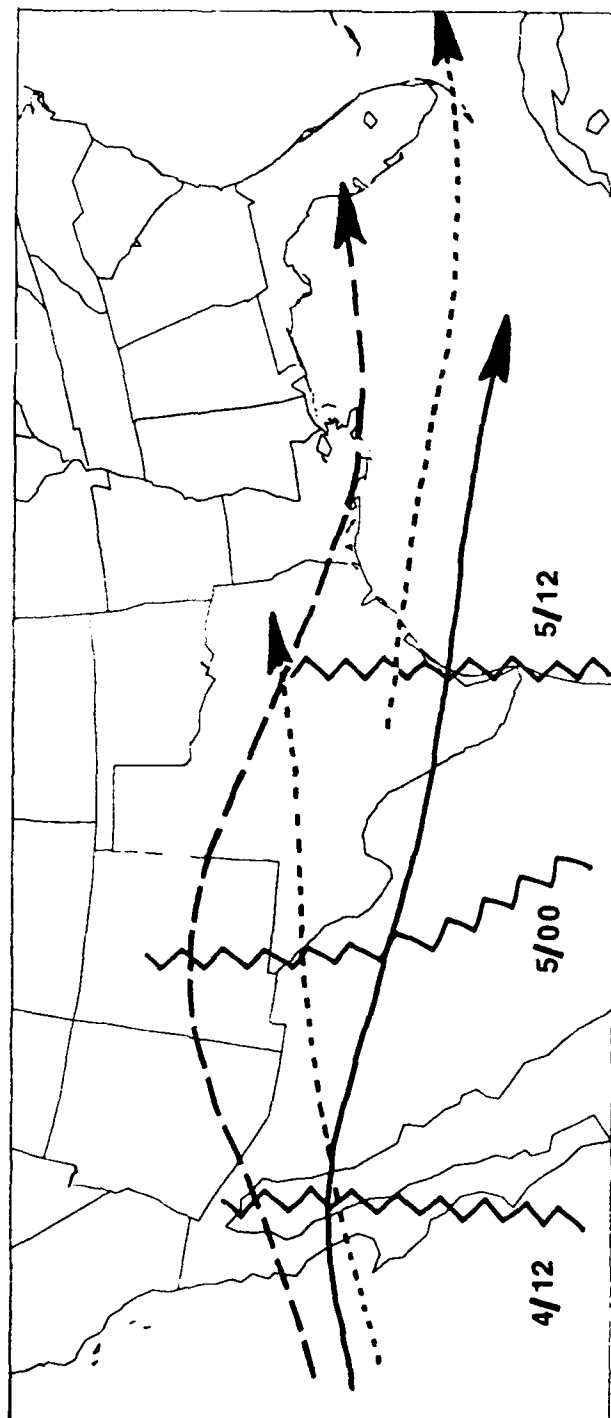


Figure 5.7. Positions of subjectively analyzed 200-mb jet and its ridge axis over the region of the subtropical jet. The location of the jet's ridge axis is shown by the jagged line, and is labelled for each time. Jet positions are displayed for 1200 UTC 4 April (solid line), 0000 UTC 5 April (long dashed line), and 1200 UTC 5 April (short dashed lines).

under negative relative vorticity for most of the first 24 h of the lid cycle, resulting in unfavorable conditions for maintenance of any high lapse rate layers in the midtroposphere over this area. By 1200 UTC 5 April, the jet and ridge had shifted to the south and east, and conditions became favorable for low static stability layers to form and persist in the midtroposphere over northern Mexico.

#### 5.2.2 The Return-Flow Stage (0000 UTC 6 April-0000 UTC 7 April)

By 0000 UTC 6 April, the surface anticyclone that dominated the Great Plains and western Gulf of Mexico on the 4th and 5th was starting to weaken as lower tropospheric warm-air advection began to dominate most of the region. At this time, a surface high was located over the western Gulf with a central pressure of 1019 mb. Examination of the 850- and 700-mb analyses for 0000 UTC 6 April show that the warm-air advection over the western Plains was stronger than over the western Gulf, which weakened the surface ridge faster over the Plains than over the Gulf. Although surface mixing processes over the Gulf were modifying the low level cold air, the 850-mb thermal analyses in Fig. 5.4c-e indicate that this airmass modification was a slow process.

During the next 12 h, the surface high remained quasi-stationary in the western Gulf and maintained its strength. The low level moist layer began to return slowly into the Rio Grande valley, consistent with the climatological composites for this stage (see Chapter 3). The slowness of the moist layer's return into Texas at this stage is due to the presence of the surface high over the western Gulf and the lack of a strong southerly low level jet (LLJ). However, it is also during this



stage that LLJ development begins to take place. The warm-air advection over the western Plains results in surface pressure falls over the Front Range of the Rockies, leading to the formation of a lee-side trough. At 1200 UTC 6 April, there is not yet a lee-side trough (see Fig. 5.1c), but the strengthening pressure gradient over the Front Range has resulted in the formation of a LLJ over the western Plains (Fig. 5.8). Although the western Plains LLJ is out of phase with the returning moist layer, a second LLJ from southern Texas to central Oklahoma has also formed, suggesting that transport of the moist layer into Texas is imminent.

The EML over the western U.S. expanded during the day on 5 April, and a new area started to form over northern Mexico, as shown by the 700-500 mb lapse rate analysis for 0000 UTC 6 April, in Fig. 5.9a. The area of relatively low static stability over Texas and southern Louisiana has expanded eastward since 1200 UTC, and sounding analysis reveals that the western edge of this layer may actually be the beginning of the EML's emergence into the western Plains. The appearance of a deeper Mexican PBL at 0000 UTC coincides with the passage of the subtropical jet's ridge axis out of northern Mexico, and the beginning of upper level diffluence between the subtropical jet over northwestern Mexico and the approaching polar jet just entering the southwest U.S. at this time. The diffluent jets allow for upward vertical motion over northwestern Mexico and the southwestern U.S., resulting in a favorable environment for the EML to maintain its depth.

By 1200 UTC 6 April (Fig. 5.9b), the western U.S. EML has begun to move into the Great Plains, while the Mexican EML has moved toward

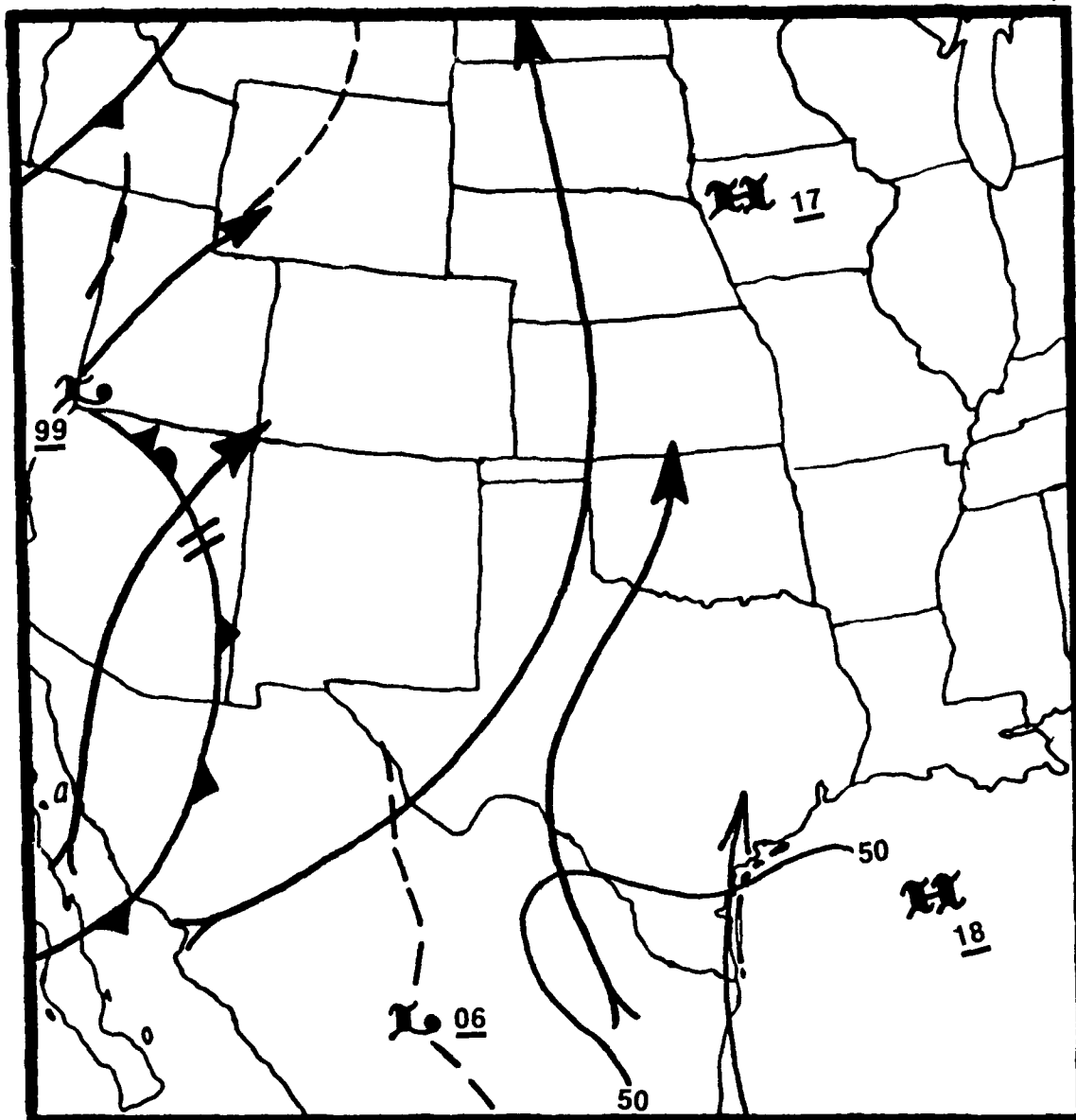
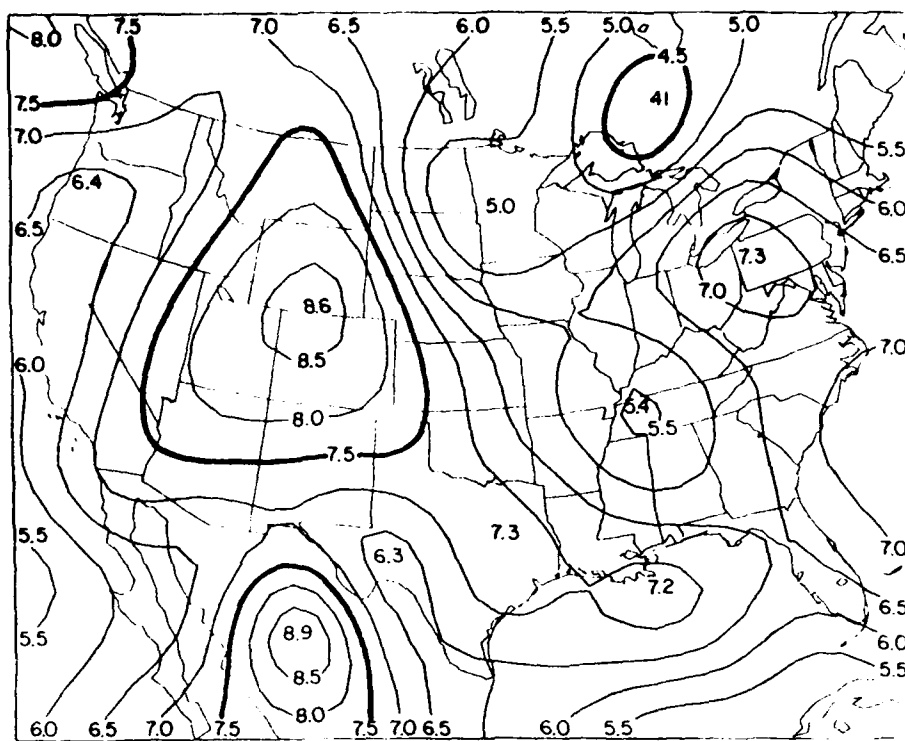
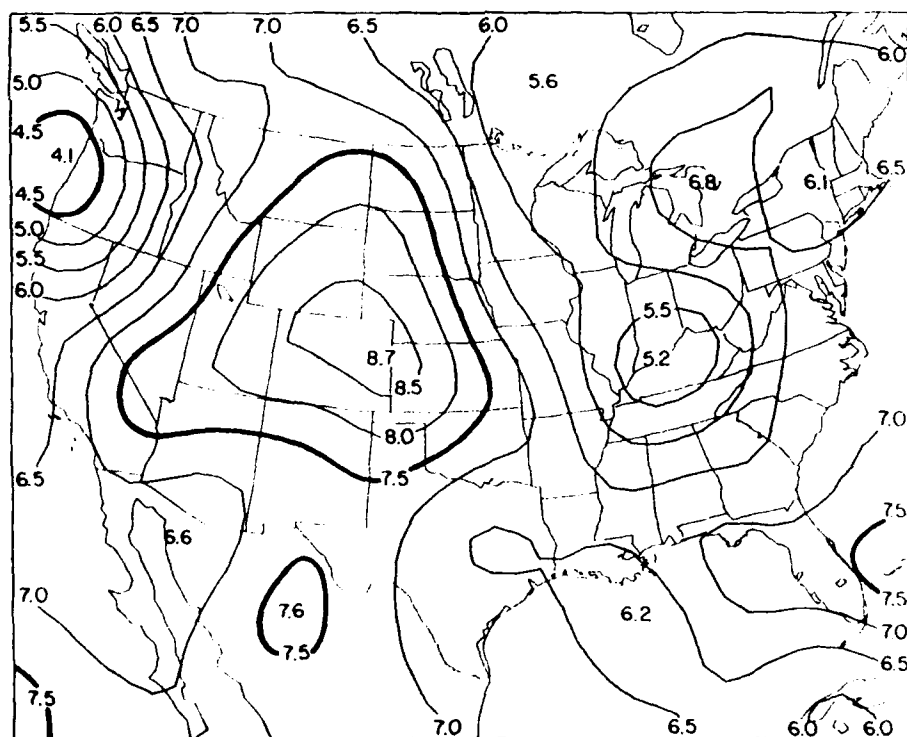


Figure 5.8 Low level features at 1200 UTC 6 April. Surface fronts, troughs, highs, and lows are shown using conventional symbols. The solid line denotes the 50°F isodrosotherm, and the solid lines with arrows denote the LLJ as determined from the winds aloft observations for the second standard level above the surface. The thin line with the open arrowhead over south Texas is a streamline indicating the flow direction over this area.



700 TL7  
FRI 00Z 06-AP-84

a



700 TL7  
FRI 12Z 06-AP-84

b

Figure 5.9. As in Fig. 5.6, except for a) 0000 UTC and b) 1200 UTC 6 April.

southwest Texas. The two EML source areas shown in Fig. 5.9 may account for the appearance of two EML frequency maxima over the central Plains and the southern Plains in the climatological composite for the return-flow stage, shown in Figs. 3.5b and 4.8c. Such a double maximum in the midtropospheric lapse rate field has also been observed in other severe-storm case studies (e.g., Fig. 2 in Doswell et al. 1985).

#### 5.2.3 Lid Genesis (0000 UTC-1200 UTC 7 April)

After 1200 UTC 6 April, the surface moist layer began to move into Texas more rapidly, as illustrated by a continuity chart of the 50°F surface isodrosotherm over Texas from 1200-2100 UTC 6 April (Fig. 5.10). During the late morning on 6 April, the surface high, which had been quasi-stationary over the western Gulf, started to drift east, while surface pressures continued falling over the Front Range and the western Plains. By 1800 UTC, a lee-side low with a central pressure of 1000 mb had formed over the eastern Colorado-New Mexico border. An accompanying lee-side trough extended from this low into northern Mexico. By 2100 UTC, dryline genesis was taking place over west Texas, and the surface low had deepened to 996 mb. The development of the lee-side trough strengthened the low level southerly flow of moist air into Texas, so that by 0000 UTC 7 April, a well-defined moist layer was established over west-central Texas and extreme western Oklahoma (Fig. 5.11). Low level jets were well-established along the Rio Grande valley into the Texas panhandle, and from the Texas Gulf coast into the western portions of Nebraska and South Dakota.

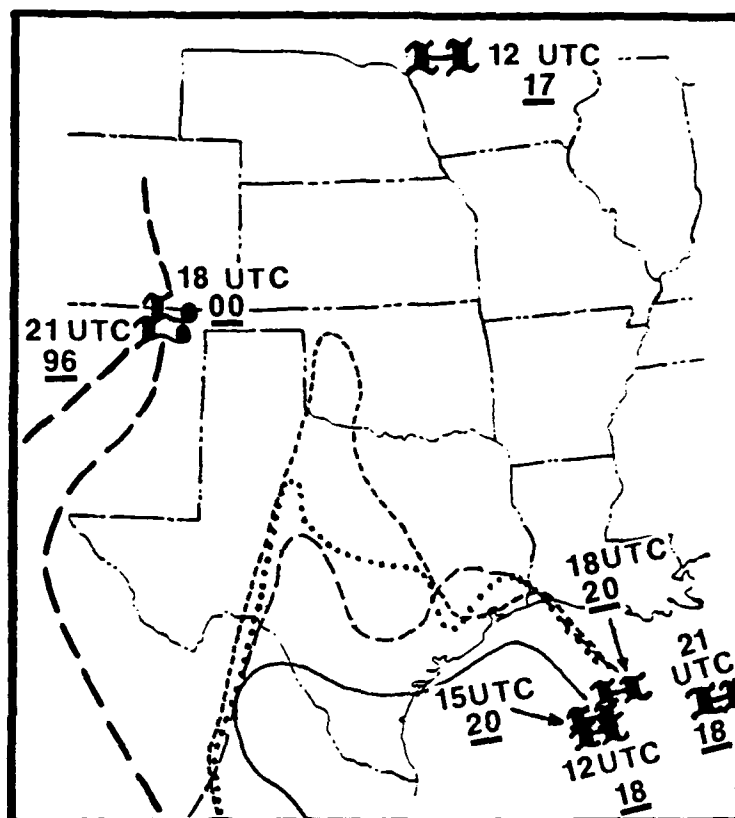


Figure 5.10. Temporal continuity of 50°F isodrosotherm and surface highs and lows for the period 1200-2100 UTC 6 April. Isodrosotherm locations are coded as follows: 1200 UTC = solid line, 1500 UTC = long dashed line, 1800 UTC = dotted line, and 2100 UTC = short dashed line. The locations of pressure troughs (heavy long dashed lines) are for 2100 UTC only.

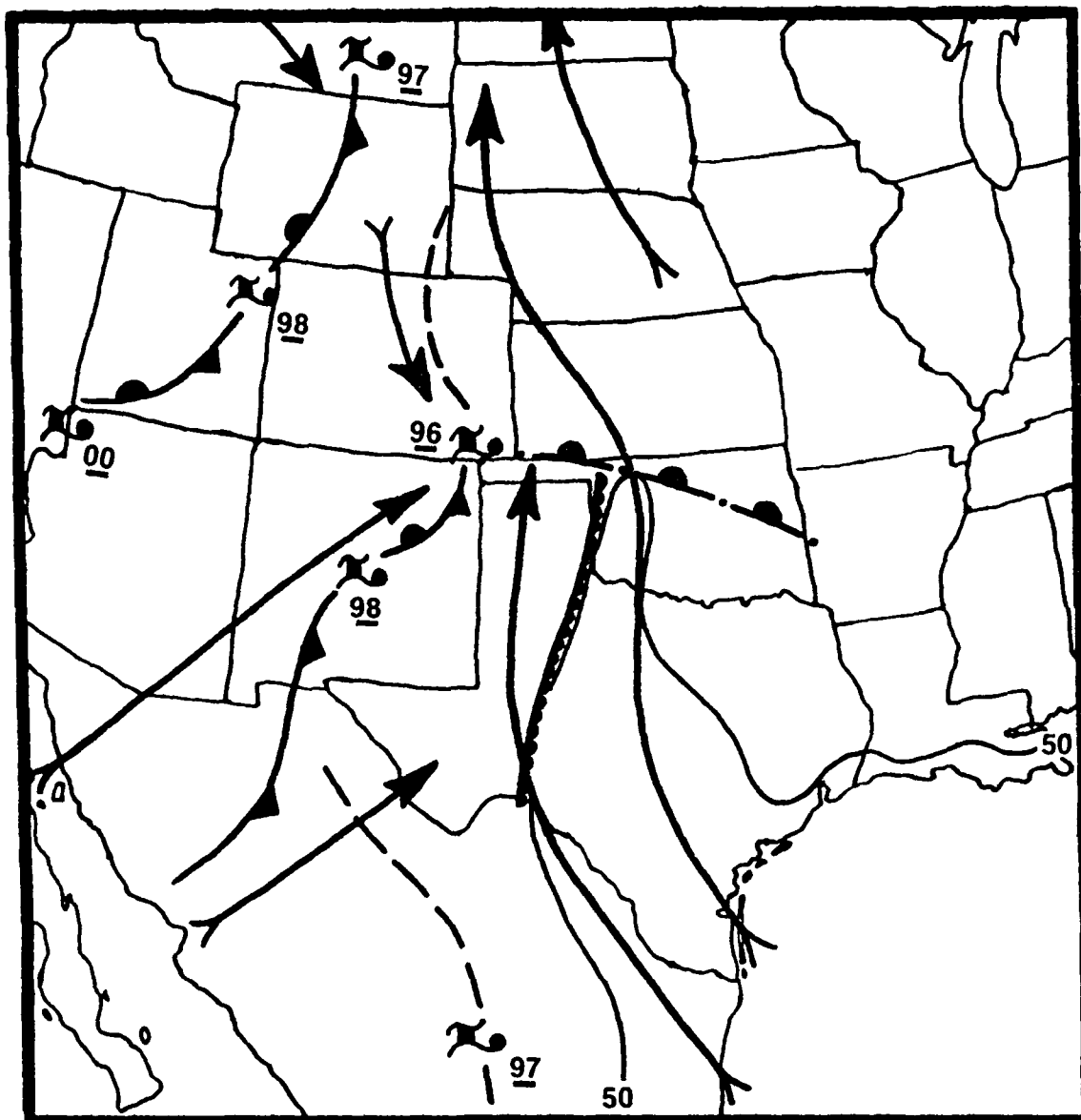
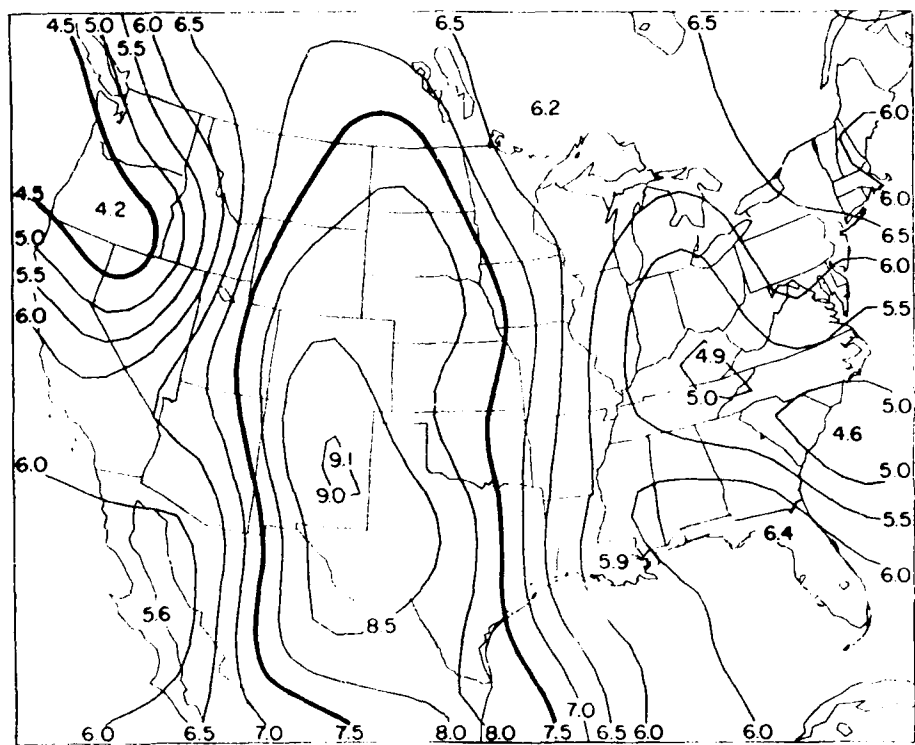


Figure 5.11. As in Fig. 5.8, except for 0000 UTC 7 April. Surface dryline is shown using a solid, scalloped line.

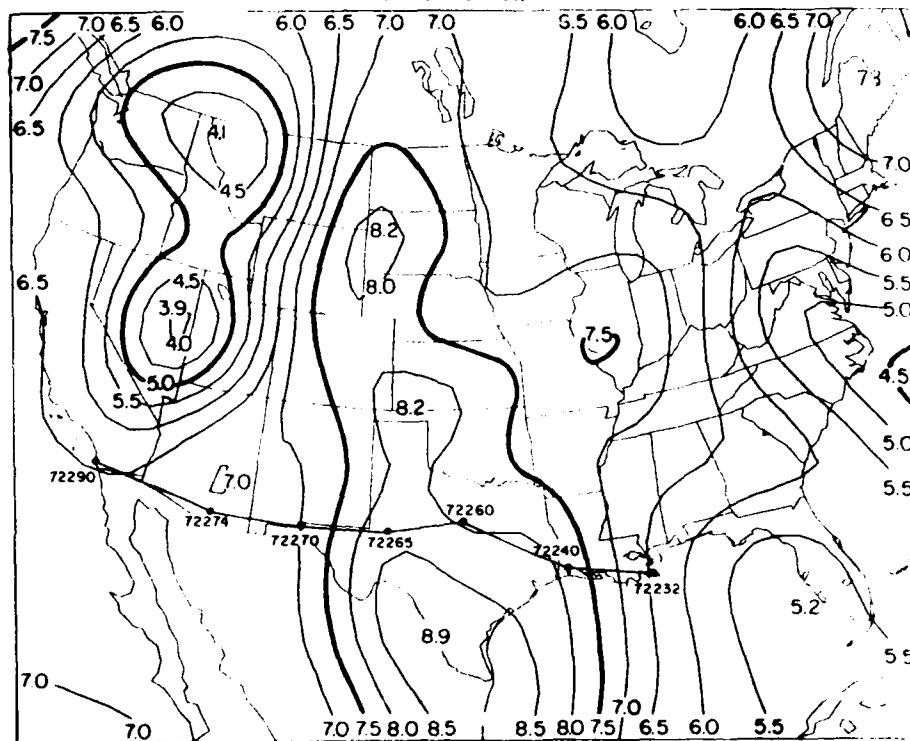
While the moist layer was returning into Texas, the EML areas over the Rockies and northern Mexico began to consolidate, resulting in a continuous north-south-oriented area of low static stability from the western Plains of Montana and North Dakota into central and eastern Mexico (see the 700-500 mb lapse rate analysis for 0000 UTC 7 April in Fig. 5.12a). The maximum value of  $9.1^{\circ}\text{C km}^{-1}$  over eastern New Mexico is associated with the EML generated over northern Mexico, which has undergone its second day of surface heating. Although the EML area is continuous, analysis of mean EML potential temperatures (not shown) reveals that Texas is under the influence of the Mexican airmass, with mean  $\theta$  values around  $42^{\circ}\text{C}$ , while the area to the north, affected by the western U.S. EML, has mean  $\theta$  values around  $33^{\circ}\text{C}$ .

Given the locations of the EML and moist layer, there should be some overlap of these two layers, resulting in the formation of a lid. A 0000 UTC analysis of lid strength and buoyancy (refer to section 2.2.1 for definitions) over the EML area in the central U.S. (Fig. 5.13a) reveals that the area around Del Rio, Texas now has a lid stratification by virtue of the EML's presence and an unstable value of the buoyancy term. Note that Midland and Stephenville do not have lid soundings at 0000 UTC, but their buoyancy terms are low enough so that a lid could exist there if the soundings were to be further destabilized. The analysis shown in Fig. 5.13 demonstrates the value of examining lid strength and buoyancy *throughout* the EML region, not just where a lid exists, especially in the early stages of lid formation.

From 0000 UTC to 1200 UTC 7 April, the lid area began to grow as the moist layer expanded eastward through Texas, while the Mexican EML



700 TL7  
SAT 00Z 07-AP 84



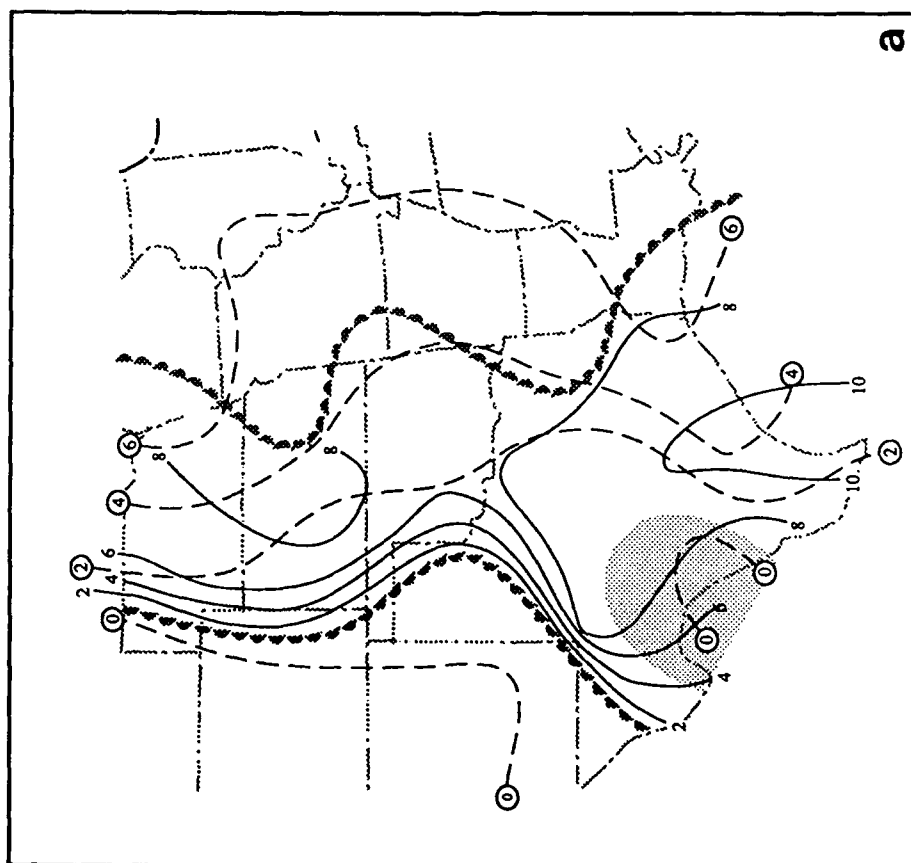
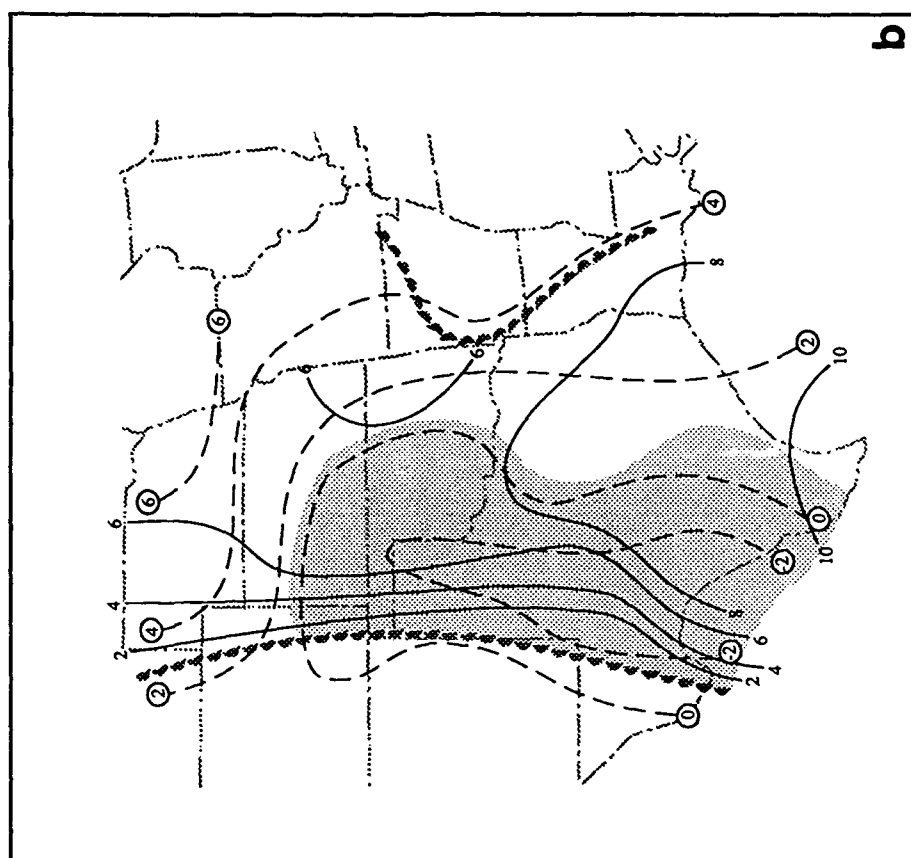
700 TL7  
SAT 12Z 07-AP-84

Figure 5.12. As in Fig. 5.6, except for a) 0000 UTC and b) 1200 UTC 7 April. The location of the cross section shown in Fig. 5.20 is displayed in panel (b).





Figure 5.13. Lid strength (LS) and buoyancy (BUO) term analyses for a) 0000 UTC and b) 1200 UTC 7 April. Lid strengths are only analyzed where an EML is present, within the scalloped borders. Isopleths of lid strength are shown by solid lines, contoured every 2°C, and buoyancy term isopleths are displayed as dashed lines, and are also contoured every 2°C. The location of the lid-coverage area is shown by the shaded region.



continued to move across the Great Plains. The 700-500 mb lapse rate analysis for 1200 UTC (Fig. 5.12b) reveals that the low static stability area over the northern Plains has decreased in size, and the highest lapse rates now exist over southern Texas. The 1200 UTC lid strength and buoyancy analysis (Fig. 5.13b) shows that the lid-coverage area has expanded as far north as Kansas, and as far east as central Texas and eastern Oklahoma. The area with the highest 700-500 mb lapse rate (northwest of Brownsville, Texas) does not have a lid stratification yet, owing to a buoyancy term of  $+1.0^{\circ}\text{C}$ . Figure 5.13b shows that there is a strong gradient of lid strength over much of western Texas. Analysis of the entire EML area in Fig. 5.13b allows us to identify a north-south axis of maximum lid strength from western Kansas into southern Texas. The locations of this maximum-lid-strength zone and the area of the strongest gradient will be important when the severe weather outbreak is discussed in the next section.

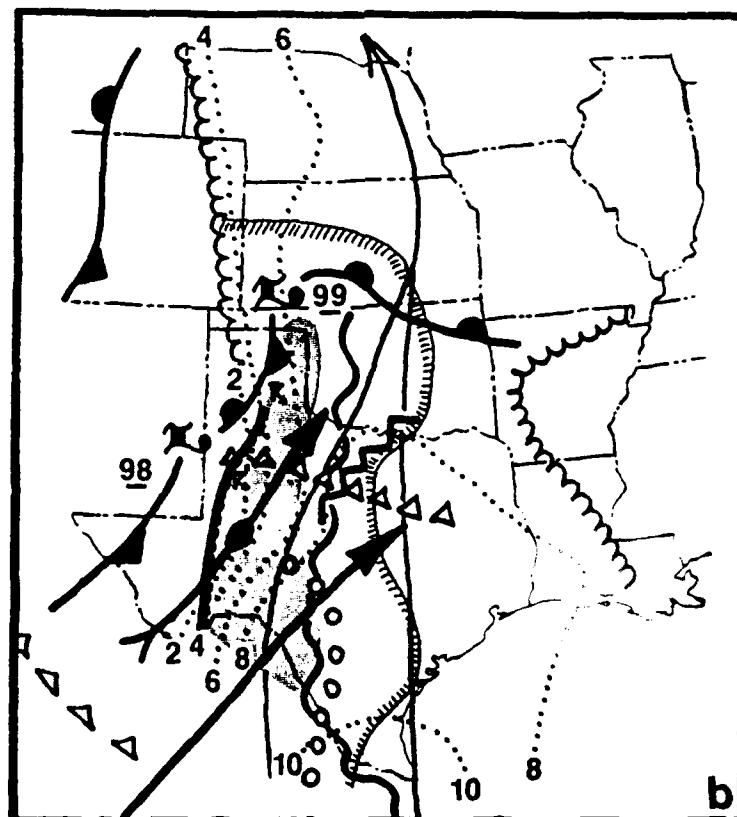
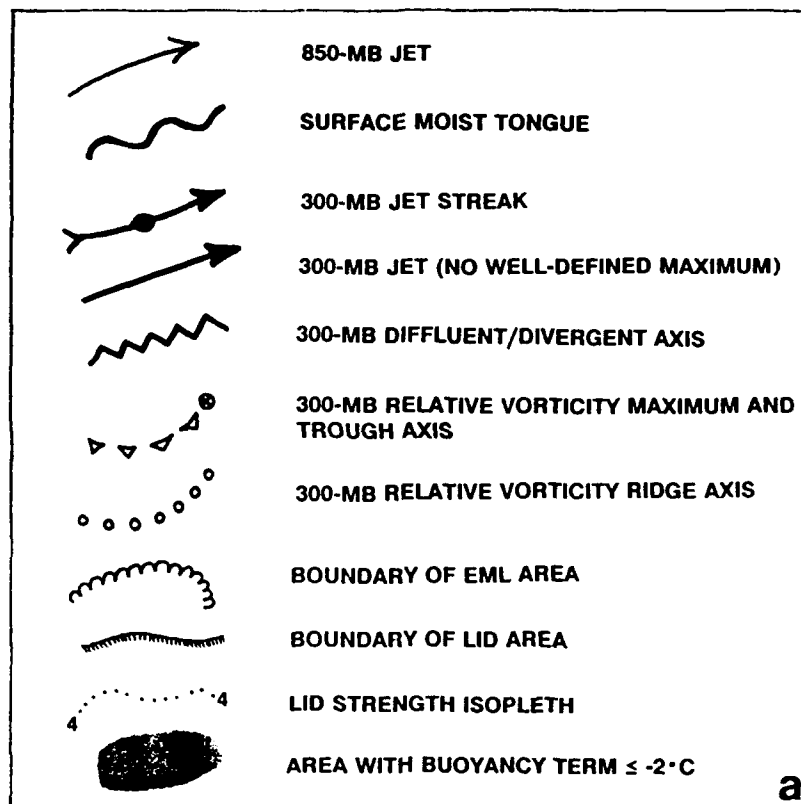
#### 5.2.4 The Lid-Maximum Stage and Severe-Weather Outbreak (1200 UTC 7 April-1200 UTC 8 April)

The meteorological situation over the southern Plains on the morning of 7 April was very complex. Figure 5.14b displays a surface/upper-air composite analysis for 1200 UTC 7 April (a legend is shown in Fig. 5.14a). At this time, an emerging frontal system with a double-low structure and well-developed dryline exist over the western Plains. The cold frontal position is nearly identical to that in the climatological composite for the lid-maximum stage, shown in Fig. 3.5d. The polar and subtropical jets are so closely aligned that it is difficult to distinguish between them (also see Fig. 5.1d). This

Figure 5.14. Composite surface/upper-air analysis for 1200 UTC 7 April (panel 'b'). Symbols are shown in the legend panel (a).



## LIST OF SYMBOLS



situation is different from that depicted in the climatological composite for the lid-maximum stage (Fig. 4.8e), where the mean jets were separated by a large enough distance so that they could be distinguished from each other. There is one jet maximum located over Midland, Texas, and a second jet (with no clearly defined maximum) to its south, over northern Mexico and southern Texas. The locations of relative vorticity troughs and ridges are used to determine favorable vertical motion areas associated with this complex double-jet pattern. Positive vorticity advection is observed over northern Texas and Oklahoma, as well as over southwest Texas.

The portion of west Texas between the surface dryline and the Midland jet streak is favorable for severe weather since it is in the exit region of the jet, contains buoyancy term values less than  $-2^{\circ}\text{C}$ , and has relatively weak lid strengths (less than  $4^{\circ}\text{C}$ ). Over northern Texas, upper level diffluence/divergence and positive vorticity advection will weaken the strong lid and allow convection to occur after the region of high buoyant instability is transported over the area of the surface moist tongue. A third area of favorable conditions for deep convection is over southern Texas, between the dryline, the moist tongue, and the two upper jets. Strong positive vorticity advection moving into this area from the southwest will eventually remove the strong lid and allow deep convection to occur in the highly buoyant moist layer. Another factor favoring the development of severe storms in this area is the strong veering between the LLJ and the southern 300-mb jet. Of the three favorable areas for severe weather identified in Fig. 5.14, one is along the western lid edge and two are located



within the lid interior at 1200 UTC. If one examines the severe weather events associated with the lid-maximum stage, mean composite analysis for this flow type (Fig. 4.8e), it is observed that a considerable amount of severe weather is reported within the "interior" region of high lid-occurrence, which is analogous to the strong lid interior region shown in Fig. 5.14. An examination of the 1235 UTC manually digitized radar summary (not shown) reveals that there already was one cell with a digital video integrator processor (DVIP) intensity level of 3, located north of Midland with a maximum top of 30,000 ft. A second, smaller cell to the southeast of Amarillo had a maximum top of 36,000 ft. The locations of these cells are denoted in Fig. 5.14b by the "thunderstorm" symbols.

By 1500 UTC, the situation was beginning to change over the southern Plains (see the surface analysis in Fig. 5.15a). The warm front was weakening over Kansas, Oklahoma, and Arkansas, and the low from eastern New Mexico was moving northward along the cold front. The cold front started to move slowly eastward, while the dryline remained quasi-stationary except for a bulge near Lubbock. The westward movement of the surface moist tongue over Texas and Oklahoma, and the appearance of the dryline bulge over west Texas suggest that low level convergence is intensifying to the east of the dryline. The radar overlay in Fig. 5.15a now indicates several cells to the east of the dryline, along the area of maximum lid strength gradient at 1200 UTC (recall Figs. 5.13b and 5.14b). The cell that was near Amarillo at 1200 UTC moved into northwestern Oklahoma and produced wind damage at Gage (also see Fig. 5.2a).

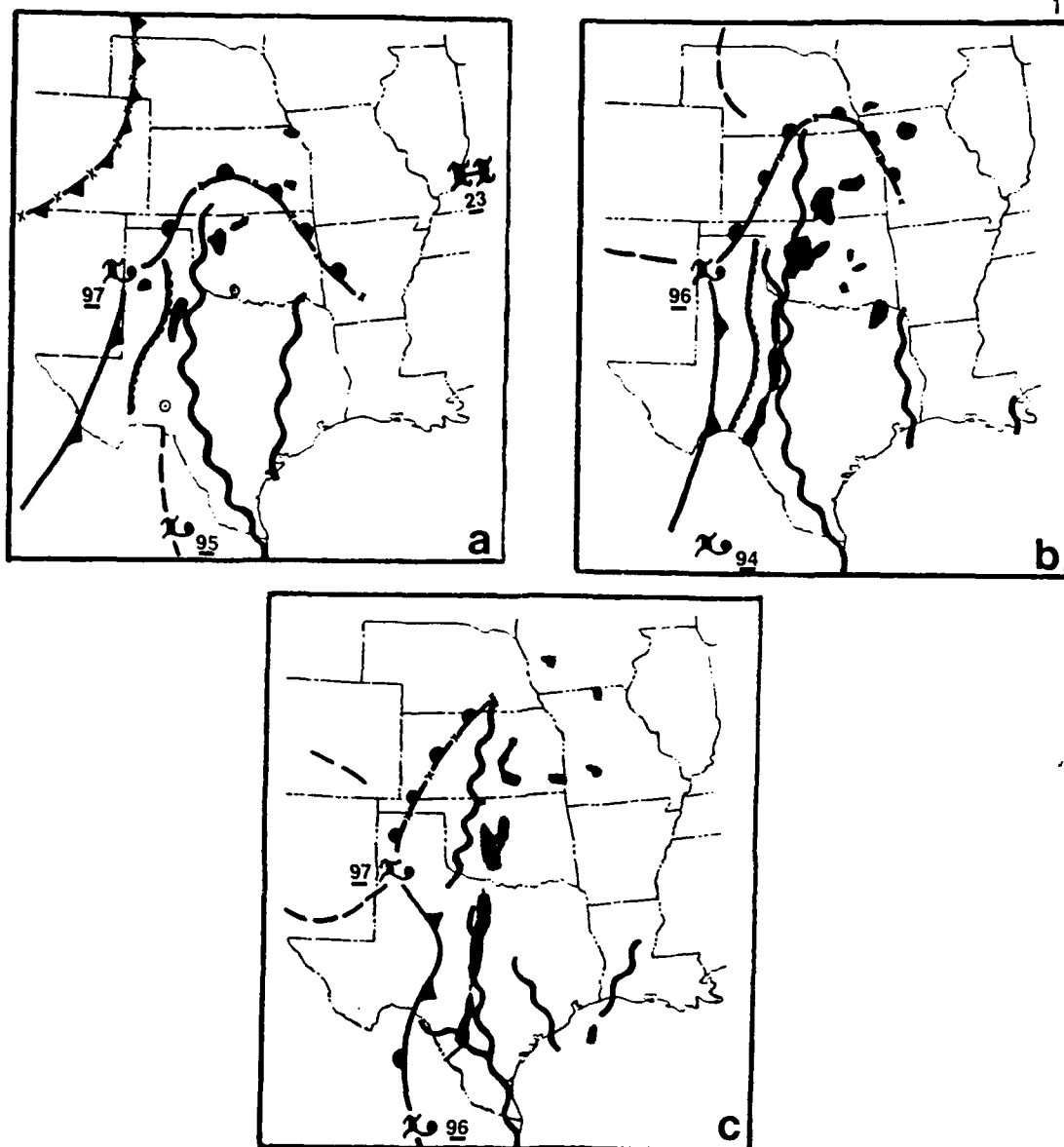


Figure 5.15. Surface analysis and manually digitized radar summary overlay. Surface fronts, troughs, highs, and lows are shown using conventional symbols. The locations of surface moist tongues are shown using the same symbol as in Fig. 5.14a. The locations of radar echoes with DVIP level of 3 or greater are shown as dark shaded regions. A circle with a dot inside denotes the first observation of a particular echo. Thin solid lines connecting the shaded regions denote a squall line. Analysis/radar summary times are a) 1500/1535 UTC, b) 1800/1835 UTC, and c) 2100/2035 UTC 7 April

Figure 5.15a indicates that the convective cells over Texas and Oklahoma were nearly coincident with the surface moist tongue at 1500 UTC. Within the next hour, a squall line formed from the Texas-Oklahoma border into the Big Bend region. This squall line moved east across Texas during the next 6-7 h, and was responsible for the two severe-weather areas displayed in Fig. 5.2a. For the most part, the squall line was most active along its northern and southern portions. In the 1800 UTC surface analysis (Fig. 5.15b), the primary low was located southwest of Amarillo, and the cold front was just passing Midland. The radar overlay clearly shows how the squall line was aligned with the surface dryline. The convective cells from western Oklahoma into central Texas were nearly coincident with the surface moist tongue. Examining both Figs. 5.15b and 5.2a, we see that the cells along the northern portion of the squall line were tornadic (maximum tops of 50,000 ft), while the southern portion (with maximum tops of 48,000 ft) produced a line echo wave pattern and wind gusts of 51 kt at Del Rio.

The surface analysis for 2100 UTC (Fig. 5.15c) shows a frontal wave appearing to the south of the Rio Grande valley as a surface low in northern Mexico is overtaken by the cold front. The dryline was also overtaken by the front during this time. The radar overlay in Fig. 5.15c indicates more of a discontinuity between the northern and southern portions of the squall line than there was 2 h before. The southern part of the squall line is now moving into the region of the surface moist tongue. The severe-weather summary in Fig. 5.2a shows that the primary severe-weather activity over Texas was along the southern part of the squall line after 1430 CST (2030 UTC), and that

this activity became tornadic around 2100 UTC. The increased severity of the convection along the southern part of the squall line and the cessation of severe-weather activity along the northern portion suggest that the upper level dynamical forcing has shifted to southern Texas during the late afternoon. Recall from the composite analysis for 1200 UTC (Fig. 5.14b) that strong positive vorticity advection was moving into southern Texas, but the high lid strengths there would have delayed any deep convection from occurring immediately.

The squall line over Texas began to weaken after 2300 UTC, according to the radar summaries (not shown). A composite meteorological analysis for 0000 UTC (Fig. 5.16) shows that the northern portion of the surface front over Texas had moved little over the last 3 h and was starting to occlude, while the southern portion continued to move eastward. At 300 mb, two jets can still be identified over Texas. A new jet streak with a 110-kt maximum appears over Del Rio, while the southern jet appears along the Gulf coastal region. Positive vorticity advection and diffluence/divergence are observed between the two jets over the eastern half of Texas, while negative vorticity advection is analyzed over south Texas, essentially "finishing off" the southern portion of the squall line. The presence of ample low level moisture and strong dynamical forcing over the Texas coast suggest that this area may be favorable for deep convection, but the southern half of the coastal region has lid strengths which are too high to allow the convection to occur there immediately. The northern half of the coast has weaker lid strengths and a strong veering wind profile, but is just beyond the northern edge of the most unstable buoyancy values. The 0000

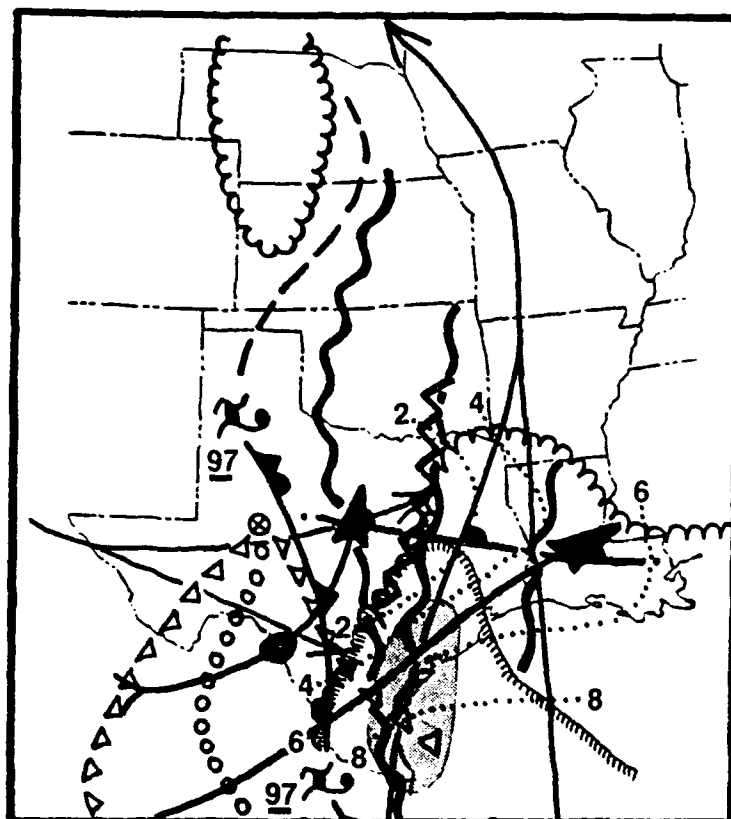


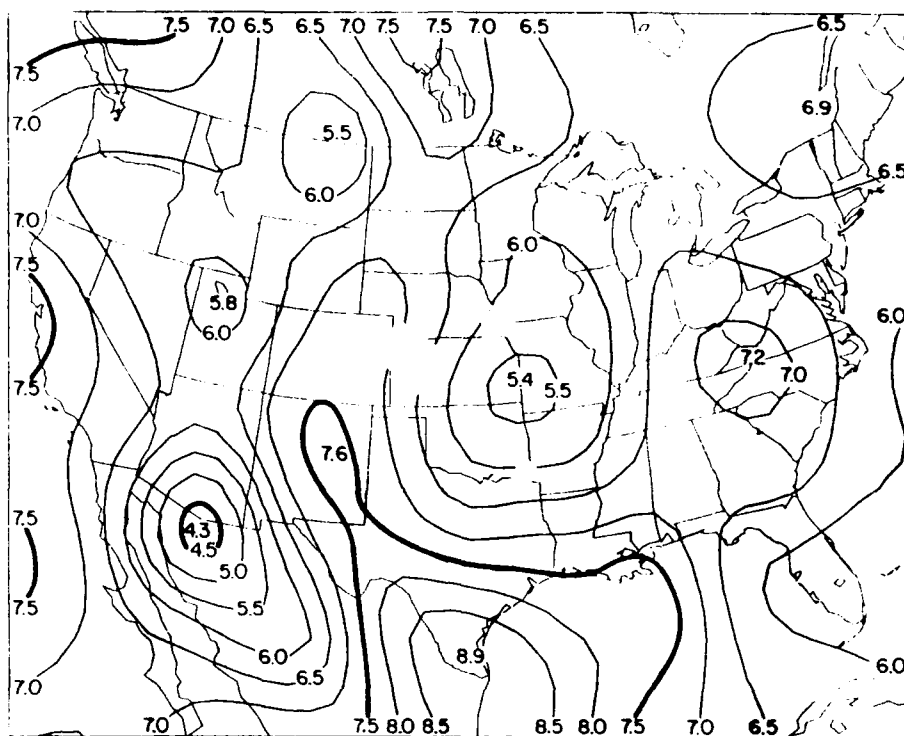
Figure 5.16. As in Fig. 5.14, except for 0000 UTC 8 April. See Fig. 5.14a for symbols.

UTC analysis suggests that deep convection is possible over the northern part of coastal Texas if the buoyantly unstable area expands northward. Figure 5.2a shows that only isolated severe weather occurred near the Texas-Louisiana border after midnight on 8 April.

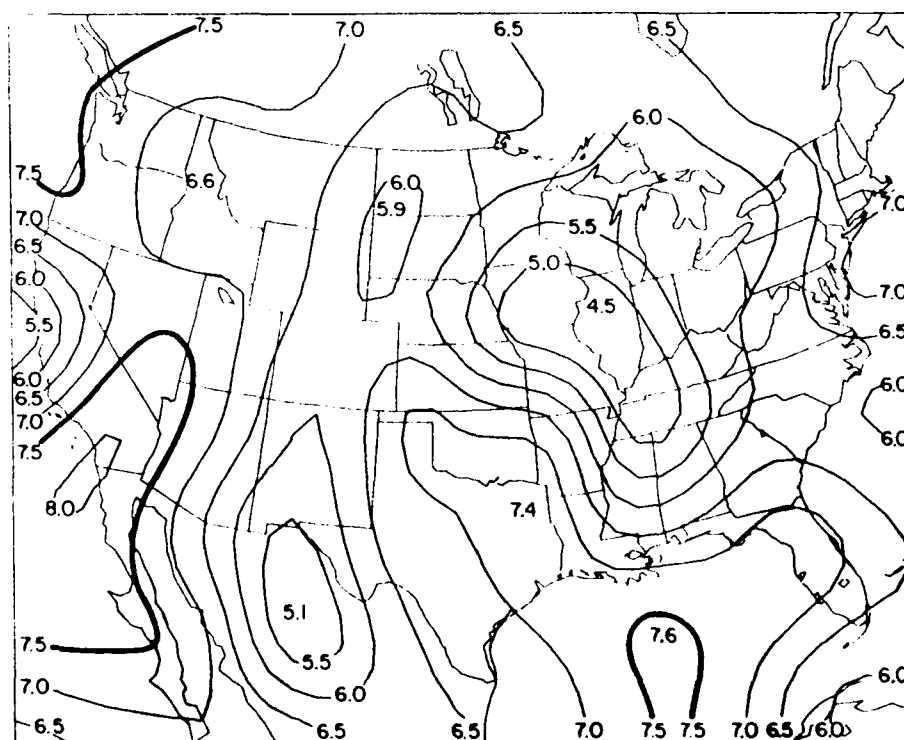
#### 5.2.5 The Post Lid-Maximum Stage and the Second Severe-Weather Outbreak (1200 UTC 8 April-0000 UTC 9 April)

During the evening of 7 April, the surface low and front moved across Texas, and the upper level low moved into the southern Plains. The movement of the frontal system and upper trough across the southern Plains effectively cut off the EML source region of northern Mexico, as westerly winds transported the EML into the Gulf. The transport of the EML into the western Gulf is illustrated by a 12-h sequence of 700-500 mb lapse rate analyses for 0000 UTC and 1200 UTC on 8 April (Fig. 5.17). These lapse rate analyses also reveal that the EML over the northern and central Plains no longer exists.

A composite surface/upper air analysis for 1200 UTC on 8 April is shown in Fig. 5.18. The lid/EML region at this stage is similar to the orientation in the climatological composites in Figs. 3.5e and 4.8f. The double-jet structure which had been observed for the past several days is now barely discernable. Over northern Louisiana and eastern Arkansas, upper level positive vorticity advection and strong diffluence/divergence are analyzed, along with a weakened lid strength area. However, the areas of buoyancy term values of less than  $-2^{\circ}\text{C}$  and the low level moist tongue are to the west of this area, over eastern Texas; the occurrence of deep convection over Louisiana and Arkansas



700 TL7  
SUN 00Z 08-AP-84



700 TL7  
SUN 12Z 08-AP-84

Figure 5.17. As in Fig. 5.6, except for a) 0000 UTC and b) 1200 UTC 8 April.

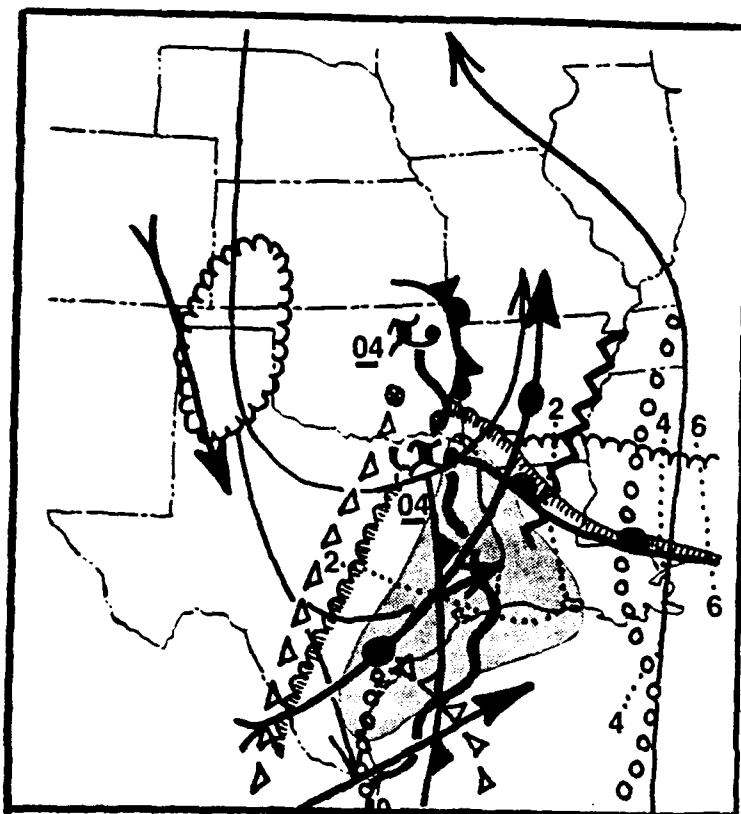


Figure 5.18. As in Fig. 5.14, except for 1200 UTC 8 April. See Fig. 5.14a for symbols.

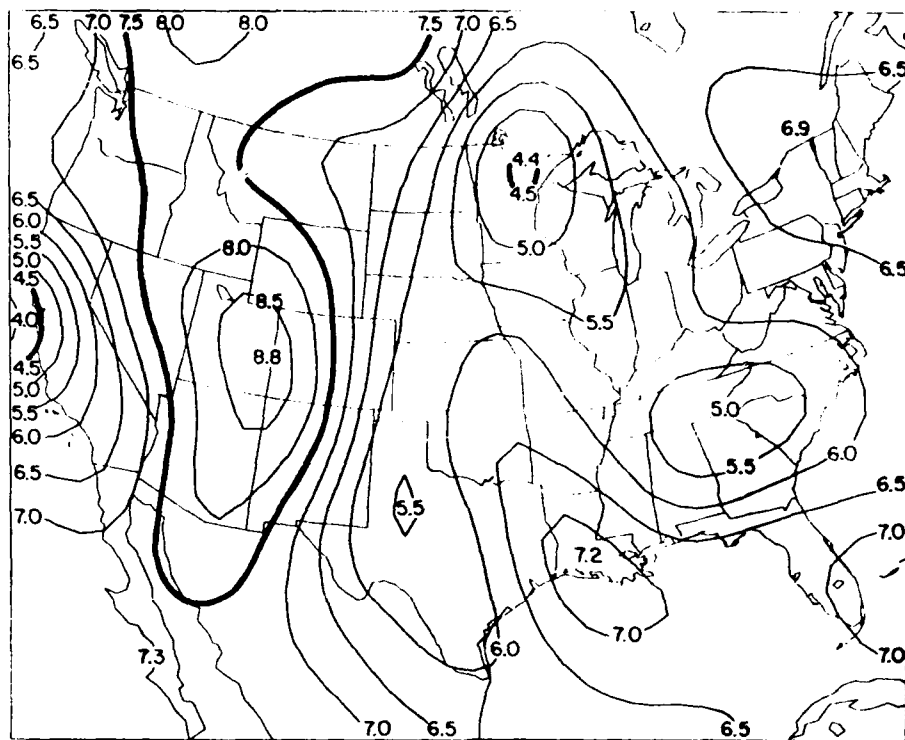


will be delayed until the moist tongue and high buoyant instability region move into the area of favorable vertical motion.

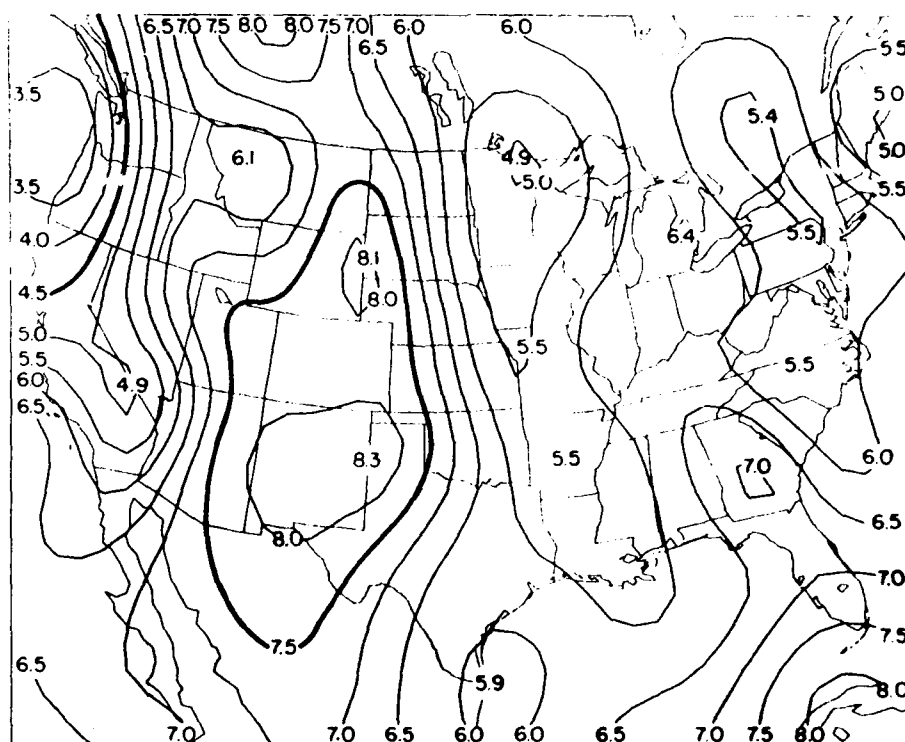
The severe weather outbreak over Arkansas, Louisiana, and Mississippi on 8 April was discussed in section 5.1 and documented in Fig. 5.2b. As expected, the outbreak commenced when the moist tongue moved into position below the upper diffluence/divergence area in western Arkansas and northern Louisiana. The severe weather continued in the northernmost portion of the surface warm sector, along the surface moist tongue and within the diffluent/divergent portion of the upper jet. By 0000 UTC on 9 April, the upper jet and diffluence/divergence area had migrated well to the north and east of the surface moist tongue (analysis not shown). The EML continued to move across the Gulf coast and adjacent waters, but gradually became weaker and more difficult to identify on the soundings in this region, and there no longer were any areas with a buoyancy term values of less than  $-2^{\circ}\text{C}$ . Convection continued across Mississippi, Alabama and the Florida panhandle, but no severe weather was reported with these cells after 0115 UTC on 9 April.

#### 5.2.6 The End Stage of the Cycle (0000 UTC-1200 UTC 9 April)

By 0000 UTC 9 April, the next EML was forming over the western U.S., as illustrated by the 0000 UTC 700-500 mb lapse rate analysis in Fig. 5.19a. However, this low static stability layer had entered the western U.S. 12 h before, with lapse rate values already in excess of  $7.5^{\circ}\text{C km}^{-1}$  (see Fig. 5.17b). An examination of the lapse rate analyses from 1200 UTC 4 April and 0000 UTC 5 April (Figs. 5.6a,b) reveals that



700 TL7  
MON 00Z 09-AP-84



700 TL7  
MON 12Z 09-AP-84

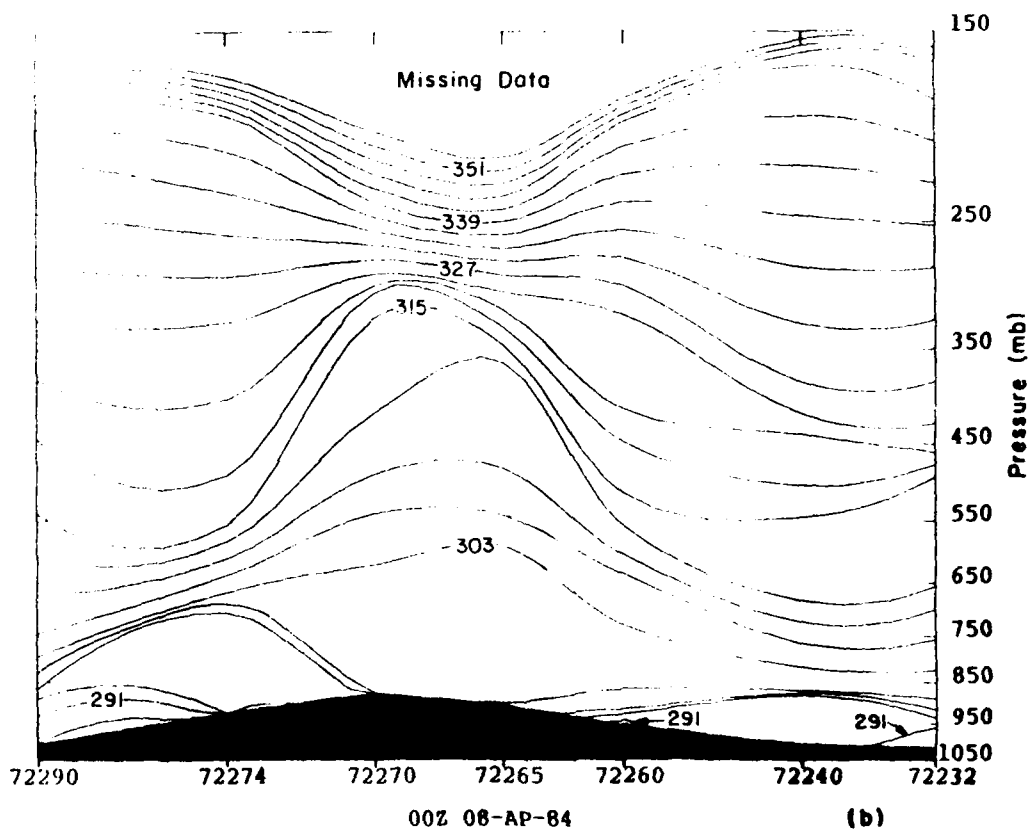
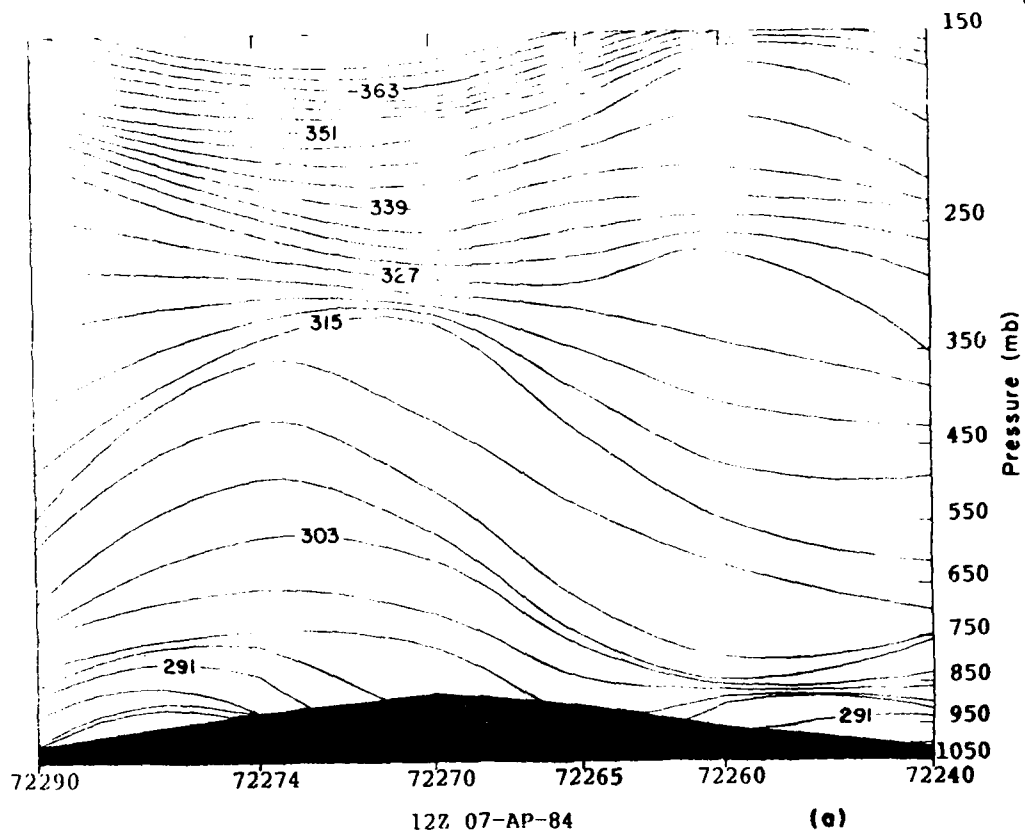
Figure 5.19. As in Fig. 5.6, except for a) 0000 UTC and b) 1200 UTC 9 April.

the layer which moved into the west coast on 4 April and became an EML over the Desert Southwest, also had a relatively higher lapse rate than its surroundings before becoming an EML. The fact that these layers already had somewhat lower static stabilities when they moved into the west coast of North America suggests a possible dynamic connection between the location of the layer and the baroclinic structure of the upper level wave itself. Such a dynamic connection is a subject for future investigation.

As discussed in section 5.1, a key feature that was absent in the final stage of the lid cycle is the presence of a polar-air outbreak and surface anticyclone following the frontal passage over the Great Plains on 7 and 8 April. The airmass that moved into the central U.S. behind the front was dry but not very cold, especially at the surface. This is a well-known characteristic of Pacific airmasses that move into the Great Plains from the west during the spring, and is illustrated by a series of isentropic cross sections taken along a west-east transect from southern California to the Louisiana coast, from 1200 UTC 7 April to 1200 UTC 8 April (Fig. 5.20). The cold dome over the western U.S. can be identified all the way down to the surface at 1200 UTC 7 April (Fig. 5.20a). As the cold dome continued eastward across the Great Plains during the day on 7 April, it experienced strong heating from below, with the result being an erosion of the lower portion of the cold dome over Texas by 0000 UTC 8 April (Fig. 5.20b). The front is still discernable at about 850 mb, near Stephenville, Texas (station 72260) at this time. The cold dome continued eastward during the next 12 h, and by 1200 UTC on 8 April it was situated over eastern Texas, but the cold



Figure 5.20. Isentropic cross sections from southern California to the Louisiana coast (see Fig. 5.12b for exact location) for the following times: a) 1200 UTC 7 April, b) 0000 UTC 8 April, and c) 1200 UTC 8 April. Isentropes (in K) are analyzed at 3 K intervals, and are labelled every 12 K. The vertical coordinate is log pressure, and is labelled in 100 mb intervals along right side of figure.



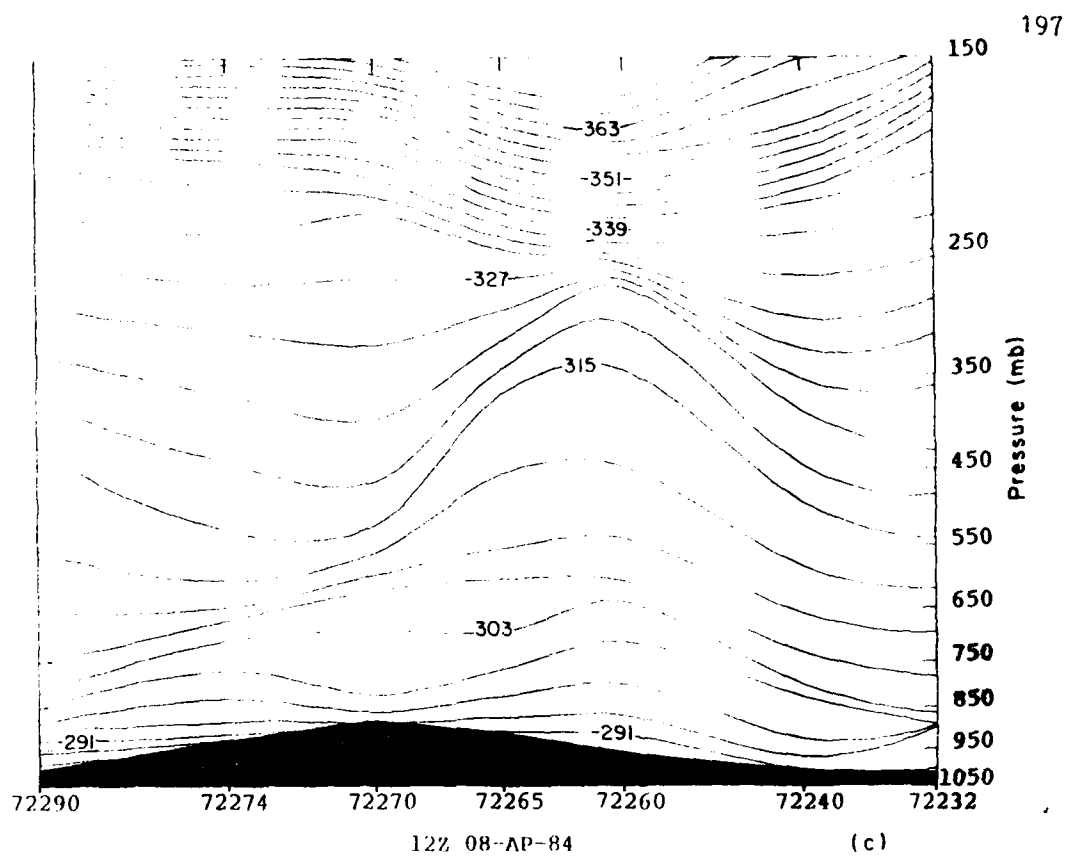


Figure 5.20. (Continued)

front was still difficult to identify at the surface, located west of Lake Charles, Louisiana (station 72240).

The portion of the cross section in Fig. 5.20c over the Desert Southwest shows a shallow dome of cold air associated with the Pacific ridge observed over this area on the surface analysis (also see Fig. 5.1e). However, as the EML was created in this area during the subsequent daytime heating cycle, the surface pressures decreased, eliminating the possibility of a cold anticyclone moving into the Great Plains at the end of the lid cycle. Because of the lack of such a polar anticyclone over the southern Plains, the low level moist layer was never driven very far into the Gulf, and it remained along the coasts of Texas and Louisiana during the early morning hours of 9 April. An interesting phasing problem is apparent between the moist layer and the EML emerging into the western Plains at this time. Figure 5.19b shows the location of the EML in the 700-500 mb layer over the Rockies and the western Plains at 1200 UTC 9 April. Although the relative locations of the EML and moist layer are similar to those observed on the morning of 6 April, the lack of the surface anticyclone makes this situation different from that on 6 April. In the present situation, a strong southerly flow cannot develop over Texas until the frontal system over the Rockies (see Fig. 5.1f) moves into the western Plains and induces a strong lee-side trough. By contrast, on 6 April, the return flow strengthened in the strong pressure gradient zone between the developing lee-side trough and the retreating polar anticyclone. Thus, a new H cycle is not possible, and the subsequent synoptic patterns do not follow the typical early-season sequence outlined in the conceptual



model of Chapter 3. In such a scenario, the forecaster must analyze the situation and evaluate how the features of the severe-storm environment will be different from the ideal case, and adjust his/her forecast accordingly.

## Chapter 6

NUMERICAL SIMULATION OF THE 4-9 APRIL 1984 LID CYCLE  
WITH THE PENN STATE/NCAR MESOSCALE MODEL

The analysis of the 4-9 April 1984 lid cycle in the last chapter raises interesting questions about some of the physical processes operating over North America and the Gulf of Mexico during the various stages of the cycle. The Penn State/NCAR mesoscale model (MM4) is utilized to examine certain aspects of the large scale environment during various stages of this lid cycle. Using a mesoscale model to examine an example of an early-season lid cycle allows us to gain a better understanding of the relevant physical processes than is possible from simply studying the composite datasets from the synoptic climatology. The results of both the observational study (Chapter 5) and the modeling study (Chapter 6) can then be used to refine specific aspects of the synoptic climatology. This chapter begins with a summary of the general characteristics of MM4, and the special modifications that were made for this case. A general evaluation of the model simulation is then in order to determine the degree to which MM4 reproduces critical aspects of the 4-9 April lid cycle. Finally, we examine some of the physical processes operating during various stages in the cycle.

## 6.1 MM4 Characteristics

### 6.1.1 General Description

For a specific discussion of the model equations and physical parameterizations, the reader is referred to Anthes and Warner (1978) and Anthes et al. (1987). The model is three-dimensional, hydrostatic, and uses the flux form of the primitive equations to predict horizontal wind, temperature, surface pressure, and specific humidity. The model's vertical coordinate, sigma ( $\sigma$ ), is defined as follows:

$$\sigma = (p - p_{top}) / (p_{sfc} - p_{top}), \quad (6.1)$$

where  $p$  is pressure,  $p_{top}$  is the pressure at the top of the model, and  $p_{sfc}$  is the surface pressure. A staggered horizontal grid is used, where the momentum variables are defined at "dot" points and the other variables are defined at "cross" points, following the "B" grid of Arakawa and Lamb (1977). See Fig. 4.1 in Anthes et al. (1987) for a schematic diagram of the staggered horizontal grid system. The model variables are also staggered in the vertical, with vertical velocity ( $d\sigma/dt$ ) diagnosed at the "full  $\sigma$  levels," and the other variables defined at "half  $\sigma$  levels" which are located halfway between the full  $\sigma$  levels. The model's initial meteorological conditions are generated in several steps. First-guess fields of the predictive variables are derived from archived 2.5° latitude/longitude surface and pressure-level analyses from the European Centre for Medium-Range Weather Forecasting (ECMWF), available every 12 h. An objective analysis takes the

rawinsonde and surface observations, and uses a set of isotropic and anisotropic weighting functions (see Benjamin and Seaman 1985) to modify the initial fields at both the surface and user-specified pressure levels. The version of the model used in this study employs "relaxation" lateral boundary conditions, which essentially "nudge" the predictive variables toward a large scale analysis (Davies and Turner 1977). The lateral boundary conditions are also defined using 12-hourly surface and rawinsonde data available during the period of the model simulation. The objectively analyzed fields are interpolated to the model sigma levels, and a static initialization procedure is used to remove the vertically integrated column divergence from the initial windfields (Washington and Baumhefner 1975).

The model parameterizations include second-order vertical and horizontal diffusion, a "slab" surface energy budget equation with surface radiation effects (Benjamin 1983), a high-resolution PBL (Blackadar 1976, 1979), and a moist convection scheme (Kuo 1974; Anthes 1977). An important feature of the cumulus parameterization is the cloud base/top determination and stability check. This procedure determines the equivalent potential temperature,  $\theta_e$ , of an air parcel most likely to form a cloud, and determines the lifting condensation level (LCL) for that parcel. The saturation  $\theta_e$  is then computed for all levels above the LCL until a "parcel equilibrium level" is found (overshooting is also accounted for). If the cloud thickness  $\delta\sigma$  is below a threshold of 0.3, then convection is not permitted. Following this, the available buoyant energy (ABE) of the grid column is computed,

and convection is allowed only if the ABE is positive (see Eq. 3.5.27 in Anthes et al. 1987).

#### 6.1.2 Specific Characteristics of the Version of MM4 Used in This Study

Several features of MM4 were specifically modified for this study. First, a horizontal diffusion procedure designed by Benjamin (1983) was adapted for use in this modeling study. In this procedure, second-order diffusion of the predictive variables is performed on pressure instead of sigma surfaces, in order to prevent heat and moisture from being diffused upslope in areas of strong topographic gradients. This is especially important in our case, in which steep terrain exists over areas such as the Rocky Mountains and the Sierra Madre ranges of Mexico. In this study, the pressure-level diffusion scheme was applied at every level in the model atmosphere except at the top and bottom levels. In addition to the pressure-level diffusion, a factor, DFAC, was introduced to modify the horizontal diffusion coefficient,  $K_h$ , given by

$$K_h = (A \times DFAC) (K_{ho} + 2.9 \times 10^8 D), \quad (6.2)$$

where A is an amplification factor that is a function of location on the model domain,  $K_{ho}$  is a background horizontal diffusion term that is a function of grid size and time step, and D is a horizontal wind deformation term (Smagorinsky et al. 1965), which is typically on the order of  $10^{-5} \text{ s}^{-1}$ . In this study,  $K_{ho} = 3 \times 10^4 \text{ m}^2 \text{ s}^{-1}$ , and the constant multiplied by the deformation is on the order of  $10^3 \text{ m}^2 \text{ s}^{-1}$ . In this model version, DFAC was reduced to 0.2 (it normally is set = 1.0) in

order to reduce the effects of the horizontal diffusion (Stauffer, personal communication). Since it is also important to minimize the vertical diffusion in this simulation in order to properly maintain the inversion associated with the lid, the background value of the vertical diffusion coefficient was reduced from its default value of  $1.0 \text{ m}^2 \text{ s}^{-1}$  to  $0.1 \text{ m}^2 \text{ s}^{-1}$ . For more details on the horizontal and vertical diffusion schemes, see sections 3.1 and 3.4 in Anthes et al. (1987).

A unique aspect of this modeling study is the multiple time and space scales that prevail during the period of interest. Since a typical early-spring lid cycle length is about seven days (see section 3.3.1), this necessitates using a large model domain and performing long simulations. The typical lid-cycle time scale is well beyond the normal simulation length for most mesoscale models. However, exceptions exist such as the Saharan dust layer study of Karyampudi and Carlson (1988), and the four-dimensional data assimilation (FDDA) studies of Seaman et al. (1991). The first study used a horizontal grid spacing of 220 km with 13 vertical levels, and a  $51 \times 31$  domain. The simulations were 120 h in length, and used data from the GARP Atlantic Tropical Experiment to study the formation and evolution of the Saharan dust layer from its source region over North Africa to its elevated downstream location over the tropical Atlantic Ocean. The FDDA studies covered a smaller area (the eastern two-thirds of the continental U.S.), using an 80-km horizontal mesh and 15 vertical levels to produce 120-h simulations that were continuously adjusted by the assimilation of both surface and rawinsonde observations. The present study is similar to these two in terms of the simulation length (120 h), but it differs from

them in terms of using a finer horizontal grid mesh (60 km), 30 vertical levels, and a large domain (118 x 68, covering  $2.9 \times 10^7 \text{ km}^2$ ). Also, no data assimilation was employed. The lateral boundary conditions are over oceanic regions along every border except the northern one. This means that the model simulation will be almost like a true forecast, since the ECMWF first-guess analyses are primarily determined by their prediction model over these data-sparse regions.

The model domain used in this study is shown in Fig. 6.1, and the location of the sigma levels is shown in Table 6.1. Determining the location of the vertical levels is based on the experience with previous studies of the severe-storm environment (e.g., Benjamin and Carlson 1986; Lakhtakia and Warner 1987; Lanicci et al. 1987), as well as computations of the levels of relative humidity breaks, and EML bases and tops throughout the entire lid cycle. Analysis of sounding data for this period led to the strategy of concentrating more than half of the sigma levels below 700 mb. The combination of a large domain and long simulation length, along with the fine horizontal and vertical grid structures, allows us to examine not only the larger scale processes that are important in the lid cycle, but also the finer structures that are created on smaller time scales. The severe-storm environment simulations of Anthes et al. (1982) showed that a mesoscale model initialized with synoptic-scale data was capable of generating and maintaining mesoscale phenomena in the 0-24 h time period, and suggested that such features are predictable over time periods longer than their individual lifetimes. Studies of the entire cycle of moist layer evolution over the Gulf of Mexico (e.g., Johnson 1976; Karnavas 1978;

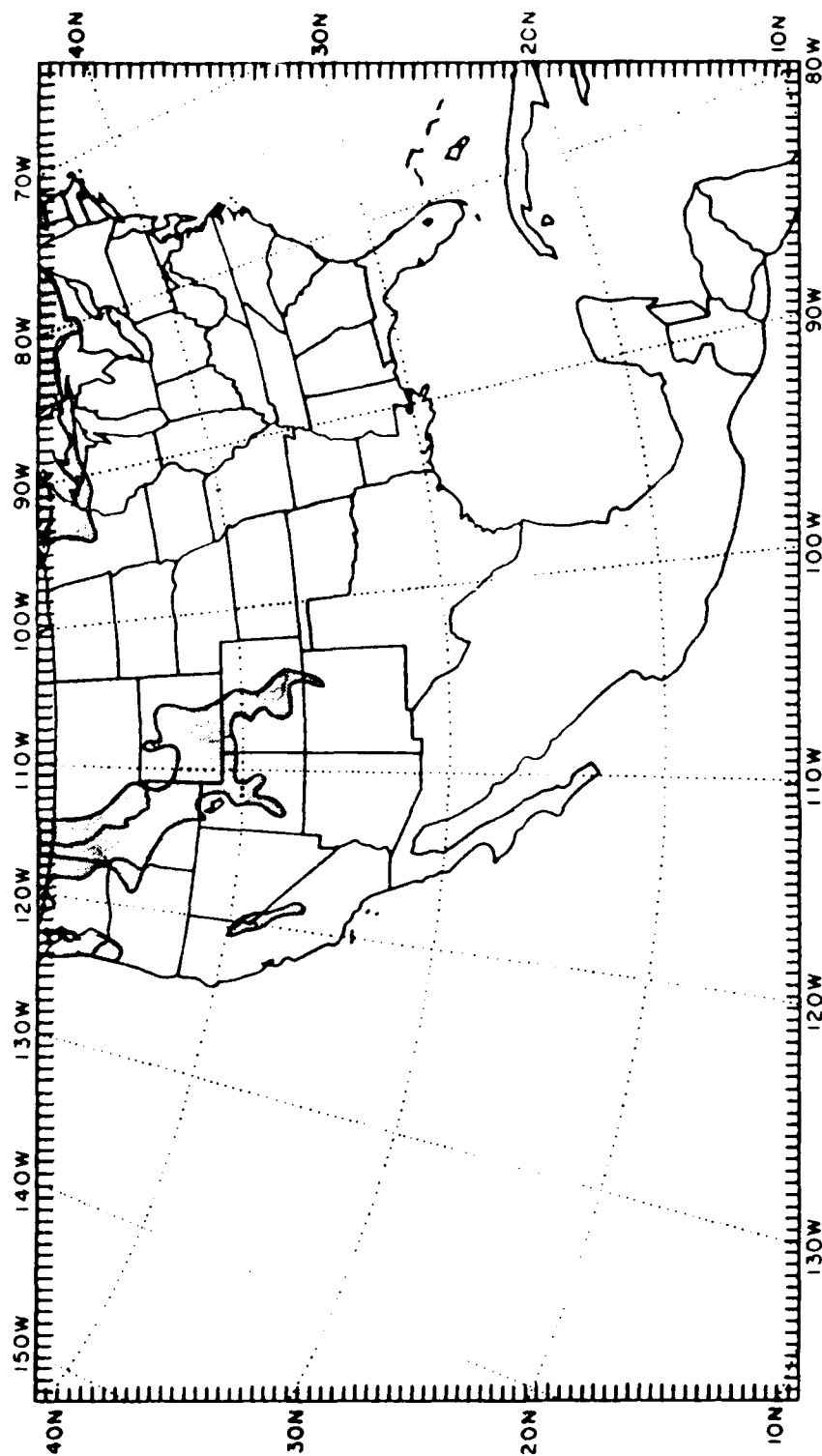


Figure 6.1. Map of the model domain showing the location (shaded areas) of the persistent snow cover used for the simulation.



Table 6.1 Full and Half Sigma Levels and Standard Pressure  
(assumed  $P_{sfc} = 1000$  mb) For MM4

Vertical Index	Full Sigma Level	Standard Pressure (mb)	Half Sigma Level	Standard Pressure (mb)
1	0.000	100.0		
2	0.090	181.0	0.045	141.5
3	0.170	253.0	0.130	217.0
4	0.250	325.0	0.210	289.0
5	0.310	379.0	0.280	352.0
6	0.370	433.0	0.340	406.0
7	0.430	487.0	0.400	460.0
8	0.470	523.0	0.450	505.0
9	0.510	559.0	0.490	541.0
10	0.550	595.0	0.530	577.0
11	0.590	631.0	0.570	613.0
12	0.630	667.0	0.610	649.0
13	0.670	703.0	0.650	685.0
14	0.690	721.0	0.680	712.0
15	0.710	739.0	0.700	730.0
16	0.730	757.0	0.720	748.0
17	0.750	775.0	0.740	766.0
18	0.770	793.0	0.760	784.0
19	0.790	811.0	0.780	802.0
20	0.810	829.0	0.800	820.0
21	0.830	847.0	0.820	838.0
			0.840	856.0

Table 6.1 (continued)

Vertical Index	Full Sigma Level	Standard Pressure (mb)	Half Sigma Level	Standard Pressure (mb)
22	0.850	865.0		
23	0.870	883.0	0.860	874.0
24	0.890	901.0	0.880	892.0
25	0.910	919.0	0.900	910.0
26	0.930	937.0	0.920	928.0
27	0.950	955.0	0.940	946.0
28	0.970	973.0	0.960	964.0
29	0.990	991.0	0.980	982.0
30	1.000	1000.0	0.995	995.0

Wade et al. 1988) indicate that in order to understand properly the physical processes involved in the polar air modification and return flow, it is necessary to examine the data over periods as long as five days. In the 4-9 April case evaluated here, the creation of the two EMLs and moist layer took place over several diurnal heating cycles, subsequently leading to the creation of the sharp gradients of moisture and lid strength observed over the southern Plains some 72 h after the beginning of the cycle.

Considerable effort was made in determining appropriate surface boundary conditions for the model simulation. An accurate specification of snow cover, soil moisture availability, and sea-surface temperatures (especially in the Gulf of Mexico) is essential because of the length of the simulation. Determination of the snow cover over the model domain must result in a field that is representative of the "mean," or persistent snow cover conditions over the domain during the five-day period. The method we used employs the National Oceanic and Atmospheric Administration's (NOAA) weekly satellite-based snow cover analyses. Analyses covering the periods 26-31 March and 2-8 April were examined, and overlaps between the two analyses were used to define persistent snow cover areas. Studies of the NOAA analyses by Wiesnet et al. (1987) have determined that these NOAA analyses are more representative of the end of the chart period, so overlaps in the snow cover for these two periods (26-31 March; 2-8 April) should yield a reasonable representation of persistent snow cover for the 4-9 April case study. The results of the NOAA analyses were cross checked against daily snow cover charts available from the National Meteorological Center (NMC) and

GOES visible satellite imagery, to validate their accuracy. The resulting snow cover analysis is shown in Fig. 6.1.

The sea surface temperature (SST) analysis over the Gulf of Mexico is likely to be crucial to an accurate simulation of the moist layer during this lid cycle. Archived SST data are available on the 2.5° latitude/longitude grid for the ocean portions of the model domain. Over the Gulf, however, such a coarse grid mesh cannot resolve features such as the Loop Current, which has been shown to be potentially important in the modification of polar airstreams passing over it (Molinari 1987). A composite 50-km SST analysis for 5-10 April 1984 over the Gulf and western Caribbean from the Marine Products Branch of the NMC was chosen to represent the model SST over this area. The accuracy of the NMC composite analysis was cross checked against 50-km gridded analyses for individual days (3 April and 10 April) during the period of interest. Since the SST changes slowly, use of a five-day mean analysis is deemed appropriate for this study. The data from the NMC composite were then manually digitized onto the appropriate cross point locations of the model grid. The resulting SST analysis is shown in Fig. 6.2. Figure 6.2 reveals the presence of the Loop Current to the north of the Yucatan Peninsula of Mexico, and a strong SST gradient to the north of the current.

Perhaps the most difficult parameter to determine for the model domain is the land-use category, because its determination involves the greatest amount of scientific "guesswork." In MM4, the land-use categories are defined based on a highly detailed, digitized vegetation-cover database. For each category, surface parameters such as soil-

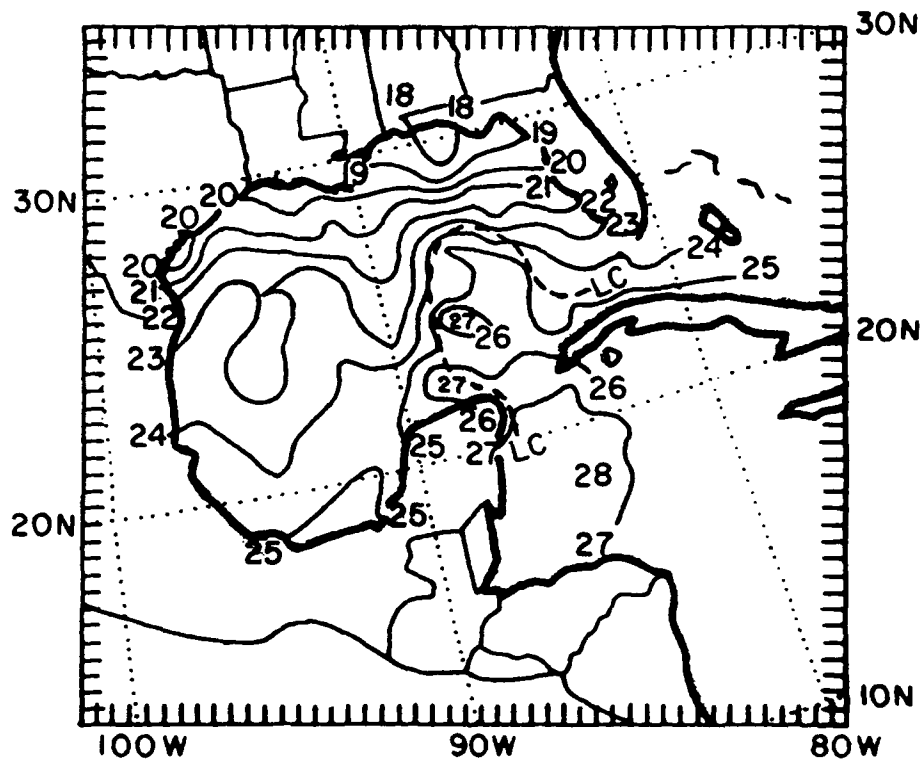


Figure 6.2. Sea surface temperatures (in °C, isoplethed every degree) used in the model over the Gulf of Mexico and adjacent waters. The position of the Loop Current (LC) is marked by the dashed line.

moisture availability, albedo, emissivity, roughness length, and thermal inertia are assigned values that remain spatially and temporally constant. The surface parameters within a land-use category are allowed to vary seasonally from Winter to Summer. The 4-9 April case falls towards the end of the winter "season" (15 October-15 April). The studies of Zhang and Anthes (1982) and Lanicci et al. (1987) found that the model surface parameter which has the greatest effect on the PBL development and the greatest impact on the evolution of the model severe-storm environment is the soil-moisture availability,  $M$ . The value of  $M$  is proportional to  $E/E_p$ , where  $E$  is the surface evaporation from the model surface, and  $E_p$  is the potential evaporation, defined as that occurring from a saturated surface. Previous modeling studies of the lid/severe-storm environment used a set of land-use categories based primarily on rainfall climatology, satellite imagery, and climatological atlases. For this study, the standard MM4 land-use categories were subjectively "blended" with the set from those severe-storm modeling studies, to arrive at a modified set of land-use categories that is tailored to the early-spring rainfall climatology, yet retains the detail of the standard MM4 dataset. The resulting set contains 14 categories, which are described in Table 6.2 and depicted over the model domain in Fig. 6.3.

Table 6.2 Description of MM4 Land-Use Categories and Surface Parameters in This Modeling Study

Land-Use Category	Moisture Avail.	Albedo	Roughness Length (cm)	Emissivity (9 $\mu\text{m}$ wavelength)	Thermal Inertia ( $\text{cal cm}^{-2}\text{K}^{-1}\text{s}^{-\frac{1}{2}}$ )
Desert	0.02	0.25	10.0	0.85	0.02
Urban	0.10	0.18	50.0	0.88	0.03
Range/ Grassland	0.10	0.23	10.0	0.92	0.04
Plateau Coniferous Forest	0.15	0.12	50.0	0.95	0.05
Savannah	0.15	0.20	15.0	0.92	0.03
Transition: Range to Agriculture	0.30	0.23	5.0	0.92	0.04
Colorado/ Utah Conif. Forest	0.30	0.23	50.0	0.95	0.05
Agriculture	0.60	0.23	5.0	0.92	0.04
Deciduous Forest	0.70	0.17	50.0	0.93	0.05
Coniferous Forest	0.70	0.12	50.0	0.95	0.05
Tropical/ Subtropical Forest	0.70	0.12	50.0	0.95	0.05
Mixed Forest & Marsh	0.75	0.14	40.0	0.95	0.06
Marsh	0.83	0.14	20.0	0.95	0.06
Ocean/Lake	1.00	0.08	0.01	0.98	0.06

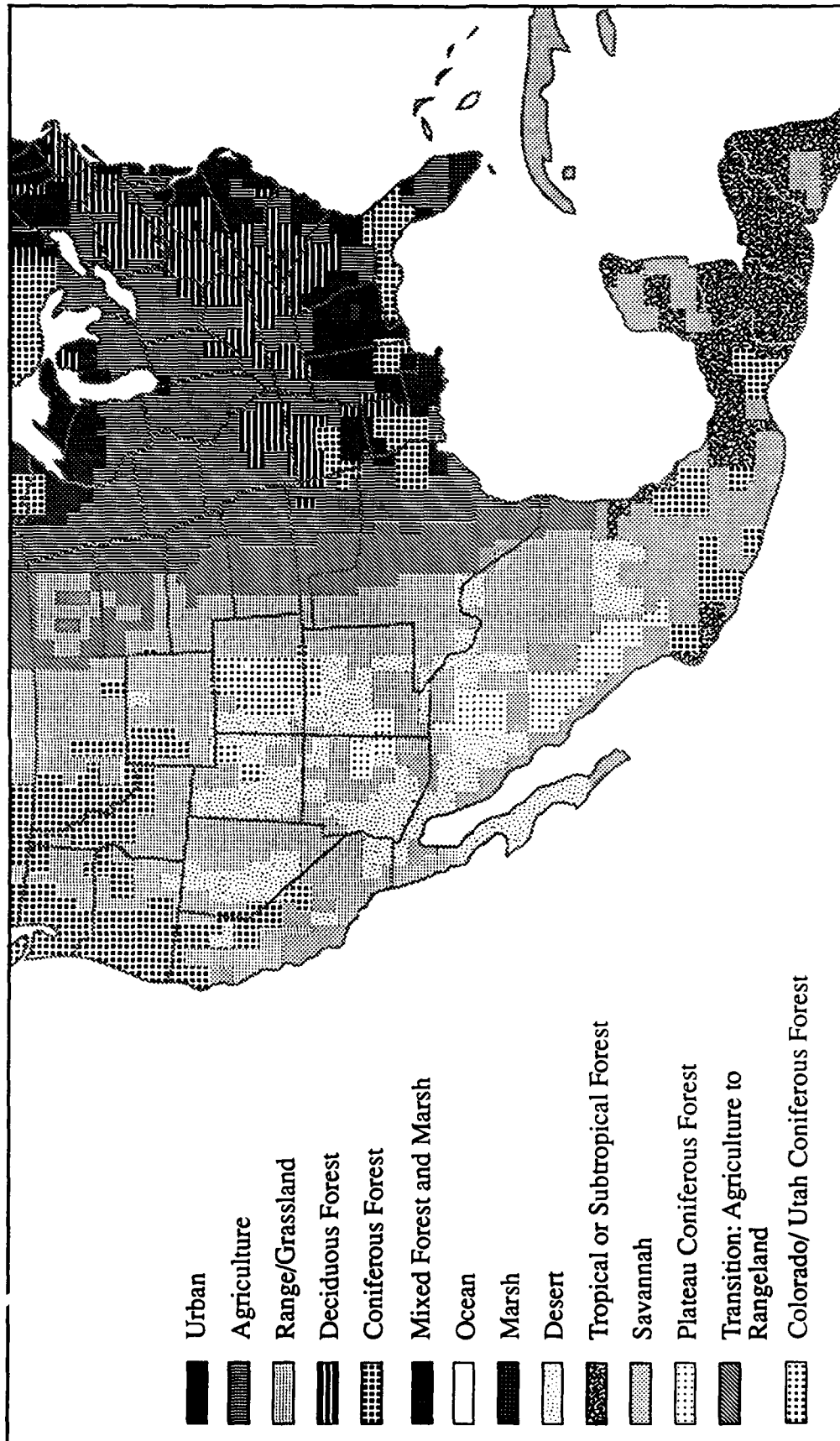


Figure 6.3. Map of the model land-use categories used in this study. A legend is shown to the left of map.



## 6.2 Model Verification of Large Scale Flow Features During the Lid Cycle

Verification of the 120-h simulation begins with a general examination of the evolution of important large scale features at different levels in the atmosphere. During the high-pressure stage, the model simulated the formation of the surface pressure ridge over the southern Plains and western Gulf during the first 24 h of the lid cycle, as well as the movement of the upper trough into the southwestern U.S. The model simulation through the lid-maximum stage continued to be accurate. The model analysis of relevant surface and 500-mb features at  $t = 72$  h (1200 UTC 7 April; Fig. 6.4) reveals an accurate placement of the surface front coming into the western Plains. Although the model only predicts a single surface low over the Oklahoma panhandle, the central pressure is only 2 mb lower than observed and only about 100 km south of the observed position in Fig. 5.1d! The location of the 500-mb trough moving through the western U.S. is also accurate, being only about  $1^\circ$  east of the observed position. Although the simulated dryline shown in Fig. 6.4 is to the east of the observed surface position, it should be noted that the simulated position is based on the  $8 \text{ g kg}^{-1}$  mixing ratio isopleth at  $\sigma = 0.96$ , which is about 36 mb (close to 300 m) above the surface. At 1200 UTC, the vertical moisture slope of the dryline is normally quite small; the simulated surface dryline location is closer to the observed position. Data from the 0.96 sigma level are used for the figure because they are representative of the daytime PBL and are less likely to be noisy.

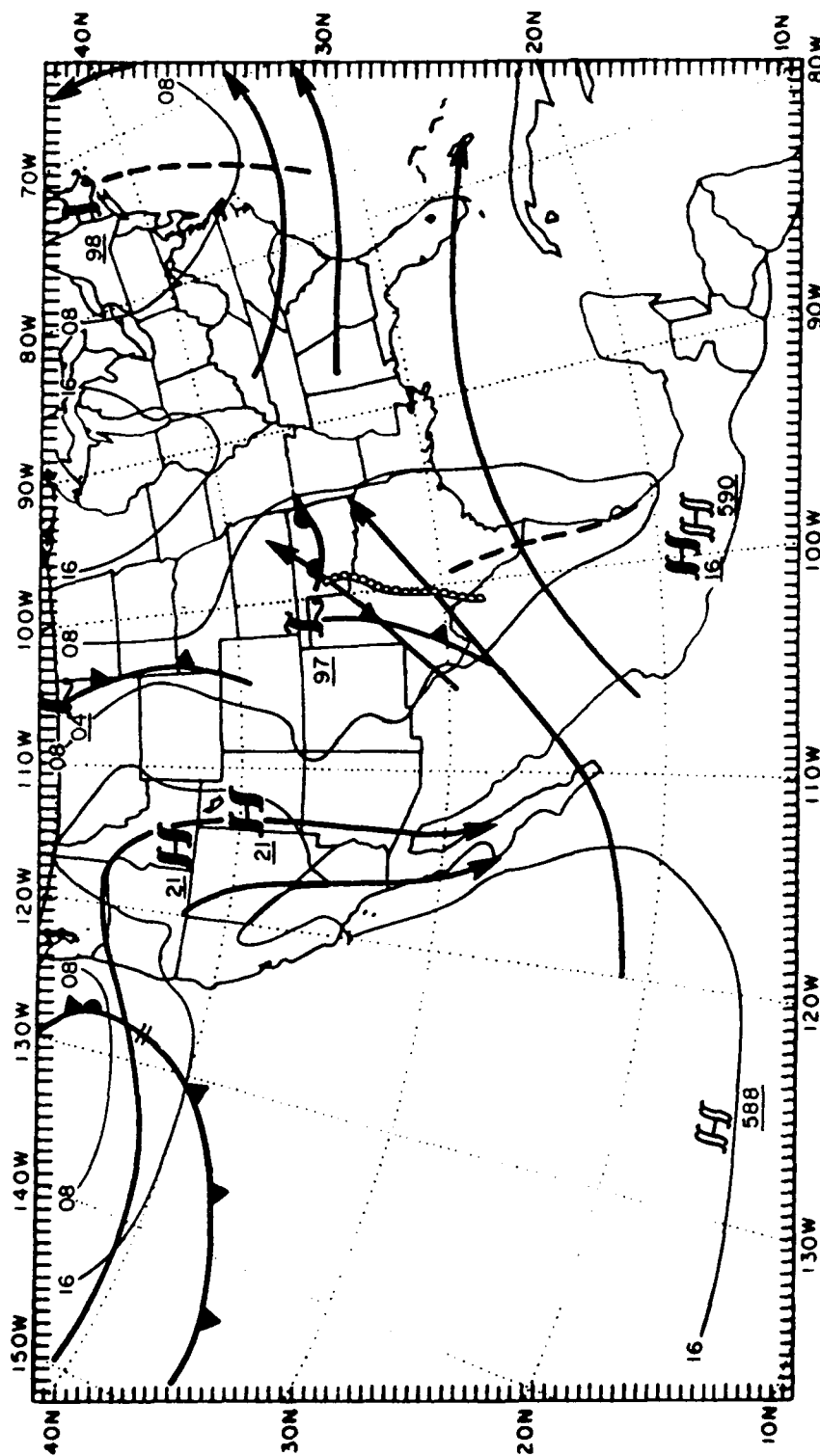


Figure 6.4. Model-derived analysis of surface and 500-mb features at 1200 UTC 7 April 1984. The symbols used are identical to those in Fig. 5.1, except the dryline at  $\sigma = 0.96$  is shown using an open scalloped line.

The most serious problems in the model simulation are phase errors in the positions of the western U.S. frontal system and the upper trough and ridge during the return-flow stage of the cycle (0000 UTC 6 April-0000 UTC 7 April). This error is largest at the 48-h point of the simulation, but then decreases by 72 h. Given the long west-east extent of the model domain (about 7100 km) and the timing of the phase error, we hypothesize that the lateral boundary conditions driven by the ECMWF analyses may be responsible. Investigation of the upper level (above 500 mb) windfields in the model reveals a strong southwesterly jet originating at the boundary near 18°N latitude, 140°W longitude. At the boundary, this jet consistently maintains speeds of 50-70 kt, which the model subsequently moves northeastward towards northern Mexico and the Desert Southwest. The intensity of this jet at the boundary is nearly constant throughout the simulation, but begins to decrease after the 60-h point of the simulation, which is about the time when the phase error starts to lessen. By  $t = 72$  h, the simulated windspeeds are about 10-15 kt slower than they were at  $t = 60$  h. A decrease in the upper level winds at the southwest boundary should decrease the phase error by advecting slower windspeeds towards the northeast. However, a more important factor in the decrease of the model's phase error is the fact that the upper trough over the western U.S. is also deepening during the return-flow and lid-formation stages, resulting in a slower phase speed for the upper level wave.

### 6.3 Examination of Physical Processes Involved in the Formation and Evolution of the EML and Moist Layer

The model simulation of the EML and moist layer is examined using several analysis methods. The EML evolution is investigated by

determining the locations of both the source region (the area which has a deep, surface-based PBL) and the elevated region (the area in which the deep PBL is located aloft). Evaluation of the horizontal and vertical extent of the EML source region and the downstream elevated region is made using model soundings from 159 locations over the domain. The source region at 0000 UTC is determined by locating the soundings which have a surface-based PBL above the 900-mb level that is 1.) well-mixed in terms of potential temperature and mixing ratio, 2.) is at least 80 mb in depth, and 3.) extends to at least 750 mb. The EML soundings at 0000 UTC are determined using criteria (1) - (4) from section 2.2.1. At 1200 UTC, the source-region soundings and EML soundings are distinguished as follows:

- 1) The source-region soundings must be based above 900 mb, and contain a layer at least 80 mb deep with dry static stability below  $4.5^{\circ}\text{C } 100 \text{ mb}^{-1}$ . The base of the layer must extend from the top of a surface-based inversion and must have a top  $\geq 750 \text{ mb}$ .
- 2) The EML soundings must meet criteria (1) - (4) as outlined in section 2.2.1, and the base of the layer must extend from the top of an inversion that is *not* surface-based.

Recall from section 2.2.1 that EML criterion (4) (RH must increase with height in the EML) was dropped in the climatological study, based on instrumentation and reporting considerations, as well as on observational studies of PBL moisture profiles. In the modeling study, criterion (4) is used only to help determine the EML top, in conjunction with the lapse rate of  $\theta$  in the EML.

A second technique that is used to examine both the EML and the moist layer employs "parcel" trajectories calculated from the model output fields. The trajectory scheme is used to evaluate the horizontal and vertical evolution of the parcels making up the EML and moist layer. Evaluation of the horizontal and vertical parcel displacements reveals information about the dynamical processes taking place during various stages of the lid cycle. Additionally, interpolated grid-point values of  $\theta$  and  $q$  along the trajectory are examined in order to determine the extent of diabatic modifications to the EML and moist-layer parcels from surface heating/cooling and evaporation within the model PBL.

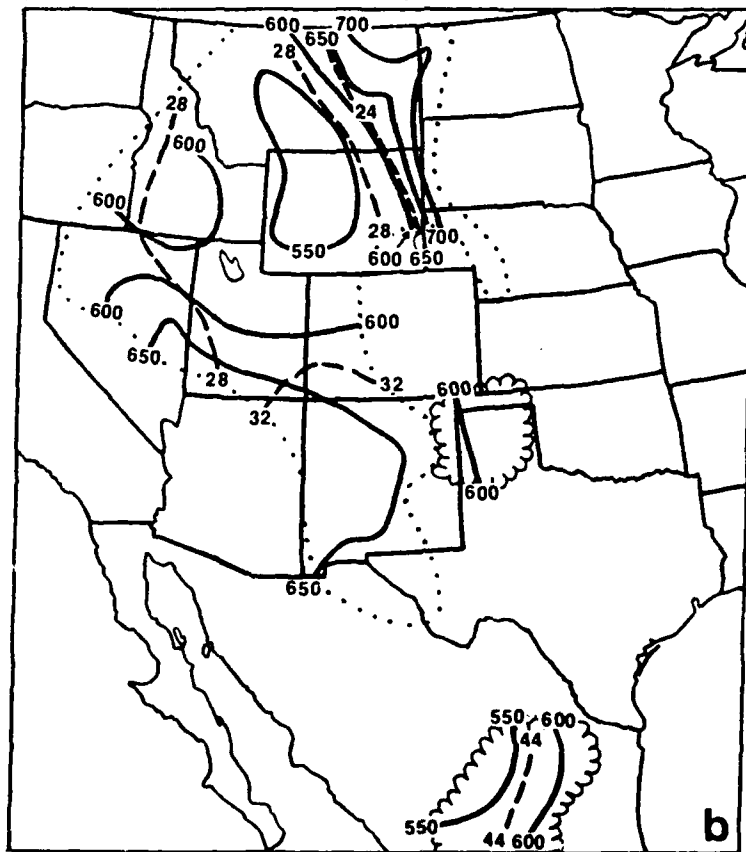
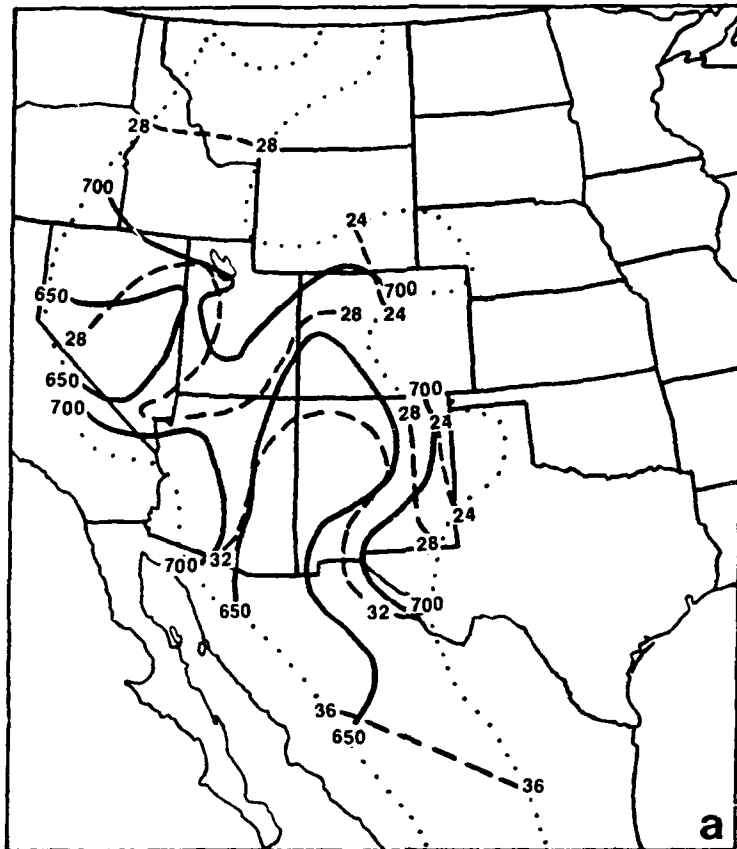
#### 6.3.1 Formation of the Western U.S. and Mexican EMLs

In Chapter 5, it was determined that separate EMLs evolved over the western U.S. and northern Mexico during the high-pressure and return-flow stages of the 4-9 April lid cycle. It was shown that the western U.S. EML source region formed over the Desert Southwest during the afternoon of 4 April, and that the presence of the subtropical jet and its associated region of subsidence over northern Mexico prevented the Mexican source region from activating until 24 h later. The two EMLs were observed to evolve separately until 0000 UTC on 7 April, when they began to merge over the western Plains and Texas (see Fig. 5.12a).

An analysis of the simulated EML source region at 0000 UTC on 5 April is shown in Fig. 6.5a. At this time, a deep, well-mixed PBL is observed from western Montana into northern Mexico. The highest PBL tops (above 625 mb) are observed over central Nevada, western New Mexico, and southeastern Arizona. Mean PBL  $\theta$  values over the western U.S. are



Figure 6.5     EML source-region and elevated-region analysis for a) 0000 UTC 5 April and b) 1200 UTC 5 April. Location of model-generated EML source region is outlined by dotted lines. Location of the elevated region is outlined by scalloped lines. Mean potential temperature in the source/elevated region ( $^{\circ}\text{C}$ ) is shown by dashed lines and is isoplethed at  $4^{\circ}\text{C}$  intervals; the pressure at the top of the layer is shown by the solid lines, is labelled in mb, and is isoplethed every 50 mb.





mainly in the upper 20's to lower 30's ( $^{\circ}\text{C}$ ), and are in the mid 30's over northern Mexico. By  $t = 24$  h (1200 UTC 5 April), the EML source region has generally shifted to the north and east (see Fig. 6.5b). As in the observations (Fig. 5.6c), the EML source-region soundings have higher tops at 1200 UTC over Wyoming and Montana, while the thermal stratification over northern Mexico has become more stable since 0000 UTC, and does not meet the criteria for an EML source region.

An example of the lower-tropospheric stabilization over northern Mexico is shown by the series of model soundings taken over Torreon (Fig. 6.6a; location is shown in Fig. 6.7). Noticeable warming and drying took place in the 600-750 mb layer over Torreon during the 0000-1200 UTC period, while the winds in the layer became more westerly. The evolution of representative air parcels comprising the surface-600 mb layer of the 1200 UTC sounding is evaluated by means of 24-h backward-in-time trajectories originating at Torreon, commencing at 1200 UTC on 5 April, and ending at 1200 UTC 4 April. Use of such backward trajectories reveals information about the source-region characteristics of the air making up the lowest 300 mb of the 1200 UTC 5 April sounding. The results of the backward trajectories show that the stable air in the lowest 300 mb came from vastly different sources, as displayed by the horizontal trajectory history in Fig. 6.7. The horizontal trajectories in Fig. 6.7 indicate a great deal of veering wind shear between the lower and middle troposphere, which is also reflected in the soundings of Fig. 6.6a. This shear is caused by a combination of the southward advancing polar anticyclone to the east of the plateau, which causes the low level flow to have an easterly component, and the strong westerly

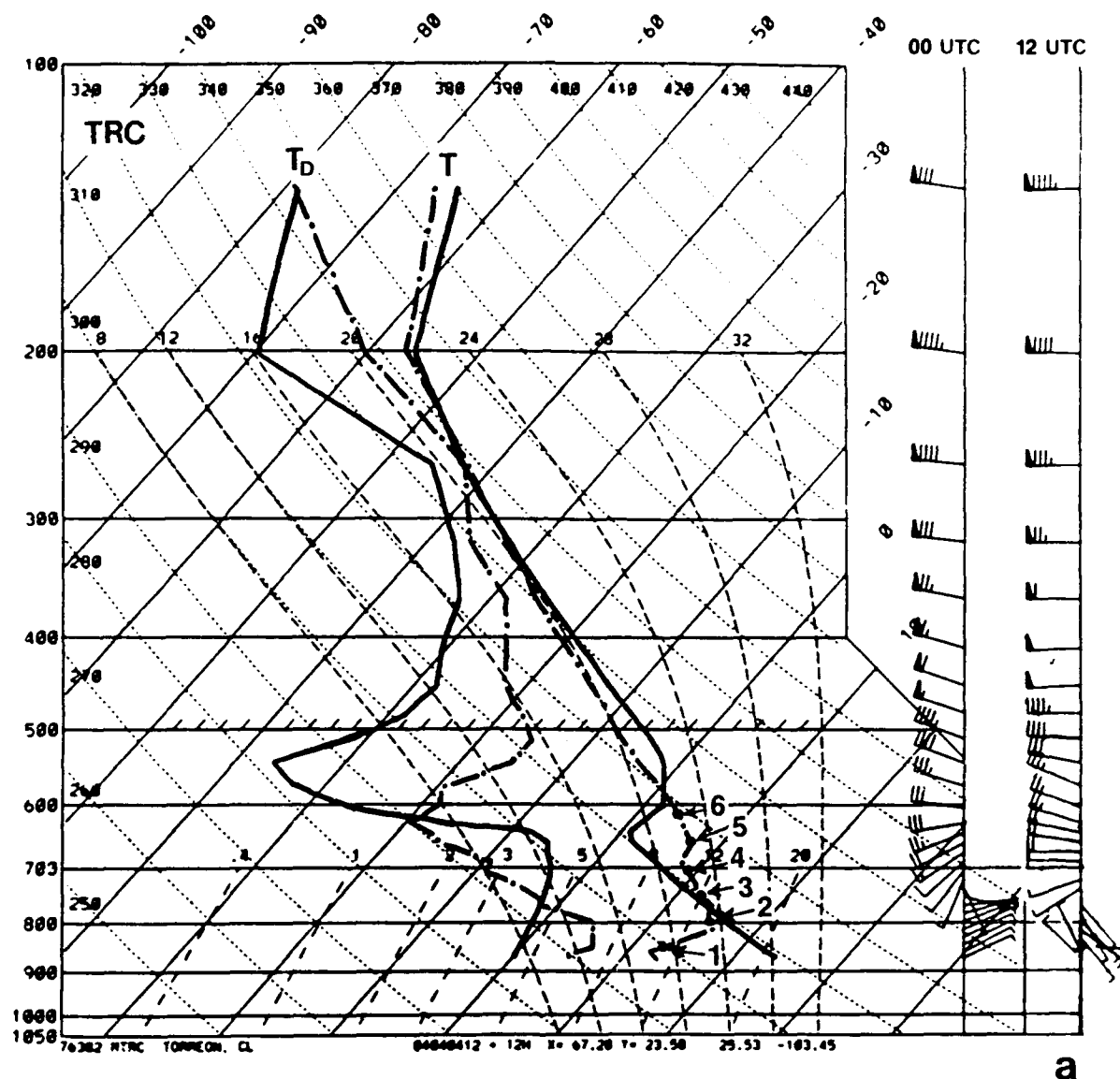


Figure 6.6 Model temperature/dewpoint soundings (skew T log P) for 0000 UTC (solid lines) and 1200 UTC (dot-dashed lines). Locations of soundings are a) Torreon, Mexico (TRC); b) Albuquerque, New Mexico (ABQ); and c) Lander, Wyoming (LND). Wind profiles for both times are displayed at the right; wind speeds are in kt. The parcel locations for the trajectories discussed in the text are shown by large solid dots with numbers.



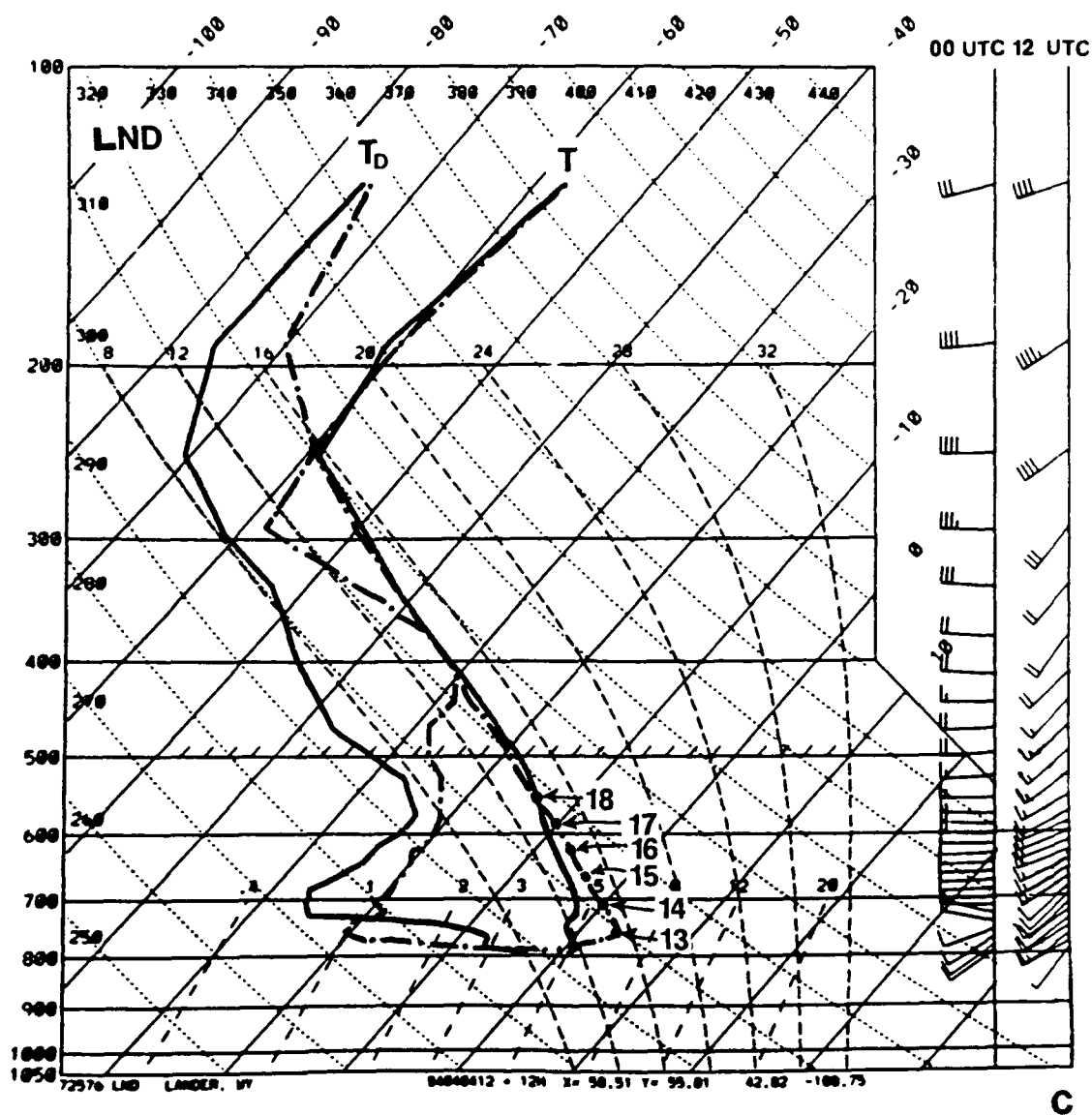


Figure 6.6c.

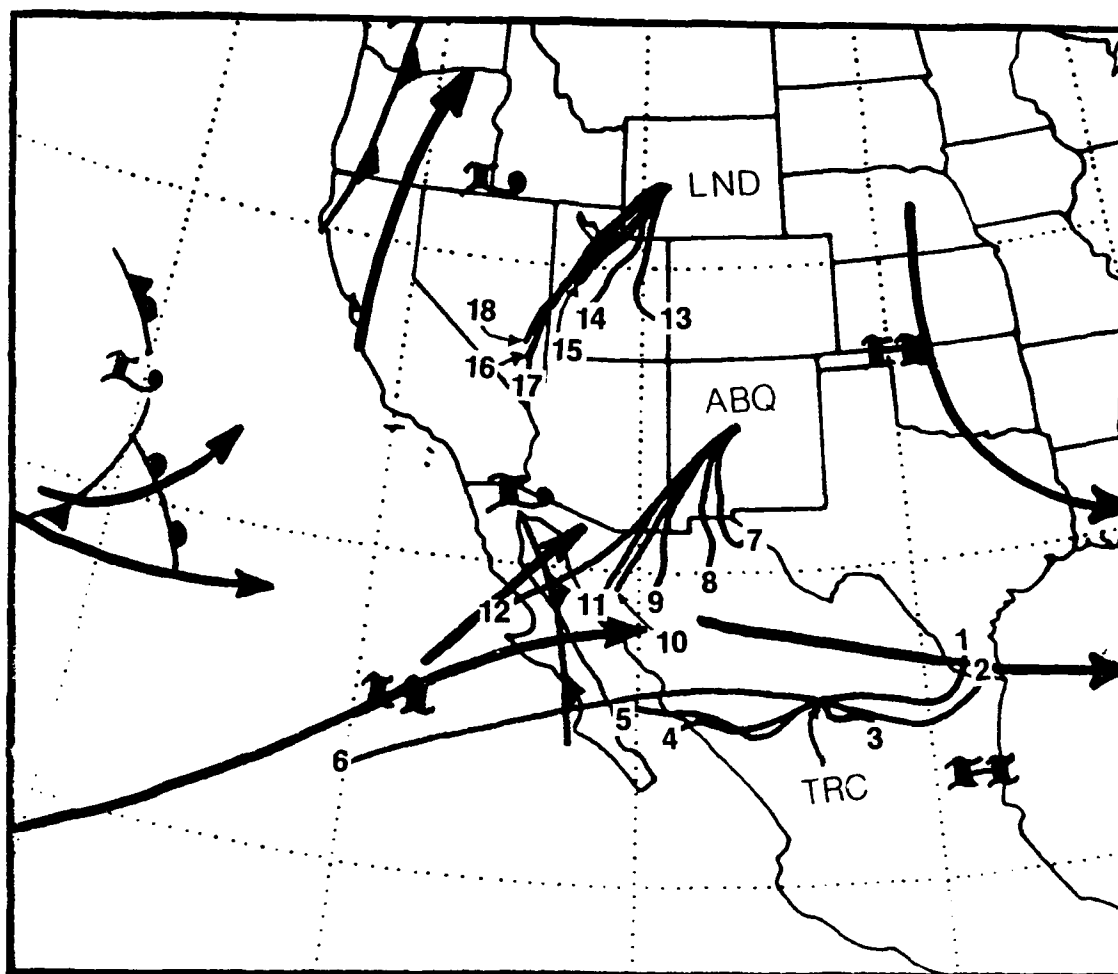


Figure 6.7 Horizontal parcel trajectories for the three sounding locations in Fig. 6.6. Trajectories are displayed as thin, solid lines and are labelled with numbers. Simulated surface and 500-mb features are shown for the temporal midpoint of the trajectories (0000 UTC 5 April) and are shown using the notation of Fig. 5.1.

flow aloft due to the presence of the subtropical jet over northern Mexico.

Potential temperature and vertical displacement (using sigma coordinates) histories for these parcels were also prepared, and are shown for Torreon in Figs. 6.8a and b, respectively. The potential temperature history shows that the distinctive source regions for the Torreon sounding have vastly different initial potential temperatures. Parcels 1-5 experience different degrees of diabatic heating during the first 12 h of the simulation, which lessens some of the original  $\theta$  difference between them, but is not enough to eliminate the vertical variation in  $\theta$ . The vertical displacement history shows that the lowest three parcels either maintain a constant elevation above local terrain or rise slightly during the 24-h period. The amount of time spent by parcels within the lowest 100 mb of the model atmosphere during the daytime heating cycle explains the reason for the varying amounts of diabatic heating they receive during the day on 4 April. Notice that parcels 1 and 2 spent the entire period within the lowest layers, and they experience the greatest amount of  $\theta$  increase during the first 12 h of the simulation (around 8-12°C). Parcels 4 and 5 experience subsidence relative to the local surface through the first 15 h of the simulation. An examination of the pressure-level displacements for all six parcels (not shown) reveals that parcels 5 and 6 also subside with respect to pressure, but parcel #4 actually experiences a 24-h net rise in elevation, suggesting that the local terrain "rises" below that parcel during this period.

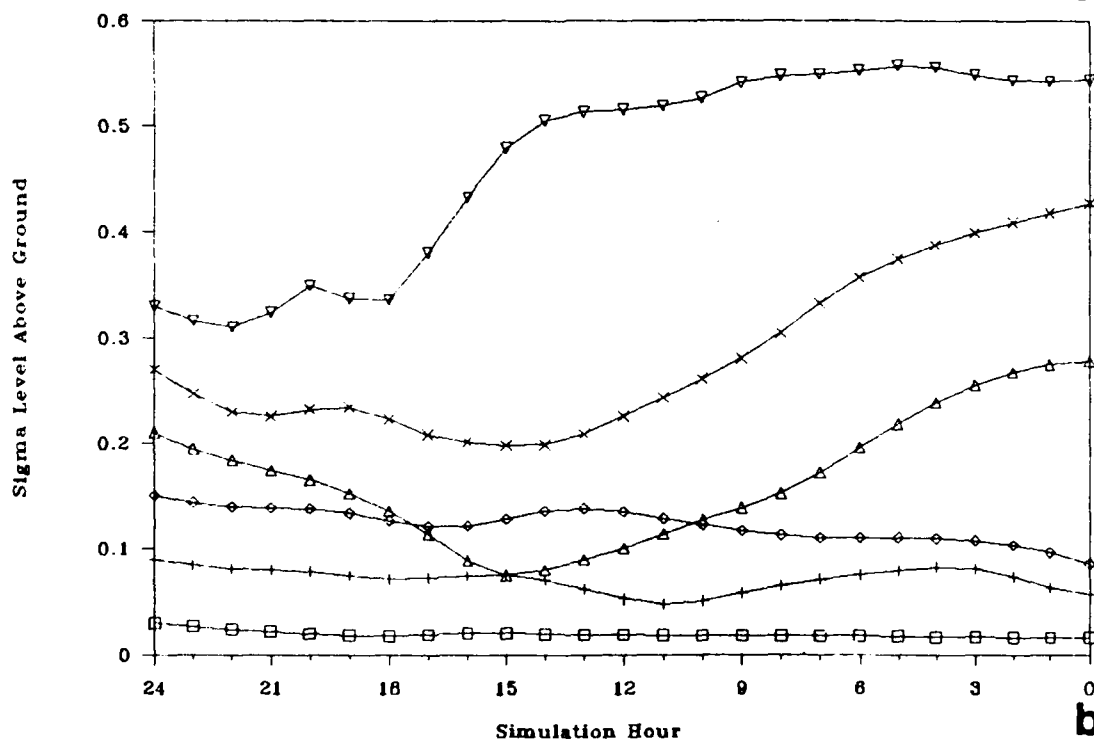
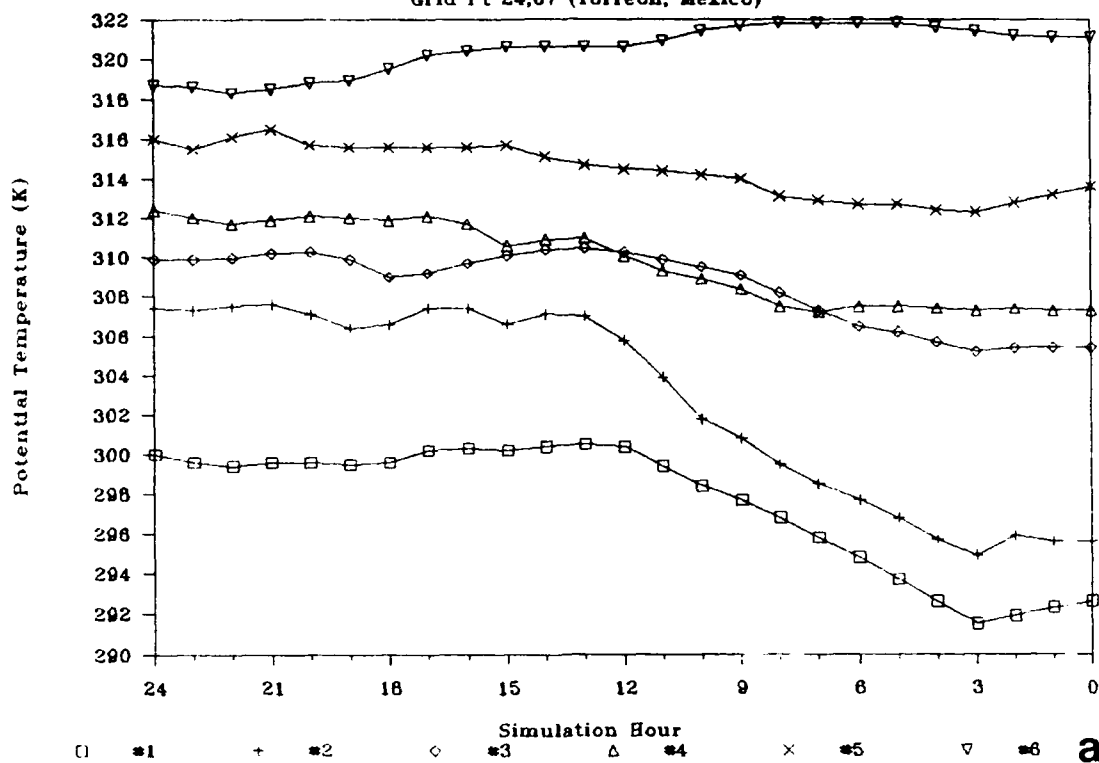


Figure 6.8      Parcel histories for the trajectories originating at the three sounding locations in Fig. 6.6. Potential temperature history is shown in panels (a), (c), and (e). The ordinate displays the potential temperature (in K), and the abscissa shows the hour of the simulation (note that time is read from right to left). A key below the abscissa indicates the symbols used to denote each parcel. Vertical displacement history is shown in panels (b), (d), and (f). The ordinate displays the sigma level above the local surface (see Eq. 6.1 for a definition of the sigma vertical coordinate; the ordinate value is obtained by subtracting the sigma value from 1.0). The abscissa and the legend are the same as in the potential temperature histories.



## Parcel Histories

Grid Pt 24,67 (Torreon, Mexico)



## Parcel Histories

Grid Pt 41,62 (Albuquerque, New Mexico)

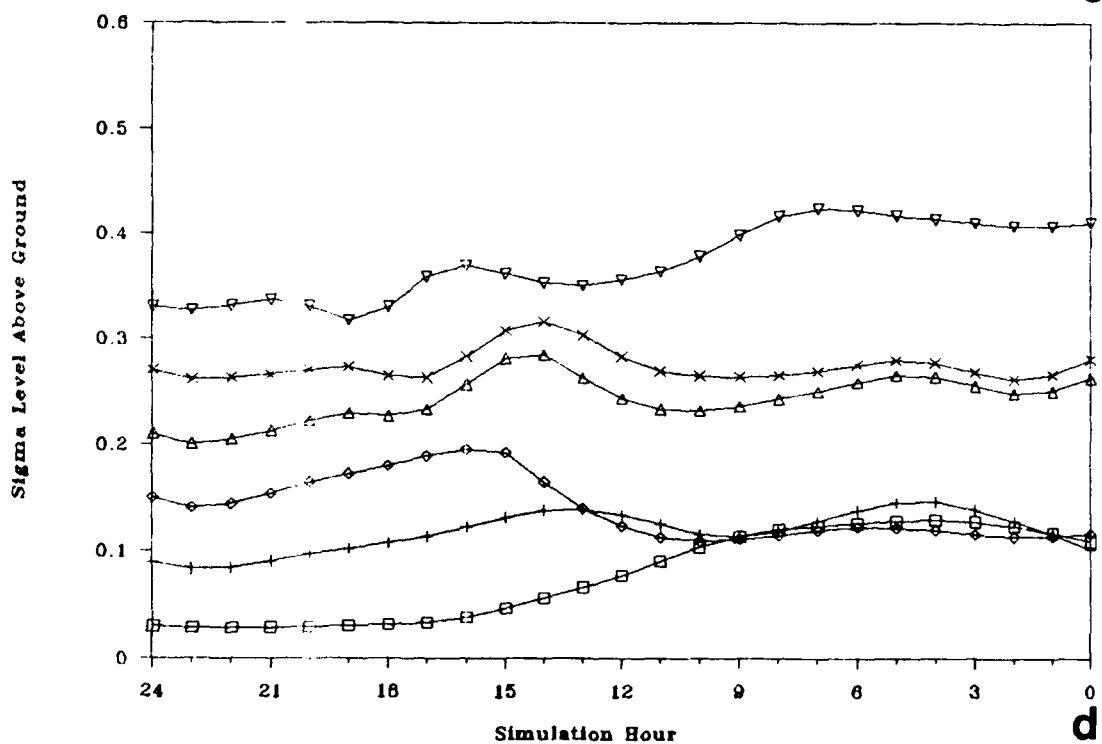
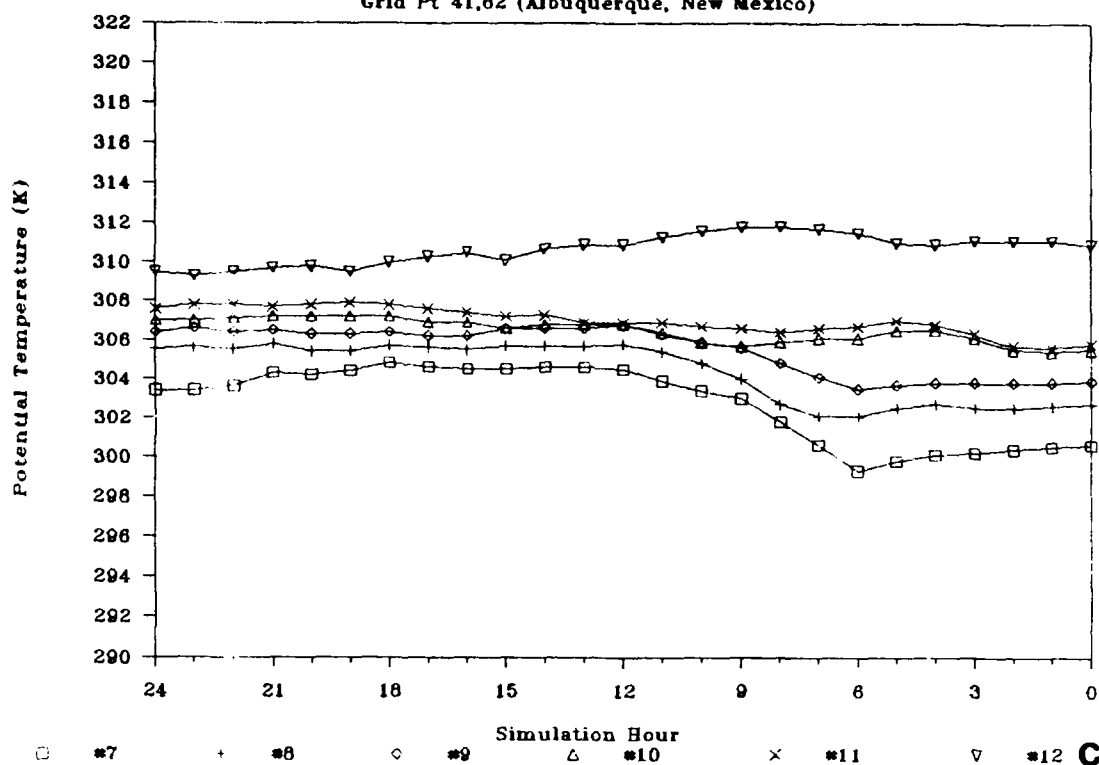


Figure 6.8. (Continued)

## Parcel Histories

Grid Pt 55,58 (Lander, Wyoming)

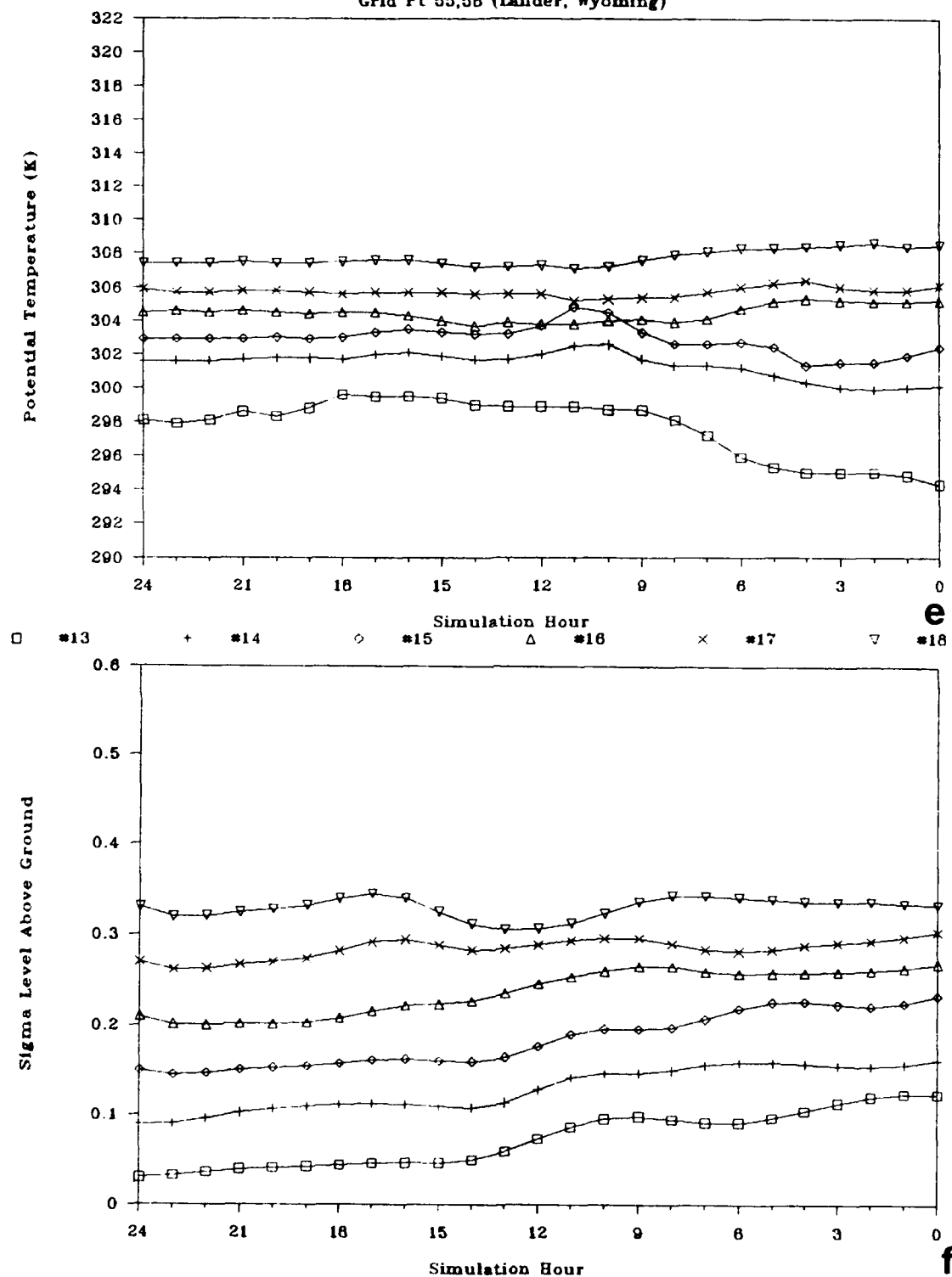


Figure 6.8. (Continued)

As shown in Fig. 6.5, the area to the north of the subtropical jet maintains its EML source-region characteristics after 0000 UTC on 5 April. A series of model soundings for the 0000-1200 UTC period at Albuquerque, New Mexico, is shown in Fig. 6.6b. In contrast to Torreon, the deep PBL at 0000 UTC is mainly preserved during the next 12 h, and the winds develop an increased southerly component. Backward trajectories originating from this location were prepared, distributed over the lowest 200 mb of the atmosphere. The horizontal trajectories (Fig. 6.7) show less diversity in source region than did those for Torreon, and there is also less veering wind shear. The low level airstreams over New Mexico were not influenced as much by the advancing surface anticyclone as they were near Torreon, mainly because of the higher terrain elevations. Consequently, the parcels making up the potential temperature history of the Albuquerque sounding (Fig. 6.8c) have greater "isentropic homogeneity" (i.e., the  $\theta$  values of the parcels are relatively close) than do the parcels from the Torreon sounding. Parcels 7-9 experience the greatest diabatic heating during the first 12-h period, their  $\theta$  values approaching those of parcels 10-12. The vertical displacement history (Fig. 6.8d) shows that parcels 7-9 spent the first 12 h within the lowest 100 mb of the model atmosphere. Net vertical displacements for the 24-h period show that five of the six parcels experience net sinking motion relative to the local surface, although the magnitude is less than for parcels 4-6 at Torreon. However, the pressure-level displacements indicate that all 6 parcels rose in absolute elevation during the same period. Given the information displayed in Figs. 6.7 and 6.8c,d, it appears that the EML

observed over New Mexico on the morning of 5 April originates over northwestern Mexico in a generally weak, southerly to southwesterly flow just to the west of the upper level ridge during this time. Examination of midlevel tropospheric lapse rates over northwestern Mexico at 1200 UTC 4 April (see Fig. 5.6a) reveals that this was an area of relatively low static stability (near  $7^{\circ}\text{C km}^{-1}$  in the 700-500 mb layer), located between two stable areas over Colorado and southern Baja. While the static stability in this area was not extremely low, the parcels in the layer had enough isentropic homogeneity so that the diabatic modification of the lowest half of the layer during its transit over the Desert Southwest results in the production of a low-static stability layer over Albuquerque at the end of this 24-h period.

The third area of interest in the early development of the EML source region is over Wyoming and Montana. Most of this region did not have a static stability low enough to be considered an EML source region at 0000 UTC on 5 April, but had EML source-region soundings with tops above 525 mb 12 h later. An example of the evolution of the thermal structure over this area is shown by the series of model soundings for Lander, Wyoming, for 0000 UTC and 1200 UTC, in Fig. 6.6c. A gradual destabilization occurs from the surface to 400 mb during the 12-24 h period, with warming below about 550 mb and slight cooling above. As at Albuquerque, the winds become more southerly during this period. If one computes the static stability in the 750-500 mb layer on the 1200 UTC sounding, it is approximately  $3.5^{\circ}\text{C 100 mb}^{-1}$ , which is at the stable end of the EML range (see Fig. 2.2). However, this layer is in the early

stages of development as an EML source region, as suggested by the  $q$  profile in Fig. 6.6c, which is nearly well-mixed throughout the 750-500 mb layer.

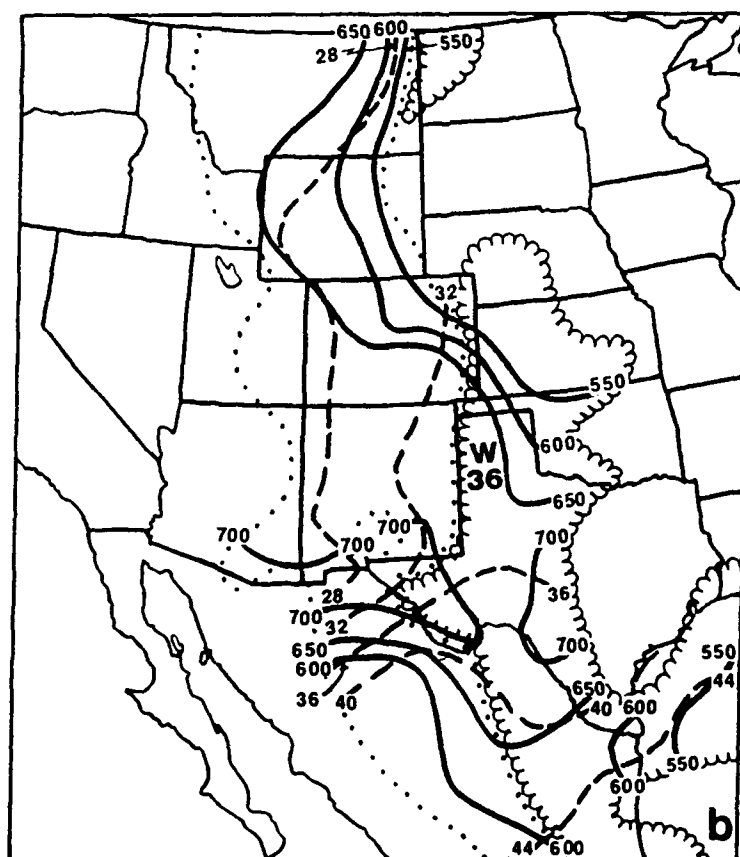
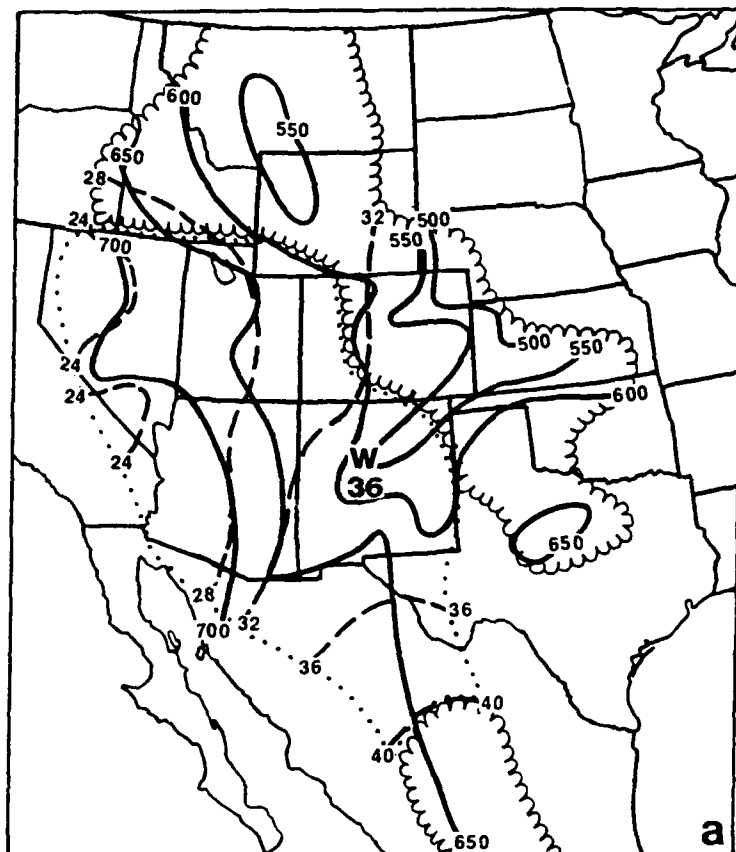
Backward horizontal trajectories originating from the 1200 UTC Lander sounding are displayed in Fig. 6.7. The source region for all six parcels is Utah and eastern Nevada, indicating even less directional veering than over Albuquerque. As at Albuquerque, the parcels have a fair amount of  $\theta$  homogeneity, as shown by the potential temperature history in Fig. 6.8e. Parcels 14-15 experience some degree of diabatic heating during the day on 4 April, and as a result they attain nearly the same potential temperature as parcels 16-18 above. Parcels 16-18 maintain a nearly constant potential temperature throughout the 24-h period. The vertical displacement history (Fig. 6.8f) shows that five of the six parcels experience subsidence relative to the surface during this period. Examination of the net pressure-level displacements shows that the layer consisting of parcels 13-18 actually stretches during this time, as the lower portion of the layer subsides and the upper portion rises. Thus, the combination of diabatic surface heating of the lower portion of the layer and the stretching of the entire layer results in the "appearance" of the EML source region over Wyoming and Montana at 1200 UTC 5 April.

Consistent with the observational study, the simulated western U.S. EML source region experiences a second day of surface heating during the day on 5 April, while a deep PBL reappears over northern Mexico during the same period. The model EML evolution on this second day is shown by the EML analysis for 0000 UTC 6 April (Fig. 6.9a). The analysis shows



Figure 6.9      Same as Fig. 6.5, except for a) 0000 UTC 6 April, and b)  
1200 UTC 6 April. Maximum potential temperature values  
within the EML source/elevated regions are indicated by a  
'W', with the value shown below (in °C).





that the EML source-region air over New Mexico has the highest PBL potential temperatures in the western U.S., with values in the mid 30's. A portion of the western U.S. source-region air has emerged as an EML into sections of Kansas, Oklahoma, and Texas by this time. Meanwhile, the Mexican source-region air remains restricted mainly to extreme southwest Texas and northern Mexico.

The EML analysis for 1200 UTC on 6 April (Fig. 6.9b) reveals a general eastward shift in the source-region and elevated-region areas. The local EML  $\theta$  maximum over New Mexico at 0000 UTC appears to "migrate" into the Texas panhandle, while the warmer Mexican source-region air has now moved into parts of southern Texas as an EML. As in the observations, the two EML areas remain distinct in terms of their thermal characteristics.

Two sets of backward trajectories are used to illustrate the separate evolutions of the western U.S. and Mexican EML source regions. Both sets of trajectories originate within EML source-region layers at 1200 UTC 6 April, and terminate at 1200 UTC 5 April. The first set originates at a model sounding located approximately 200 km to the east of Chihuahua, Mexico, and represents the Mexican source region, while the second set originates at a sounding taken approximately 60 km to the west of Amarillo, Texas, and represents the western U.S. source region.

The horizontal trajectories for the Mexican location are displayed in Fig. 6.10. Although there is little directional shear evident in the horizontal trajectories, there is considerable variation in distance travelled, indicating the presence of speed shear in the model atmosphere over northern Mexico during this time. This result is

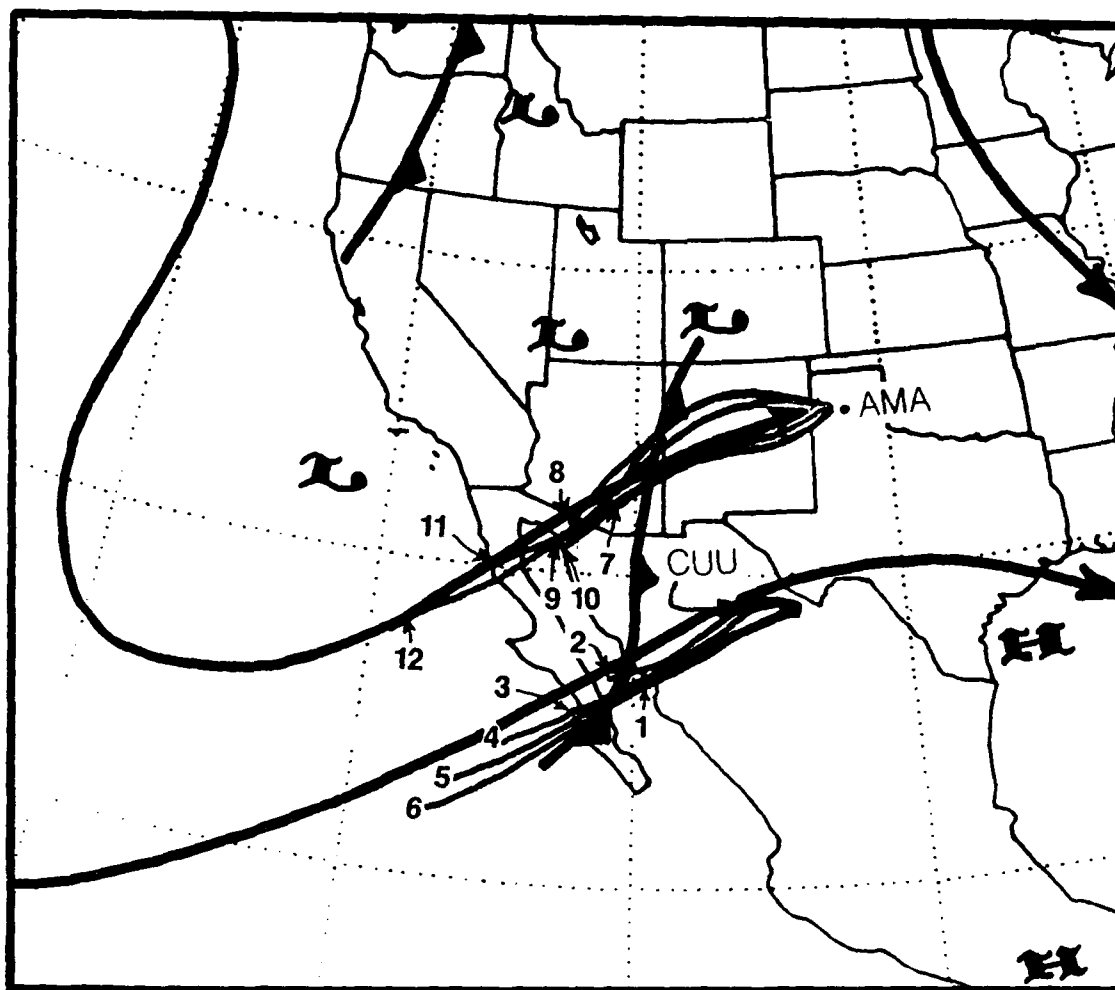


Figure 6.10 Same as Fig. 6.7, except for the horizontal trajectories originating at locations near Chihuahua, Mexico (CUU) and Amarillo, Texas (AMA). Meteorological features are shown for the temporal midpoint of the parcel trajectories (0000 UTC 6 April).

consistent with the strong southwesterly midtropospheric jet observed moving into Baja and northern Mexico in the model simulation during this time. The potential temperature history for these parcels (Fig. 6.11a) shows that only parcel #1 experiences diabatic heating during the daytime heating cycle on 5 April. Otherwise, the  $\theta$  values of the parcels remain relatively constant, or they cool slightly, through the 24-48 h period. The 1-2°C cooling observed for parcels 5 and 6 is likely a result of horizontal thermal diffusion. This effect would be the greatest for parcels originating southwest of Baja, in an area of warm midtropospheric air and a strong southwesterly jet, in which the horizontal wind deformation term  $D$  in Eq. 6.2 can become important. The most interesting part of this evolution lies in the vertical displacement history shown in Fig. 6.11b. Parcels 2-6 experience a significant perturbation in their vertical motion, and the "staggering" in time of the parcels' transit through the perturbation indicates that the feature causing it is stationary. The sinusoidal undulation in the parcel displacements suggests that this feature is a standing mountain wave induced by the strong southwesterly flow crossing the crests of the Sierra Madre Occidental. This is confirmed by plotting the locations of the parcels' perturbations and examining horizontal wind analyses from the simulation to establish the existence of the associated low level jet in the lee of the mountain range. The appearance of a mountain wave in this simulation is consistent with the existence of a mountain wave and an associated low level jet in the lee of the Mexican plateau in the modeling studies of the SESAME I case by Anthes et al. (1982) and Benjamin and Carlson (1986). In our case, the associated low level jet

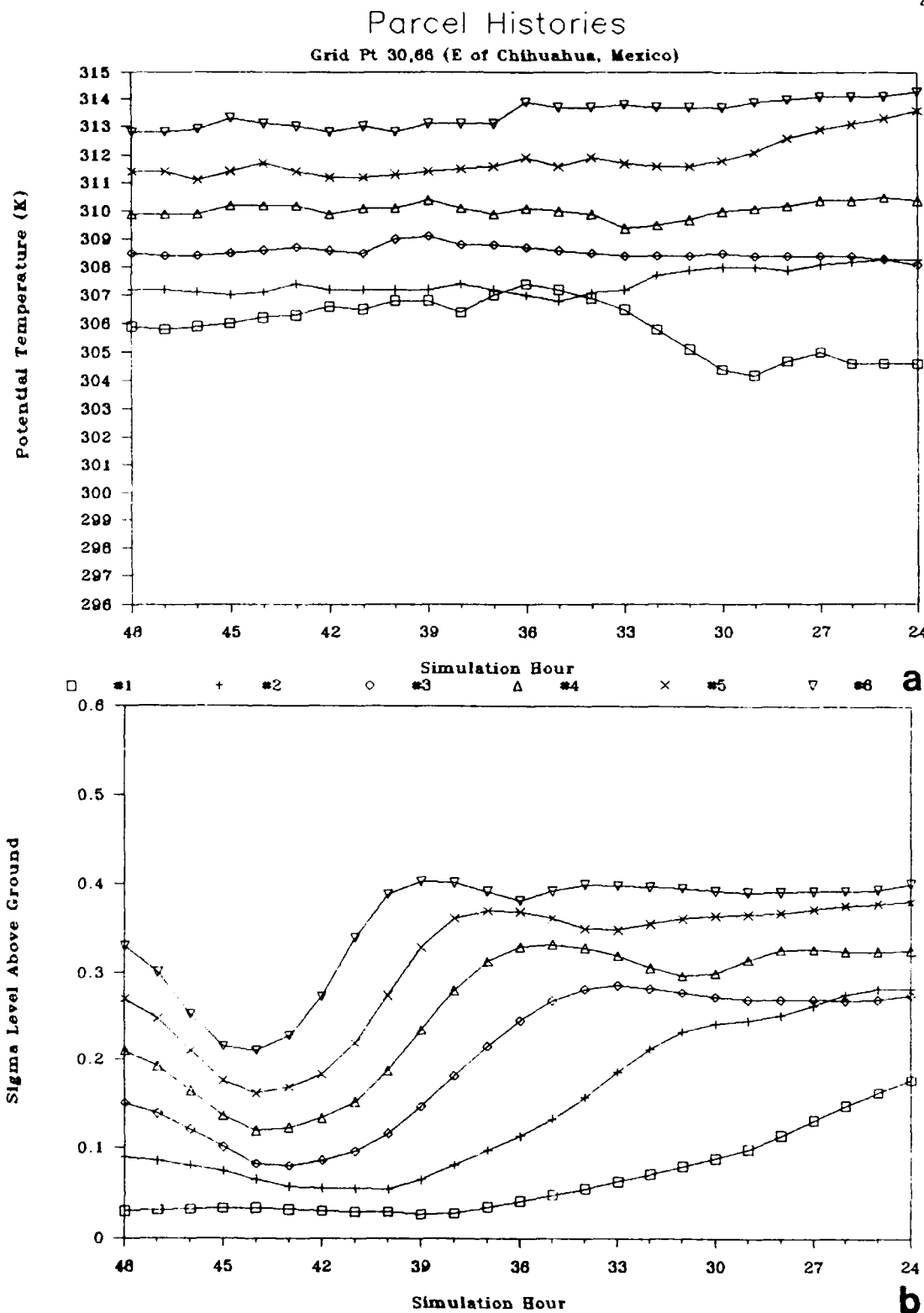


Figure 6.11 Same as Fig. 6.8, except for the locations shown in Fig. 6.10. Potential temperature histories are displayed in panels (a) and (c), and vertical displacement histories are displayed in panels (b) and (d).

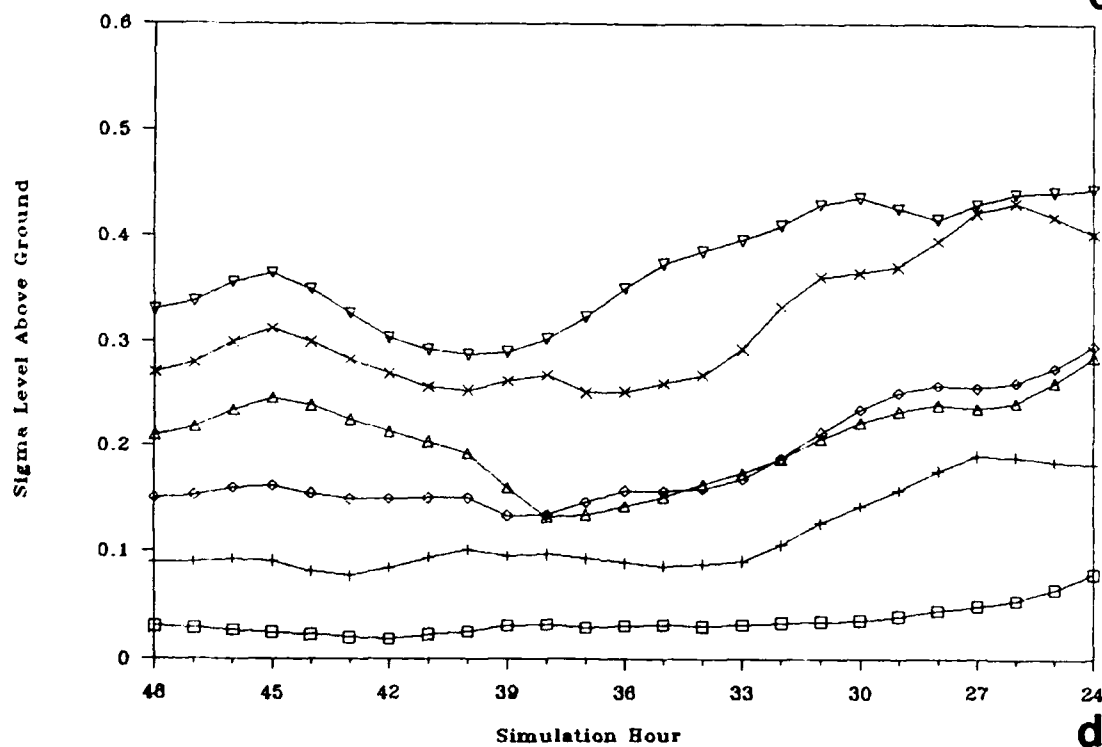
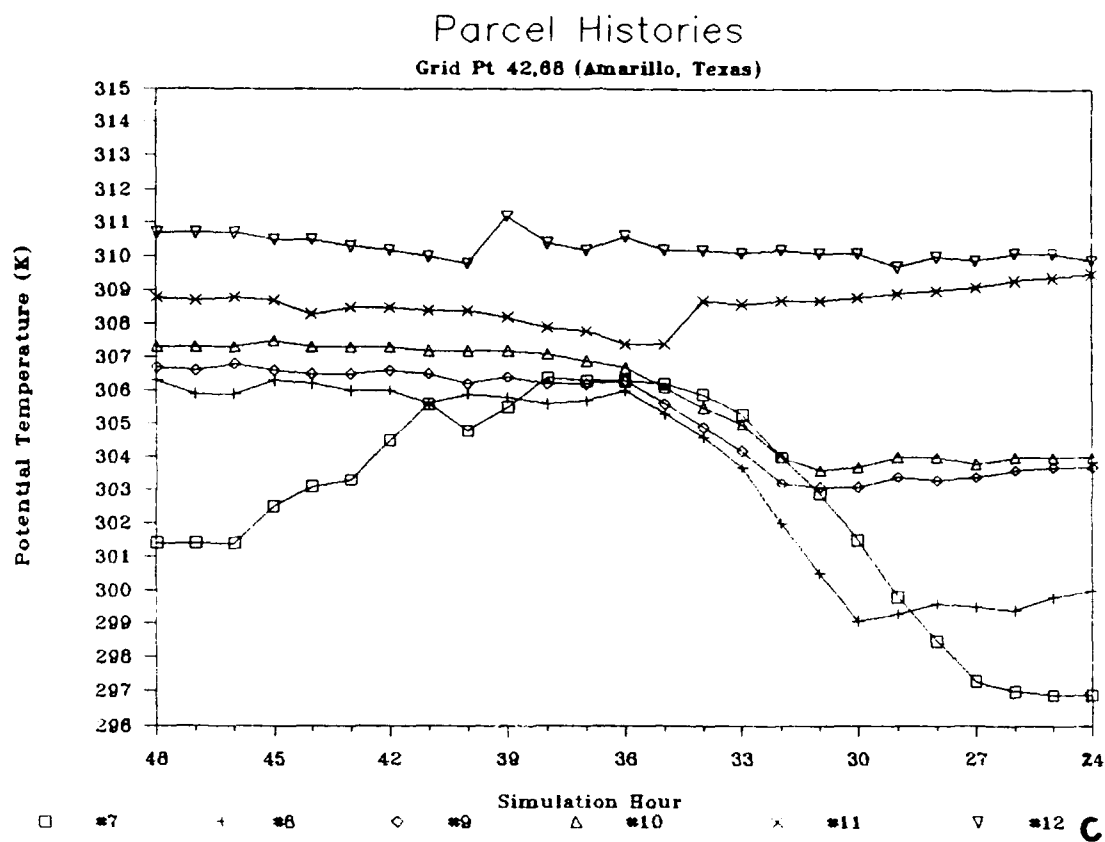


Figure 6.11. (Continued)

appears in the lowest 100 mb of the model atmosphere between 0600 and 0900 UTC 6 April, and has a speed maximum of about  $20 \text{ m s}^{-1}$ .

Compared to the SESAME-I mountain wave, the one in this simulation is distinct in two ways. First, the fact that the location of this mountain wave is upstream of that documented in the SESAME I simulations suggests that, earlier in the lid cycle the standing wave pattern sets up farther west due to the location of the strong midlevel jet at this stage of the cycle. Second, and perhaps more important, is that the mountain-wave circulation has the effect of lowering the dry static stability of the layer making up the 1200 UTC sounding over the Mexican EML source region. We can explain this in the following way. Since the effect of the perturbation decreases with height, the mountain-wave circulation has a decreasing influence on the net vertical displacements of the parcels travelling through it. Examination of the 24-h vertical displacements in Fig. 6.11b along with the pressure-level displacements shows that differential subsidence occurs in this layer as the lower parcels sink more than the upper parcels; this results in a destabilization of the Mexican EML source-region layer. In this case, the static stability of the layer is also lowered by diabatic heating of parcel #1 and the diffusion-related cooling of parcels 5 and 6.

The horizontal trajectories originating in the low static stability layer of the sounding near Amarillo are shown in Fig. 6.10. As in the Mexican trajectories, there is some directional shear, but there is also considerable speed shear as evidenced by the increasing horizontal displacement, with height for each parcel. The potential temperature

history of this layer (Fig. 6.11c) shows that the well-mixed thermal characteristics of the EML source-region layer (parcels 8-12) result mostly from the considerable diabatic heating of parcels 8-10 during the daytime heating cycle of 5 April over the semi-arid regions of Arizona and New Mexico. This heating enabled the parcels to attain a potential temperature close to that of parcels 11 and 12 above. The vertical displacement history in Fig. 6.11d shows that parcels 7 and 8 spent time in the lowest 100 mb of the model atmosphere during the 24-36 h period of the simulation, but the fact that parcels 9 and 10 also experience diabatic heating suggests that the PBL over New Mexico and Arizona was probably around 200 mb deep during this time. Examination of both the net vertical displacements in Fig. 6.11d and the pressure-level displacements shows that this layer generally sinks during its transit over the Desert Southwest and the western Plains, suggesting that diabatic heating of the lower half of this layer is primarily responsible for producing the low static stability observed in the Amarillo area at 1200 UTC 6 April.

### 6.3.2 Formation of the Moist Layer Over the Gulf of Mexico

The study of the moist-layer formation and evolution during the model simulation has two objectives. The first objective is to examine the moist-layer structure over the Gulf coast of Mexico during the high-pressure and return-flow stages, and evaluate the degree of airmass modification taking place over the Gulf waters during this period. The second objective is to determine the effect that the track of the surface anticyclone has on the trajectories of parcels originating in



the offshore flow along the Gulf coast at the beginning of the lid cycle. A related objective is to determine whether any parcel trajectories that pass over the Loop Current region in the eastern Gulf play any role in defining the moist layer that returned into southern Texas on 6 and 7 April.

As noted in the observational study of Chapter 5, a key event during the high-pressure stage of the 4-9 April lid cycle is the "trapping" of the low level moist layer along coastal Mexico as the cold surge and surface pressure ridge advanced southward through the western Gulf during the first 24 h of the cycle. Figure 6.12a shows the 12-h prediction of 850-mb temperature. The simulated cold surge is located to the west of the observed area (see Fig. 5.4b), and is concentrated along coastal Mexico in a narrow band about 300 km wide. Because of the sparsity of the rawinsonde data over eastern Mexico and the Gulf, it is not possible to definitively state whether the model's location of the low level cold surge is in error. If the same physical feature that was observed in Tilley's (1990) Front Range cold surge (topographically trapped edge waves) is prevailing over the slopes of the Sierra Madre Oriental in this case, then the model solution is actually more physically realistic than is the analysis shown in Fig. 5.4b. A model time-height cross section of potential temperature, mixing ratio, and winds at Veracruz (location shown in Fig. 6.12a) for the high-pressure stage of the cycle is displayed in Fig. 6.12b. The cold surge first appears in the 925-750 mb layer between 1800 UTC 4 April and 0000 UTC 5 April, and reaches its peak at 1200 UTC 5 April (consistent with observations). The strongest northerly winds at Veracruz appear at 0600

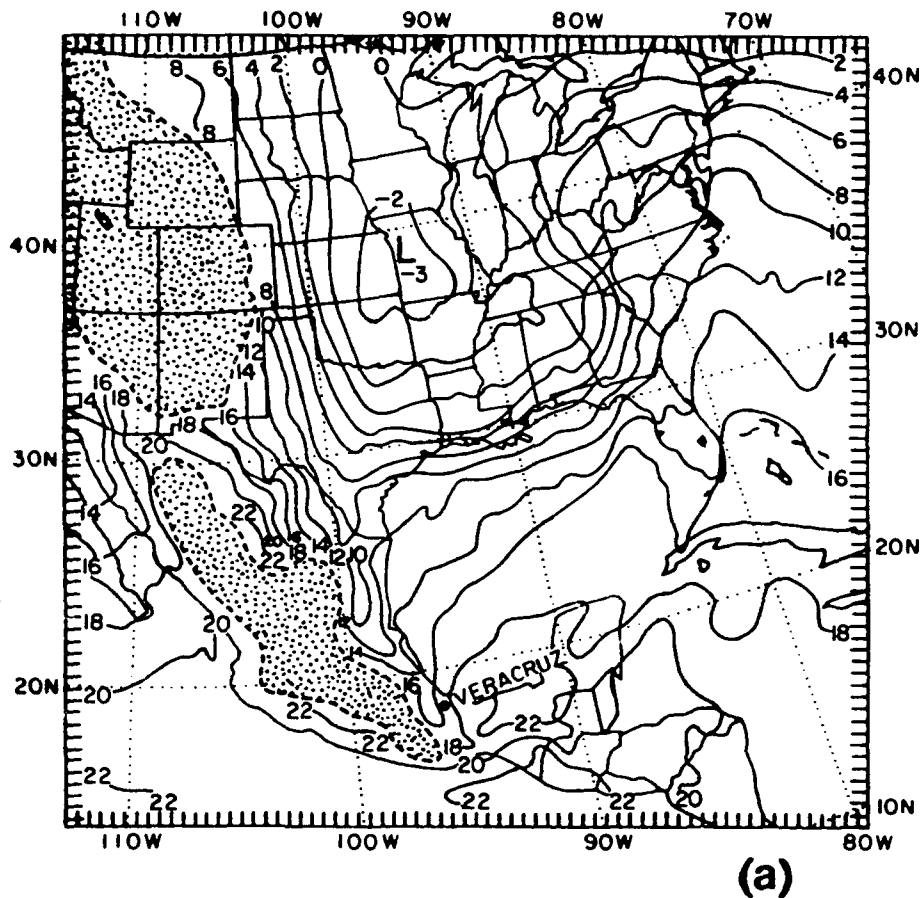
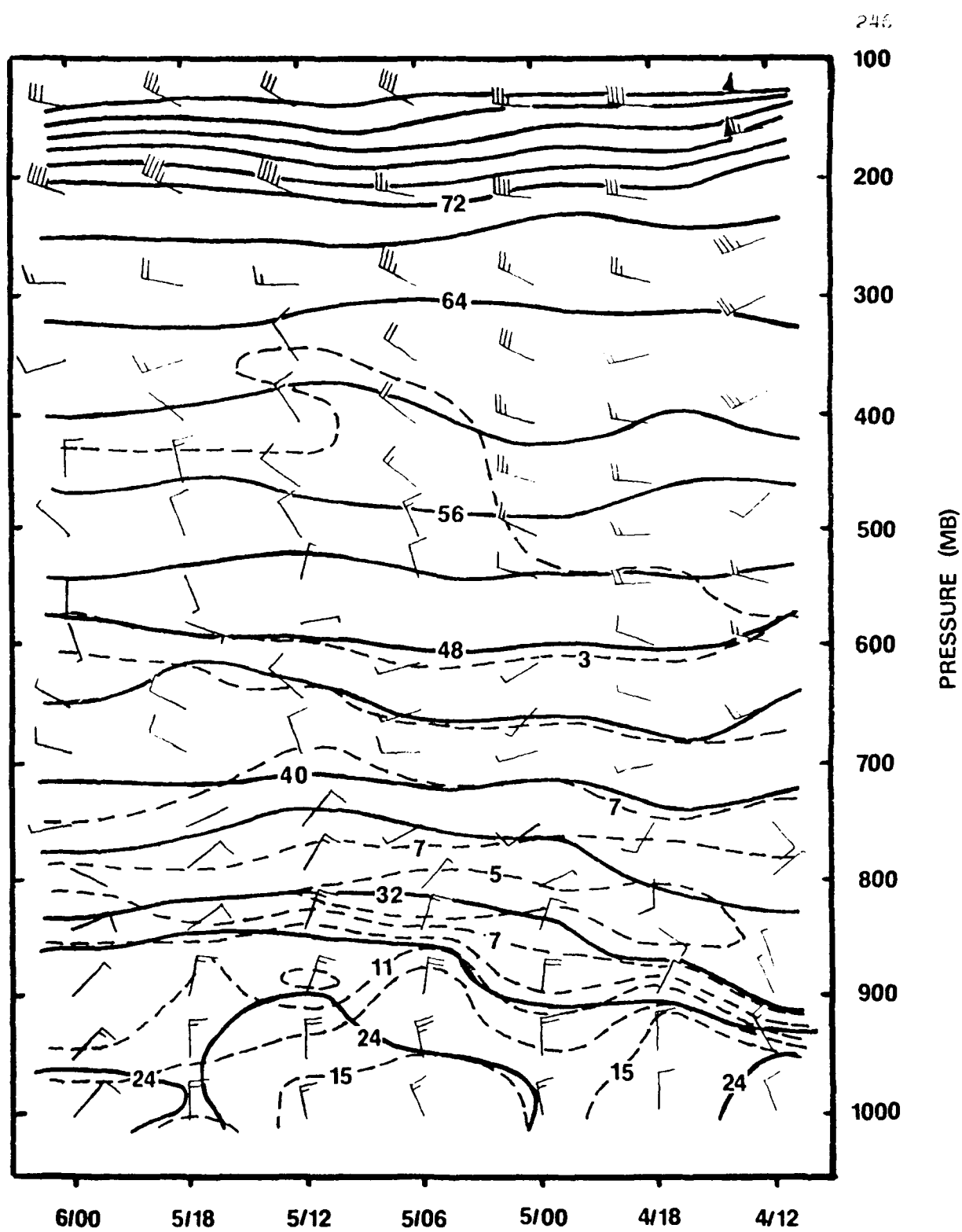


Figure 6.12 Model simulation of 850-mb temperature (panel 'a'), analyzed in  $^{\circ}\text{C}$  and isoplethted every  $2^{\circ}\text{C}$ , for 0000 UTC 5 April. The intersection of the 850-mb surface with the ground is depicted by the dashed line. Panel (b) shows a time-height cross section of potential temperature (solid lines labelled in  $^{\circ}\text{C}$ , isoplethted every  $4^{\circ}\text{C}$ ), mixing ratio (dashed lines labelled in  $\text{g kg}^{-1}$ , isoplethted every  $2 \text{ g kg}^{-1}$ ), and wind direction and speed (in kt) for Veracruz, Mexico from 1200 UTC 4 April to 0000 UTC 6 April. Note that time is read from right to left.



(b)

Figure 6.12. (Continued)

UTC 5 April at around 950 mb, and are about 25 kt. The evolution of the model's  $q$  field during the first 24 h of the simulation shows some drying between 800 and 900 mb, but relatively little change below this level. The time-height cross section for Veracruz indicates that the entire depth of the moist layer remains intact over this portion of coastal Mexico during the high-pressure stage.

Another feature associated the trapped moist layer in this stage of the cycle is the area of low cloudiness along the eastern slopes of the Sierra Madre Oriental and adjacent coastline (recall Fig. 5.5). While other studies of the return flow over the Gulf of Mexico (e.g., Johnson 1976; Karravas 1978) attribute the formation of this low cloud layer to radiational cooling of the moist airmass along the coastal area, we believe that the cloud region in this case forms as a result of upslope flow along the Sierra Madre Oriental range. In order to test this hypothesis, we released some forward-in-time parcel trajectories originating in the PBL along the Texas coastline at the initial time (1200 UTC 4 April), and terminating at  $t = 72$  h (1200 UTC 7 April). Figure 6.13 shows an example of one such trajectory, which originates in the low level offshore flow to the east of the surface pressure ridge at the initial time (see the surface analysis in Fig. 5.1a). The horizontal trajectory and the vertical displacement history in Fig. 6.13 show that the parcel moves south over the Gulf waters and subsides slightly during the first 21 h, then begins to rise as it approaches the Mexican coast. During the first 24 h of the trajectory, the parcel's mixing ratio increases by  $9.1 \text{ g kg}^{-1}$ , while its potential temperature increases by  $6.3^\circ\text{C}$ . The temperature increase is somewhat

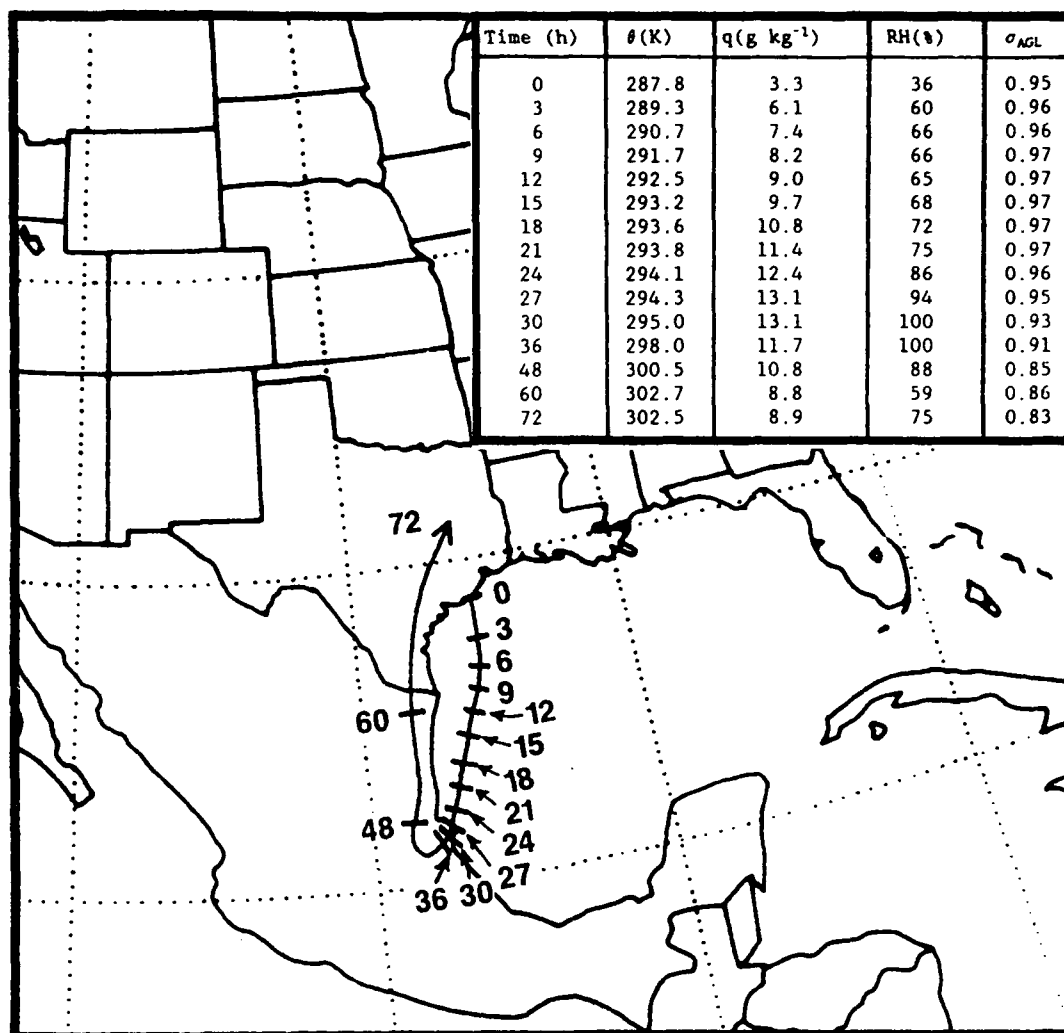


Figure 6.13 Horizontal trajectory for parcel originating in offshore PBL flow along Texas coast at initial time (1200 UTC 4 April). Tick marks along the trajectory are used to denote the simulation hour; the table inset displays parcel values of potential temperature, mixing ratio, relative humidity, and sigma level above the ground at these times.

less than those reported in the Gulf polar-air modification studies of Henry and Thompson (1976), Karnavas (1978), and Molinari (1987), who employed a simple Lagrangian trajectory model based on bulk aerodynamic assumptions, using both observed and climatological data for the winter season. An assumption used in the above-mentioned studies is that the parcel's elevation remains constant throughout the trajectory. The table accompanying Fig. 6.13 illustrates that this assumption is true for the 9-21 h period of this trajectory; after the 24-h point, the vertical motion of the parcel becomes an important factor. The parcel begins to rise before it is actually over land, and reaches 100% RH about the time it moves onshore (1800 UTC 5 April). However, after completing the upslope journey along the Sierra Madre range, at about  $t = 48$  h (1200 UTC 6 April), the parcel undergoes a second modification as it becomes warmer and drier as it travels above the coastal PBL through eastern Mexico. By the 72-h point, the parcel, which resided in the Mexican coastal moist layer 48 h earlier, is now located over eastern Texas above the PBL, and is  $7.5^{\circ}\text{C}$  warmer and  $4.2 \text{ g kg}^{-1}$  drier than it was at the time of saturation along the Mexican coast.

After examining the evolution of a "representative" parcel through the moist layer in Fig. 6.13, two questions come to mind: does the track of the surface anticyclone plays a role in this evolution, and is the parcel trajectory in Fig. 6.13 representative of the evolution of parcels residing within the coastal moist layer during the return-flow stage of the cycle. In order to better address these questions, two more sets of forward trajectories are released. Each set consists of parcel trajectories originating at five sigma levels, from  $\sigma = 0.97$  to  $\sigma$

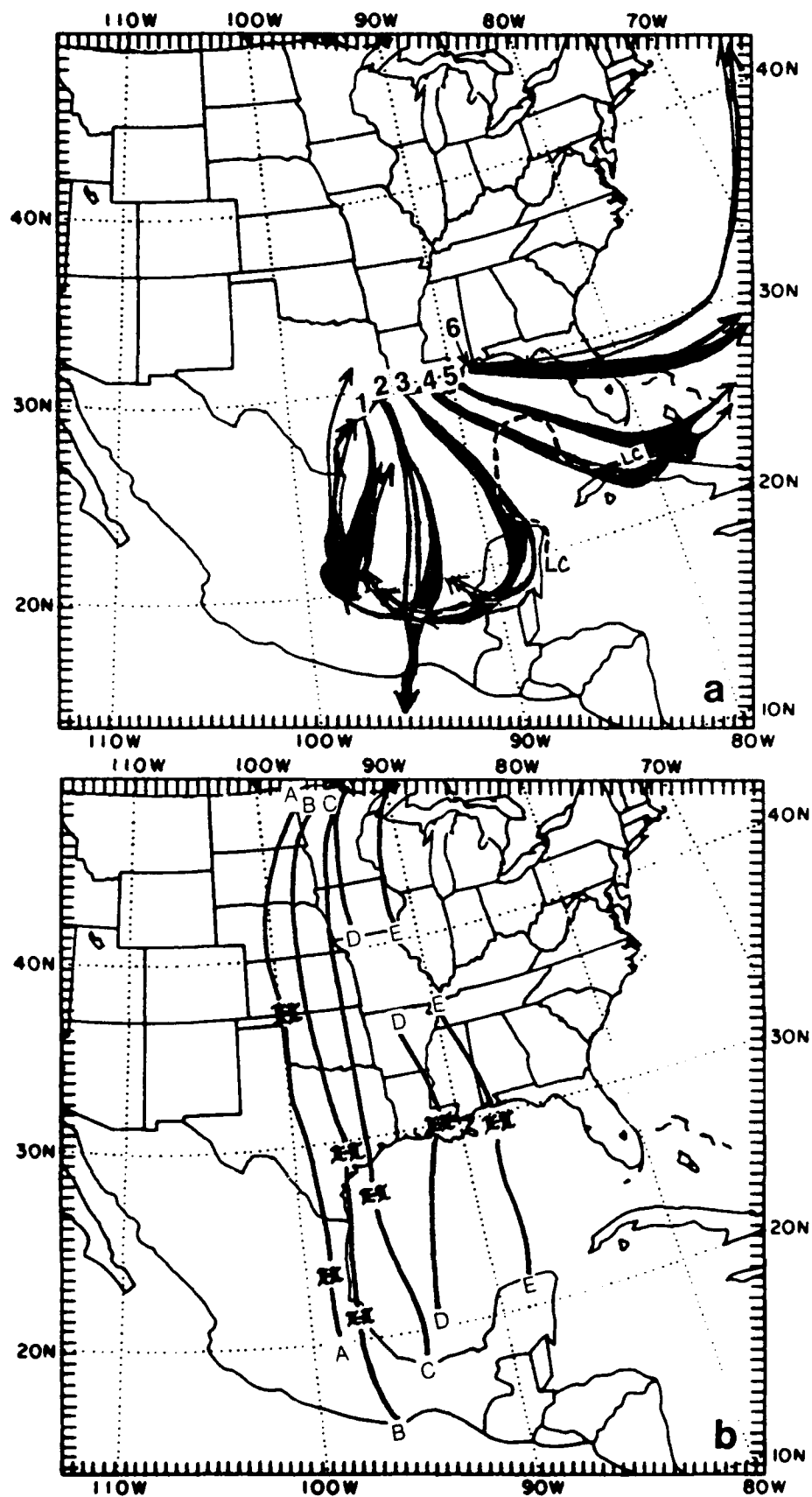
= 0.89. The first set of parcels originates over the Gulf coastal PBL from Texas to Mississippi at the initial time (1200 UTC 4 April). These trajectories terminate at the 72-h point of the simulation, and are intended to evaluate the role of the surface anticyclone's track on the offshore flow originating along the Gulf coast at the beginning of the cycle. The second set of parcel trajectories originates within the PBL along the Gulf coast of Mexico at  $t = 36$  h (0000 UTC 6 April), which marks the beginning of the return-flow stage of the lid cycle. These parcels, which are initially located within the coastal moist layer, are also tracked until the 72-h point, and are intended to test the representativeness of the trajectory described by Fig. 6.13.

The horizontal displacements for the first set of trajectories are shown in Fig. 6.14a. In this figure and in Fig. 6.15, the vertical overlap of the trajectories is shown by a thick solid line. Only the set of parcels whose origin is closest to the surface ridge axis (set #1 in Fig. 6.14a) is able to move in a southerly direction, and return northward into Texas by the lid-maximum stage. Parcel set #2 becomes incorporated into the northerly flow associated with the advancing surface anticyclone and actually crosses the Isthmus of Tehantepec into the Pacific Ocean! Parcel set #3 experiences anticyclonic curvature along its trajectories, and some of the parcels cross a portion of the Loop Current area in the eastern Gulf, but none are able to return to the southern Plains region by the 72-h point. Although the fourth set of parcels crosses a considerable portion of the Loop Current area, it is travelling eastward by the morning of 7 April, so it appears that the Loop Current *did not* play a role in determining the moisture content of





Figure 6.14 Horizontal trajectories for six sets of parcels originating in the offshore PBL flow along the Gulf coast at the initial time (panel 'a'). Circled numbers denote the origin of each parcel set; parcel trajectories are indicated by solid lines with arrows. The position of the Loop Current in the eastern Gulf is shown using the same symbol as in Fig. 6.2. Panel (b) shows simulated surface anticyclone position (conventional notation) and pressure ridge position (solid lines) during the high-pressure and return-flow stages of the lid cycle. Labels are used to indicate the simulation time: A = 12 h, B = 24 h, C = 36 h, D = 48 h, and E = 60 h.



the air returning into the southern Plains on 6 and 7 April. Figure 6.14b shows the temporal continuity of the model surface anticyclone and pressure-ridge axis during the high-pressure and return-flow stages of the cycle. Comparison of Figs. 6.14a and b reveals that the southward movement of the surface anticyclone results in the divergence of the parcel trajectories originating in the offshore flow along the Gulf Coast, and a return flow layer that is restricted largely to the western Gulf, where the SST values are generally cooler than over the eastern Gulf (see Fig. 6.2).

The horizontal displacements for the sets of parcel trajectories originating in the coastal moist layer at  $t = 36$  h are shown in Fig. 6.15. An examination of the vertical displacement,  $\theta$  and  $q$  histories, for these parcels indicates that nearly all of them experience the same upslope motion and warming/drying that the parcel in Fig. 6.13 experiences after the 48-h point of the simulation. Thus, the evolution of the moist layer during the high-pressure stage is mainly characterized by modification of the continental polar airstreams over the Gulf waters and formation of a low cloud layer along the coastal region of Mexico through upslope motion. At the beginning of the return-flow stage, the parcels continue the upslope journey through the Sierra Madre Oriental range, and then turn northward and undergo a second air mass modification (warming and drying) associated with the journey over the eastern portion of the arid Mexican plateau region. In the next section, we will explore the characteristics of the moist layer that eventually resides under the lid inversion by employing backward

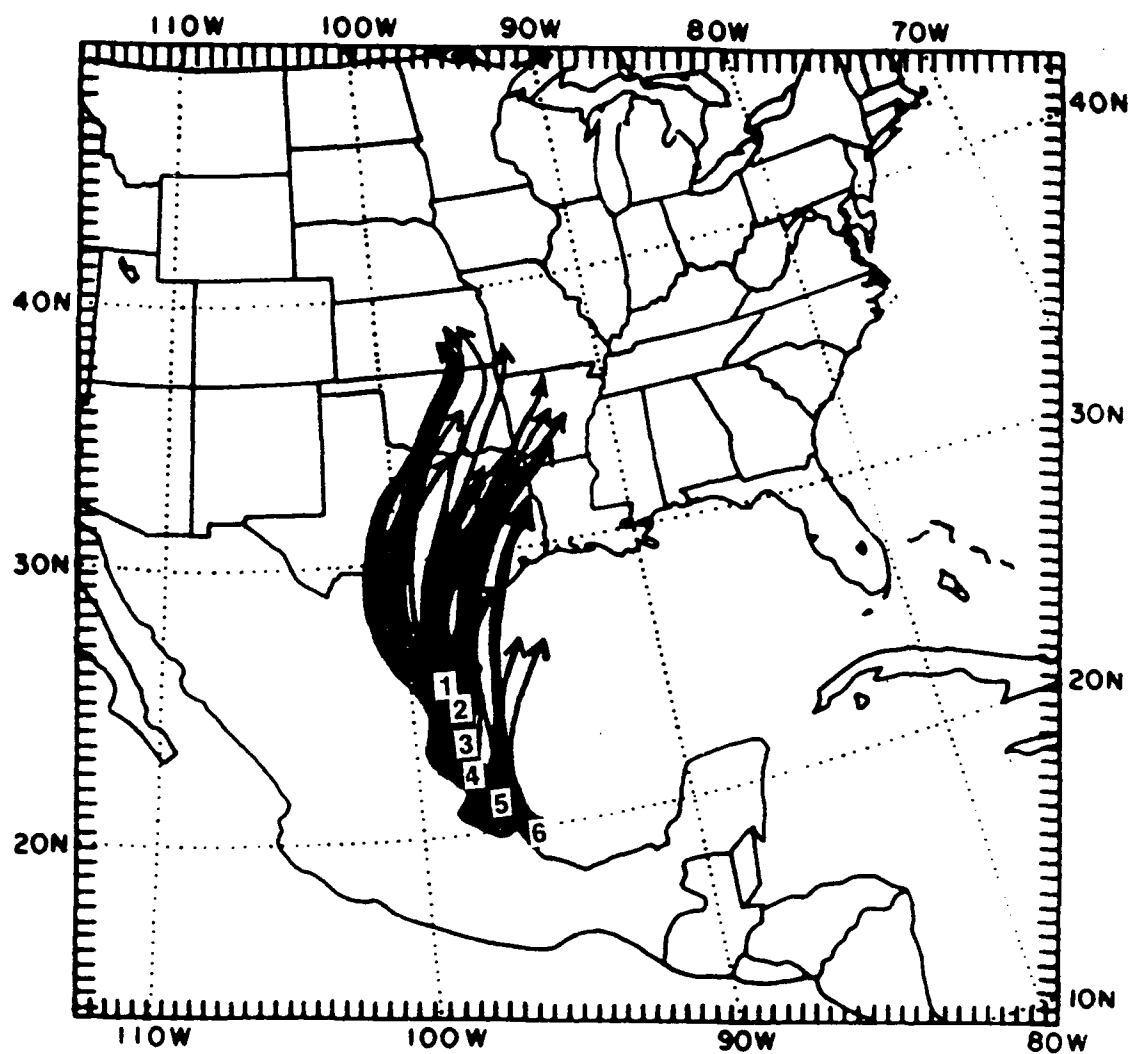


Figure 6.15 Same as Fig. 6.14a, except for six sets of parcels originating within the moist layer over coastal Mexico at the 36-h point, and ending at the 72-h point.

trajectories originating from a lid sounding over Texas near the time of lid-coverage maximum.

#### 6.4 Formation of the Lid Over the Southern Great Plains

The formation of the lid over the southern Plains during the evening of 6 April took place as a result of the superposition of the moist tongue from the Rio Grande valley and the EMLs from the western U.S. and northern Mexico, which were already in place over much of Kansas, Oklahoma, and Texas. The EML analysis for 0000 UTC 7 April is shown in Fig. 6.16. Based on examination of the mean EML  $\theta$  values over the southern Plains, and the parcel trajectory results of section 6.4.1, we can conclude that the EML from the Texas-Oklahoma border and to the north is of western U.S. origin, while most of Texas, eastern Mexico, and the adjacent Gulf waters has EML air originating over northern Mexico. There is a narrow zone extending through western Kansas, west-central Texas, and northeastern Mexico, where the presence of the moist layer has allowed the buoyancy term to drop below  $0.5^{\circ}\text{C}$ , indicating the presence of a lid. A comparison of the model lid area with the observations for 0000 UTC and 1200 UTC 7 April (Figs. 5.13a,b) suggests that the simulated lid formation is about 6 h fast.

A composite meteorological analysis for the model simulation at 0600 UTC 7 April is shown in Fig. 6.17a (the legend is in Fig. 6.17d). This analysis shows a strong veering wind profile between 850 and 300 mb over much of west-central Texas. However, the model lid strengths in this area are high ( $> 8^{\circ}\text{C}$ ), so moist convection is unlikely in the simulation over this area. The most favorable area for the model to

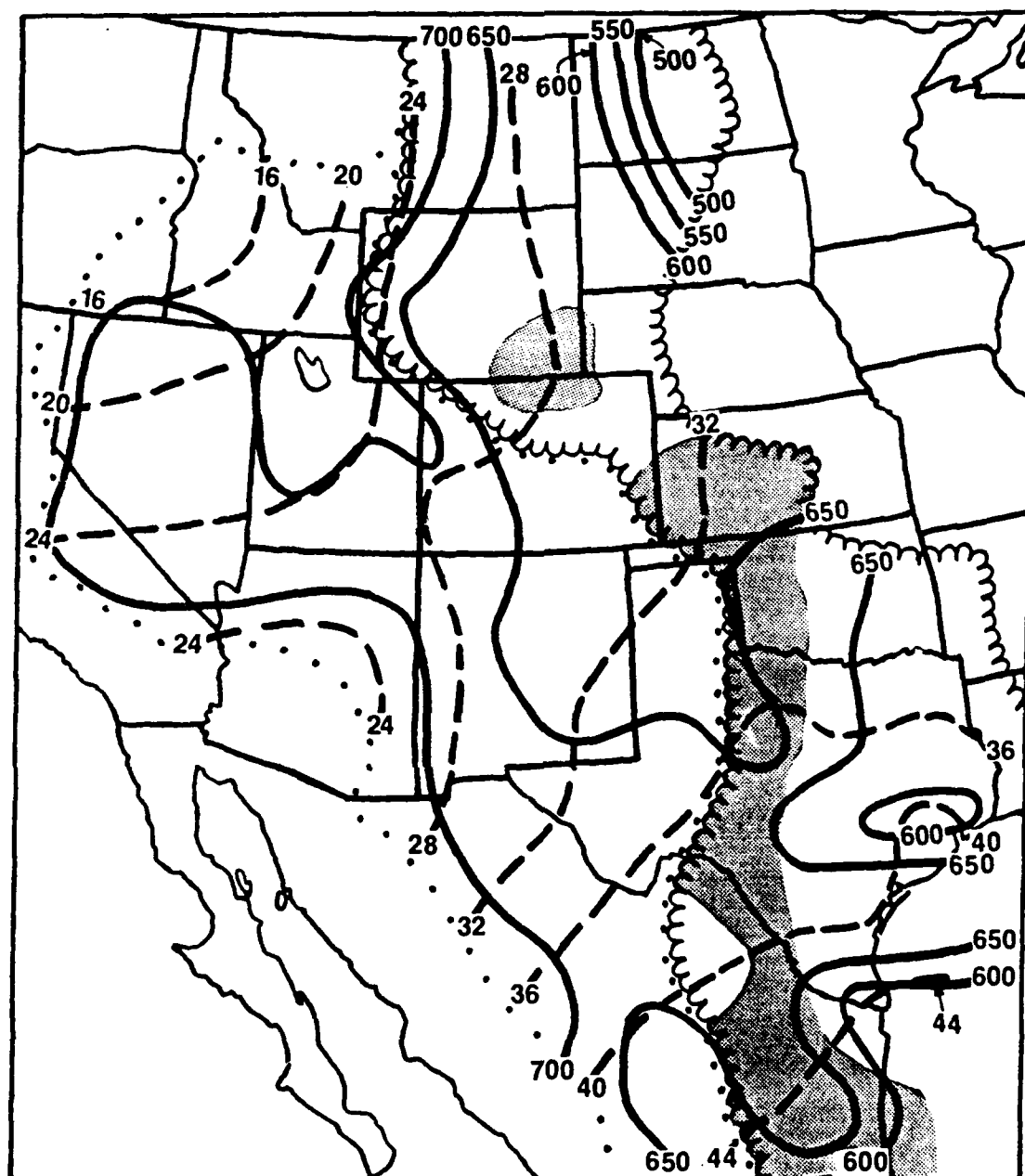
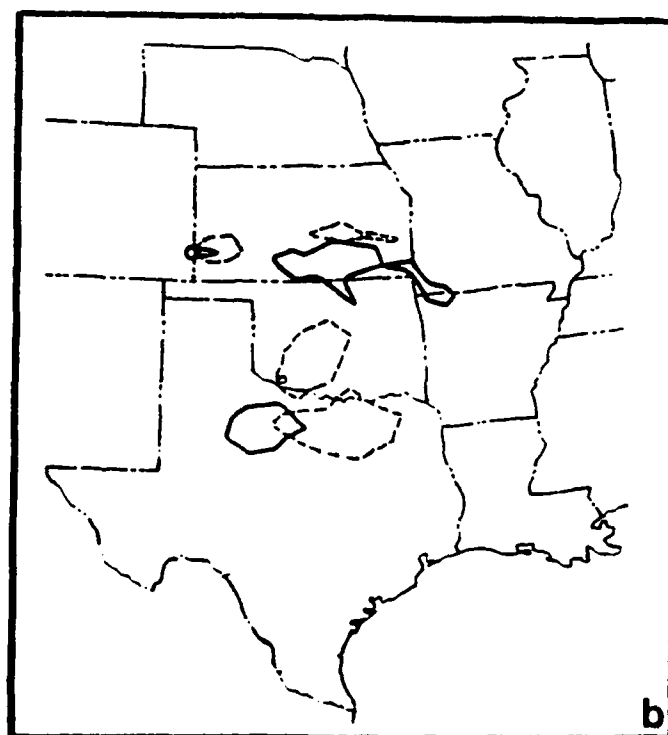
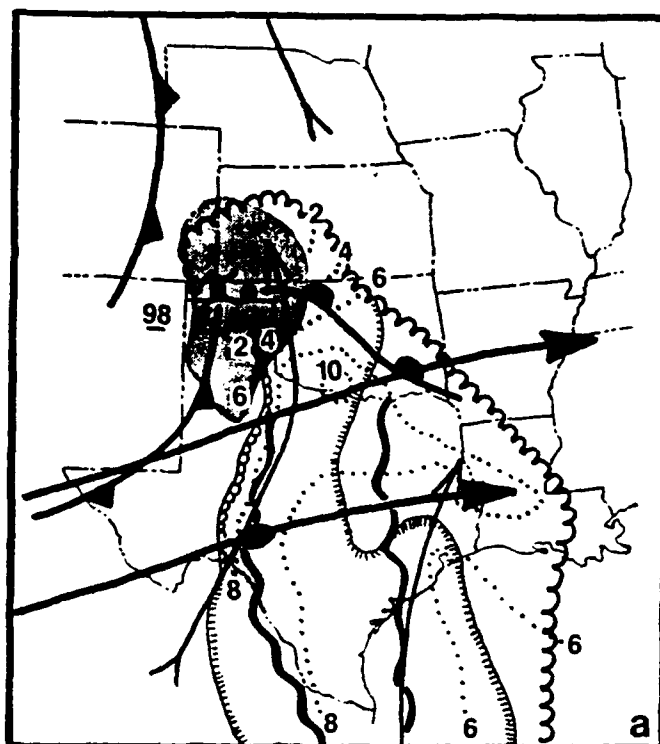


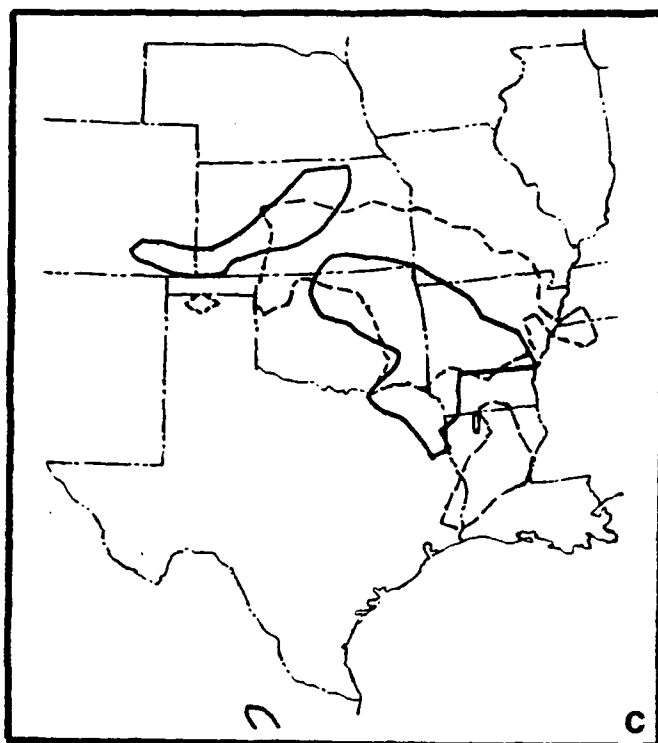
Figure 6.16 Same as Fig. 6.5, except for 0000 UTC 7 April. The area with a lid stratification is shown by the shading.



Figure 6.17 Major surface and upper-air features in model simulation at the 66-h point (0600 UTC 7 April; panel 'a'). Symbols are shown in the legend panel (d). Panel (b) displays the model precipitation amounts greater than 0.3 cm for the periods 0600-0900 UTC (solid) and 0900-1200 UTC (dashed) 7 April. Panel (c) is identical to panel (b) except for 1500-1800 UTC 7 April (solid) and 2100 UTC 7 April-0000 UTC 8 April (dashed).







### LIST OF SYMBOLS

	850-MB JET
	MOIST TONGUE AT $\sigma = 0.96$
	300-MB JET WITH SPEED MAXIMUM
	BOUNDARY OF EML AREA
	BOUNDARY OF LID AREA
	LID STRENGTH ISOPLETH
	AREA WITH BUOYANCY TERM $\leq -2^{\circ}\text{C}$

d

Figure 6.17. (Continued)

produce convective precipitation is from northwestern Oklahoma into southern Kansas. There, the lid strengths are lower ( $2-4^{\circ}\text{C}$ ), the veering wind profile exists, there is cyclonic vorticity to the north of the 300-mb jet, and the presence of the warm front provides a source of forced ascent for the moist air coming from the south. The presence of high buoyant instability to the west of this zone, and the fact that the moist tongue is still over west-central Texas, indicate that widespread moist convection will be delayed several hours until these features move into place over northern Oklahoma and southern Kansas.

The resulting model precipitation for the period 0600 7 April to 0000 UTC 8 April is summarized in Figs. 6.17b and c, respectively. The model produces convective rainfall in the favored areas of northern Oklahoma and southern Kansas during the 0600-1200 UTC period (Fig. 6.17b). This area subsequently expands north and east during the next 12 h of the simulation (Fig. 6.17c). Although the simulated convective precipitation areas shown in Figs. 6.17b,c are located north of the actual severe-weather event areas (Fig. 5.2a), it should be pointed out that there was considerable convective rainfall to the north of the severe-storm area, in western and central Oklahoma, and southeastern Kansas.

A large area of precipitation develops in the simulation over northern Texas and southern Oklahoma during the 0600-1200 UTC period (recall Fig. 6.17b). This precipitation begins along the model dryline and subsequently moves into the strong lid region shown in Fig. 6.17a. The simulated rainfall is generated by the nonconvective module, indicating that this area would be favorable for convective

precipitation were it not for the strong lid (recall the discussion of the convective parameterization's stability check in section 6.2.1). Since this nonconvective precipitation begins after 0600 UTC, we chose to generate a set of backward trajectories originating at a 0600 UTC lid sounding, in order to examine the characteristics of the moist layer and EML at the time of lid-coverage maximum in the model simulation. The sounding location is Abilene, Texas (ABI, shown in Fig. 6.19), which is just east of the dryline, within the area of the moist tongue, and just south of the nonconvective precipitation area that developed after 0600 UTC.

The 0600 UTC Abilene sounding is shown in Fig. 6.18. This sounding has a lid strength of  $4.9^{\circ}\text{C}$  and a buoyancy of  $-1.4^{\circ}\text{C}$ . The backward trajectories from this sounding cover a 66-h period, and end at the initial time of the simulation (1200 UTC 4 April). The horizontal trajectories for this sounding are displayed in Fig. 6.19; only those parcels existing in the EML and moist layer of the 0600 UTC Abilene sounding are shown. The parcels existing in the moist layer at 0600 UTC originate over the western Plains. The horizontal trajectories show that the moist-layer parcels spend a limited time over the waters of the northwest Gulf. The mixing ratio history for these parcels is shown in Fig. 6.20a. The continental origin of all three parcels is evident here. Airmass modification takes place over a 15-18 h period, which is consistent with the time of the over-water trajectory in Fig. 6.19. During this period, the mixing ratios of the three parcels increase by  $6-9 \text{ g kg}^{-1}$ . Parcels 1 and 2 experience a second period of moistening during the day on 6 April, resulting in an additional  $q$  increase of 2-3

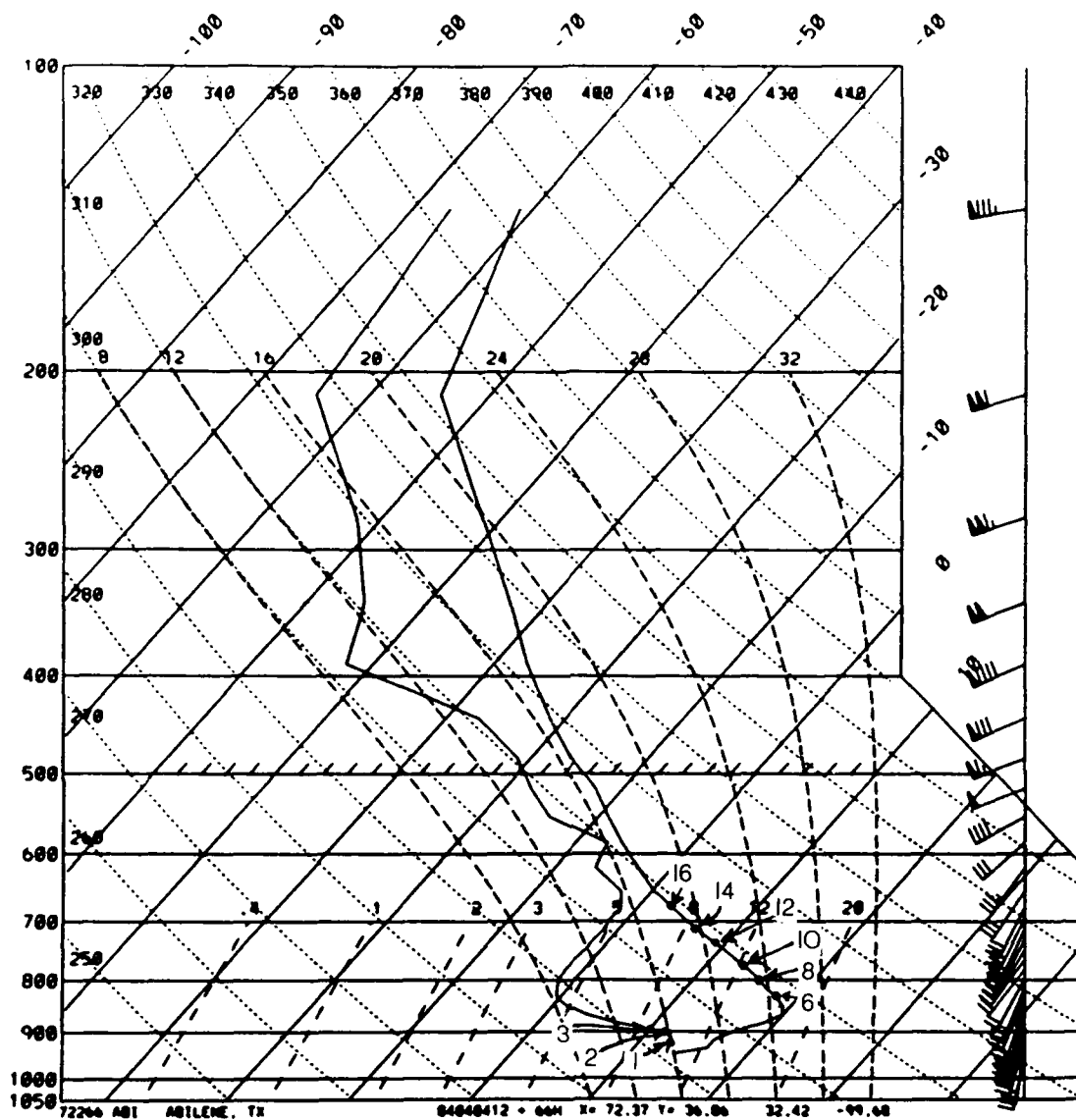


Figure 6.18 Same as Fig. 6.6, except for single sounding time (0600 UTC 7 April), at Abilene, Texas.

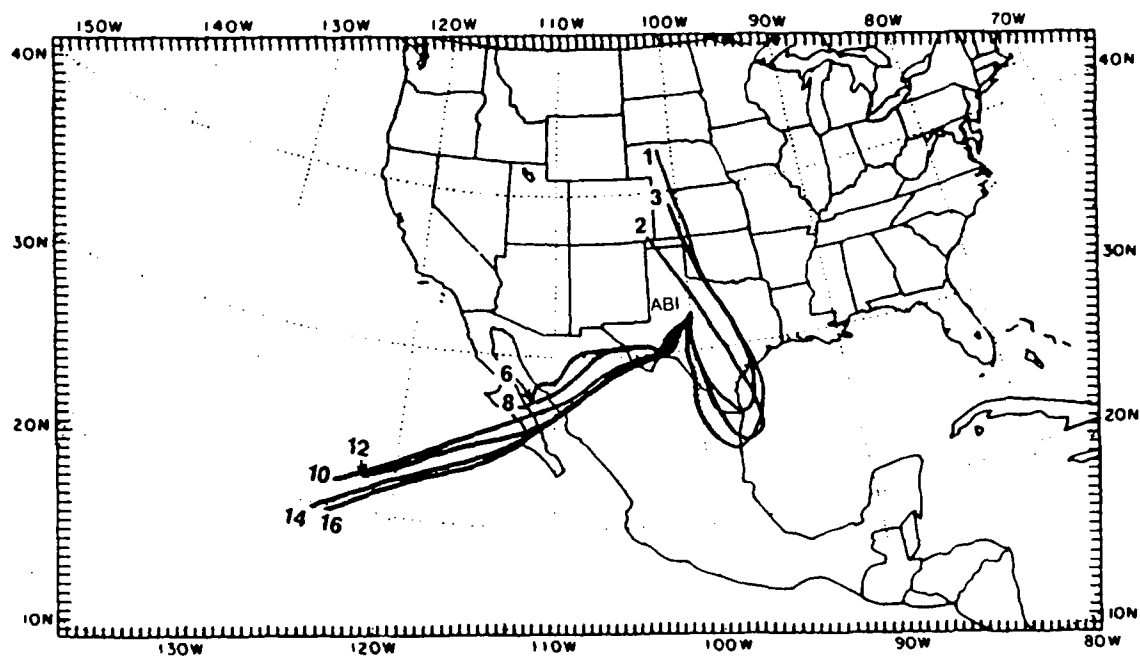


Figure 6.19 Same as Fig. 6.7, except for moist-layer parcels (1-3), and EML parcels (6-16), originating at the 0600 UTC Abilene sounding.

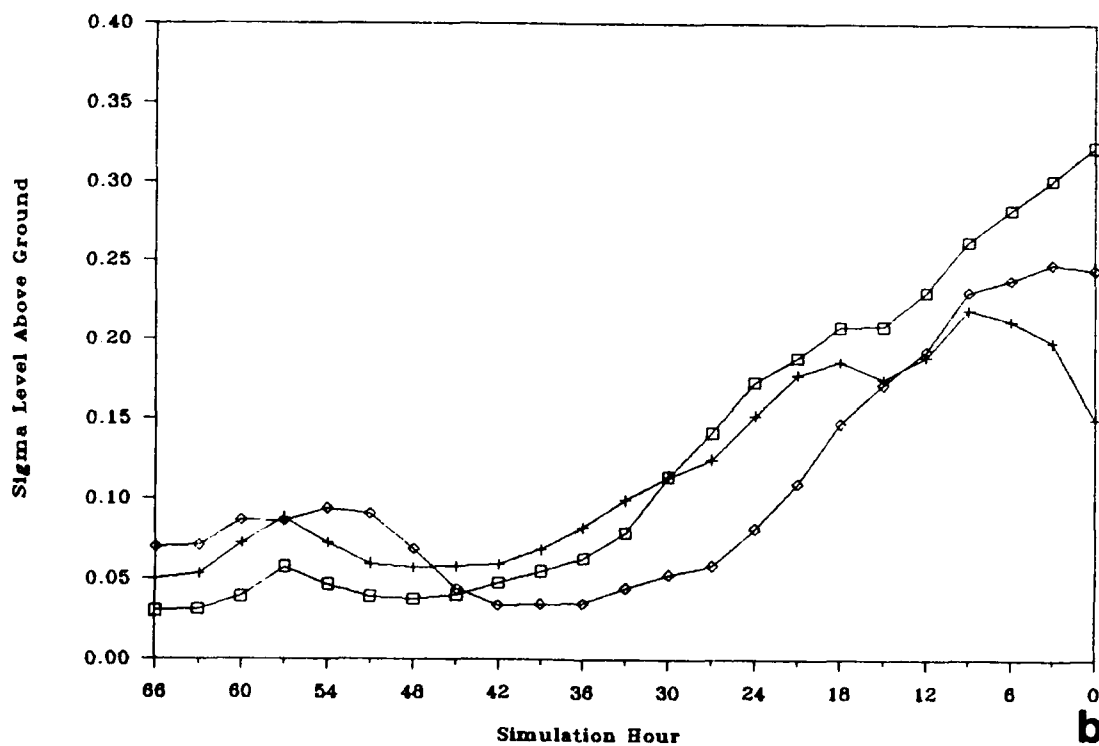
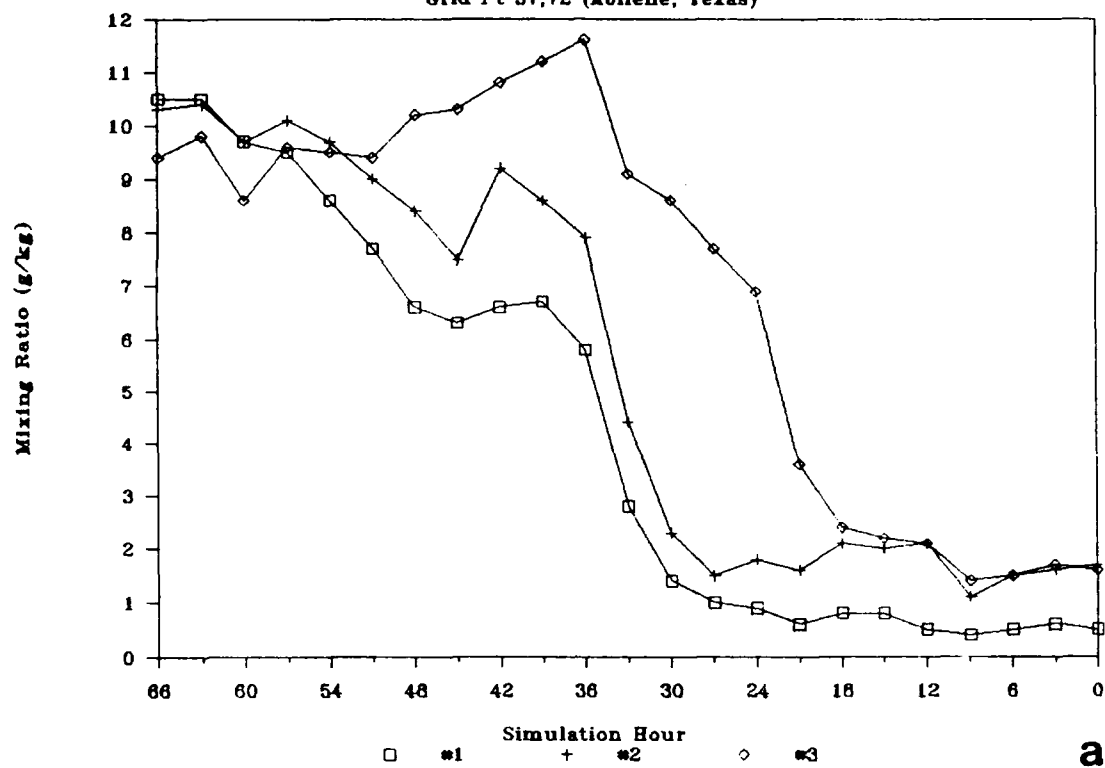


Figure 6.20 Same as Fig. 6.8, except for parcels originating in the moist layer and EML of the 0600 UTC Abilene sounding. Panel (a) displays a mixing ratio history for parcels 1-3, with the ordinate denoting the parcel mixing ratio in  $\text{g kg}^{-1}$ , and the abscissa denoting simulation time (note that the time is read from right to left). A legend below the abscissa shows the symbols used for each parcel. Panel (b) shows the vertical displacement history for parcels 1-3. Panel (c) illustrates the potential temperature history for EML parcels (6-16), and panel (d) denotes the vertical displacement history for the EML parcels.



## Parcel Histories

Grid Pt 37,72 (Abilene, Texas)



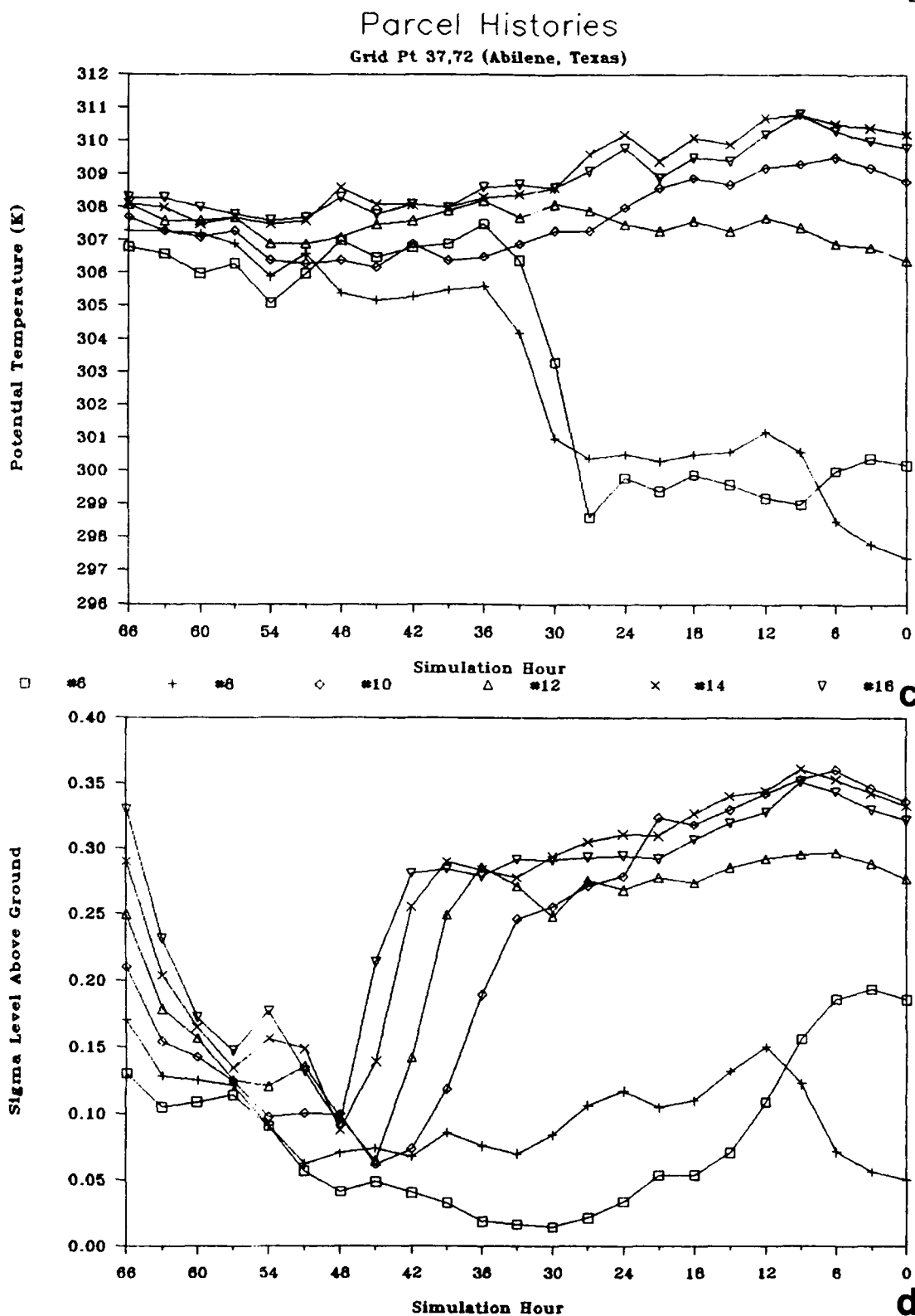


Figure 6.20. (Continued)

$\text{g kg}^{-1}$ . The vertical displacement history of the moist-layer parcels is shown in Fig. 6.20b. This history explains the timing of the initial modifications of parcels 1-3. Parcel #3 begins to undergo moistening as it descends into the lowest 100 mb of the model atmosphere after 0900 UTC 5 April, whereas parcels 1 and 2 do not reach the marine PBL until 9 h later.

There is strong subsidence evident during all three parcels' trajectories, and it is somewhat surprising to note that all three moist-layer parcels have their origin in the continental midtroposphere instead of the subtropical oceanic PBL. The results from this set of moist-layer trajectories, as well as those from the preceding section, suggest that during lid cycles in which a blocking surface anticyclone is observed in the western Gulf, the moist airstream trajectories behave differently than those in the classic Carlson-Ludlam lid model (see Figs. 19 and 24 in Carlson and Ludlam 1968). In contrast to their conceptual model in which the moist airstreams originate over the western Caribbean and have a long trajectory over the open waters of the Gulf, *our moist airstreams originate over the continental midtroposphere and descend into the marine PBL over the western Gulf for a limited period.* We can speculate that in situations where the track of the surface high is located across the Mississippi River valley, there is a greater possibility that the moist-layer trajectories follow the classic Carlson-Ludlam model more closely, because the blocking pressure ridge is located to the *north* of the Gulf.

The horizontal displacements of the EML air are shown in Fig. 6.19. The source regions for the EML range from the Gulf of California to the

subtropical Pacific Ocean near  $20^{\circ}\text{N}$  latitude. All six parcel trajectories indicate some degree of anticyclonic curvature over northern Mexico followed by cyclonic curvature over southwest Texas as the upper level ridge moves through northern Mexico. The ridge passage is followed by southwesterly flow associated with the approaching trough over the western U.S. The potential temperature and vertical displacement histories for these parcels are shown in Figs. 6.20c,d, respectively. Parcels 10, 14, and 16 originate in the same general oceanic area (see Fig. 6.19) near the same level. As a result, these parcels are isentropically homogeneous from the initial time on. These three parcels also experience the same  $1\text{-}2^{\circ}\text{C}$  of cooling that was observed over the Mexican EML source region during the 24-48 h period (recall Fig. 6.11a). Since these parcels originate over a similar subtropical ocean region as the upper parcels of the nascent Mexican EML source region, it is likely that horizontal temperature diffusion is also affecting them as they move away from the area of warm midlevel air. As observed in other EML trajectories, the lower portion of the layer is affected by diabatic heating within the model PBL. Notice from Fig. 6.20c that parcel #8 is affected by diabatic heating from the daytime heating cycles on both 4 and 5 April; examination of the vertical displacement history (Fig. 6.20d) shows that parcel #8 is the only one of the six that spends time within the local PBL on two different days.

An interesting feature in the vertical displacement history is the sharp descent of parcels 10-16 during the 33-48 h period. Examination of the horizontal displacements shows that these parcels traverse the

crest of the Sierra Madre Occidental range during the 45-48 h period. Recall that this period coincides with the occurrence of the mountain-wave circulation over this area (recall Fig. 6.11b), and the evidence suggests that these parcels are affected by the mountain wave as well. These same parcels undergo a period of sharp ascent after the 57-h point of the simulation (2100 UTC 6 April). Examination of the horizontal displacements shows that all four parcels enter southwestern Texas at this time; examination of upper level wind fields in the simulation for this time (not shown) indicates that this region is located within a diffluent/divergent zone between the subtropical and polar jets. The vertical displacements during the last 9 h of this period illustrate that the layer is undergoing vertical stretching, which further destabilizes the EML as it moves into west-central Texas.

The EML over Abilene at 0600 UTC is a result of a combination of different processes affecting the layer at different times during the lid cycle. In the early stages, slowly subsiding high-potential-temperature air originates over the subtropical oceanic region, and subsequently passes through a mountain-wave circulation over the Sierra Madre Occidental, which causes the layer to destabilize through differential subsidence. The lower portion of this layer originates near the west coast of Mexico, and is modified by diabatic surface heating over western Mexico on 4 and 5 April. As the layer moves across northern Mexico, it begins to vertically combine into an EML; it subsequently approaches the diffluent region between the subtropical and polar jets over southwestern Texas, and the layer is stretched, which

causes further destabilization before it finally moves over the moist layer in west-central Texas to form a lid sounding.

## Chapter 7

## CONCLUSIONS AND DISCUSSION

7.1 Summary of Results

The focus of this research is on the generation of a representative synoptic climatology of the lid and its component structures (i.e., the EML and moist layer), and the establishment of the relationship of the lid to the occurrence and nonoccurrence of severe local storms. The approach of analyzing the lid statistics and classifying the synoptic patterns over the southern Great Plains for the four-year study period results in a better understanding of the independent evolution of the EML and moist layer, and of how this evolution is affected by the changes in the large scale circulation during the spring. The classification scheme used in this study is unique in that it is not just a statistical procedure used to generate a set of patterns, but is based on a dynamical relationship (the thermal wind). That is, the simultaneous employment of the classification method at two levels allows us to obtain information about the thermal advection in the lower troposphere and how it relates to the formation of the lid stratification.

The synoptic climatology presented in Chapters 2-4 produces the following results concerning the formation and evolution of the EML, moist layer, and lid:

- 1) The appearance of the lid over the southern Great Plains has a periodic character, and a typical lid cycle has a mean period of about five to seven days.

- 2) There are two types of lid cycles, based on the synoptic flow pattern that initiates the cycle:
  - a) The H cycle begins with a surface anticyclonic incursion into the region, and is associated with the passage of baroclinic waves in the westerlies.
  - b) The R cycle begins with an already established moist layer within a persistent southerly flow from the Gulf of Mexico, and is associated with subtropical circulations and weak short wave features after the polar jet has retreated northward.
- 3) The life cycle of the lid has various stages that control the development of its component structures.
  - a) The high-pressure stage (observed only in the H cycle) exists when the EML forms over the western U.S. and cold, dry air dominates the Great Plains.
  - b) The return-flow stage is when the EML emerges into the western Plains and the moist layer begins to return into southern Texas after the surface anticyclone moves eastward; in the late-season R cycle the moist layer already exists over the Great Plains as there is no polar anticyclone over the region.
  - c) The large lid-coverage stages prevail when the EML begins to phase together with the moist layer, forming the necessary stratification for a lid sounding; this stage is further divided into pre-lid-maximum, lid-maximum, and post-lid-maximum stages.



- d) The end stage is when a surface front and/or upper trough move through the Great Plains and transport the EML out of the area by cutting off the source region; in the early spring, a polar anticyclone follows the front into the region and replaces the moist layer with cold, dry air, signalling the start of a new cycle.

The synoptic climatology reveals the following facts about the seasonal evolution of the lid environment.

- 1) The classic flow regime associated with the Carlson-Ludlam lid conceptual model (i.e., a strong low level southerly flow with southwest flow aloft), is observed most often in April and May, during which time it accounts for a large percentage of lid occurrences and the largest mean lid-coverage areas.
- 2) By midspring, the Rocky Mountains and the Great Basin of the U.S. have become EML source regions, and increasing surface evapotranspiration exists over the moist soil areas of the southern Plains. The result is that the lid begins to appear with additional flow patterns besides the classic southwesterly type.
- 3) By late spring, the lid appears more often in flow patterns associated with large scale subsidence, such as midlevel northwesterly and anticyclonic flows. In such situations, the lid base lowers from the source region eastward, in stark contrast to the southwesterly flow type in which the lid base gradually rises in an environment of large scale ascent.

- 4) The lid-coverage area expands northward during the spring, from the southern Plains states in April into the northern Plains by June. This northward expansion is controlled mostly by the expansion of the EML source region as outlined in (2). The maximum lid-frequency axis shifts westward during the season, through the east-central portions of Texas, Oklahoma, and Kansas in April, and from southwest Texas into the western portions of Kansas and Nebraska by June. This westward shift is controlled mostly by the westward shift in the mean  $\theta_w$  axis and the appearance of high  $\theta_w$  values along the Gulf coast, with the latter resulting in an increased occurrence of uncapped EML soundings over this area.

The synoptic climatology also examines the relationship between the occurrence/size of the lid and the occurrence/size of severe weather outbreaks.

- 1) There is a relationship between the size of a severe weather outbreak and the area of the antecedent lid. This relationship is best defined in April, and deteriorates rapidly from May to June. Within the lid-coverage area, the size of the area with buoyancy term  $\leq -2^\circ\text{C}$  has the best correlation with the size of severe weather events in all three months.
- 2) In early-spring H lid cycles, the high-pressure, return-flow, and end stages are associated with isolated severe weather events and with non events. There is a well-defined

relationship between severe-weather outbreak size and antecedent lid area during the large lid-coverage stages of the early-season H cycle, with the peak lid/severe weather activity appearing in the lid-maximum and post-lid-maximum stages.

- 3) In late spring, both the H and R lid cycles are capable of supporting severe weather outbreaks at all stages, and in the H cycle, the peak severe weather/lid activity occurs during the lid-maximum stage. In the R cycle, there is no clear relationship between lid coverage and severe weather, as large areas of low level moisture and buoyantly unstable air are present throughout the cycle, and the synoptic pattern mainly controls the evolution of the EML.
- 4) In the H cycle, examination of composite mean analyses from representative synoptic types shows that there is a fairly clear geographic relationship between the mean location of the antecedent lid edge and the appearance of severe weather events. In the pre-lid-maximum stage, the events are observed in the vicinity of and along the western and northern lid edges. During the lid-maximum stage, events are observed both along the lid-edge zones as well as within the high lid-frequency regions, a result of both lid-edge convection as well as convection associated with lid removal in the interior.
- 5) In the R cycle, composite mean analyses of two frequently occurring synoptic types show that when the Bermuda

anticyclone dominates the eastern half of the U.S., the majority of severe weather events are reported in a region of low-level cyclonic flow and weak vertical shear. A buoyant instability gradient and localized potential instability characterize this environment, and are influenced by the presence of both an EML as well as a subsidence layer, the latter originating in the western branch of the Bermuda cell. The analyses representing the period when the Pacific anticyclone dominates the western half of the U.S. shows that the majority of severe weather events occur to the east of the lid edge, in a region of buoyant instability and strong directional shear, especially between the surface and 850' mb.

The case study examined in Chapters 5 and 6 illustrates how case-dependent characteristics of the atmospheric structure are superimposed on the general features defined in the synoptic climatology. Aspects of EML genesis during the high-pressure stage were examined using a combination of conventional data and mesoscale model output. Two EML source regions for this case were identified over the Desert Southwest and northern Mexico. The EML source-region analyses and model-generated parcel trajectories reveal that it is very difficult to generalize the EML's evolution because the composition of an individual sounding is a result of airstream trajectories which are not always isentropic, or homogeneous in terms of source region and potential temperature characteristics. *The nascent EML does not move in a uniform direction as a single, homogeneous airmass.* Instead, one must examine different areas of the EML source region in order to determine the importance of

various dynamic and physical processes in generating and maintaining the EML source region and elevated areas.

In this case, the presence of strong directional shear between the low level easterlies and midlevel westerlies over northern Mexico during the high-pressure stage results in the superposition of airstreams from vastly different source regions with different thermal characteristics, and causes the stabilization of this layer during the 12-24 h period of the cycle. North of the subtropical jet, a combination of low-level diabatic heating and layer stretching results in the "northward transport" of a low static stability layer into Wyoming and Montana during the same period. During the 24-48 h period, a combination of diabatic heating in the PBL and dynamical processes allows the EML source region over the western U.S. to continue developing, and allows the Mexican source region to redevelop. Over northern Mexico, the appearance of a strong southwesterly jet crossing the Sierra Madre Occidental results in a mountain-wave circulation and lee-side low level jet. The layer crossing this region is destabilized by this circulation, because of differential subsidence and vertical stretching of the layer downstream over the northern Mexican plateau. The model trajectories reveal that the higher  $\theta$  values in the Mexican EML source region are a result of the downward transport of high  $\theta$  air in the subsiding layer that originates over the subtropical oceanic region. By the time this EML reaches Texas and forms a lid over the moist layer, it is undergoing further destabilization from layer stretching associated with strong upward motion occurring within the upper diffluent/divergent zone between the subtropical and polar jets over Texas.

Perhaps the most interesting result from the case study is that regarding the creation and evolution of the moist layer. Use of conventional analyses, satellite imagery, and model output reveals that the moist layer originates as a continental airstream in the offshore flow at the beginning of the cycle and undergoes modification over the western Gulf waters during the first 24 h of the cycle. The low cloud layer observed along coastal Mexico in the high-pressure and return-flow stages results from upslope motion of the moist-layer airstreams approaching the coastal area. Vertical motion plays an important role in the moist layer's evolution, since the airstreams spend only a limited time in the marine PBL environment before rising above it and undergoing warming and drying as they travel northward along the eastern edge of the Mexican plateau. In the lid-maximum stage, the parcel trajectories show that the moist layer beneath the lid inversion originates in the continental midtroposphere before descending into the marine PBL over the western Gulf. Our results show that the southward movement of the surface anticyclone into the western Gulf (which is a commonly occurring feature according to the synoptic climatology) results in moist-layer trajectories that are vastly different from the Carlson-Ludlam conceptual model, in that they spend a limited time in the marine environment and are restricted to the western Gulf waters.

Another important result from the model simulation of the 4-9 April case is that the use of a large domain with relatively fine horizontal and vertical grid meshes, reduced horizontal and vertical diffusion coefficients, and carefully determined surface conditions (i.e., snow cover, SST, and soil moisture), allows for successfully creating and

maintaining the component structures of the lid environment, and reproducing the detailed vertical and horizontal structures observed over the southern Plains during the large lid-coverage stages. Equally important in such a simulation are the lateral boundary conditions, which make this simulation much like an operational forecast because the model boundaries are located in data-sparse regions where the analyses are largely determined by the operational model prediction.

## 7.2 Suggestions for Future Research

The synoptic climatology described in this study raises some important issues for future research on the lid/severe-storm environment. One issue that is potentially very important is the interannual variability in the occurrence of different types of synoptic patterns (e.g., the H and R lid cycles), and the onset of semipermanent circulation features (i.e., Bermuda and Pacific anticyclones) that delineate the early and late season lid cycles. A related question involves the effect of year-to-year changes in the mean positions and intensities of large scale troughs and ridges on the occurrence of the lid and severe weather. Regarding the sensitivity of the lid-cycle evolution to large scale surface conditions such as snow cover, soil moisture gradients, and SST conditions over the Gulf of Mexico, there is a need to examine the evolution of the lid cycle in "anomalous" years. Such anomalous years may include greater or less than normal snow cover over the Rockies, soil moisture anomalies (Lanucci et al. 1987), and SST anomalies over the Gulf and other oceanic areas. Such situations would be useful subjects for modeling sensitivity studies.

In the terms of the synoptic climatology, an interesting area for further study involves the transition period between the early-spring and late-spring lid regimes. Within this context, lid cycles could be further subdivided on the basis of the flow type that *ends the cycle*. Such a subdivision would reveal new information about the appearance of subtropical circulations within or at the end of H cycles, or polar-air outbreaks occurring at the end of R cycles. Along these same lines, analysis of longer wave influences on the lid cycle would also be of interest. Such longer waves could potentially be linked to circulation features with seasonal time scales, and may reveal the reasons why certain flow types, such as southwesterly, have a greater tendency to have a multi-day persistence than other types.

The case study discussed in Chapters 5 and 6 also suggests some interesting areas for additional study. The 4-9 April 1984 case illustrates how case-dependent characteristics of the atmospheric structure are superimposed on the general features of the early-season H cycle. It seems reasonable that examples of the late-season H and R cycles would yield similar results for those cycles. Especially in the case of the R cycle, a complementary modeling study would be useful in order to properly evaluate the roles that surface diabatic processes have in the creation of the late-season EML and persistent moist layer over the Great Plains. The selection of certain model parameterizations and development of adequate surface boundary conditions would likely be more difficult and challenging for a late-spring case than for an early-spring example.



## REFERENCES

- Anthes, R.A., 1977: A cumulus parameterization scheme utilizing a one-dimensional cloud model. *Mon. Wea. Rev.*, **105**, 270-286.
- Anthes R.A., and T.T. Warner, 1978: The development of mesoscale models suitable for air pollution and other mesometeorological studies. *Mon. Wea. Rev.*, **106**, 1045-1078.
- Anthes, R.A., Y.-H. Kuo, S.G. Benjamin, and Y.-F. Li, 1982: The evolution of the mesoscale environment of severe local storms: Preliminary modeling results. *Mon. Wea. Rev.*, **110**, 1187-1213.
- Anthes, R.A., E.-Y. Hsie, and Y.-H. Kuo, 1987: Description of the Penn State/NCAR Mesoscale Model Version 4 (MM4). NCAR/TN-282+STR, National Center for Atmospheric Research, Boulder CO, 66 pp.
- Arakawa, A., and V.R. Lamb, 1977: Computational design of the basic dynamical process of the UCLA general circulation model. *Methods in Computational Physics*, **17**, Academic Press, 173-265.
- Arritt, R.W., and G.S. Young, 1990: Elevated stable layers generated by mesoscale boundary-layer dynamics over complex terrain. *Preprints, Fifth Conference on Mountain Meteorology*, June 25-29, 1990, Boulder CO, Amer. Meteor. Soc., 114-117.
- Augustine, J.A., E.I. Tollerud, and B.D. Jamison, 1989: Distributions and other general characteristics of mesoscale convective systems during 1986 as determined from GOES infrared imagery. *Preprints, 12th Conference on Weather Analysis and Forecasting*, October 2-6, 1989, Monterey CA, Amer. Meteor. Soc., 437-442.
- Bartels, D.L., J.M. Skradski, and R.D. Menard, 1984: Mesoscale Convective Systems: A Satellite-Data-Based Climatology. NOAA Tech. Memo. ERL ESG-8, Boulder CO, 58 pp. Available from the National Technical Information Service, Springfield VA 22161 as PB85-187862.
- Beebe, R.G., 1956: Tornado composite charts. *Mon. Wea. Rev.*, **84**, 127-142.
- Beebe, R.G., 1958: Tornado proximity soundings. *Bull. Amer. Meteor. Soc.*, **39**, 195-201.
- Benjamin, S.G., 1983: Some Effects of Surface Heating and Topography on the Regional Severe Storm Environment. Ph.D. Thesis, Department of Meteorology, The Pennsylvania State University, University Park PA 16802, 265pp.

- Benjamin, S.G., 1986: Some effects of surface heating and topography on the regional severe-storm environment. Part II: Two-dimensional idealized experiments. *Mon. Wea. Rev.*, 114, 330-343.
- Benjamin, S.G., and T.N. Carlson, 1986: Some effects of surface heating and topography on the regional severe-storm environment. Part I: Three-dimensional simulation. *Mon. Wea. Rev.*, 114, 307-329.
- Benjamin, S.G., and N.L. Seaman, 1985: A simple scheme for objective analysis in curved flow. *Mon. Wea. Rev.*, 113, 1184-1198.
- Blackadar, A.K., 1976: Modeling the nocturnal boundary layer. *Preprints, Third Symposium on Atmospheric Turbulence, Diffusion and Air Quality*, October 19-22, 1976, Raleigh NC, Amer. Meteor. Soc., 46-49.
- Blackadar, A.K., 1979: High resolution models of the planetary boundary layer. *Advances in Environmental Science and Engineering*, 1, No. 1, Pfafflin and Ziegler, Eds., Gordon and Breach Sci. Pub., New York NY, 50-85.
- Brownlee, K.A., 1965: *Statistical Theory and Methodology in Science and Engineering*, 2nd Ed. Wiley and Sons, Inc., New York NY, pp. 413-414.
- Bryson, R.A., and W.P. Lowry, 1955: Synoptic climatology of the Arizona summer precipitation singularity. *Bull. Amer. Meteor. Soc.*, 36, 329-339.
- Bryson, R.A., and F.K. Hare, 1974: The climates of North America. In *World Survey of Climatology*. Vol. 11: *Climates of North America*, H.E. Landsberg, Ed. Elsevier Scientific, 1-47.
- Caracena, F., and J.M. Fritsch, 1983: Focusing mechanisms in the Texas Hill Country flash floods of 1978. *Mon. Wea. Rev.*, 111, 2319-2332.
- Carleton, A.M., 1985: Synoptic and satellite aspects of the Southwestern U.S. summer 'monsoon.' *J. Climatology*, 5, 389-402.
- Carleton, A.M., 1986: Synoptic-dynamic character of "bursts" and "breaks" in the Southwestern U.S. summer precipitation singularity. *J. Climatology*, 6, 605-623.
- Carleton, A.M., 1987: Summer circulation climate of the American Southwest. *Ann. Assoc. Amer. Geog.*, 77, 619-634.
- Carlson, T.N., R.A. Anthes, M.N. Schwartz, S.G. Benjamin, and D.G. Baldwin, 1980: Analysis and prediction of severe storms environment. *Bull. Amer. Soc.*, 61, 1032.

- Carlson, T.N., S.G. Benjamin, G.S. Forbes, and Y.-F. Li, 1983: Elevated mixed layers in the severe storm environment-Conceptual model and case studies. *Mon. Wea. Rev.*, 111, 1453-1473.
- Carlson, T.N., and F.H. Ludlam, 1968: Conditions for the formation of severe local storms. *Tellus*, 20, 203-226.
- Carlson, T.N., and J.M. Prospero, 1972: The large scale movement of Saharan air outbreaks over the North equatorial Atlantic. *J. Appl. Meteor.*, 11, 283-297.
- Cressman, G.P., 1959: An operative objective analysis scheme. *Mon. Wea. Rev.*, 87, 367-374.
- Cunning, J.B., 1986: The Oklahoma-Kansas preliminary regional experiment for STORM-Central. *Bull. Amer. Meteor. Soc.*, 67, 1478-1486.
- Darkow, G.L., 1969: An analysis of over sixty tornado proximity soundings. *Preprints, Sixth Conference on Severe Local Storms*, April 8-10, 1969, Chicago IL, Amer. Meteor. Soc., 218-221.
- Darkow, G.L., and M.G. Fowler, 1971: Tornado proximity sounding wind analysis. *Preprints, Seventh Conference on Severe Local Storms*, October 5-7, 1971, Kansas City MO, Amer. Meteor. Soc., 148-151.
- David, C.L., 1976: A study of upper air parameters at the time of tornadoes. *Mon. Wea. Rev.*, 104, 546-551.
- Davies, H.C., and R.E. Turner, 1977: Updating prediction models by dynamical relaxation: An examination of the technique. *Quart. J. Roy. Meteor. Soc.*, 103, 225-245.
- Davies, J.M., 1989: On the use of shear magnitudes and hodographs in tornado forecasting. *Preprints, 12th Conference on Weather Analysis and Forecasting*, October 2-6, 1989, Monterey CA, Amer. Meteor. Soc., 219-224.
- DiMego, G.J., L.F. Bosart, and G.W. Endersen, 1976: An examination of the frequency and mean conditions surrounding frontal incursions into the Gulf of Mexico and Caribbean Sea. *Mon. Wea. Rev.*, 104, 709-718.
- Djuric, D., and D.S. Ladwig, 1983: Southerly low-level jet in the winter cyclones of the southwestern Great Plains. *Mon. Wea. Rev.*, 111, 2275-2281.
- Doswell, C.A. III, 1987: The distinction between large-scale and mesoscale contribution to severe convection: A case study example. *Wea. Forecasting*, 2, 3-16.

- Doswell, C.A. III, 1990: Comments on "A Winter Mesocyclone over the Midwestern United States". *Wea. Forecasting*, 5, 162-165.
- Doswell, C.A., III, F. Caracena, and M. Magnano, 1985: Temporal evolution of 700-500 mb lapse rate as a forecasting tool---A case study. *Preprints, 14th Conference on Severe Local Storms*, October 29-November 1, 1985, Indianapolis IN, Amer. Meteor. Soc., 398-401.
- Farrell, R.J., 1988: The Role of a Lid in the 31 May 1985 Tornado Outbreak. M.S. Thesis, The Pennsylvania State University, University Park PA 16802, 158 pp.
- Farrell, R.J., and T.N. Carlson, 1989: Evidence for the role of the lid and underrunning in an outbreak of tornadic thunderstorms. *Mon. Wea. Rev.*, 117, 857-871.
- Fawbush, E.J., R.C. Miller, and L.G. Starrett, 1951: An empirical method of forecasting tornado development. *Bull. Amer. Meteor. Soc.*, 32, 1-9.
- Fawbush, E.J., and R.C. Miller, 1952: A mean sounding representative of the tornadic airmass environment. *Bull. Amer. Meteor. Soc.*, 33, 303-307.
- Fawbush, E.J., and R.C. Miller, 1954: The types of airmasses in which North American tornadoes form. *Bull. Amer. Meteor. Soc.*, 35, 154-165.
- Fawbush, E.J., R.C. Miller, and L.G. Starrett, 1957: Severe local storms and mid-tropospheric flow patterns. *Bull. Amer. Meteor. Soc.*, 38, 115-123.
- Ferrel, W., 1885: Recent Advances in Meteorology. Report of the Chief Signal Officer for 1885, Appendix 71, 324-325, 327.
- Finley, J.P., 1890: Tornadoes. *Amer. Meteor. J.*, 7, 165-179.
- Galway, J.G., 1956: The lifted index as a prediction of latent instability. *Bull. Amer. Meteor. Soc.*, 37, 528-529.
- Galway, J.G., 1977: Some climatological aspects of tornado outbreaks. *Mon. Wea. Rev.*, 105, 477-484.
- Giordano, L.A., 1987: Northwest Flow Aloft and Strong Convective Events Within the Mid-Atlantic States. M.S. Thesis, The Pennsylvania State University, University Park PA 16802, 75 pp.
- Gutnick, M., 1958: Climatology of the trade-wind inversion in the Caribbean. *Bull. Amer. Meteor. Soc.*, 39, 410-420.

- Graziano, T.M., and T.N. Carlson, 1987: A statistical evaluation of lid strength on deep convection. *Wea. Forecasting*, 2, 127-139.
- Hagemeyer, B.C., and G.L. Darkow, 1988: Tropical easterlies as a source of extreme potential convective instability for mid-latitude severe storm generation. *Preprints, 15th Conference on Severe Local Storms*, February 22-26, 1988, Baltimore MD, Amer. Meteor. Soc., 263-266.
- Henry, W.K., 1979: Some aspects of the fate of cold fronts in the Gulf of Mexico. *Mon. Wea. Rev.*, 107, 1078-1082.
- Henry, W.K., and A.H. Thompson, 1976: An example of polar air modification over the Gulf of Mexico. *Mon. Wea. Rev.*, 104, 1324-1327.
- Humphreys, W.J., 1926: The tornado. *Mon. Wea. Rev.*, 54, 501-503.
- Johns, R.H., 1982: A synoptic climatology of Northwest flow severe weather outbreaks. Part I: Nature and significance. *Mon. Wea. Rev.*, 110, 1653-1663.
- Johns, R.H., 1984: A synoptic climatology of Northwest flow severe weather outbreaks. Part II: Meteorological parameters and synoptic patterns. *Mon. Wea. Rev.*, 112, 449-464.
- Johns, R.H., and W.R. Sammler, 1989: A preliminary synoptic climatology of violent tornado outbreaks utilizing radiosonde standard level data. *Preprints, 12th Conference on Weather Analysis and Forecasting*, October 2-6, 1989, Monterey CA, Amer. Meteor. Soc., 196-201.
- Johnson, J.R., 1976: The Origin, Structure, and Modification of Return Flow over the Gulf of Mexico. M.S. Thesis, Dept. of Meteorology, Texas A&M University, College Station TX 77843, 69 pp.
- Karayampudi, V.M., 1986: A Numerical Study of the Evolution Structure, and Energetics of the Saharan Air Layer. Ph.D. Dissertation, The Pennsylvania State University, University Park PA 16802, 287 pp.
- Karyampudi, V.M., and T.N. Carlson, 1988: Analysis and numerical simulation of the Saharan air layer and its effect on easterly wave disturbances. *J. Atmos. Sci.*, 45, 3102-3136.
- Karnavas, G.R., 1978: On Polar Air Modification Over the Gulf of Mexico During Periods of Return Flow and Development of Low Clouds. M.S. Thesis, Department of Meteorology, Texas A&M University, College Station TX 77843, 69 pp.

- Kelly, D.L., J.T. Schaefer, R.P. McNulty, C.A. Doswell III, and R.F. Abbey Jr., 1978: An augmented tornado climatology. *Mon. Wea. Rev.*, 106, 1172-1183.
- Kelly, D.L., J.T. Schaefer, and C.A. Doswell III, 1985: Climatology of nontornadic severe thunderstorm events in the United States. *Mon. Wea. Rev.*, 113, 1997-2014.
- Keyser, D., and T.N. Carlson, 1984: Transverse ageostrophic circulations associated with elevated mixed layers. *Mon. Wea. Rev.*, 112, 2465-2478.
- Kuo, H.L., 1974: Further studies of the parameterization of the influence of cumulus convection on large-scale flow. *J. Atmos. Sci.*, 31, 1232-1240.
- Lakhtakia, M.N., and T.T. Warner, 1987: A real-data numerical study of the development of precipitation along the edge of an elevated mixed layer. *Mon. Wea. Rev.*, 115, 156-168.
- Lanicci, J.M., 1984: The Influence of the Soil Moisture Distribution on the Severe-Storm Environment of the Southern Great Plains: A Numerical Study of the SESAME IV Case. M.S. Thesis, Department of Meteorology, The Pennsylvania State University, University Park PA 16802, 237 pp.
- Lanicci, J.M., T.N. Carlson, and T.T. Warner, 1987: Sensitivity of the Great Plains severe-storm environment to soil-moisture distribution. *Mon. Wea. Rev.*, 115, 2660-2673.
- Lanicci, J.M., and T.T. Warner, 1991a: A synoptic climatology of the elevated mixed-layer inversion over the southern Great Plains in Spring. Part 1: Structure, dynamics, and seasonal evolution. Accepted in *Wea. Forecasting*.
- Lanicci, J.M., and T.T. Warner, 1991b: A synoptic climatology of the elevated mixed-layer inversion over the southern Great Plains in Spring. Part 2: The life cycle of the lid. Accepted in *Wea. Forecasting*.
- Lanicci, J.M., and T.T. Warner, 1991c: A synoptic climatology of the elevated mixed layer inversion over the southern Great Plains in Spring. Part 3: Relationship to severe-storms climatology. Accepted in *Wea. Forecasting*.
- Lewis, J., and C. Crisp, 1989: Climatology of return flow in the Gulf of Mexico. *Preprints, 12th Conference on Weather Analysis and Forecasting*, October 2-6, 1989, Monterey CA, Amer. Meteor. Soc., 490-493.

- Lewis, J.M., C.M. Hayden, R.T. Merrill, and J.M. Schneider, 1989: GUFMEX: A study of return flow in the Gulf of Mexico. *Bull. Amer. Meteor. Soc.*, 70, 24-29.
- Livingston, R.L., and L.F. Wilson, 1986: Relating antecedent surface conditions to violent tornado-producing thunderstorms. *Preprints, 11th conference on Weather Analysis and Forecasting*, June 17-20, 1986, Kansas City MO, Amer. Meteor. Soc., 229-234.
- Lloyd, J.R., 1942: The development and trajectory of tornadoes. *Mon. Wea. Rev.*, 70, 65-75.
- Maddox, R.A., 1976: An evaluation of tornado proximity wind and stability data. *Mon. Wea. Rev.*, 104, 133-142.
- Maddox, R.A., 1983: Large-scale meteorological conditions associated with midlatitude, mesoscale convective complexes. *Mon. Wea. Rev.*, 111, 1475-1493.
- Maddox, R.A., and C.A. Doswell III, 1982a: An examination of jet stream configurations, 500mb vorticity advection and low-level thermal advection patterns during extended periods of intense convection. *Mon. Wea. Rev.*, 110, 184-197.
- Maddox, R.A., and C.A. Doswell III, 1982b: Forecasting severe thunderstorms: A brief consideration of some accepted techniques. *Nat. Wea. Dig.*, 110, 26-30.
- Mahrt, L., 1976: Mixed layer moisture structure. *Mon. Wea. Rev.*, 104, 1403-1407.
- McNulty, R.P., 1978: On upper tropospheric kinematics and severe weather occurrence. *Mon. Wea. Rev.*, 106, 662-672.
- McNulty, R.P., 1980: Differential advection of wet-bulb potential temperature and convective development: An evaluation. *Preprints, Eighth Conference on Weather Analysis and Forecasting*, June 10-13, 1980, Denver CO, Amer. Meteor. Soc., 286-291.
- Means, L.L., 1952: On thunderstorm forecasting in the central United States. *Mon. Wea. Rev.*, 80, 165-189.
- Miller, R.C., 1959: Tornado-producing synoptic patterns. *Bull. Amer. Meteor. Soc.*, 40, 465-472.
- Miller, R.C., 1972: Notes on Analysis and Severe-Storm Forecasting Procedures of the Air Force Global Weather Central. Air Weather Service Tech. Rep. 200 Rev. (AWSTR-200), HQ Air Weather Service, Scott AFB IL.

- Molinari, R.L., 1987: Air mass modification over the eastern Gulf of Mexico as a function of surface wind fields and the Loop Current position. *Mon. Wea. Rev.*, 115, 646-652.
- Moller, A.R., 1979: The Climatology and Synoptic Meteorology of Southern Plains Tornado Outbreaks. M.S. Thesis, University of Oklahoma, Norman OK, 70 pp.
- Notis, C., and J.L. Stanford, 1973: The contrasting synoptic and physical character of northeast and southeast advancing tornadoes in Iowa. *J. Appl. Meteor.*, 12, 1163-1173.
- Orlanski, I., 1975: A rational subdivision of scales for atmospheric processes. *Bull. Amer. Meteor.*, 56, 527-530.
- Parker, S.S., J.T. Hawes, S.J. Colucci, and B.P. Hayden, 1989: Climatology of 500-mb cyclones and anticyclones, 1950-85. *Mon. Wea. Rev.*, 117, 558-570.
- Reed, T.R., 1933: The North American high-level anticyclone. *Mon. Wea. Rev.*, 61, 321-325.
- Reed, T.R., 1937: Further observations of the North American high-level anticyclone. *Mon. Wea. Rev.*, 65, 364-366.
- Rhea, J.O., 1966: A study of thunderstorm formation along dry lines. *J. Appl. Meteor.*, 5, 58-63.
- Riehl, H., 1945: Subtropical Flow Patterns in Summer. Miscellaneous Reports No. 22, Department of Meteorology, University of Chicago, Chicago IL.
- Rockwood, A.A. and R. A. Maddox, 1988: Mesoscale and synoptic scale interactions leading to intense convection: The case of 7 June 1982. *Wea. Forecasting*, 3, 51-68.
- Sanders, F., 1988: A climatology of intense convective systems. *Preprints, 15th Conference on Severe Local Storms*, February 22-26, 1988, Baltimore MD, Amer. Meteor. Soc., 520-522.
- Schaefer, J.T., 1973: The Motion and Morphology of the Dryline. NOAA Tech. Memo. ERL NSSL-66, U.S. Dept. of Commerce (NOAA), National Severe Storms Laboratory, Norman OK 73069, 81pp.
- Schaefer, J.T., 1974: The life cycle of the dryline. *J. Appl. Meteor.*, 13, 444-449.
- Schaefer, J.T., 1983: On the synoptic differentiation between tornado outbreak types. *Preprints, 13th Conference on Severe Local Storms*, October 17-20, 1983, Tulsa OK, Amer. Meteor. Soc. 142-145.



- Schaefer, J.T., 1986: The dryline. *Mesoscale Meteorology and Forecasting*, P.S. Ray, Ed., American Meteorological Society, Boston MA, 549-572.
- Schaefer, J.T., and C.A. Doswell III, 1984: Empirical orthogonal function expansion applied to progressive tornado outbreaks. *J. Meteor. Soc. Japan*, 62, 929-936.
- Schaefer, J.T., and J.G. Galway, 1982: Population biases in the tornado climatology. *Preprints, 12th Conference on Severe Local Storms*, January 12-15, 1982, San Antonio TX, Amer. Meteor. Soc., 51-54.
- Schaefer, J.T., and R.L. Livingston, 1988: The structural characteristics of tornado proximity soundings. *Preprints, 15th Conference on Severe Local Storms*, February 22-26, 1988, Baltimore MD, Amer. Meteor. Soc., 537-540.
- Seaman, N.L., J.S. Chang, D.R. Stauffer, and P. Middleton, 1991: Four-dimensional data assimilation used in a meteorological model for regional acid deposition studies. Submitted to *J. Appl. Meteor.*
- Showalter, A.K., and J.R. Fulks, 1943: A Preliminary Report on Tornadoes: The Tornado, an Analysis of Antecedent Meteorological Conditions. U.S. Weather Bureau, Washington DC, 162pp. Reprinted by U.S. Office of Naval Operations as NAVAER 50-1R-41, 1950.
- Smagorinsky, J., S. Manabe, and J.L. Holloway, Jr., 1965: Numerical results from a nine-level general circulation model of the atmosphere. *Mon. Wea. Rev.*, 93, 727-768.
- Tang, M., and E.R. Reiter, 1984: Plateau monsoons of the Northern Hemisphere: A comparison between North America and Tibet. *Mon. Wea. Rev.*, 112, 617-637.
- Tilley, J.S., 1990: On the Application of Edge Wave Theory to Terrain-Bounded Cold Surges: A Numerical Study. Ph.D. Dissertation, Department of Meteorology, Pennsylvania State University, University Park PA 16802, 353 pp.
- Tollerud, E.I., and D.L. Bartels, 1988: A comparative study of the environment of severe-weather-producing mesoscale convective systems: MCCs, meso-beta systems, and large convective lines. *Preprints, 15th Conference on Severe Local Storms*, February 22-26, 1988, Baltimore MD, Amer. Meteor. Soc., 544-547.
- Uccellini, L. W., 1980: On the role of upper tropospheric jet streaks and leeside cyclogenesis in the development of low-level jets in the Great Plains. *Mon. Wea. Rev.*, 108, 1689-1696.

- Uccellini, L.W., and D.R. Johnson, 1979: The coupling of upper and lower tropospheric jet streaks and implications for the development of severe convective storms. *Mon. Wea. Rev.*, 107, 682-703.
- Varney, B.M., 1926: Aerological evidence as to the causes of tornadoes. *Mon. Wea. Rev.*, 54, 163-165.
- Velasco, I., and J.M. Fritsch, 1987: Mesoscale convective complexes in the Americas. *J. Geophys. Res.*, 92, No. D8, 9591-9613.
- Wade, G.S., C.M. Hayden, J.M. Lewis, and R.T. Merrill, 1988: Modification of air masses over the Gulf of Mexico - Progress report from a VAS viewpoint. *Preprints, 15th Conference on Severe Local Storms*, February 22-26, 1988, Baltimore MD, Amer. Meteor. Soc., 484-487.
- Washington, W.M., and D. P. Baumhefner, 1975: A method of removing Lamb waves from initial data for primitive equation models. *J. Appl. Meteor.*, 14, 114-119.
- Weiss, S.J., 1989: An examination of NMC numerical model forecasts of surface (MSL) pressure preceding three cool season severe storm outbreaks. *Preprints, 12th Conference on Weather Analysis and Forecasting*, October 2-6, 1989, Monterey CA, Amer. Meteor. Soc., 606-611.
- Wexler, H., and J. Namias, 1938: Mean monthly isentropic charts and their relation to departures of summer rainfall. *Trans. Amer. Geophys. Union*, 19, 164-170.
- Whitney, L.F., 1977: Relationship of the subtropical jet stream to severe local storms. *Mon. Wea. Rev.*, 105, 398-412.
- Wiesnet, D.R., C.F. Ropelewski, G.J. Kukla, and D.A. Robinson, 1987: A discussion of the accuracy of NOAA satellite-derived global seasonal snow cover measurements. *Large Scale Effects of Seasonal Snow Cover (Proceedings of the Vancouver Symposium, August 1987)*, IAHS Publ. NO. 166, 291-304.
- Willis, T.G., 1969: Characteristics of the tornado environment as deduced from proximity soundings. *Preprints, Sixth Conference on Severe Local Storms*, April 8-10, 1969, Chicago IL, Amer. Meteor. Soc., 222-229.
- Williams, R.J., 1976: Surface parameters associated with tornadoes. *Mon. Wea. Rev.*, 104, 540-545.
- Zhang, D.-L, and R.A. Anthes, 1982: A high-resolution model of the planetary boundary layer - Sensitivity tests and comparisons with SESAME-79 data. *J. Appl. Meteor.*, 21, 1594-1609.

## VITA

John M. Lanicci was born in the Bronx, New York, on January 18, 1957. He graduated in 1975 from Clarkstown North High School in New City, New York. He attended Manhattan College, Bronx, New York, on a four-year Air Force ROTC scholarship, graduated summa cum laude with a Bachelor of Science degree in Physics in 1979, and was commissioned as an officer in the U.S. Air Force. Under Air Force sponsorship, he received a Bachelor of Science degree with highest distinction in Meteorology from Penn State in 1980, and a Master of Science degree in Meteorology from Penn State in 1984.

John Lanicci's military decorations include the Air Force Meritorious Service Medal with oak leaf cluster, the Air Force Commendation Medal, the Air Force Achievement Medal, and the National Defense Service Medal. He is a member of the American Meteorological Society, the National Weather Association, and a half-dozen honorary societies. His research interests over the last 10 years have been concentrated in numerical weather prediction, severe local storms, wind flow over complex terrain, and applied climatology. His professional publications include four Air Force technical reports, and papers in *Monthly Weather Review* and *Weather and Forecasting*.

John Lanicci is married to the former Kathleen Benson of South Nyack, New York. They have two sons, Michael, 9 and Mark, 5.